ON-SITE FLEXIBLE ROTOR BALANCING AND CRACK CHARACTERIZATION IN ROTOR-BEARING SYSTEM THROUGH VIRTUAL EXCITATION BY ACTIVE MAGNETIC BEARINGS

A Thesis Submitted in Partial Fulfillment of the Requirements for the Degree of

DOCTOR OF PHILOSOPHY

by

GYAN RANJAN

(Roll no. 176103027)

DEPARTMENT OF MECHANICAL ENGINEERING

INDIAN INSTITUTE OF TECHNOLOGY GUWAHATI

GUWAHATI 781039, INDIA

NOVEMBER 2022

TH-2966_176103027

TH-2966_176103027

Department of Mechanical Engineering
Indian Institute of Technology Guwahati
Guwahati-781039, INDIA

CERTIFICATE

It is certified that the work contained in the thesis titled "**On-Site Flexible Rotor Balancing and Crack Characterization in Rotor-Bearing System Through Virtual Excitation by Active Magnetic Bearings"** submitted by **Mr. Gyan Ranjan** (Roll. no. 176103027) to the Indian Institute of Technology Guwahati for the award of the degree of Doctor of Philosophy has been carried out under my supervision in the Department of Mechanical Engineering, Indian Institute of Technology Guwahati. This work has not been submitted elsewhere for the award of any other degree or diploma.

November 2022

Dr. Rajiv Tiwari
Professor
Department of Mechanical Engineering
Indian Institute of Technology Guwahati
Guwahati – 781039, INDIA

TH-2966_176103027

TH-2966_176103027



This thesis is dedicated to my parents, Vijay, Saroj, and my brother Shashi for their constant support and unconditional love

TH-2966_176103027

TH-2966_176103027

ACKNOWLEDGMENTS

While bringing out this thesis to its final form, I came across a number of people whose contributions in various ways helped my field of research, and I would like to convey my gratitude to all of them.

First and foremost, I would like to express my deep sense of gratitude and indebtedness to my supervisors, Prof. Rajiv Tiwari and Prof. H. B. Nemade, for their invaluable support, suggestions, and encouragement that provided me with an extraordinary experience throughout my research work. The insightful and meticulous suggestions provided by them have helped me to find solutions for the problems and widen my research work. I would like to especially thank Prof. Rajiv Tiwari for having faith in me and for providing me this opportunity and time to work on such an exciting area of Rotor Dynamics. It is a great honor to be a part of his research family, and I hope to learn and correspond with him in the future days.

The thesis work would have been incomplete without the suggestions and support from my doctoral committee members comprising Prof. Debabrata Chakraborty, Dr. Arup Nandi, and Prof. Praveen Kumar. Their useful insights and comments throughout my progress seminars have helped me to shape my research work in the proper way.

I would like to thank the Department of Mechanical Engineering, IIT Guwahati, for providing me with the infrastructure to carry out my research work. I am grateful to receive the MHRD fellowship that helped me to be financially stable in my personal and research life.

TH-2966_176103027

I sincerely thank Dr. Dhrubajyoti Bordoloi for providing me with constant help and support in both analytical and experimental work that has been carried out in the Vibration and Acoustics Laboratory. I would also like to thank Mr. N. K. Das and all the members of the Mechanical Workshop, along with the members of TRTC Amingaon, Guwahati, who contributed to developing my experimental rotor test rig.

This journey would have been incomplete without the cooperation and support extended by my lab mates Dr. Dipendra Kumar Roy, Dr. Nilakshi Sarmah, Dr. Prabhat Kumar, Ms. Gargi Mazumdar, Dr. Purushottom Gangser, and Dr. Janani Shruti Rapur. The interesting discussions related to research and all the fun activities have helped me to get through my stay at IIT Guwahati. I would also thank my colleagues and friends of Vibration and Acoustics Laboratory, Mr. Pantha Pradeep Das, Mr. Atul Gautam, Mr. Raghavendra Rohit, Mr. Pravin Telshinge, Mr. Chitranjan Goel, Mr. Rahul Ray, Mr. Thashreef P. A., and Ms. Twinkle Mandawat, for their cooperation and creating a positive environment in the laboratory. I would also like to thank Mr. Deepak Kumar and Mr. Animesh Kundu for making my stay at IITG memorable.

My parents, Vijay and Saroj, and my brother Shashi have been a great source of inspiration for me, and I am thankful for all their love and support that has kept me standing against all the hurdles in my life. Their faith in me and my decisions has helped me to remain focused on my work. Finally, I would like to express my gratitude and thanks to the Almighty for providing me with this life and the courage to grow and prosper.

"Research is to see what everybody else has seen and to think what nobody else has thought."

November 2022 **Gyan Ranjan**

TH-2966_176103027

ABSTRACT

The conventional influence coefficient method is being widely utilized for on-site balancing of the rotor system. For the balancing of the flexible rotor, the system is required to be operated above critical speeds, which is difficult in the presence of residual unbalances. Also, repetitive stopping and the opening and closing of the casing of the rotor system for the manual addition of trial unbalances (conventional method), the system may get contaminated with foreign particles. To solve the above difficulties, a new balancing method has been proposed using the Virtual Trial Excitation Influence Coefficient Method (VTEICM) for a flexible rotor system integrated with Active Magnetic Bearing (AMB). The AMB is utilized for both controlling vibrations while accelerating through various critical speeds during measurements and generating virtual trial unbalance (VTU) as magnetic excitation. The VTU allows the identification of unbalances with a lesser number of rotor runs and manual effort than the conventional method. Initially, for numerical illustration of the VTEICM, the mathematical model of the rotor-AMB system is developed using the finite element method. The effectiveness of the VTEICM is shown through the balancing of the rotor-AMB system with the estimated unbalances.

However, the occurrence of failure in the system while surpassing critical speed even in the presence of a control structure is required to be reduced. The periodic balancing of the flexible rotor system with the change in the level of unbalances is required to be carried out while operating the system at low speeds. A Virtual Excitation at Low-Speed for High-Speed Balancing (VELSHSB) technique is developed that utilizes the influence coefficients obtained at high speed and unbalances identified at the low speed to effectively

TH-2966_176103027

estimate the balance masses required for the high-speed flexible rotor balancing. The influence coefficients at high speeds are required to be obtained just once, whereas the balance masses can be estimated periodically by identifying the unbalances at low speeds. This method allows online condition monitoring of the system periodically with VTUs to reduce the impairment of high-speed machinery.

The dual rotor system is widely being utilized in aero-engines because of its compact structure and efficient operation. Due to the compact structure of the system, it is difficult to balance the rotor system with the manual addition of the trial unbalances. Hence, a novel balancing strategy, i.e., Multiple Virtual Excitation for Dual rotor Balancing (MVEDRB), has been utilized to balance the dual rotor system with AMB control and excitation. The low- and high-pressure rotor frequency excitation is generated through the AMB integrated into the inner rotor to estimate the residual unbalances in both the inner and outer rotor simultaneously. The excitation forces in the inner rotor affect the displacement responses in the outer rotor due to the coupling effect of the intermediate flexible bearing. The finite element modeling of the dual rotor system is carried out to generate the displacement responses for the validation of the developed balancing methodology.

There is a lot of practical difficulty in high-speed balancing with accelerating the rotor system above its critical speed in the presence of AMB. The control structure of the AMB requires a large magnitude of bias current to accommodate the excessive control current near the critical speed that increases the heating of coils and power consumption. So, the implementation of VTEICM for high-speed balancing of experimental rotor test rig supported on the conventional bearings and integrated with the AMB is also carried out. The control structure with PID controller is developed on dSPACE-SIMULINK

TH-2966_176103027

platform based on the differential driving mode control. To limit the utilization of bias current, the switching of bias current is performed that allows the rotor-AMB system to switch between high and low values of the bias current on the requirement. The practical difficulties in synchronizing the excitation frequency of VTU and operating speed are addressed with voltage/speed factor and phase-lag correction in the motor speed control unit.

Most of the research works on the cracked rotor system are carried out to analyze the fault signatures in the vibrational response or identify the system's faults based on the numerical model of the industrial systems. It would be beneficial to identify the faults parameters based on the system's response with the least knowledge of the rotating machinery. Therefore, in the present work, an identification algorithm is designed to obtain the fault parameters in the cracked rotor system integrated with AMB based on the Multiple Harmonic Influence Coefficient Method (MHICM). The identification algorithm requires only the vibrational response of the system and the values of multi-harmonic magnetic excitation generated through AMB. The internal damping due to the rubbing of crack faces or rotating components is also introduced to analyze the stability condition of the system. The present approach allows us to monitor the behavior of a fatigue crack in the system and to successfully estimate the additive crack stiffness, residual unbalances, and the internal damping factor in the system. The effectiveness of the present algorithm is verified through the numerical simulation as well as through experiments performed on the cracked rotor-AMB system.

TH-2966_176103027

TH-2966_176103027

TABLE OF CONTENTS

ABSTRACT ix

TABLE OF CONTENTS xiii

LIST OF FIGURES xxi

LIST OF TABLES xxxvi

NOMENCLATURE xxxix

CHAPTER 1

INTRODUCTION AND LITERATURE REVIEW 1

1.1. Significance of the study 1

1.2. Vibration-based fault detection techniques 2

1.2.1. Collection of vibration data 3

1.2.2 Signal processing 6

1.2.3 Diagnosis of rotor faults 8

1.3. Description of Various Rotor Faults 10

1.3.1 Unbalance 11

1.3.2 Shaft cracks 13

1.3.3 Misalignment 15

1.3.4 Residual shaft bow 16

1.4. Active vibration control with magnetic bearings 17

TH-2966_176103027

1.4.1 Actuator 19

1.4.2 Position Sensor 23

1.4.3 Amplifier 24

1.4.4 Controller 25

1.4.5 Functionality of the rotor-AMB system 31

1.5. Reduction of residual unbalances in rotor-AMB system 36

1.5.1. Offline balancing techniques 37

1.5.1.1. Rigid rotor balancing 38

1.5.1.2. Flexible rotor balancing 43

1.5.2. Online balancing techniques with AMB control 51

1.6. Multiple fault estimation in the cracked rotor with unbalances 54

1.7. Gaps in the literature survey 58

1.8. Proposed work 61

1.9. Outline of the thesis 63

CHAPTER 2

IN-SITU BALANCING OF FLEXIBLE ROTOR-BEARING SYSTEM INTEGRATED WITH ACTIVE MAGNETIC BEARING USING VIRTUAL TRIAL UNBALANCES 67

2.1. Introduction 67

2.2. Assumption and descriptions of the rotor-AMB system 69

TH-2966_176103027

2.3. Description of the Conventional and Virtual Trial Exciatation Influence Coefficient Method....70

2.3.1. Conventional Influence Coefficient Method....71

2.3.2. Formulation of Virtual Trial Excitation Influence Coefficient Method (VTEICM)....74

2.3.2.1. Introduction of virtual trial unbalance....74

2.3.2.2. Identification of force current factor (k_i)....77

2.3.2.3. Estimation of influence coefficients and residual unbalances....79

2.4. Finite Element Modelling of Rotor-AMB system....82

2.4.1 Flexible shaft....82

2.4.2 Rigid discs....85

2.4.3 Support bearings....85

2.4.4 Active Magnetic Bearings (AMBs)....86

2.4.5. Equations of motion of the overall system....88

2.5. Numerical Simulation of the Proposed Balancing Method....90

2.5.1 Vibration suppression with AMB....96

2.5.2 Estimation of the force current factor (k_i)....100

2.5.3 Estimation of the discrete and distributed unbalances....101

2.5.4 Comparison of percentage reduction in displacement amplitude obtained using different methods....105

2.5.5 Identification of suitable AMB location....107

TH-2966_176103027

2.6 Remarks 111

CHAPTER 3

IN-SITU BALANCING OF FLEXIBLE ROTOR-BEARING-AMB SYSTEM USING VIRTUAL TRIAL UNBALANCES AT SLOW RUN 113

3.1. Introduction 113

3.2. Estimation of influence coefficients at high speeds (One-time estimates) 114

3.3. Formulation of Virtual Excitation at Low-Speed for High-Speed Balancing (VELSHSB) method 118

3.4. Numerical simulations of the proposed balancing method 120

3.4.1. Evaluation of the mode shapes 125

3.4.2. Working of Virtual Excitation at Low-Speed for High-Speed Balancing (VELSHSB) method 128

3.4.2.1. Unbalance estimation using VTEICM with multiple AMB 130

3.4.2.2. Unbalance estimation using VELSHSB method 131

3.4.3. Verification of the identification algorithm 131

3.4.4. Unbalance estimation considering both discs and shaft unbalances 132

3.5. Remarks 142

CHAPTER 4

DYNAMIC BALANCING OF DUAL ROTOR-AMB SYSTEM THROUGH MULTIPLE VIRTUAL TRIAL UNBALANCES AS MAGNETIC EXCITATIONS 143

TH-2966_176103027

4.1. Introduction 143

4.2. Formulation of the Multiple Virtual Excitation for Dual rotor Balancing (MVEDRB) method 145

4.2.1. Initial run without additional excitation 146

4.2.2. Subsequent run with low-pressure rotor frequency (ω_L) excitation 147

4.2.3. Subsequent run with high-pressure rotor frequency (ω_H) excitation 148

4.2.4. Estimation of the residual unbalances 149

4.3. Finite element modelling of the dual rotor-AMB system 151

4.3.1. Discretization of high pressure and low pressure rotors 152

4.3.1.1. Flexible shafts with randomly distributed unbalances 153

4.3.1.2. Rigid discs with discrete unbalances 155

4.3.1.3. Support bearings and intermediate flexible bearings 156

4.3.1.4. Active magnetic bearing (AMB) 157

4.3.2. Assembled equation of motion of the rotor system 158

4.4. Simulation results 161

4.4.1 Vibration suppression in the dual-rotor system with AMB control 165

4.4.2 Unbalance estimation of dual-rotor system with AMB control and MVEDRB 170

4.4.2.1 Initial run of rotor system without external excitation 171

4.4.2.2 Additional low-pressure rotor frequency (ω_L) magnetic excitation at the AMB 171

4.4.2.3 Additional high-pressure rotor frequency (ω_H) magnetic excitation at the AMB 173

TH-2966_176103027

4.4.3 Balancing of dual-rotor system with AMB control 180

4.5. Concluding Remarks 183

CHAPTER 5

EXPERIMENTAL INVESTIGATION ON THE BALANCING OF HIGH-SPEED ROTOR-AMB SYSTEMS WITH SWITCHING MODE BIAS CURRENT CONTROL USING VIRTUAL TRIAL UNBALANCE 185

5.1. Introduction 185

5.2. Description of the Rotor-AMB Test-Rig 186

5.2.1 Electromagnetic actuator 188

5.2.2 Eddy current sensor 189

5.2.3 dSPACE-SIMULINK platform 190

5.2.4 Power Amplifier 192

5.2.4.1. PWM (Pulse Width Modulation) 194

5.2.4.1. H-bridge MOSFET driver 195

5.2.5. Current probes 195

5.3. Physical connection of the rotor-AMB system 196

5.4. Control Structure for High-Speed Operation with Switching Mode Control 197

5.5. Generation of Synchronized Virtual Trial Unbalances as Magnetic Excitations 204

5.6. Estimation of Residual Unbalances at High-Speed 210

5.6.1. Estimation of the phase and amplitude of the displacement signals 210

TH-2966_176103027

5.6.2. Estimation based on manually added trial unbalances (ICM) 213

5.6.3. Estimation based on virtual trial unbalances as magnetic excitation (VTEICM)..... 215

5.7 Remarks 221

CHPATER 6

ON-SITE ESTIMATION OF CRACKED ROTOR-AMB SYSTEM FAULT PARAMETERS USING MULTIPLE HARMONIC INFLUENCE COEFFICIENT METHOD 223

6.1. Introduction 223

6.2. Description of the cracked rotor-AMB system 224

6.3. Development of the Multi Harmonic Influence Coefficient Method 225

6.4. Finite Element Modelling of the cracked rotor-AMB system 231

6.4.1. Crack force 231

6.4.2. Internal damping force 235

6.4.3. Equations of motion of the rotor system 236

6.5. Numerical simulation of the proposed identification algorithm 238

6.5.1. Suppression of vibrational response using AMB control 243

6.5.2. Numerical estimation of AMB force current stiffness coefficient (k_i) 248

6.5.3. Estimation of fault parameters 250

6.6. Experimental identification of faults present in cracked rotor-AMB system 255

6.6.1 Electrical circuit 256

TH-2966_176103027

6.6.2 AMB control with run-up above the critical speed 258

6.6.3 Experimental estimation of the AMB current stiffness factor (k_i) 264

6.6.4 Estimation of fault parameter of cracked rotor system 264

6.6. Final Remarks 269

CHAPTER 7

CONCLUSIONS AND SCOPES FOR FUTURE WORK 273

7.1. Summary of Present Work 273

7.2. Major conclusions from the present work 276

7.3. Major contributions from present work 278

7.4. Limitations of the present work 279

7.5. Scope for future work 280

APPENDIX A. Influence Coefficient Matrices 283

APPENDIX B. Eigenvalues and damping coefficient estimation 285

APPENDIX C. Identification matrices 287

REFERENCES 289

List of Publications from the Present Research 319

TH-2966_176103027

LIST OF FIGURES

Fig. 1. 1. Types of transducers utilized in the measurement of vibration responses. 4

Fig. 1. 2. Unbalances in the rigid rotor system. 12

Fig. 1. 3. Transverse and slant cracked shaft. 14

Fig. 1. 4. Types of misalignments in the rigid rotor system. 16

Fig. 1. 5. Types of magnetic bearings. 17

Fig. 1. 6. Types of actuators in AMB system. 20

Fig. 1. 7. A schematic diagram of a) homopolar magnetic bearing, (b) 3-pole heteropolar magnetic bearing, c) 8-pole heteropolar magnetic bearing with field directions. 21

Fig. 1. 8. A block diagram showing different design factors considered in the design of actuators of AMB. 22

Fig. 1. 9. A block diagram showing different types of controllers utilized in the rotor system. 26

Fig. 1. 10. A line diagram of a (a) PD controller, (b) PI controller, and (c) PID controller system for the generation of control current. 27

Fig. 1. 11. A schematic of working of an adaptive control-based controller. 28

Fig. 1. 12. A schematic of an active magnetic bearing with a rotor. 33

Fig. 1. 13. A working AMB system in differential mode of a controller. 34

Fig. 1. 14. A schematic of a cradle balancing machine. 39

Fig. 1. 15. A schematic of rotor system (a) without trial unbalance (b) with trial unbalance on the left plane and (c) with trial unbalance on the right plane. 40

Fig. 1. 16. (a) A rigid rotor system and (b) flexible rotor system supported on conventional bearings 43

TH-2966_176103027

Fig. 1. 17. Distribution of measurement and balancing planes for flexible rotor balancing. 46

Fig. 2. 1. An illustrative representation of a flexible rotor-bearing system integrated with AMBs. 69

Fig. 2. 2. A line diagram of a flexible rotor-bearing system with residual unbalances and measurement locations. 71

Fig. 2. 3. A line diagram of a flexible rotor-bearing system with additional trial unbalance at the disc (D-1). 72

Fig. 2. 4. A line diagram of a flexible rotor-AMB system with residual unbalances and measurement locations. 76

Fig. 2. 5. A line diagram of a flexible rotor-AMB system with additional virtual trial unbalances at the AMB location. 80

Fig. 2. 6. The flexible shaft presenting different segments with randomly distributed unbalance forces. 84

Fig. 2. 7. The flexible rotor-AMB system is supported on conventional bearings (Model 1). 90

Fig. 2. 8. The distribution of the random shaft unbalances, and the discrete disc unbalances along the axis of the shaft. 91

Fig. 2. 9. Diagram of the rotor-AMB system model in SIMULINK. 91

Fig. 2. 10. Flow chart of the balancing procedure using conventional ICM and VTEICM for the flexible rotor system. 92

Fig. 2. 11. Campbell diagram of the rotor-AMB system depicting different forward and backward whirls. 93

TH-2966_176103027

Fig. 2. 12. A process chart for the calculation of correct phase of displacement during rotor run–up using the FFT. 94

Fig. 2. 13. The displacement amplitude vs. frequency plots for different acceleration values without and with AMB control..... 98

Fig. 2. 14. (a) and (b) rotor run-up time domain displacement response along *x*-axis, (c) and (d) rotor run-up frequency domain displacement amplitude vs. speed plot, (e) and (f) rotor run-up displacement phase (rad) vs. speed plot without and with AMB control at Disc 1 and AMB location respectively (Model 1). 99

Fig. 2. 15. For a static load of 2 N at the AMB location (a) Control current (b) Shaft displacement at the AMB location. 100

Fig. 2. 16. Control current vs. time plot before and after balancing along the *x*-axis (at AMB for Model 1)..... 102

Fig. 2. 17. (a) and (b) rotor run-up time domain displacement response along *x*-axis, (c) and (d) rotor run-up frequency domain displacement amplitude vs. speed plot, (e) and (f) rotor run-up displacement phase (rad) vs. speed plot before and after balancing at Disc 1 and AMB location respectively (Model 1, including AMB control). 103

Fig. 2. 18. (a) and (b) rotor run-up time domain displacement response along *x*-axis, (c) and (d) rotor run-up frequency domain displacement amplitude vs. speed plot, (e) and (f) rotor run-up displacement phase (rad) vs. speed plot before and after balancing at Disc 1 and AMB location respectively (Model 1, excluding AMB control). 104

Fig. 2. 19. (a) and (b) rotor run-up frequency domain displacement amplitude vs. speed plot, (c) and (d) rotor run-up displacement phase (rad) vs. speed plot before and after

TH-2966_176103027

balancing at Disc 1 and AMB location respectively using balance estimates of conventional ICM and VTEICM (Model 1, excluding AMB control). 106
Fig. 2. 20. The flexible rotor-AMB system supported on conventional bearings (Model 2). 107
Fig. 2. 21. The flexible rotor-AMB system supported on conventional bearings (Model 3). 107
Fig. 2. 22. (a) and (b) rotor run-up frequency domain displacement amplitude vs. speed plot, (c) and (d) rotor run-up displacement phase (rad) vs. speed plot before and after balancing at Disc 1 and AMB location respectively (Model 2, excluding AMB control). 108
Fig. 2. 23. (a) and (b) rotor run-up frequency domain displacement amplitude vs. speed plot, (c) and (d) rotor run-up displacement phase (rad) vs. speed plot before and after balancing at Disc 1 and AMB location respectively (Model 3, excluding AMB control). 109
Fig. 2. 24. Percentage reduction in vibrational response of the rotor system without and with AMB control after balancing using conventional ICM and VTEICM. 109
Fig. 2. 25. (a) Polar representation of magnitude and phase for different trial unbalances generated through AMB as magnetic forces (b) Polar representation of magnitude and phase for different residual unbalances at the three discs locations, obtained using trial unbalances. 110
Fig. 3. 1. The rotor-AMB model with unbalance forces ($f_{u,1}$ to $f_{u,p}$) at different node locations. 116
Fig. 3. 2. The rotor-AMB model with unbalance forces and virtual trial unbalances (f_T). 116
Fig. 3. 3 (a) An illustrative representation of the rotor-AMB model supported on two conventional bearings with three balancing planes as rigid discs and (b) A pictorial

TH-2966_176103027

representation of disc unbalances on the *x*-*y* plane, the orientation and magnitude of the unbalance is shown in degree and kg-m. 122

Fig. 3. 4. The magnitude of random shaft unbalances ('*') and discrete disc unbalances ('•') in kg-m is represented at different orientations in *x*-*y* plane along the *z*-axis. 123

Fig. 3. 5. A pictorial representation of the SIMULINK model developed to solve the differential equation in MATLAB platform using Runge-Kutta solver. 123

Fig. 3. 6. The Campbell diagram of the rotor system under AMB control for a spin speed of 0-700 rad/s displaying both forward and backward whirls. 124

Fig. 3. 7. Shaft translational displacement (in meters) along *x*-axis vs. time (in seconds) plot at (a) disc D-1, (b) disc D-2, (c) disc D-3 (d) AMB-2 locations without and with AMB control as represented by grey and black lines (same line width) respectively; reduction in amplitude is achieved with AMB control; ramp-up speed 5-700 rad/s. 124

Fig. 3. 8. (a) Shaft translational displacement amplitude along *x*-axis vs. frequency plot and (b) phase vs frequency plot at the disc (D-1) location with and without AMB control as represented by solid and dotted lines; amplitude reduction is achieved throughout the ramp-up speed. 125

Fig. 3. 9. (a) Configuration-1 and (b) configuration-2 with distance between the rotor-AMB components in meters along *z*-axis. 126

Fig. 3. 10. Mode shapes corresponding to the first three natural frequencies with and without consideration of AMBs in the system for configuration-1; symbols □, ○, and + represent 1st 2nd and 3rd bending modes with AMB control and symbols ■, ●, and ▽ represents respective mode shapes without AMB control. 127

TH-2966_176103027

Fig. 3. 11. Mode shapes corresponding to the first three natural frequencies with and without consideration of AMBs in the system for configuration-2; symbols □, ○, and + represent 1st 2nd and 3rd bending modes with AMB control and symbols ■, ●, and ▽ represents respective mode shapes without AMB control. 127

Fig. 3. 12. The comparative flow chart of the identification algorithms namely VTEICM and VELSHSB. 129

Fig. 3. 13. (a) Current (in Amperes) vs. time plot; the current increases and stabilizes after 6 seconds (b) Shaft's displacement (in meters) vs. time plot at the AMB-1 location; displacement diminishes after 6 seconds equilibrium location achieved and (c) Current vs. time plot, (d) Shaft's displacement vs. time plot at the AMB-2 location. 130

Fig. 3. 14. Displacement (in meters) vs. time (in seconds) plot at (a) disc D-1, (b) disc D-2, (c) disc D-3 and (d) AMB-2 before and after balancing using slow-speed estimates as represented by grey and black lines (same line width) respectively; moderate reduction in amplitude after balancing without AMB control. 135

Fig. 3. 15. Displacement (in meters) vs. time (in seconds) plot at (a) disc D-1, (b) disc D-2, (c) disc D-3 and (d) AMB-2 before and after balancing using high-speed estimates as represented by grey and black lines (same line width) respectively; higher reduction in amplitude after balancing without AMB control. 136

Fig. 3. 16. Displacement (in meters) vs. time (in seconds) plot at (a) disc D-1, (b) disc D-2, (c) disc D-3 and (d) AMB-2 before and after balancing using high-speed estimates as represented by grey and black lines (same line width) respectively; highest reduction in amplitude after balancing with AMB control. Spin speed varies from 5-700 rad/s. 137

TH-2966_176103027

Fig. 3. 17. (a) Displacement amplitude vs run-up spin speeds, (b) Displacement phase vs. run-up spin speeds before and after balancing using high-speed estimates as represented by dotted and solid lines; amplitude reduction is achieved after balancing throughout the ramp-up speed at disc-1 location without AMB control. 138

Fig. 3. 18 (a) Displacement amplitude vs run-up spin speeds, (b) Displacement phase vs. run-up spin speeds before and after balancing using high-speed estimates as represented by dotted and solid lines; amplitude reduction is achieved after balancing throughout the ramp-up speed at disc-1 location with AMB control. 138

Fig. 3. 19. The percentage reduction in the maximum time domain displacement of the rotor system throughout all node locations after balancing of the rotor system with and without AMB control. 139

Fig. 3. 20. The current (in amperes) vs time (in seconds) plot along *x*-axis at (a) AMB-1, and (b) AMB-2 locations before and after balancing as represented by grey and black lines (same line width); reduction in control current is achieved after balancing. 139

Fig. 4. 1 A pictorial representation of dual rotor-AMB system comprising of LPR and HPR supported on flexible bearings..... 146

Fig. 4. 2. A finite element model considered for the dual-rotor AMB system with elements and node locations. 152

Fig. 4. 3. Random distribution of the residual unbalances throughout the span of the low pressure rotor 154

Fig. 4. 4. Randomly distributed residual shaft unbalances along the z-axis in both low-pressure rotor and high-pressure rotor systems. 162

TH-2966_176103027

Fig. 4. 5. First three modes of the free vibration in both HPR and LPR systems along the shaft axis (z-axis). 163

Fig. 4. 6. Campbell diagram of the dual-rotor system showing the forward and backward whirl frequencies. 163

Fig. 4. 7. Bode plot for the PID controller utilized in the AMB system. 167

Fig. 4. 8. Bode plot for the dual rotor-AMB system at the disc location in LPR system with the variation in the proportional gain. 167

Fig. 4. 9. Bode plot for the dual rotor-AMB system at the disc location in LPR system with the variation in the derivative gain. 168

Fig. 4. 10. Percentage reduction of displacement amplitude of the dual rotor system with the variation of proportional gain (k_P) of the PID controller in the dual rotor-AMB system. 168

Fig. 4. 11. Displacement vs time plot at (a) CD-1 in LPR system, (c) CD-2 in HPR system at operating speed of 100 rad/s in LPR and ω_r = 1.5. Ramp-up displacement response vs time plot (b) CD-1 in LPR system, (d) CD-2 in HPR system with an angular acceleration of 23.17 rad/s^2 and ω_r = 1.5 with and without AMB control. 169

Fig. 4. 12. Percentage reduction of displacement amplitude of the dual rotor system with the variation of derivative gain (k_D) of the PID controller in the dual rotor-AMB system. 170

Fig. 4. 13. Displacement vs time plot at (a) CD-1 in LPR system, (c) CD-2 in HPR system, (e) AMB in LPR system and displacement amplitude vs frequency plot at (b) CD-1 in LPR system, (d) CD-2 in HPR system, (f) AMB in LPR system depicting change in

TH-2966_176103027

displacement response with addition of virtual trial magnetic excitation of low-pressure rotor frequency (125.7 rad/s). 172

Fig. 4. 14. (a) Displacement vs time plot at AMB location in LPR system (b) control current vs time plot in AMB system due to static load of 2 N at AMB location. 172

Fig. 4. 15. Displacement vs time plot at (a) CD-1 in LPR system, (c) CD-2 in HPR system, (e) AMB in LPR system and displacement amplitude vs frequency plot at (b) CD-1 in LPR system, (d) CD-2 in HPR system, (f) AMB in LPR system depicting change in displacement response with addition of virtual trial magnetic excitation of high-pressure rotor frequency (188.5 rad/s). 174

Fig. 4. 16. Ramp-up displacement vs time plot at (a) CD-1 in LPR system, (c) CD-2 in HPR system, (e) AMB in LPR system and ramp-up displacement amplitude vs frequency plot at (b) CD-1 in LPR system, (d) CD-2 in HPR system, (f) AMB in LPR system depicting change in displacement response after balancing of rotor system with an angular acceleration of 23.17 rad/s^2 and frequency ratio, $\omega_r = 1.5$. 180

Fig. 4. 17. Ramp-up displacement vs time plot at (a) CD-1 in LPR system, (c) CD-2 in HPR system, (e) AMB in LPR system and ramp-up displacement amplitude vs frequency plot at (b) CD-1 in LPR system, (d) CD-2 in HPR system, (f) AMB in LPR system depicting change in displacement response after balancing of rotor system with an angular acceleration of 23.17 rad/s^2 and frequency ratio, $\omega_r = -1.5$. 182

Fig. 5. 1 (a) An experimental RK4 rotor test-rig integrated with AMB, (b) slot near flexible coupling to obtain the reference signal, and (c) balancing disc mounting with groves. ... 187

Fig. 5. 2 (a) An 8-pole electromagnetic actuator and (b) orientation of poles with minimum flux leakage. 189

TH-2966_176103027

Fig. 5. 3. (a) Eddy current sensors mounted in horizontal and vertical directions and (b) Bently Nevada proximitor assembly for amplification of sensor output. 190

Fig. 5. 4. The dSPACE hardware with A/D and D/A converters. 191

Fig. 5. 5. The dSPACE control desk for real-time simulation of the designed controller. 192

Fig. 5. 6. A servo drive with different pin settings used as an amplifier. 193

Fig. 5. 7. The high-frequency voltage output of the amplifier with a (a) large duty cycle, and (b) small duty cycle as measured in an oscilloscope. 194

Fig. 5. 8. A block diagram of H-bridge MOSFET driver. 195

Fig. 5. 9. The 1146B KEYSIGHT AC/DC current probe used for control current measurement. 196

Fig. 5. 10. The physical connection of different components in the experimental rotor-AMB test rig. 197

Fig. 5. 11. The block diagram of the AMB closed-loop control model developed at the dSPACE-SIMULINK interface with switching of bias current. 200

Fig. 5. 12. (a) Percentage reduction in displacement response with the variation of the proportional gain (k_P) at 15 Hz (b) Percentage reduction in the displacement amplitude after four cycles with the variation of the derivative gain (k_D) in the impulse test. 201

Fig. 5. 13. (a) Displacement at AMB location along *y*-axis vs. time plot with impulsive force and (b) displacement amplitude at AMB location vs. frequency plot. 203

Fig. 5. 14. (a) Frequency (Hz) vs. time plot with AMB control for the system accelerating from 6.67 to 63.33 Hz with an acceleration of 12 rad/s^2, (b) displacement at AMB location vs. time plot, and (c) overall current (bias + control) at AMB vs. time plot along the *x*-axis. 204

TH-2966_176103027

Fig. 5. 15. The block diagram of the AMB closed-loop control model developed at the dSPACE-SIMULINK interface with switching of bias current and SVTU. 205

Fig. 5. 16. The trial excitation current along *x*-axis to generated magnetic excitation force in the rotor-AMB system. 207

Fig. 5. 17. (a) Frequency (Hz) vs. time plot with AMB control for the accelerating rotor system with V/S error and lag error in SVTU generation, (b) displacement at AMB location vs. time plot, and (c) overall current (bias + control) at AMB along the *x*-axis vs. time plot. 208

Fig. 5. 18. (a) Frequency (Hz) vs. time plot with AMB control for the accelerating rotor system with lag error in SVTU generation, (b) displacement at AMB location along *x*-axis vs. time plot, and (c) overall current (bias + control) at AMB along *x*-axis vs. time plot. 209

Fig. 5. 19. (a) Frequency (Hz) vs. time plot with AMB control for the accelerating rotor system without SVTU and with SVTU after error correction, (b) displacement at AMB location along *x*-axis vs. time plot, and (c) overall current (bias + control) at AMB along *x*-axis vs. time plot. 210

Fig. 5. 20. The schematic showing generation of the reference signal (x_g) with the orientation of the key slot and sensor for time $t = 0$ and $t = t_1$. 211

Fig. 5. 21. Estimated balance masses at (a) left and (b) right balancing plane utilizing the different combination of added MTU and generated SVTU. 217

Fig. 5. 22. (a) Displacement response at AMB location (b) Control current for a load of 50 gm. 218

TH-2966_176103027

Fig. 5. 23. Displacement vs. time plot before and after balancing of rotor system utilizing estimated values of balance masses in VTEICM (a) pair I, (b) pair II, (c) pair III, and (d) pair IV. 219

Fig. 5. 24. Displacement amplitude vs. frequency plot before and after balancing of rotor system utilizing estimated values of balance masses in VTEICM (a) pair I, (b) pair II, (c) pair III, and (d) pair IV. 219

Fig. 5. 25. Displacement phase vs. frequency plot before and after balancing of rotor system utilizing estimated values of balance masses in VTEICM (a) pair I, (b) pair II, (c) pair III, and (d) pair IV. 220

Fig. 5. 26. Overall current vs. time plot before and after balancing of rotor system utilizing estimated values of balance masses in VTEICM (a) pair I, (b) pair II, (c) pair III, and (d) pair IV. 221

Fig. 6. 1. A rotor-AMB system with a cracked shaft supported on flexible bearings. 225

Fig. 6. 2. The rotor system showing forces and measurement locations of displacement responses (a) without and (b) with addition of multi-harmonic excitation force (f_T) at the AMB location..... 226

Fig. 6. 3. The representation of translational and rotational coordinate systems for the cracked shaft. 233

Fig. 6. 4. A pictorial representation of the rotor-AMB system with elements and measurement planes considered in FEM modeling. 239

Fig. 6. 5. A schematic diagram of the SIMULINK model utilized in the generation of displacement responses. 239

TH-2966_176103027

Fig. 6. 6. Campbell diagram depicting forward and backward whirl frequencies for the rotor system. 241

Fig. 6. 7. The displacement (m) vs time curve at (a) Disc-1, (b) crack, (c) Disc-2 and (d) AMB locations along *x*-axis. 242

Fig. 6. 8. The displacement (m) vs time curve at (a) Disc-1, (b) crack, (c) Disc-2 and (d) AMB locations along *y*-axis. 242

Fig. 6. 9. The orbit plot of the displacement response at (a) Disc-1, (b) crack, (c) Disc-2 and (d) AMB locations for 26 Hz spin speed. 243

Fig. 6. 10. The full-spectrum response amplitude of the rotor system at Disc-1 location versus frequency. 244

Fig. 6. 11. The full-spectrum response phase of the rotor system at Disc-1 location versus frequency. 244

Fig. 6. 12. The orbit plot of the displacement response at Disc-1 location at (a) 28 Hz and (b) 30Hz. 246

Fig. 6. 13. The orbit plot of the displacement response at Disc-1 location at 60 Hz (a) without AMB (b) with AMB and at 95 Hz with AMB and (c) with internal damping and (d) without internal damping. 247

Fig. 6. 14. The variation in the modal damping coefficient (c_m) and the threshold speed of the rotor system with the variation of derivate gain (k_D) of the AMB controller. 248

Fig. 6. 15. (a) Displacement (m) at AMB location versus time (s) plot and (b) Control current (A) versus time (s) plot along *x*-axis after the application of a static load of 5N. 249

Fig. 6. 16. The flow chart describes the estimation algorithm (MHICM). 250

TH-2966_176103027

Fig. 6. 17.The orbit plot of the (a) displacement response at Disc-1 and (b) control current at 30 Hz before and after application of virtual trial multi-harmonic force as magnetic excitations. 252

Fig. 6. 18. The experimental test rig setup supported on ball bearings and integrated with AMB. 257

Fig. 6. 19. (a) Fatigue crack developed in the mild steel shaft at the notch location, (b) 8-pole AMB actuator with silicon steel core, and (c) zoomed view of crack surface in the shaft. 257

Fig. 6. 20. The additional component of AMB control structure with dSPACE A/D and D/A panel, amplifiers, and DC supply source. 258

Fig. 6. 21. The block diagram of the AMB closed-loop control model developed at dSPACE-SIMULINK interface. 260

Fig. 6. 22. Natural frequency of the system without and with AMB {(a) , (d)} crack face in downward direction {(b), (e)} crack face is in horizontal direction {(c), (f)} crack face is in upward direction. 260

Fig. 6. 23. (a) Displacement response vs time plot at disc location with, (b) control + bias current plot vs. time, (c) orbit plot of displacement response and (d) orbit plot of control + bias current at 20 Hz operating speed. 262

Fig. 6. 24. (a) Displacement amplitude vs. frequency plot at disc location with AMB control and (b) phase vs. frequency plot at 20 Hz operating speed. 263

Fig. 6. 25. (a) Orbit plot of displacement response at disc location with and without AMB control. 263

TH-2966_176103027

Fig. 6. 26. (a) Displacement (m) at AMB location versus time (s) plot and (b) Control current (A) versus time (s) plot along y-axis after the application of a static load of 500 gram. 264

Fig. 6. 27. The reference signal obtained at the slots present in the spindle of the motor with respect to time. 266

Fig. 6. 28. Orbit plot of (a) displacement response and (b) control + bias current without and with addition of multi harmonics excitation force. 267

Fig. 6. 29. The fatigue crack behavior as per estimated participation factor of experimental crack force and switching crack force along (a) *y*-axis and (b) *x*-axis with respect to the orientation of the crack face 269

`

TH-2966_176103027

LIST OF TABLES

Table 1. 1. Sources of unbalances in the rotor system with their signatures in vibrational responses. 38

Table 2. 1. Parameters of the flexible rotor system. 95

Table 2. 2. Parameters of the conventional bearings 96

Table 2. 3. Parameters of AMB system. 96

Table 2. 4. Estimated value of the force current factor (k_i) in numerical model for different values of constant load (assumed value = 42.1 N/A)..... 101

Table 2. 5. Comparison of the unbalance magnitudes and phases estimated using VTEICM from assumed values considering residual unbalances only at discs for a rotor with 0% noise. 105

Table 2. 8. Percentage change in the value of unbalance magnitude and phase of the estimated with variation in the level of noise. 111

Table 3. 1. Physical parameters of the rotor-AMB system..... 121

Table 3. 2. Estimated disc unbalances at balancing planes using the VTEICM and VELSHSB methods. 133

Table 3. 3. Estimated unbalances at balancing planes for the rotor system with both discrete disc and randomly distributed shaft unbalances. 134

Table 3. 4. Estimated percentage change in unbalances at the balancing planes using VELSHSB with addition of different percentage of random noise. 135

Table 3. 5. Estimated unbalances at the balancing planes using VELSHSB and influence coefficients obtained at the slow and high speeds with 5% of random noise. 137

TH-2966_176103027

Table 3. 6. Estimated unbalances at the balancing planes using both methods with variations in support bearing's properties. 141

Table 4. 1. Physical properties of the LPR and HPR system. 164

Table 4. 2. Physical properties of the AMB system 165

Table 4. 3. Assumed and estimated magnitude of residual discs unbalances with the variation of different percentages of noise for $\omega_r = 1.5$ and $\omega_r = -1.5$. 176

Table 4. 4. Assumed and estimated phases of residual discs unbalances with the variation of different percentages of noise for $\omega_r = 1.5$ and $\omega_r = -1.5$. 177

Table 4. 5. Assumed and estimated magnitude of overall discrete discs and randomly distributed shaft unbalances with the variation of different percentages of noise for $\omega_r = 1.5$ and $\omega_r = -1.5$. 178

Table 4. 6. Assumed and estimated phase of overall discrete discs and randomly distributed shaft unbalances with the variation of different percentages of noise for $\omega_r = 1.5$ and $\omega_r = -1.5$. 179

Table 5. 1. Geometrical details of stator 189

Table 5. 2. Specification of the A25A100 PWM servo drive. 193

Table 5. 3. Percentage reduction in displacement response and control currents in the time domain after balancing using different pairs of balance masses obtained in VTEICM. ... 220

Table 6. 1. Design parameters of the rotor system 240

Table 6. 2. Design parameters of the AMB system. 240

Table 6. 3. Estimated values of force current stiffness coefficient (k_i) of AMB 249

Table 6. 4. The magnitude and phase of the trial multi-harmonic excitation force generated at the AMB location. 251

TH-2966_176103027

Table 6. 5. The assumed and estimated values of the fault parameters with and without the addition of 5% of random noise (15-29 Hz). 253

Table 6. 6. The assumed and estimated values of the fault parameters with the addition of 5% of random noise for a different combination of speeds. 254

Table 6. 7. Physical properties of the rotor-AMB test rig. 256

Table 6. 8. Amplitudes and phases of the excitation current corresponding to different harmonics. 267

Table 6. 9. Estimated for parameters of the cracked rotor-AMB system for a different combination of the operating speed. 268

TH-2966_176103027

NOMENCLATURE

Symbols	Definition
$\boldsymbol{a}$, $\boldsymbol{b}$	Influence coefficient column vector related to low and high-pressure rotor system
A_g	Area of air gap between rotor and the poles of AMB actuator
A_L	Area of cross section of the shaft
$\mathbf{A}$	Influence coefficient matrix for rotor-AMB system utilized in VTEICM
$\mathbf{A}_c$	Identification matrix related to displacement responses in cracked rotor-AMB system
$\mathbf{B}$	Location matrix of the support bearings
$\mathbf{B}_I$	Influence coefficient matrix for rotor system utilized in conventional ICM
c_H	Internal damping coefficient
$\mathbf{C}_b$	Damping matrix of the support bearings
d_h	Displacement responses at measurement planes in rotor system without AMB
e_d	Eccentricity of the unbalance considered at balancing plane
e_T	Eccentricity of trial unbalance considered at AMB location
E	Young's modulus of elasticity
f_c	Crack force
f_i	Internal damping force
f_h	Magnitude of the multi-harmonic excitation force

TH-2966_176103027

f_l	Static load at AMB location
f_T	Virtual trial unbalance force
$\mathbf{f}_n$	Unbalance force vector considered at different balancing planes
$\mathbf{f}_u$	Unbalance force vector considered at different measurement planes
g	Acceleration due to gravity
$\mathbf{G}_d$	Gyroscopic matrix of the rigid discs
i_b, i_c	Bias current and control current
i_l, i_T	Static current and trial current
I	Area moment of inertia of the shaft
j	$\sqrt{-1}$
k	Number of AMBs
k_i	Current stiffness factor of AMB
k_P, k_I and k_D	Proportional, Integral and Derivative gain of PID controller
k_s	Displacement stiffness factor of AMB
$\mathbf{K}_b$	Stiffness matrix of the support bearings
$\mathbf{K}_s$	Stiffness matrix of the shaft
l_e	Length of the element of the shaft
l_g	Air gap between the rotor and the actuator of AMB
l_k	length of section considered in the element of the shaft
m_d	Mass of the unbalance considered at balancing plane
m_T	Mass of the trial unbalance considered at AMB location
$\mathbf{M}_d$	Mass matrix of the rigid discs
$\mathbf{M}_s$	Mass matrix of the shaft

TH-2966_176103027

n	Number of balancing planes
N	Influence coefficient related to displacement responses and excitation forces in the cracked rotor-AMB system
$\mathbf{N}_r$	Influence coefficient matrix related to displacement responses and excitation forces in the cracked rotor system
P	Participation factor corresponding to switching behavior model of the crack
q	Number of conventional bearings
r_d	Displacement responses at disc locations
r_m	Displacement response at AMB location
$\mathbf{S}$	Location matrix for the AMB
$\mathbf{S}_c$	Identification matrix related to control current in cracked rotor-AMB system
T_R	Manually added trial unbalance
w_s	Static deflection in the cracked-rotor system due to gravity
x, y	Axis perpendicular to the axis of the shaft
z	Axis of the shaft
$\mathbf{Z}_h$	Influence coefficient at high speed for rotor-AMB system
$\mathbf{Z}_l$	Influence coefficient at low speed for rotor-AMB system

Greek symbols

α	Influence coefficient related to displacement responses and unbalance forces in the rotor-AMB system (VTEICM)

TH-2966_176103027

β	Influence coefficient related to displacement responses and unbalance forces in the rotor system (conventional ICM)
γ	Influence coefficient related to displacement responses and unbalance forces in the rotor-AMB system (VELSHSB)
Δk	Additive crack stiffness
$\boldsymbol{\eta}$	Displacement response vector of finite element model
κ	Influence coefficient related to displacement responses and unbalance forces in the HPR system
λ	Influence coefficient related to displacement responses at AMB location and unbalance forces in the HPR system
ρ	Density of the shaft
σ	Switching crack excitation function
ϕ_d	Phase of the unbalance considered at balancing plane
χ	Influence coefficient related to displacement responses and unbalance forces in the LPR system
ω	Spin speed of the rotor system

Subscripts

d	Disc location
e	Element of shaft
h	Multi harmonics in the displacement response of cracked rotor system
H, L	High and Low-pressure rotor
l	Due to static load

TH-2966_176103027

m	Magnetic bearing location
t	Final operating speed of the rotor

Superscript

e	Element of shaft
T	Transpose of matrix
$'$	Represents response generated with addition of virtual trial unbalance
$\dot{}, \bar{}$	Derivative and Integration of the displacement response

Abbreviations

VELSHSB	Virtual Excitation at Low-Speed for High-Speed Balancing
AMB	Active Magnetic Bearing
A/D and D/A	Analog to Digital and Digital to Analog
FFT	Fast Fourier Transform
HPR	High Pressure Rotor
ICM	Influence Coefficient Method
LPR	Low Pressure Rotor
MVEDRB	Multiple Virtual Excitation for Dual rotor Balancing
MHICM	Multi Harmonic Influence Coefficient Method
MSCU	Motor Speed Control Unit
PID	Proportional Integral Derivative
PWM	Pulse Width Modulation
SVTU	Synchronized Virtual Trial Unbalance

TH-2966_176103027

VTU	Virtual Trial Unbalance

TH-2966_176103027

CHAPTER 1

INTRODUCTION AND LITERATURE REVIEW

This chapter deals with the literature survey of the various common rotor faults that appear in the rotating machinery. The major focus is given on the residual unbalances that cause excessive vibration in machines and lead to fatigue failures. The role of Active Magnetic Bearings (AMBs) in the active suppression of the vibrational responses using different control strategies is also discussed. Various techniques adopted to identify the faults present in the rotor systems with and without AMB control are described. Important outcomes of the literature survey, along with the objectives derived for the thesis work, are presented.

1.1. Significance of the study

The importance of rotating machinery can be seen in the generation of electrical energy through turbines and generators, transportation, and manufacturing processes in industries. The characteristics and performance of such rotating systems are therefore essential to be analyzed and improved. The irregular loading stress, inadequate environmental condition, accumulation of dust and foreign particles, and improper assembly of the rotating components, results in the unexpected failure of the machinery. The fault can also generate gradually with time, depicting a marginal change in the dynamic responses of the rotor system until any recognizable damage appears in the components. The rotor faults, such as the residual unbalances, residual bow, misalignment, fatigue crack, and wear and tear develop that generates excessive stress with an unavoidable large amplitude of vibration.

TH-2966_176103027

Therefore, it is necessary to monitor and identify the intensity of the rotor faults in order to avoid any catastrophic failure of the machinery. The most common fault in the rotating machinery is the presence of residual unbalances that arise due to manufacturing errors, improper commissioning, and wear and tear. With the increase of the operating speed of the machinery, the amplitude of vibration increases rapidly due to the presence of unbalance. Several balancing methods have been adopted to remove the effect of residual unbalances present in the rotor systems. Also, with the advent of technological advancement, active vibration control strategies are being deployed with the help of AMB. The AMB suppresses the vibration response within a specified limit as well as allows the user to identify the fault parameters in high-speed systems. The application of AMB as a fault identification tool along with vibration control structure can be beneficial in the condition monitoring of the machinery (Penny *et al*., 2006; Sawicki *et al*., 2008; Srinivas *et al*., 2018).

1.2. Vibration-based fault detection techniques

In vibration-based fault detection, vibration signals from the rotating machinery are analyzed to identify the deviation of the system's behavior from the normal operating conditions (Adams, 2000; Matsushita *et al*., 2017; Randall, 2021). Vibration transducers are utilized to collect the time-indexed signal data over a particular period of time. The vibration data usually represents displacement, velocity, acceleration, and forces based on the transducer used to obtain the signals. The faults in the rotating machinery contribute to a particular signature, feature, or characteristic in the vibration responses. As the vibration responses can be monitored continuously, the sudden variation can predict the generation

TH-2966_176103027

of the severe fault and might prevent the machinery from catastrophic failure. There are preferentially three phases in vibration-based fault detection, which include (i) Collection of vibration data, (ii) Signal processing, and (iii) Diagnosis of rotor faults. These are now described in more detail.

1.2.1. Collection of vibration data

The first phase in the fault detection is to obtain the vibration data from the rotating machinery, which includes the utilization of transducers, data acquisition system, and amplifiers linked to storage devices (Broch, 1980; Sujatha, 2010; Sinha, 2015; Tiwari, 2017). The transducers are required to convert the vibrational response of the rotor components into electrical signals. The electrical signal is required to be amplified to get the required intensity for further processing of the signals. The signals are then required to be converted into digital data with the help of Analog-to-Digital (A/D) converters. The digital data of vibration responses over a certain time period are then stored in the storage devices (Austerlitz, 2002; Kirianaki *et al*., 2002). The measurement done with the help of transducers is generally affected by the finishing of the machine surface as well as the homogeneity of the material in the vicinity of the transducers. The classification of the transducers used in the measurement of vibrational responses is shown in Fig. 1.1. The displacement sensors are utilized to measure the linear and rotational displacement in the machinery (Nyce, 2004). In Linear Variable Differential Transducers (LVDT), a magnetic core is placed inside a solenoid. When the core moves relative to the coils, the magnetic flux linked to the coil changes, and the displacement is obtained in terms of analog data. The rotary movement of the mechanical components is measured with the help of a Rotary Variable Differential Transducer (RVDT). This transducer generates an AC voltage in

TH-2966_176103027

response to the angular displacement of the system. Proximity transducers are the non-contact sensors that measure the vibration of the rotor components by generating an electrostatic or electromagnetic field (Usher and Keating, 1996; Sinclair, 2000).

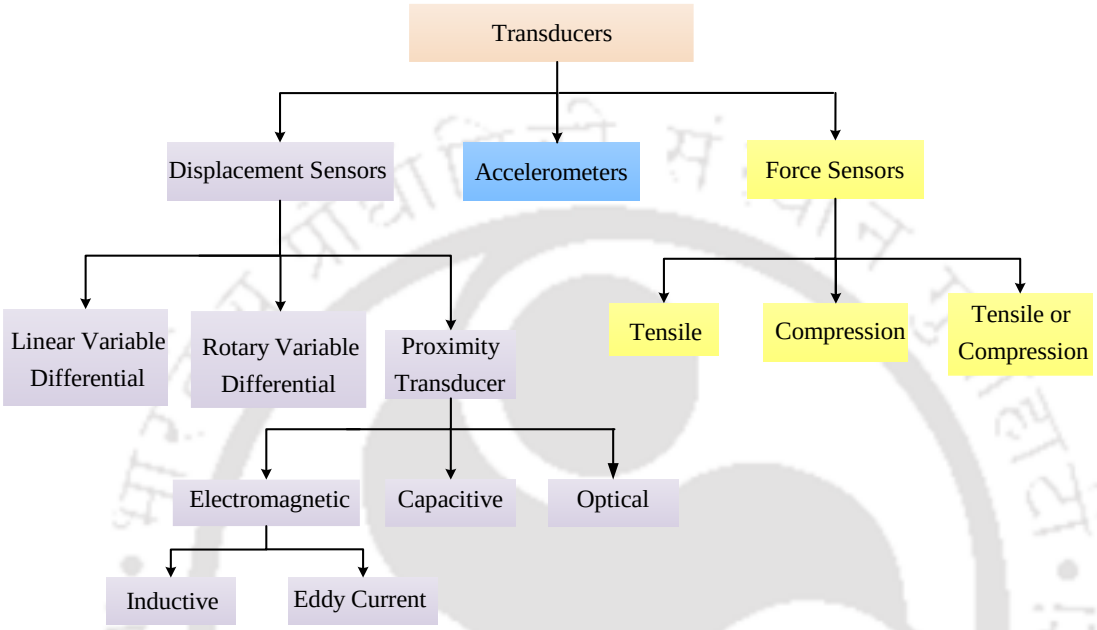


Fig. 1. 1. Types of transducers utilized in the measurement of vibration responses.

The change in the field due to the relative motion of the rotor components produces the desired signal. The three types of transducers are

1. *Electromagnetic transducer*: This type of transducer utilizes an inductive load or eddy current to identify the displacement of the target material. In an inductive type sensor, the inductance of the magnetic circuit fluctuates inversely to the change in the air gap between the sensor and the ferromagnetic object. In the eddy current type sensor, with the change in the air gap, the eddy current loss varies in the magnetic circuit. This change in energy of the oscillating circuit provides the displacement of the target material in terms of analog output.

TH-2966_176103027

2. *Capacitive transducer*: In this type of transducer, the dielectric constant of the capacitive load changes in response to the change in the gap between the sensor and the target. However, the performance of the transducer is affected by the presence of dust particles, oil, etc.
3. *Optical transducer*: In this type of sensor, the target object is kept in the path of light coming from the light source. The light after obstruction from the object is directed to the photosensitive material. The variation in the intensity of the light is converted in the form of analog output.

Apart from the sensors described above, accelerometers are used to measure the acceleration of the target material in a wide range of frequencies. A typical accelerometer consists of a small mass attached to a piezoelectric material. As the target attached to the accelerometer vibrates, a voltage signal is generated in proportion to the acceleration of the target. The tensile or compressive force applied by the object can be measured with the help of force sensors (Stefanescu, 2011). The force sensors consist of a strain gauge connected in a Wheatstone bridge circuit. As the load is applied, the strain gauge deforms that changes its resistance. The change in resistance causes a change in voltage drop in proportion to the applied force. The vibration and force signals measured by different types of sensors are processed to identify the intensity and type of fault present in the rotating machinery. The force sensors also work based on the piezoelectric effect that utilizes a piezoelectric material and generates electric potential under the action of mechanical stress. The voltage generated is proportional to the stress applied to the sensors.

TH-2966_176103027

1.2.2 Signal processing

The useful information related to the operating condition of the machinery is required to be extracted from the raw data obtained with the help of transducers. The vibration signals are analyzed based on the time domain, frequency domain, and time-frequency domain methodologies (Jardine *et al*., 2006). These feature extraction techniques allow identifying faults based on their characteristics in the vibration response. The time-domain analysis of the raw signal is usually carried out in two ways, i.e., visual inspection and feature-based inspection. In visual inspection, the vibration signal of the operating machinery is compared to the vibration signals obtained from heathy machines (Davies, 1998). The increment in the amplitude of the vibration responses indicates the presence of a fault in the system. This method is convenient and cheap to monitor the vibration signals using oscilloscopes or data acquisition systems connected with computer peripherals. However, the recognition of the change in behavior of time-domain signals is difficult in the presence of one or more faults (Guo *et al*., 2005). In feature-based inspection, the statistical functions can be utilized to extract the features of the signals. The mathematical parameters, such as the root-mean-square, skewness, kurtosis, peak-to-peak value, variance, and mean, are used to identify the change in the operating condition of the machinery (McFadden and Toozhy, 2000; Combet and Gelman, 2007; Nayana and Geethanjali, 2017). Also, filter-based techniques are used to extract the required signal of a particular frequency range from the time domain signal with noise. The techniques, such as demodulation and adaptive noise cancellation, are used to separate the useful information from the raw signal (Lacey, 2008; Singh and Vishwakarma, 2015).

TH-2966_176103027

The analysis of time-domain signals can be further extended to frequency domain analysis that describes detailed characteristics of the signal, which are not visible in the time domain (Diniz *et al.*, 2010). The time-domain signal usually comprises various sine waves of different amplitude and phases generated by faults present in different components of the rotor system. The frequency-domain analysis allows extracting different sine components corresponding to various frequencies from the raw signal. This type of analysis is carried out using Continuous Fourier Transform (CFT), Discrete Fourier Transform (DFT), and Fast Fourier Transform (FFT). In the nineteenth century, J. Fourier discoursed the Fourier analysis that describes that all periodic signals can be converted into a summation of a different complex exponential function. The Fourier integral for a continuous signal $x(t)$ is represented as

$$x(t) = \frac{1}{\pi}\int_{0}^{\infty}\{a(\omega)\cos(\omega t) + b(\omega)\sin(\omega t)\}\,d\omega \tag{1.1}$$

with, $a(\omega) = \int_{-\infty}^{\infty} x(t)\cos(\omega t)\,dt$; $b(\omega) = \int_{-\infty}^{\infty} x(t)\sin(\omega t)\,dt$

where, a and b are the coefficients and ω is the fundamental angular frequency of the signal. The discrete vibration signal obtained from the simulation or experimental data is evaluated using DFT. The complex representation of the discrete periodic signal (x_n) in the expanded form as per Fourier transform can be given as

$$x_n = \frac{1}{Q}\sum_{k=0}^{Q-1} x_k e^{-j2\pi nk/Q}\ ;\ n = \{0, 1, 2, \ldots, Q\text{-}1\} \tag{1.2}$$

TH-2966_176103027

where, Q is the number of discrete data points presents in the periodic signal; n = {0, 1, 2, … ,Q-1}; j = $\sqrt{-1}$. The complex response corresponding to different harmonics present in the displacement signal is given by

$$x_k = \sum_{n=0}^{Q-1} x_n e^{j2\pi nk/Q} \tag{1.3}$$

The complexity of DFT is reduced by the use of a more efficient algorithm, i.e., the FFT. In the FFT, the Q length signal is solved using the multiplication of complex value $Q\log_2 Q$ instead of multiplication of Q^2 complex values (Cooley and Tukey, 1965; Loan, 1992).

The major assumption in transforming the time domain signal into the frequency domain is that the signal remains stationary. While most of the vibration signals from the machinery are obtained at the constant operating speed, some machines are required to be analyzed while accelerating or decelerating. The nonstationary signal generated in the run-up and run-down conditions has different frequency components over periods of time (Cohen, 1995). These signals are analyzed using time-frequency methods that include Hilbert-Huang transform, wavelet transform, Short Time Fourier Transform (STFT), etc. (Al-Badour *et al*., 2011; Feldman, 2011; Feng *et al*., 2013). The characteristics obtained using the above-mentioned signal processing algorithm are then utilized to obtain the intensity and type of fault in the rotor systems.

1.2.3 Diagnosis of rotor faults

The raw signal obtained from the machinery usually comprises vibration responses corresponding to different components (bearings, shaft, coupling, motor, etc.) or different rotor faults (unbalances, crack, misalignment, rub, etc.). The classification of the faults

TH-2966_176103027

present in the processed vibration responses of the rotor system is done with the help of fault detection approaches, such as spectrum analysis, model-based analysis, and artificial intelligence techniques.

1. *Spectrum analysis*: This technique is widely utilized to identify the faults present in the machinery based on the frequency domain features obtained using FFT. The half spectrum or full spectrum plots (vibration amplitude vs. frequency) obtained contain different amplitude and phases of different harmonics related to various faults. The fault, such as unbalance, affects the 1X harmonics, and the amplitude of the 1X component in the frequency domain can show the severity of the unbalance fault in operating conditions (Kıral and Karagülle, 2006; Azeem and Xiaoqing, 2018). The faults, such as crack and misalignment, show the appreciable amplitude of vibration at 1X, 2X, 3X, -1X, -2X, etc. (Shravankumar and Tiwari, 2016; Tiwari, 2017) harmonics in the full spectrum plots. A detailed description of the generation and harmonic contribution of various faults is described in the next section.
2. *Model-based technique*: In this technique, the measured vibration responses are utilized along with the mathematical model of the specific machinery and the possible faults. This technique provides faster and more accurate information related to the faults than the spectrum analysis as the physical information of the rotor system is included. The location, type, and intensity of the fault can be identified in the operating condition of the machinery. The model-based techniques are divided into two categories, i.e., qualitative approaches and quantitative approaches. In qualitative approaches, to predict the behavior of the system, the relationship between the variables is defined in the form of qualitative functions, such as the abstraction

TH-2966_176103027

hierarchy or casual models (Venkatasubramanian *et al*., 2003). Whereas, in the quantitative methods, models are designed using the differential equation, transfer function, state-space method, etc. (Bachschmid *et al*., 2004; Lees *et al*., 2009; Sudhakar and Sekhar, 2011; Singh and Tiwari, 2016). The complexity of the designed model is required to be less, which sometimes affects the accuracy of the identification of estimated fault parameters.

3. *Artificial Intelligence and Machine Learning (AI and ML) techniques*: AI and ML are pattern recognition tools that can be used to detect the presence of faults, identify the reasons for a machine's failure, and predict the progression of the fault. These techniques utilize knowledge of output and input system variables, symptoms of the faults, constraints of operation, and abnormality pattern of the system's condition. The intelligence of the engineers and specialists in the operating structure of the machinery is applied through AI techniques. Several techniques, such as the Case-based reasoning (CBR), Fuzzy logic (FL), Genetic algorithm (GA), and Artificial neural network (ANN), are utilized in the condition monitoring of the rotor systems (Walker *et al*., 2014; Gangsar *et al*., 2021; Brito *et al*., 2022).

1.3. Description of Various Rotor Faults

The early detection of the rotor faults is quite essential in order to avoid major breakdown of the machinery, delay in production, severe on-site accidents, and hefty financial loss. It is also essential to identify the behavior of the different faults and their source in order to take preventive measures to reduce their effects in the primary stage. The faults such as unbalance, cracks, misalignments, shaft bow, etc., are quite common in the machinery

TH-2966_176103027

operating for a longer period of time (Bachschmid *et al*., 2010; McMillan, 2020). The description of the different faults is given in the subsection below.

1.3.1 Unbalance

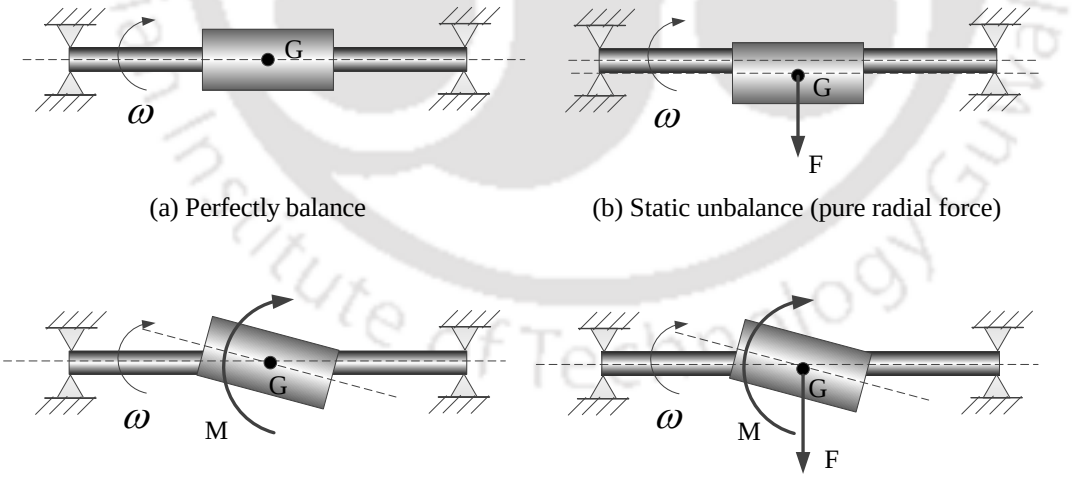
In the practical rotor system, the center of mass never lies on the rotational axis, which causes transverse bending and fatigue stress. As the unbalance force is proportional to the square of the operating speed of the rotating machinery, the resulting excessive amplitude of vibrational response at high speeds may lead to failure of the components. It is difficult to operate the system in the proximity of the critical speed due to the large increment in the displacement response at resonance. The vibration generated in the rotor system is also responsible for undesired noise and wear of the support bearings. Therefore, it is essential to monitor the change in the unbalance response to prevent catastrophic failure of the machinery. The residual unbalances generated due to various factors, such as

i. The presence of sand traps and blow holes in the casting of the rotating components goes undetected in the visual inspection (De Silva, 2007).
ii. Unsymmetrical design of the manufactured parts in the rotating machinery (Taylor, 1940; Kang *et al*., 1992; Ocampo *et al*., 2017).
iii. Insertion of keyways and keys in the coupling of different machine parts can generate unbalance. The system balanced without the addition of keys may get unbalanced after the addition of the keys (Matsushita *et al*., 2017).
iv. Removal of the materials from the rotating parts subjected to corrosion, wear and tear in pumps, turbines, etc., changes the mass distribution of the parts (De Silva, 2007).
v. Deposition of the dust or foreign particle in the operating machinery is subjected to undesirable environmental conditions (Chen *et al*., 2019).

TH-2966_176103027

vi. Trapping of oil in the rotating components or air turbulence may cause unbalance in the machinery.

The magnitude of unbalance is expressed as the product of the unbalance mass and the distance of its center of mass from the rotating axis. Various types of unbalances present in the rigid rotor system are shown in Fig. 1.2. The static unbalance, as shown in Fig. 1.2 (a), arises when the centerline axis of the rotating components shifts parallel to the rotational axis. As a result of this, the component rotates on its own due to the presence of the heavy side in the rotor. The dynamic unbalance, as shown in Fig. 1.2 (d), arises when the system has unbalance present at two different planes. This generates a moment along with force at the center of mass of the rotor. As the rotor system approaches critical speeds, the rotor undergoes appreciable deformation that bends the centerline of the system, and it experiences additional centrifugal forces. The increase in centrifugal force causes excessive vibration in the system.



(a) Perfectly balance (b) Static unbalance (pure radial force)

(c) Dynamic unbalance (pure moment) (d) Dynamic unbalance (both force and moment)

Fig. 1. 2. Unbalances in the rigid rotor system.

TH-2966_176103027

1.3.2 Shaft cracks

Cracks occur in rotors due to asymmetry in geometry, stress concentrations, such as keys, notches, threads, etc., in the shaft. The effect of the crack upsurges after the system undergoes a series of stress cycles during its operation. Therefore, it is important to detect the crack in the shaft in the early stages. The stiffness of the shaft changes in the locality of the crack, which results in the deviation of the natural frequency of the system. The change in dynamics of the system due to cracks appears after it has grown to a certain level. The detection of crack can be done by analyzing the displacement response, frequency spectrum, and natural frequency of the rotating element (Nelson and Nataraj, 1986; Wauer, 1990; Kumar and Rastogi, 2009). The geometry of the crack, i.e., the depth, orientation, and length, affect the dynamics of the rotor system in different ways. Rotor cracks based on alignment with respect to the axis of the rotor are classified as follows:

a) *Transverse Crack*: Crack developed perpendicular to the axis of the shaft as shown in Fig. 1.3 (a) is defined as transverse crack. This type of crack is common and is generated due to cyclic bending stress. The cross-sectional area of the shaft decreases, which changes the stiffness in the vicinity of the crack and may result in the serious damage to the machinery (Sabnavis *et al*., 2004; Ricci and Pennacchi, 2012).

b) *Slant crack*: Crack that originates at an angle to the axis of the shaft, as shown in Fig. 1.3 (b), is defined as the slant crack. The frequency of generation of this kind of crack is less common in the rotating components. The slant crack has a lesser effect on the dynamics of the rotor system than transverse crack and has a substantial effect in the presence of torsional stresses (Lin and Chu, 2010).

TH-2966_176103027

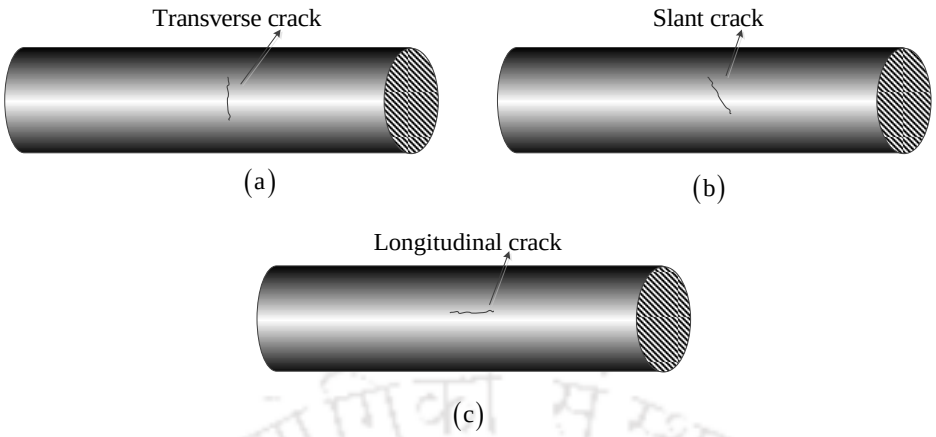


Fig. 1. 3. Transverse and slant cracked shaft.

c) *Longitudinal crack*: Crack that originates parallel to the axis of the shaft, as shown in Fig. 1.3 (c), is known as longitudinal crack. This type of crack is formed when the system is under the influence of cyclic torsion. The effect on the dynamic of the rotor system is very less.

The opening and closure of the crack faces in the rotor system are studied primarily based on two different behaviors, i.e., the switching crack and the breathing crack. In the switching crack, the opening and closure of the clack faces during rotation are sudden and are assumed to be open for half of the cycle and closed for the rest of the cycle. This type of behavior of crack introduces additional harmonics to the rotor responses, such as 2X, 3X, 5X, -1X, -3X (Wang *et al*., 2010; Singh and Tiwari, 2016). Whereas, in the breathing crack, the opening and closure of the crack faces are gradual and are assumed to be opening for a particular angle of rotation and closed for the rest of the rotation. The behavior of breathing and switching cracks are mostly influenced by the static weight of the rotor system and the level of the unbalances. For a low level of unbalances, the behavior of both the crack model is similar, but for a higher level of unbalance, the

TH-2966_176103027

breathing model represents the crack with more accuracy and generates a larger value of responses (Darpe *et al*., 2004a).

1.3.3 Misalignment

In rotating machinery, the proper alignment of driven and driving rotor components is very difficult to achieve. In almost every rotor train, the condition of misalignment is always present. The manufacturing tolerances, dependence on the use of elastic coupling, deformation of the machinery, and inaccurate alignment of the shafts, bearings, couplings, etc., are the main reasons for the generation of misalignment. The power transmission between the driving and the driven part is reduced with the increase in the level of misalignment. The reaction forces generated at the coupling and the bearing locations due to misalignment are the major cause of the vibration in machinery (Lee and Lee, 1999; Al-Hussain and Redmond, 2002). Therefore, it is necessary to evaluate the intensity of the misalignment in the rotor system to prevent wear and premature damage to the machinery. The types of misalignments that are commonly found in the rotating machinery are given as follows:

(a) *Parallel or offset misalignment*: The centerline of the shafts connected by the coupling are parallel and offset in case of parallel misalignment, as shown in Fig. 1.4. The offset can be in the vertical or horizontal direction perpendicular to the axis of the shaft (Patel and Darpe, 2009a, 2009b).

(b) *Angular misalignment*: The centerline of the shafts connected by the coupling are intersecting at an angle in case of angular misalignment, as shown in Fig. 1.4 (Al-Hussain, 2003; da Silva and Cavalca, 2019).

TH-2966_176103027

The misalignment contributes to the generation of 1X, 2X, 3X, -1X, -2X components of harmonics in the displacement response of the rotor system. In some of the cases, the 2X components can be high as the 1X component in the displacement responses.

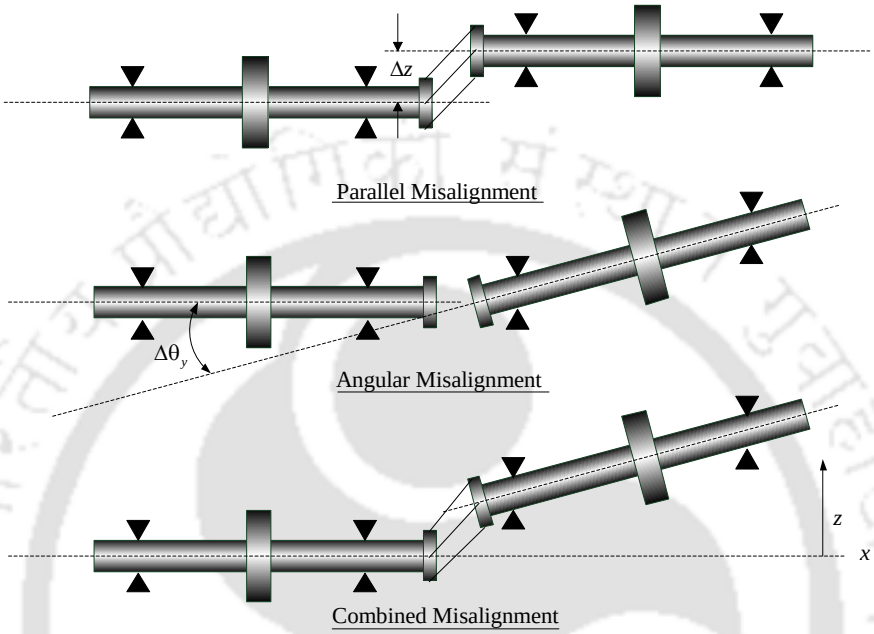


Fig. 1. 4. Types of misalignments in the rigid rotor system.

1.3.4 Residual shaft bow

The residual bow or permanent bent in the shaft generated due to large static load, thermal distortion and creep. The shaft bow affects the 1X harmonics of the displacement response similar to the unbalance force, but there is no dependency on the operating speed of the system. At low speed, the effect of the residual bow is dominant in the rotor system, whereas at high-speed residual unbalance is dominant (Nicholas *et al*., 1976a, 1976b; Song *et al*., 2013; Sanches and Pederiva, 2016).

TH-2966_176103027

1.4. Active vibration control with magnetic bearings

Magnetic bearing plays an important role in the rectification of problems associated with the dynamics of the rotor system by allowing the rotor to spin without contact, lubrication, and wear. The magnetic bearings, also known as contactless bearings, operate on the principle of magnetic suspension, allowing the system to rotate in a vacuum, extreme environmental conditions, gas, or liquid. The magnetic bearings are being utilized for vibration suppression in the rotating machinery with permanent magnets or active control of electromagnets (Chiba *et al.*, 2005; Schweitzer and Maslen, 2009; Polajzer, 2010). The magnetic bearings are classified based on the control algorithm, nature of magnetic forces, types of sensing devices, and types of loads applied, as shown in Fig. 1.5.

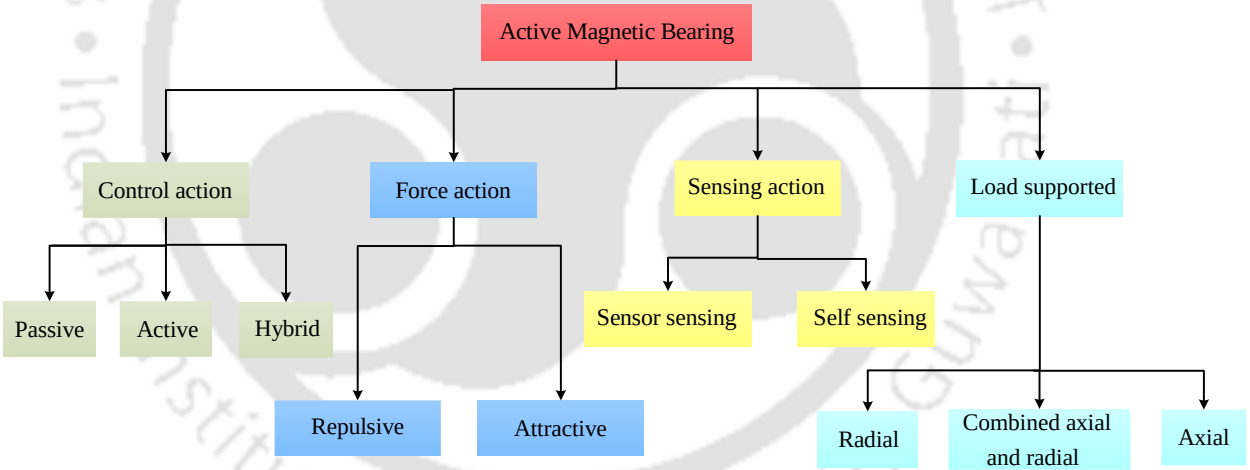


Fig. 1. 5. Types of magnetic bearings.

Based on the control action, the magnetic bearing system is divided into the following three categories:

(a) *Passive Magnetic Bearing* (PMB): This type of magnetic bearing utilizes permanent magnets to generate constant magnetic fields in order to levitate the system with

TH-2966_176103027

repulsive and attractive forces. There is no feedback control action that can control the vibration of the system within the required limit (Bachovchin *et al*., 2012).

(b) *Active Magnetic Bearing* (AMB): On contrary to PMB, AMB utilized electromagnets to generate varying magnetic fields for vibration suppression. The controlling magnetic force generated by AMB allows the rotor system to levitate with the desired level of vibration control. Based on the displacement response, the control current is generated and supplied to the AMB for feedback control (Chiba *et al*., 2005; Schweitzer and Maslen, 2009; Polajzer, 2010).

(c) *Hybrid Magnetic Bearing* (HMB): - The HMB is the combination of the advantageous straits of both PMB and AMB. The system is levitated by means of PMB whereas, the control action for the suppression of vibration is carried out by the AMB. In some HMB, instead of PMB, foil bearings are used to carry the load of the system (Pham and Ahn, 2014). Also, now the combination of rolling element bearings (REB) and AMB are being utilized, where REB supports the rotor system, and AMB controls the vibration of the system (Sarmah and Tiwari, 2020).

Some of the researchers have worked on designing a passive magnetic bearing system that is stable in all directions by using permanent magnets and control coils. Bachovchin *et al*. (2012) designed a new PMB system to levitate the rotor system in all directions. They utilized a Halbach stabilizer along with the coupled permanent magnets for levitation. The stabilizer generates a current in the stabilization coils to decrease the level of instability in the vertical direction. Pham and Ahn (2014) designed an optimized hybrid foil magnetic bearing that consists of foil bearing as support and AMB as a controller. They compared the unbalance responses of the flexible rotor supported by two

TH-2966_176103027

different bearings, airfoil and hybrid bearings. The unbalance responses of the rotor system show that the rotor vibration in bending critical speed is more suppressed by the hybrid foil bearing than the airfoil bearing only. Martynenko (2016) developed a PMB to allow the passage of the rotor system in resonance mode during run-up or run-down conditions. They utilized control windings generating variable stiffness for a short time. They also validated the suggested method of detuning the rotor from critical speeds numerically as well as experimentally.

The main problem with the passive magnetic bearings is the difficulty of achieving stability along all the axis of control. Whereas on the other hand, the AMBs are able to stabilize all the translational degrees of freedom of the rotor system. With the availability of variable damping characteristics of the AMBs, the passage of the critical speed with minimum vibration can be achieved. As a result of this, AMBs are extensively utilized in the vibration monitoring and control of the rotor systems operating at high speeds. An active magnetic bearing consists of various components that are described as follows.

1.4.1 Actuator

The actuator is an electromagnet that generates a controlling magnetic force in the AMB system based on the control current supplied to the coils wound around the soft iron core. The laminated electrical steel plates are stacked together with copper coils to control the rotor system along the orthogonal axes. The control current is fed to the coils in the actuator to generate a controlling force for levitation and attenuation of vibration in rotating machinery. The radial and thrust actuators are utilized to control the vibration in the radial and axial directions of the rotor system, respectively. The actuator is also classified based on the direction of flux flow and the number of pole pairs, as shown in Fig.

TH-2966_176103027

1.6. On the basis of the direction of flow of flux in the rotor, there are two types of actuators, i.e., homopolar and heteropolar. In the homopolar, the flow of magnetic flux is parallel to the axis of the shaft, whereas in heteropolar, the flow direction is perpendicular to the rotor axis, as shown in Fig. 1.7 (a).

The actuators are usually designed with a different number of poles or pole pairs. The lesser number of pole pairs has better cooling arrangement structure, better cost-effectiveness, cooling arrangement, and compact structure.

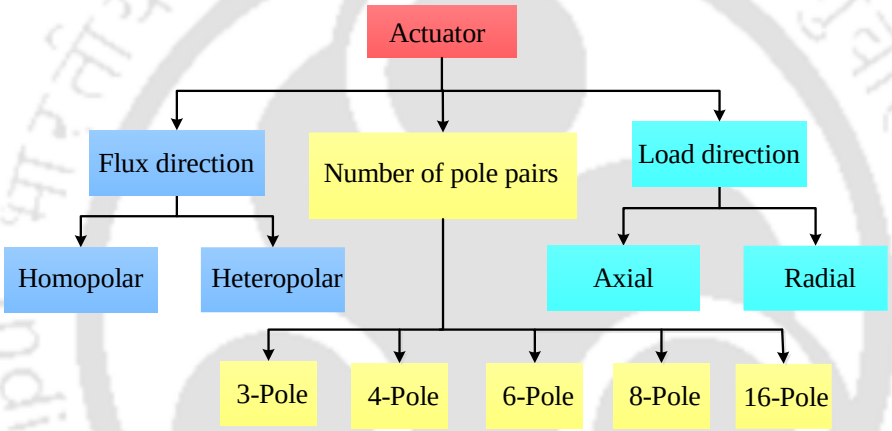


Fig. 1. 6. Types of actuators in AMB system.

The control structure utilized for 3-pole electromagnets, as shown in Fig. 1.7 (b), is quite complicated, and to stabilize the nonlinear system approach is required. In an 8-pole actuator, as shown in Fig. 1.7 (c), the control action is quite simpler, and the linearized control algorithm can be adapted to minimize the level of vibration in two orthogonal axes.

The design of the actuator is complex as its performance is dependent on various factors such as load, size, stiffness, temperature, precision, speed, losses, and dynamics, as shown in Fig. 1.8. A lot of work has been done to obtain an optimal number of stator poles to meet the space requirement as well as to decrease power loss, cost, and better heat

TH-2966_176103027

dissipation facility. Matsuda *et al*. (2007) described a methodology to estimate the optimal number of poles of the electromagnet in radial AMB for the minimum outside diameter of the stator. They concluded that a 3-pole electromagnet has the minimum stator diameter and levitated the rotor using a linear control strategy.

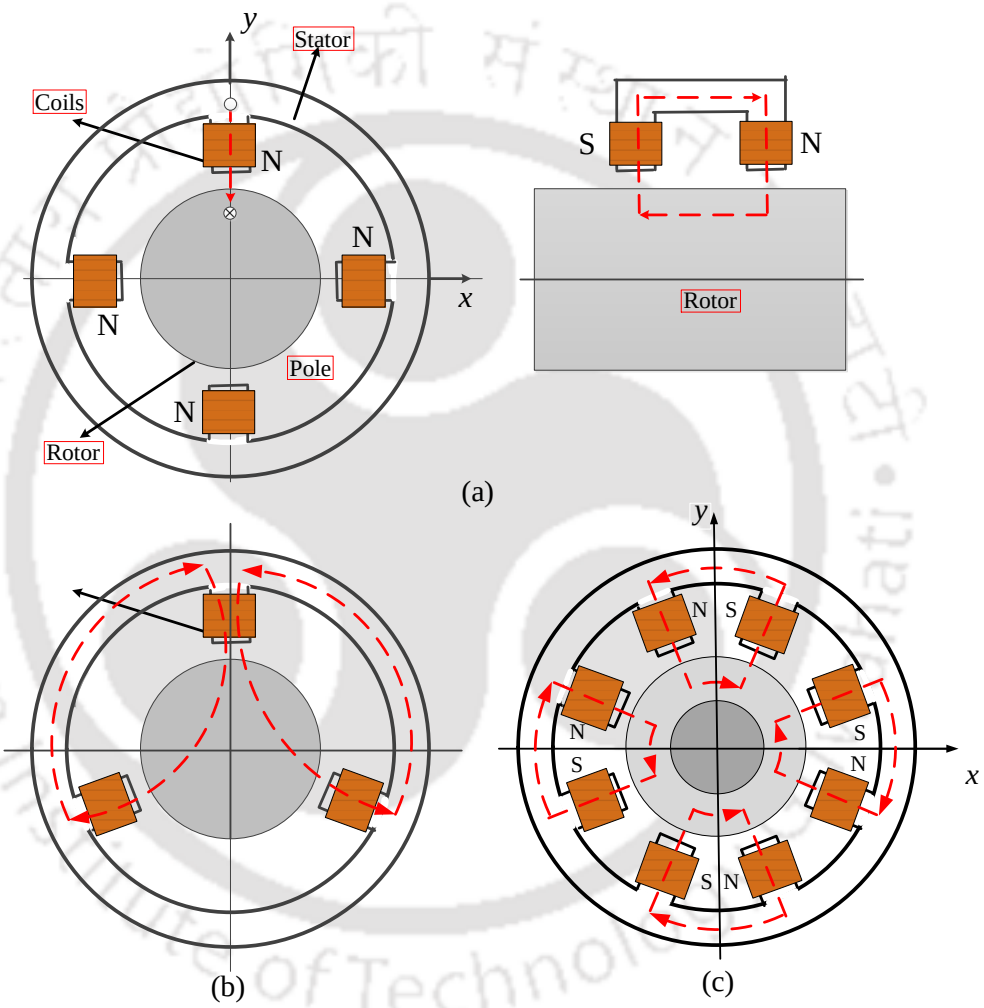


Fig. 1. 7. A schematic diagram of a) homopolar magnetic bearing, (b) 3-pole heteropolar magnetic bearing, c) 8-pole heteropolar magnetic bearing with field directions.

Weißbacher *et al*. (2009) described the improvement and application of tubular linear actuator (TLA) as an axial magnetic bearing. The TLA consists of a rotor, permanent

TH-2966_176103027

magnet, and an electromagnet part to achieve control in the axial direction. The improved TLA showed a reduction in radial instability and a lower value of the electromagnetic force current constant. Da Silva *et al*. (2011) designed a type of magnetic bearing, where the control of axial position is done actively. At the same time, the other degree of freedom is controlled by the permanent magnets. The design criterion is based on ordinary analytical models as well as FEM to reach both the highest force current ratio and magnetic radial stiffness. Xu and Fang (2013) proposed a claw active magnetic bearing (CAMB) with a compact size of a smaller radius. The CAMB has a claw-like structure, and both the stator core and coils are located along the axial direction. They analyzed the magnitude of the magnetic field produced using the magnetic circuit method and built a 3-D finite element model of CAMB.

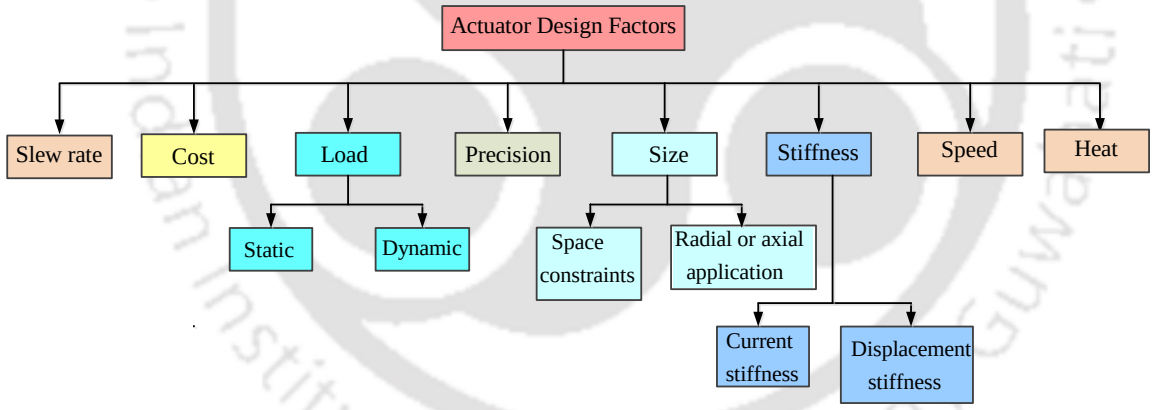


Fig. 1. 8. A block diagram showing different design factors considered in the design of actuators of AMB.

The above-mentioned designs of actuators are yet to be properly implemented in practical rotor systems. Experimental validation is required to gain the advantages of these proposed actuators, and some new adoptive and robust control methods could be implemented to make the rotor system stable.

TH-2966_176103027

1.4.2 Position Sensor

A position sensor is a device capable of sensing shaft displacement from a fixed point in the rotor-AMB system. The information provided by the sensors is used to generate controlling currents, which are then used to produce a magnetic force on the rotor system. The Hall effect sensors and the eddy current sensors are mostly used in the measurement of responses in the rotor system.

(a) *Eddy current sensors*: Eddy current displacement sensors are non-contact devices that are able to measure the displacement of a conductive object at a high resolution. It works on the principle of formation of eddy current, when the flux is linked to the ferromagnetic core changes, to measure the displacement response. The eddy current induced in the conductive object produces magnetic flux to oppose the change in the magnetic field and reduce the inductance of the electromagnetic coil. The change in the impedance of the coil is sensed by the sensor to identify the gap between the probe and the conductive material of the rotor. The sensors are set in a fixed range to obtain a linearized output of the distance measured.

(b) *Hall effect sensor*: It is a type of sensing device that detects the magnetic field and its magnitude using the principle of the Hall effect. If the current-carrying conductor is placed perpendicular to the magnetic field, a voltage gradient is developed perpendicular to the flow of the current. The velocity gradient is calibrated to obtain the magnitude of the magnetic field. The output voltage of the Hall effect sensors is very low and is required to be amplified.

The position of the sensor is also considered an important factor in the control of the AMB system. Johnson *et al*. (2003) investigated, both theoretically and experimentally,

TH-2966_176103027

the effect of the location and number of sensors and magnetic bearing actuators on vibration reduction using a feed-forward control scheme. In the results, it is shown that for any case where the same number of actuators and error sensors are used, there can be a large increase in vibrations away from error sensors at certain frequencies. Kulesza (2015) described the methodology for the virtual collocation of sensors in AMB control. The displacement at actuators' location is estimated based on the displacements at sensors' location. The approach is verified through numerical results on a flexible rotor system supported by AMBs and controlled by 4 PID controllers. Chen and Liu (2017) designed a novel sensor-less control of a 3-pole AMB system. Additional sensing coils are added along with the control coils to detect the displacement of the rotor system at the AMB location. The linear PD controller fails to stabilize the system, and it requires non-linear methods to control the AMB system.

1.4.3 Amplifier

An amplifier is a device that increases the power output of either a voltage or a current signal. The amplitude of the input signal is amplified by the use of an external power supply. The ratio of output to the input signal is the amount of amplification generated in the required signal. The controlling current from the controller is sent to the amplifier to amplify the current to generate an appreciable amount of magnetic force at the actuator of the AMB system. There are two types of amplifier circuits used, the first one is called the analog amplifier, and the second one is called the switching amplifier (Cao and Lee, 2004; Changsheng and Zhiwei, 2005).

(a) *Analog amplifiers*: This type of amplifier supplies continuous output voltage in the electronic system based on the input signal. In this type of amplifier, a voltage drop is

TH-2966_176103027

always present across the transistor, as a result of which energy dissipation as heat is high. Therefore, the use of analog amplifiers for the long term is a great issue.

(b) *Switching amplifiers*: The switching amplifier modulates a high-frequency voltage signal in such a way that the average output voltage represents the required voltage waveform. The switching frequency of the amplifier is required to be higher than the frequency of the desired control signal. In this type of amplifier, the output transistors act as switches that are either in a fully ON or fully OFF state. This reduces the overall power loss in the amplifier and is beneficial to be used for long-run applications. The Pulse Width Modulation (PWM) technique is utilized in which the width of a square waveform is varied to obtain the desired output voltage.

The analog and switching amplifiers have the same initial cost, but the running cost of the switching amplifier is quite less than that of the analog amplifier. The efficiency of the analog amplifier is around 40% to 50%, while the switching amplifier is about 80%.

1.4.4 Controller

The controller is an electronic device that utilizes a signal from the sensing device and generates the control signal based on the designed control algorithm. It is used to reduce the difference between the signal received from the sensor and the desired signal required to be achieved. The controller utilized in the control strategy of various devices is of two types, i.e., analog and digital controller. The analog controller is pre-designed electronic circuits based on a particular control algorithm. This type of controller is not costly and simple in design but has disadvantages, such as the features of filters are fixed by circuits, consistency of potentiometers, and component drift. At the same time, the digital controllers allow the user to design complex algorithms on a software platform, like

TH-2966_176103027

dSPACE or LABVIEW, and implement them in real-world problems utilizing the analog-to-digital (A/D) and digital-to-analog (D/A) converters. The advantage of the digital controller is that the control algorithm can be easily modified, and the control parameters can be varied during the runtime of the system.

Several studies have been done in the development of different controllers, as shown in Fig. 1.9, that enable better design and performance in operating situations, with acceptable levels of robustness and stability. The input given to the controller is the displacement of the rotor, and the output received is the controlling current sent to the coils of the electromagnet. The active vibration control requires an establishment of closed-loop control with the help of control laws, such as the Proportional-Derivative (PD) control, Proportional-Integral-Derivative (PID) control, Proportional-Integral (PI) control as shown in Fig. 1.10 and adaptive control laws as shown in Fig. 1.11.

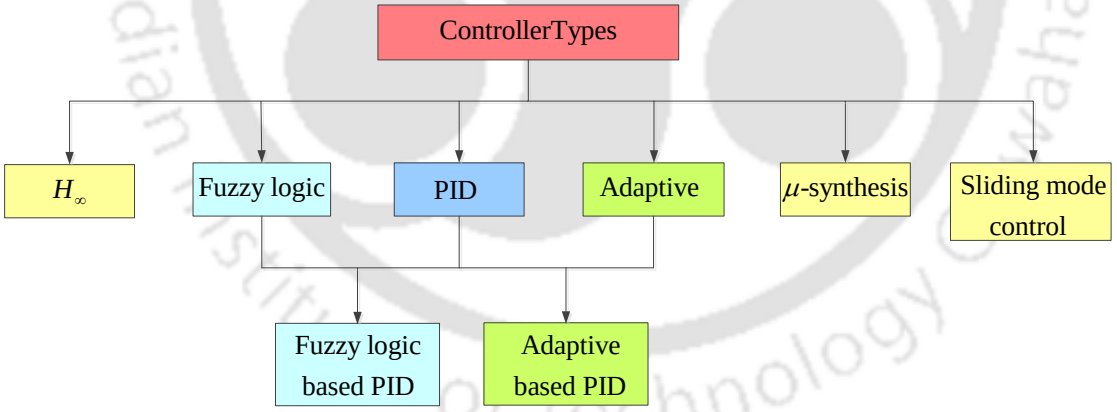


Fig. 1. 9. A block diagram showing different types of controllers utilized in the rotor system.

The PID (Proportional Integral Derivative) controller is most widely used in practice to control AMB systems. The derivative gain (k_D) increases the damping of the system, the proportional gain (k_P) increases the stiffness of the system, and the integral gain (k_I)

TH-2966_176103027

removes the steady-state error allowing the system to rotate about a fixed axis. The current output obtained from the controller is given by

$$i(t) = k_P x(\mathrm{t}) + k_I \int_0^t x(t)dt + k_D \frac{dx(t)}{dt} \tag{1.4}$$

where, x is the input signal to the controller, k_P represents proportional factor, k_I represents integral factor, and k_D represents derivative factor.

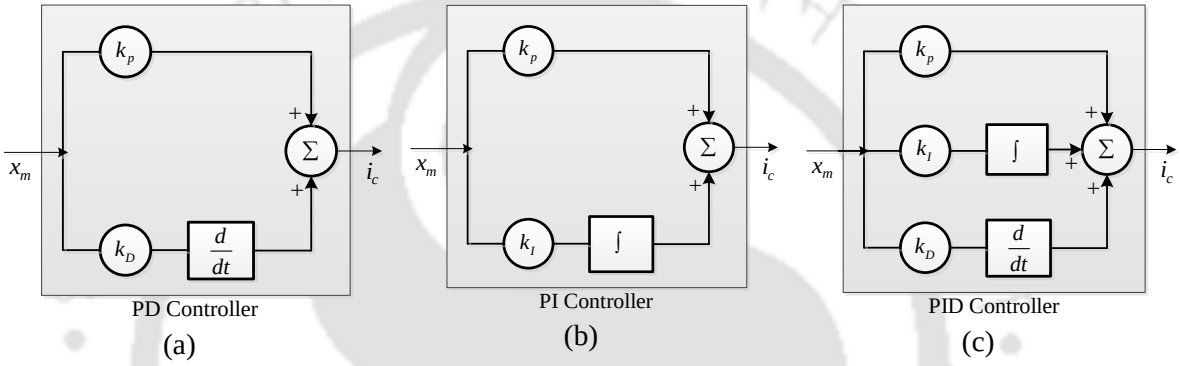


Fig. 1. 10. A line diagram of a (a) PD controller, (b) PI controller, and (c) PID controller system for the generation of control current.

However, with the use of a PID controller, the control of flexible rotors remains difficult due to spillover effects. Hung (1993) presented a fuzzy-logic-based controller design to improve the controlling action of the magnetic bearing system. They utilized a fuzzy algorithm to compensate the harmonics excitation in the rotor system and discussed the relationships of attractive force to the control currents and air gap. Tung *et al*. (2011) described a fuzzy algorithm to tune the PID controller gain for better control of the rotor-AMB system. They concluded that the utilization of force observer (integral type) improves the rotation accuracy of the rotor system. Akash *et al*. (2014) implemented an adaptive algorithm to tune the controller gains of the PID controller using the result adaptive technique. They evaluated the performance of the designed controller by

TH-2966_176103027

minimizing the setting time and overshoot in the impulse response. Folea *et al*. (2015) designed a fractional order controller and introduced a novel procedure to tune the parameters without the implementation of any optimization procedures. They showed that the designed controller is robust to the uncertainties in the model and loading conditions. Noshadi *et al*. (2016) designed objective functions based on time-domain analysis to optimize the control parameters of the PID-type fuzzy controllers. They compared the performance of the designed controller from the conventional PID controller, and it was found to be robust in reducing the vibrational response. Lyu *et al*. (2018) designed an algorithm to monitor the orbit response of the rotor-AMB system in the touchdown conditions. They presented a suspension control algorithm with a PID control technique to re-levitate the rotor system in the full rub or combined rub and bouncing situations.

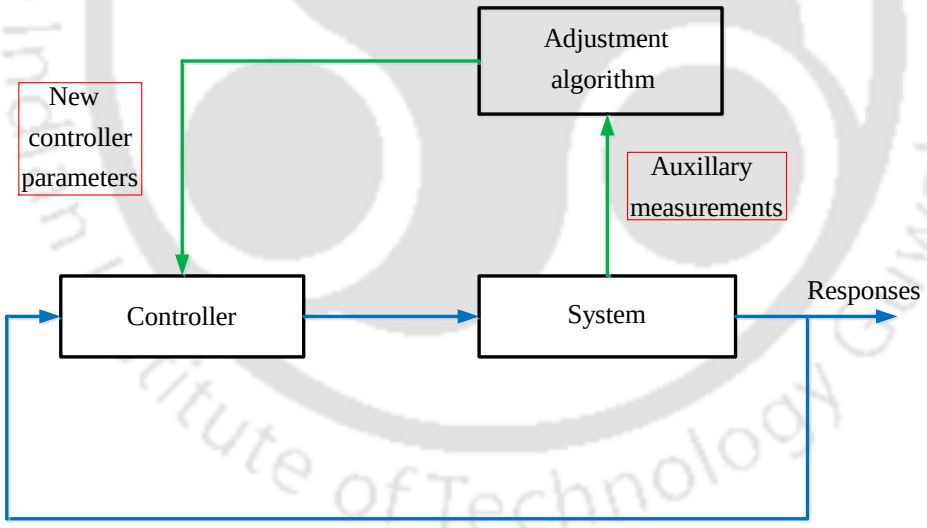


Fig. 1. 11. A schematic of working of an adaptive control-based controller.

These controllers do not perform well in complex systems such as nonlinear, time-variant, and systems including uncertainties. To overcome these problems, different control strategies have been developed, which include the fuzzy logic-based control, sliding mode

TH-2966_176103027

control, FBLMS control algorithm, ILC algorithm, and some adaptive techniques with notch filters. Hong and Langari (2000) designed a nonlinear fuzzy logic-based control algorithm to overcome the position-dependent nonlinearity of the rotor-AMB system. They utilized Takagi-Sugeno-Kang (TSK) fuzzy algorithm to tackle the problem of nonlinearities. Through experiments and simulation results, they demonstrated that the developed controller provides robustness against uncertainties in parameters and harmonic excitation. Hsu and Chen (2003) designed an integral sliding mode strategy to control the nonlinear three-pole AMB system. Through experiments and numerical simulations, they showed that the developed controller allows the rotor system to be stable. Bi *et al*. (2005) developed an automatic learning control algorithm to reduce the effect of residual unbalance present in the rotor system. The utilized variable learning gain and variable learning cycle to reduce the fluctuations in the operating speed. Through experiments, they showed that the control strategy is efficient over a wide speed range.

Sahinkaya *et al*. (2011) designed a multi-objective control algorithm to reduce the force transmitted to the base and the rotor vibration with the adaptive tuning of the controller gains. The procedure is carried out in two stages weighting strategy. Jiang and Zhu (2011) proposed a method to suppress the multi-harmonic periodic excitation in the rotor-AMB systems. The evaluation in the frequency domain is done using the Fast Block Least Mean Square (FBLMS) algorithm that allows the computations to be done irrespective of the harmonic component in the excitation response. Schuhmann *et al*. (2011) utilized Linear Quadratic Gaussian (LQG) controller to minimize the excitation response in the rotor-AMB system. The controller consists of the optimal-state feedback regulator and extended Kalman filter to improve the positional accuracy that provides

TH-2966_176103027

higher stiffness and less control power. Defoy *et al*. (2014) designed a fuzzy logic-based controller to compensate for the detrimental anisotropic behavior of the system using the inputs in polar coordinates. They compared the designed controller with the conventional PID and Single Input Single Output (SISO) controller to show the effectiveness in achieving stability in the system.

Zheng *et al*. (2014) optimized the compensation of damping in the flexible rotor system in order to maximize the use of the magnetic force. They also described the design of the AMB test rig for a 10-kW centrifugal compressor. They validated the proposed optimization approach through damping compensation experiments. Hutterer *et al*. (2015) designed a self-sensing controller to reduce the unbalance excitation that leads to saturation of the AMB actuator. They utilized an unbalance observer to identify the angle of synchronous unbalance vibration and angular velocity to remove the oscillations in the control current. Saeed and Kamel (2017) designed a position feedback controller to control the lateral vibration in a Jeffcott rotor system having cubic and quadratic nonlinearities. They investigated the bifurcation behaviors and the influence of air gap size, bias current, disc eccentricity, feedback gain, and control gain on vibration amplitudes. Chen *et al*. (2017) modified an adaptive notch filter with a phase shift to reduce the unbalance excitation without utilizing information of the angular velocity. They verified the developed controller with experimental data to ensure the robustness of the algorithm. The drawback of these methods is that the robustness properties are not taken into account. To resolve such problems, the μ-synthesis and H_∞ controller came into existence. They can tackle various problems, such as measurement noise, external disturbance, and model uncertainty, and can take several objectives into account simultaneously.

TH-2966_176103027

Lindlau and Knospe (2002) designed a high-performance controller with μ-synthesis for the linearized feedback system. They used a single degree of freedom model for AMB with the controller operated in voltage mode control. They showed that the feedback linearized controller transforms the nonlinear system to the linear system. Cole *et al*. (2004) designed a multivariable control system that can tackle different faults in the rotor-AMB system. They used H_∞ optimized disturbance rejection criteria to improve the tolerance to specific system faults. They showed the effectiveness of the control implementations by performing experiments on the flexible rotor system. Mushi *et al*. (2011) constructed a complete model of the rotor, AMB actuators, and accompanying electronics from individually verified construction models. They confirmed the model validation through the successful design and implementation of the μ-synthesis controller. Di and Lin (2014) described the working of all coefficient adaptive controller based on the characteristic model to stabilize the flexible rotor-AMB system. The μ-synthesis controller, as well as characteristics model based all coefficient adaptive control, are compared both numerically and experimentally. The control strategies implemented to the AMB system effectively reduce the vibration response of the rotor. The functionality of the AMB system with different components is discussed in the next section.

1.4.5 Functionality of the rotor-AMB system

The components of the AMB system are assembled together in the rotor test rig to establish a closed-loop control structure. The actuator with copper coil windings is mounted on the test rig to generate magnetic flux in response to the control current in the coils, as shown in Fig. 1.12. An additional core of ferromagnetic material is mounted on the shaft to maximize the attraction force between the shaft and the stationary actuator. The core is also

TH-2966_176103027

manufactured with laminated silicon steel sheets to minimize the eddy current loss. The displacement of the shaft from its equilibrium position is sensed by the eddy current sensor, which is then transferred to the controller to generate the control current as per the control algorithm designed for vibration suppression. The control signal is amplified through a power amplifier to generate the requisite amount of magnetic flux in the electromagnetic actuator. The magnetic force subjected to the ferromagnetic core attracts the rotor back to its equilibrium position. The ideal magnetic flux density (B_e) generated by the electromagnet is given as

$$B_e = \mu_0 N i_0 / l_g \tag{1.5}$$

where, i_0 is the current in the coil, N is the number of turns of the coils, l_g is the air gap between the actuator and the core, and μ_0 is the magnetic permeability of free space. Also, due to electrical and magnetic losses, the intensity of the fields mentioned in Eq. 1.5 deviates from the experimental investigation (Chiba *et al*., 2005; Schweitzer and Maslen, 2009). The magnetic force (F_e) applied by the actuator on the ferromagnetic core is given by

$$F_e = A_g B_e^2 \cos\alpha / \mu_0 \tag{1.6}$$

where, A_g is the area of the air gap. On substituting Eq. 1.5 into Eq. 1.6, we obtain the relationship between the coil current and magnetic force as

$$F_e = \mu_0 A_g N^2 i_0^2 / l_g^2 \tag{1.7}$$

TH-2966_176103027

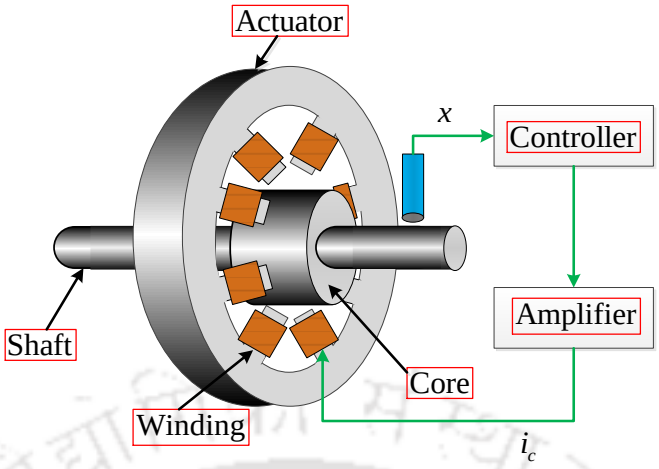


Fig. 1. 12. A schematic of an active magnetic bearing with a rotor.

The relationship between the AMB force and the coil current is non-linear, which is not suited for analysis purposes. Therefore, the magnetic force is linearized at the operating point by utilizing the bias current along with the control current. The linearization of the magnetic force is achieved by utilizing two counteracting electromagnets, and the AMB is said to be operated in the differential driving mode control. In the case of an eight-pole electromagnet, as shown in Fig. 1.13, the two pairs of poles along the horizontal direction are considered as counteracting electromagnets. In the differential mode control, a bias current (i_b) is supplied to both pair of electromagnets that produces a static magnetic field. As the rotor is displaced from its position (x_m) towards the right pair of electromagnets, a control current (i_c) is supplied in addition to the bias current to both pairs of electromagnets. The control current gets added to the left pair and gets subtracted from the right pair, which generates a restoring force on the ferromagnetic core in the direction of the left pair. The restoring force brings the rotor back to its equilibrium position. The magnetic force (f_m) subjected by the pair of electromagnets is given by

TH-2966_176103027

$$f_m = c_1 \cos\alpha \left(i_m / l_g \right)^2 \tag{1.8}$$

With, $c_1 = 0.25 \mu_0 N^2 A_g$

where, i_m is the current generated in the coils of the AMB. N is the number of turns of coil in the electromagnet poles; μ_0 is the permeability of free space; A_g is the area of the gap between the stator and ferromagnetic core; α is the half-angle between the two poles of electromagnet and l_g is the air gap.

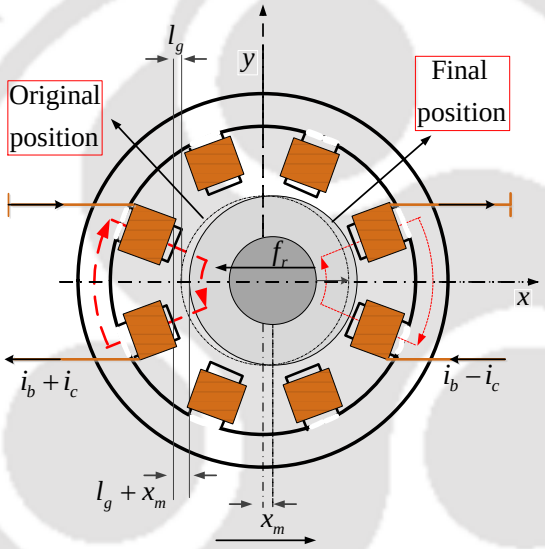


Fig. 1. 13. A working AMB system in differential mode of a controller.

Using Eq. 1.5, the restoring force (f_r) acting on the core due to counteracting pair of electromagnets is given as

$$f_r = f_{r+} - f_{r-} = c_1 \left(\frac{i_b + i_c}{l_g + x_m} \right)^2 \cos\alpha - c_1 \left(\frac{i_b - i_c}{l_g - x_m} \right)^2 \cos\alpha \tag{1.9}$$

where, i_c and i_b are the control and bias current generated in the coils of the AMB. x_m is the displacement generated by the rotor at the AMB location. As the vibration displacement

TH-2966_176103027

gets reduced by a large fraction in AMB control ($x_m << l_g$), the non-linear forces present in the system gets negligible. So, the non-linear terms of the AMB force model can be removed, and the equation takes the form as (Tiwari, 2017)

$$f_r = -k_s x_m + k_i i_c \tag{1.10}$$

with, $k_s = 4c_1 i_b^2 \cos\alpha / l_g^3 \quad k_i = 4c_1 i_b \cos\alpha / l_g^2$

where, k_s is the force-displacement factor, and k_i is the force-current factor.

The same principle is applied to the opposite pair of poles in the vertical direction to control the displacement of the rotor system along two orthogonal axes.

The identification of AMB parameters is important to improve the system performance and instability. Many of the researchers have focused on frequency response functions to identify the current and position stiffness of the AMB-rotor system using the least-squares technique. Also, different force and current measurement techniques have been developed to carry out the identification process. Lee *et al*. (1996) employed complex model testing to obtain the directional frequency responses of an AMB system. These directional frequency responses were used to identify the stiffness parameters of the AMB. Marshall *et al*. (2001) discussed a force measurement technique, which is a multipoint measurement to determine the force applied by the active magnetic bearing based on actuator geometry and control currents only, without the knowledge of the air gap. Kasarda *et al*. (2007) addressed a multi-point technique which is a current-based force measurement identification approach for an active magnetic bearing that acts as a supporting bearing. Here, they determined both gap and force by using the current perturbation method. Khader *et al*. (2014) identified the stiffness parameter of the AMB system as well as the

TH-2966_176103027

parameters related to the flexible modes of the flexible rotor system. They developed a linear state-space model to perform the identification procedure using the frequency domain responses. The stiffness parameters of the AMB system are also identified utilizing a model-based identification procedure that requires frequency domain responses of the system and control current to estimate the parameters (Tiwari and Chougale, 2014; Prasad and Tiwari, 2019). Zhou *et al*. (2016) developed an identification technique to estimate the AMB parameters using the vibration response of the rotor system due to unbalances. They modeled a rotor-AMB system using FEM to predict the errors generated due to the flexibility of the rotor system. Vuojolainen *et al*. (2017) presented a signal-based identification method for estimating AMB parameters using various artificial excitation signals, namely the pseudo-random binary sequence (PRBS), chirp signal, multi-sine, and stepped sine.

1.5. Reduction of residual unbalances in rotor-AMB system

As discussed earlier, the residual unbalances in the rotor system are the common and major cause of excessive vibrations that results in fatigue failure of the system. Therefore, there is a need to reduce the level of unbalances in the system at the starting stages of the operation and after subsequent overhauls. Various signatures are shown in the visual inspection of the rotor system that predicts the causes of unbalances as shown in Table 1.1 (Rieger, 1986). In the industrial rotor system, the unbalances are reduced using various experimental balancing techniques based on the vibration responses based on International Organization for Standardization (ISO) standards, i.e., ISO 1940-1:2003 for rigid rotors and ISO 11342 for flexible rotors. The balancing strategies allow the center of mass of the

TH-2966_176103027

rotor system to coincide with the rotating axis of the system through the addition of redistribution masses at specific locations. Based on ISO standards, the rotor systems are classified into different categories, such as

1. Rigid rotor (Class 1): These rotor systems require balancing at two planes, and the system remains balanced in the entire operating range. Example: shaft with gear wheels
2. Quasi flexible rotor (Class 2): The rotors that are not considered to be completely rigid but can be balanced at low speed with one or two balance planes. Example: Shaft with grinding wheel, jet engine compressor, etc.
3. Flexible rotor (Class 3): These rotors require high-speed balancing using the influence coefficient method or modal balancing technique. Example: Generator rotor.
4. Special flexible rotor (Class 4): These rotors fall in the category of 1, 2, or 3 type rotors but in addition have flexible components attached. Example: Rotor with the centrifugal switch that opens above a certain speed.

The methodologies employed in the reduction of the residual unbalance in the rotor systems are divided into two groups: offline balancing (no active vibration control devices are implemented) and online automatic balancing (vibration control devices such as AMB are implemented).

1.5.1. Offline balancing techniques

The identification of the residual unbalances carried out in the rotor system based on the vibration responses without active control in the level of vibration. The different types of methodologies utilized to reduce the level of vibration are as follows.

TH-2966_176103027

Table 1. 1. Sources of unbalances in the rotor system with their signatures in vibrational responses.

	Sources of unbalances	Observable signatures
1.	Eccentricity due to discs or attached components	Rotor moves to the heavy side when supported on knife edges
2.	Inaccuracies in dimension	Lack of symmetry in inspection
3.	Residual bow in the shaft	Appreciable runout at slow operating condition
4.	Accumulation of foreign particle	Increase in vibration at bearings
5.	Differential thermal expansion	Bend in the shaft with a shift in the center of mass
6.	Looseness in bolt or slip in components	Change in amplitude and phase of the vibration response, appreciable vibration after balancing
7.	Improper machining of inaccuracies in forming	Appreciable runout

1.5.1.1. Rigid rotor balancing

In industries, there is no such rotor that is perfectly rigid. If the rotor is operated much below its flexible critical speeds, then it is considered a rigid rotor system. The deformation of the rotating elements is considered to be appreciably less in the case of rigid rotors. The different types of unbalances present in the rigid rotor system are shown in Fig. 1.2. The balancing of rigid rotor system is carried out either using single plane or two plane balancing strategies (Foiles *et al*., 1998).

1. *Single plane balancing* (*static balancing*): The orientation of the center of mass is identified by allowing the rotor to rotate freely on the frictionless support (Tiwari, 2017). As the rotation stops, the heavy spot on the rotor moves to the downward side under the influence of gravity. An additional mass is applied opposite to the heavy spot to balance the system. Once balanced on rotation, the rotor stops at a position

TH-2966_176103027

other than the downside. This process is able to balance the resultant unbalance force in the rotor system. However, this balancing procedure is not effective for cases where unbalances generate an additional moment in the system.

2. *Two plane balancing* (*cradle balancing*): This method is an off-site balancing technique where the rotor is removed from the installation and placed on the cradle balancing machine, as shown in Fig. 1.14 (Broch, 1980; Hartog, 1985). The cradle is supported on springs and has two fulcrums to pivot the system. The rotor is rotated with the help of a belt drive.

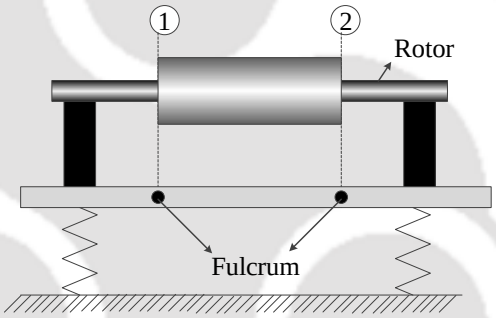


Fig. 1. 14. A schematic of a cradle balancing machine.

The system is hinged at one of the pivots (1) and operated around critical speed with additional trial mass at another pivot (2). The orientation and magnitude of the trial mass are adjusted till the vibrational response gets minimized at pivot (2). A similar procedure is followed for pivot (1) to balance the rotor system.

3. *Two plane balancing* (*Influence coefficient method*): ICM is called field balancing technique as the balancing procedure can be done on the site of operation of the rotor system. This method requires three trial runs to estimate the residual unbalances at the two balancing planes. The vibration responses obtained from the rotor system with or

TH-2966_176103027

without the application of the trial masses are utilized to identify the influence coefficients of the rotor system, as shown in Fig. 1.15. The influence coefficients are then used to predict the unbalances at the balancing planes based on the responses obtained without trial masses.

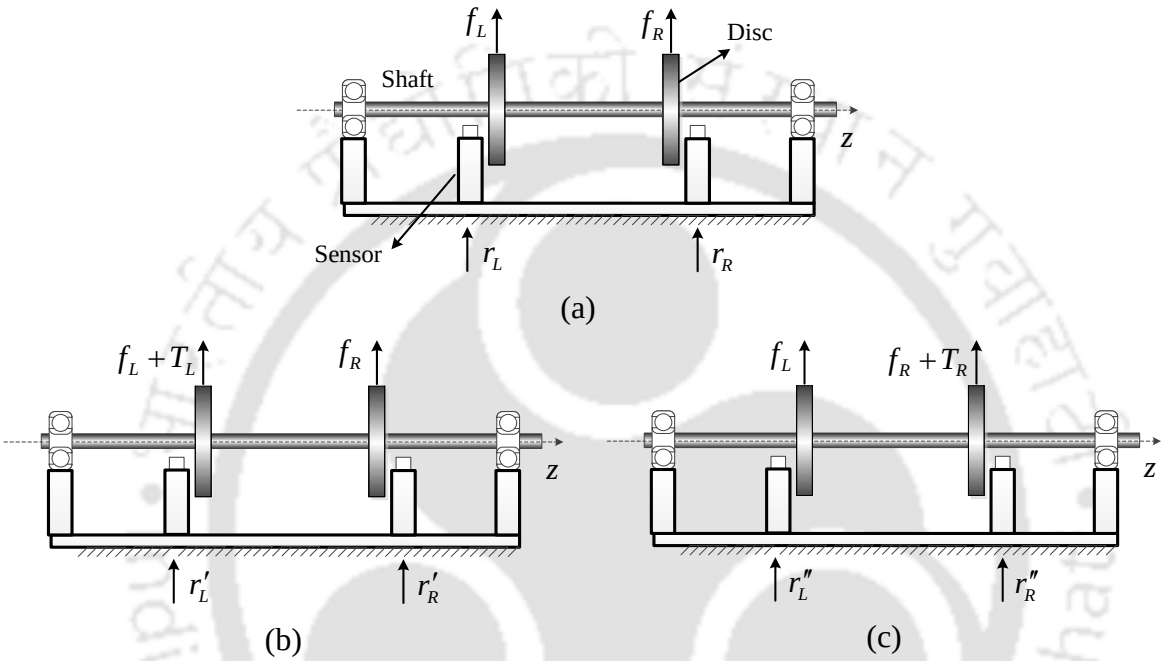


Fig. 1. 15. A schematic of rotor system (a) without trial unbalance (b) with trial unbalance on the left plane and (c) with trial unbalance on the right plane.

In ICM, the rotor system is operated at a constant speed, and the responses (r_L (left plane) and r_R (right plane)) are generated due to the unbalance forces (f_L and f_R). Now, in the second run, an additional trial unbalance (T_L) is introduced at the left plane, and the new responses (r'_L and r'_R) are obtained. In the third run, the trial unbalance (T_R) is then added to the right plane to obtain the displacement responses (r''_L and r''_R). The residual unbalances at both the planes are obtained as

$$f_L = \frac{r_R\alpha_{LR} - r_L\alpha_{RR}}{\alpha_{RR}\alpha_{LL} - \alpha_{LR}\alpha_{RL}} \quad \text{and} \quad f_R = \frac{r_L\alpha_{RL} - r_R\alpha_{LL}}{\alpha_{RR}\alpha_{LL} - \alpha_{LR}\alpha_{RL}} \tag{1.11}$$

TH-2966_176103027

with, $\alpha_{LL} = \frac{r_L' - r_L}{T_L}$; $\alpha_{RL} = \frac{r_R' - r_R}{T_L}$; $\alpha_{LR} = \frac{r_L'' - r_L}{T_R}$; $\alpha_{RR} = \frac{r_R'' - r_R}{T_R}$

The unbalances obtained at the respective planes are added at the opposite phases to balance the rotor system. The above balancing procedures are effective only if the rotor remains rigid in its operating range. Kang *et al*. (2003) developed a modified ICM to balance two crankshafts using three trial masses at a balancing plane. They improved the accuracy of the balancing by minimizing the measurement error and optimizing the influence coefficients. The researchers have also performed balancing in the crankshaft as well as compressors utilizing ICM (Ferraris *et al*., 2006; Levecque *et al*., 2011). Yu (2009) demonstrated the relation of influence coefficients between multiplane and static couple methodology on the two-plane balancing of the rotor systems. They validated their work through numerical simulation as well as experiments. Xu and Fan (2013) discussed the ICM and cross-correlation method to identify the amplitude and phase of the residual unbalances in the rotor system. They developed a dynamic model of rigid to study the vibration response of the rotor system under the influence of the unbalance forces. Thanh *et al*. (2018) discussed the methodology to improve the accuracy of dynamic balancing using ICM. They utilized sensors and microcontrollers to measure the vibration signals and FFT for the numerical analysis.

Some of the researchers have utilized several balancing devices consisting of balls or rollers in the circular tracks for automatic balancing of the rotor system (Sperling *et al*., 2002; Rodrigues *et al*., 2008). The unbalances present in the rotor system are also identified using various model-based or AI-based techniques. Su and Chong (2006) utilized the Lissajous diagram and wavelet to identify the unbalances present in the rigid rotor system. Tiwari and Chakravarthy (2009) identified unbalances along with the support

TH-2966_176103027

bearing parameters using the frequency domain responses of the rotor system. They performed both numerical and experimental investigations to show the effectiveness of the developed algorithm. De Castro *et al*. (2010) utilized the difference between the simulated responses and the experimental orbit in the hydrodynamic bearings to estimate the residual unbalances in the rotor system. Sudhakar and Sekhar (2011) identified the unbalances present in the rotor-bearing system by minimizing the difference between the estimated forces and the theoretical model of the forces. They also utilized the vibration minimization methodology to estimate the fault parameter by measuring the transverse vibration of the system. Menshikov (2013) identified the unbalance in the rotor system using the inverse problem approach through the vibration responses in the two orthogonal directions. They utilized Tikhonov regularization to obtain the required results. Wang *et al*. (2017) utilized a new measurement point vector method to estimate the unbalance in the single disc and single-span rotor system. They suggested that the developed algorithm is effective in balancing the rotor system without any external excitations or trial runs.

Yao *et al*. (2018) described an identification procedure to predict the value of unbalances as well as their location along the axis of the shaft. They utilized both the inverse problem approach and the modal expansion approach to identify the unbalance with more accuracy than obtained using conventional approaches. Deng *et al*. (2018) identified the unbalance mass in the rotor system in the 3-dimensional space. They utilized a stereo video system with high-speed cameras for the measurement of the vibration responses. Shrivastava and Mohanty (2019) utilized the model-based identification approach to predict the unbalance in the rigid rotor system. They identified unbalance forces using the joint-input state procedure and then estimated the value of the unbalances

TH-2966_176103027

using the least-squares fitting technique. Zhao *et al*. (2021) proposed a balancing method based on the transient characteristics of the responses utilizing a dynamic load identification algorithm to estimate the residual unbalances in the rotor system. They found out that the algorithm works accurately and generates results similar to those obtained using ICM. However, the present balancing procedures are valid for the system rotating below the flexible critical speeds. For the flexible rotor system operating at high speeds, the balancing is done using the procedures described in the next section.

1.5.1.2. Flexible rotor balancing

In the case of the flexible rotor, the rotating elements bend in the presence of centrifugal forces as the operating speed approaches the flexible critical speeds. Due to the bending of the shaft centerline, the rotor whirls around the rotating axis and generates additional centrifugal forces in the system. The additional deflection (y) generated due to whirling of the shaft changes the centrifugal force $\{m(y+e)\omega^2\}$ in the system as shown in Fig. 1.16. As a result of this, the rotor does not remain balanced even after the rigid rotor balancing procedure. In the case of a continuous rotor, the eccentricity of the rotor system changes throughout the axis of the shaft. To theoretically balance such system completely, an infinite number of correction masses are required to be applied corresponding to the different locations of unbalance forces, which is not feasible.

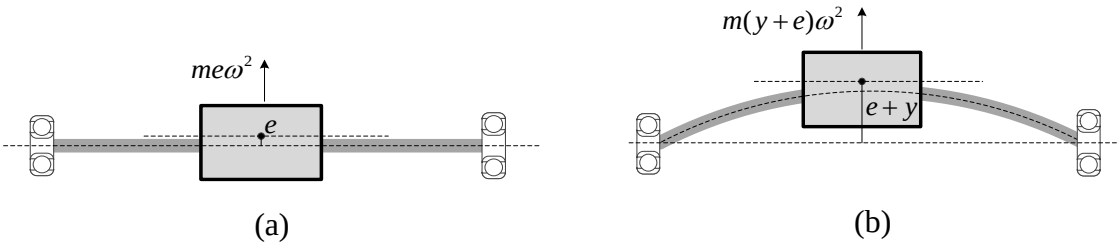


Fig. 1. 16. (a) A rigid rotor system and (b) flexible rotor system supported on conventional bearings.

TH-2966_176103027

So, to balance these rotor systems, flexible rotor balancing techniques, such as modal balancing and *n*-plane ICM, are utilized.

(a) *Modal balancing technique* (MBT): It is a multi-plane flexible rotor balancing procedure in which natural modes are balanced sequentially. The MBT is usually performed with the use of *N* or *N*+2 correction planes, where two additional planes are considered for balancing the rigid modes, especially for the case when the supports are also flexible (Bishop and Gladwell, 1959; Kellenbuger, 1972). To balance the rotor system using MBT, the selection of balance weights should be as per the modal distribution of the system at critical speeds. The rotor is operated above the first critical speed, and the radial deflection of the 1st whirl mode is located. The translational displacement and the angular position of the shaft runout are measured by the transducers. Weights are added in the planes of the maximum displacement to minimize the effects of the unbalance in the first mode. The added weight should not excite the other modes to ensure that they are added at the node position of the other modes. After balancing the first mode, the rotor is operated close to the second mode, and the same procedure is performed to balance the second mode of the system. With MBT, the rotors are balanced at higher modes without affecting the lower modes. As the balancing is done close to critical speed, the sensitivity of unbalances is high, and the balancing is quite effective. Lee *et al*. (1987, 1990) performed the balancing experiment of the flexible rotor system using modal analysis with precision balancing head controlled with the computer. The proximity probes are utilized to measure the vibrational response of the system, which are then processed in the computer to identify the modal unbalance of the system.

TH-2966_176103027

Han (2007) developed a new modal balancing technique to balance the non-isotropic rotor system. They described that displacement responses of the assumed rotor system consist of multiple harmonics, and the dominant balancing mode is extracted from the major harmonic. Li *et al*. (2013) utilized the modal balancing technique to balance the turbine rotor utilizing three balancing planes. The amplitude of response got reduced by 80% after balancing at the first critical speed of the system. Mendes and Dohnal (2018) developed a procedure similar to the traditional modal balancing technique to identify the influence coefficients of the rotor system and the corresponding balance masses. They showed that the high-speed balancing of the rotor system could be performed at low operating speeds. Zhang *et al*. (2021) also designed a modal balancing technique for balancing the rotor system without trial weights. This procedure requires the vibration data to be measured below the critical speed of the system.

However, the procedure is not effective in the presence of damping or cross-coupling in the support bearings. The procedure requires highly skilled people with knowledge of the dynamics of the system and the mode shapes.

(b) *Influence coefficient method* (*N*-plane): The ICM is widely being utilized for balancing the flexible rotor system in high damping situations without much knowledge of the dynamic model of the system. In this method, the unbalance distribution throughout the rotor is not required to be obtained. The balancing can be achieved by applying correction masses at a selected number of planes that can reduce the effect of the entire unbalance distribution in the rotor system. The balance masses at the different balancing planes can be identified based on the displacement

TH-2966_176103027

responses from the experimental test rig and the additional trial weights. To balance the rotor, *N* number of balancing planes are selected, and the measurement of the displacement responses are obtained at the *p* number of measurement locations as shown in Fig. 1.17.

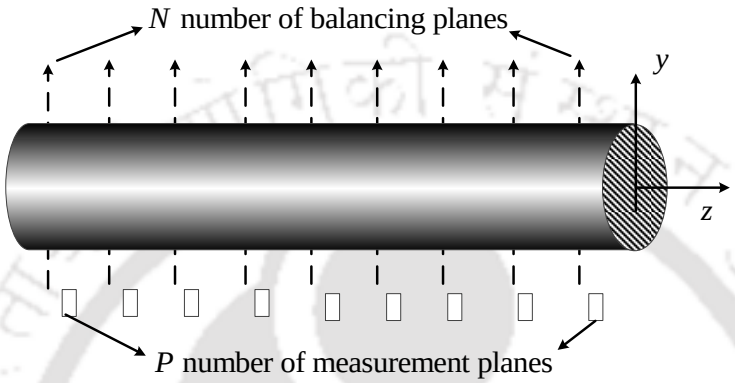


Fig. 1. 17. Distribution of measurement and balancing planes for flexible rotor balancing.

The displacement responses are related to the influence coefficient and the effective residual unbalance at the balance planes, as shown in Eq. 1.12. To identify the residual unbalances in the system, the influence coefficient mentioned are identified.

$$\begin{Bmatrix} r_1 \\ r_2 \\ \vdots \\ r_p \end{Bmatrix} = \begin{bmatrix} \beta_{11} & \beta_{12} & \cdots & \beta_{1n} \\ \beta_{21} & \beta_{22} & \cdots & \beta_{2n} \\ \vdots & \vdots & \ddots & \vdots \\ \beta_{p1} & \beta_{p2} & \cdots & \beta_{pn} \end{bmatrix} \begin{Bmatrix} f_1 \\ f_2 \\ \vdots \\ f_n \end{Bmatrix} \quad \text{or} \quad \mathbf{r}(\omega) = \mathbf{T}(\omega)\mathbf{f} \tag{1.12}$$

A trial mass is added at the 1st balancing plane, and the new displacement response is related to influence coefficients, as shown in Eq. 1.13. Subtracting Eq. 1.13 from Eq. 1.12, the influence coefficient in the first column of the **T** matrix is obtained. Similarly, by placing the trial masses at the other balancing planes, the remaining influence coefficient

TH-2966_176103027

can be obtained. This procedure is repeated for different spin speeds (low speed to above critical speeds), and the final residual unbalances are obtained utilizing the inverse of influence coefficient matrix and displacement responses as mentioned in Eq. 1.14.

$$\begin{Bmatrix} r_1' \\ r_2' \\ \vdots \\ r_p' \end{Bmatrix} = \begin{bmatrix} \beta_{11} & \beta_{12} & \cdots & \beta_{1n} \\ \beta_{21} & \beta_{22} & \cdots & \beta_{2n} \\ \vdots & \vdots & \ddots & \vdots \\ \beta_{p1} & \beta_{p2} & \cdots & \beta_{pn} \end{bmatrix} \begin{Bmatrix} f_1 + T_1 \\ f_2 \\ \vdots \\ f_n \end{Bmatrix}; \qquad \mathbf{r}'(\omega) = \mathbf{T}(\omega)\mathbf{f}' \tag{1.13}$$

$$\left\{\mathbf{r}(\omega_1) \quad \mathbf{r}(\omega_2) \quad \cdots \quad \mathbf{r}(\omega_f)\right\}^T = \left\{\mathbf{T}(\omega_1) \quad \mathbf{T}(\omega_2) \quad \cdots \quad \mathbf{T}(\omega_f)\right\}^T \mathbf{f} \tag{1.14}$$

Since the influence coefficients are obtained for the range of speeds from the experimental data, they reflect the influence of the vibration mode and bearing properties of the system. Unlike the MBT, which requires the presence of a skilled professional, ICM can be automated and computerized easily. Tessarzik *et al*. (1972) validated the exact point-speed ICM to balance the rotor systems. After a requisite number of balancing, the system was able to cross its critical speeds safely. Foiles *et al*. (1998) reviewed the literature regarding the balancing of the rotors using various methodologies, such as the ICM, modal balancing, no phase, and no amplitude methods. Xu *et al*. (2000) developed a new rotor balancing method without trial runs utilizing the ICM with the initial phase point of the holo-spectrum.

Nelson (2002) presented a procedure to balance multiple degrees of freedom flexible rotor system that includes the effect of the permanent bow. Jun (2004) derived ICs for the general, flexible rotor system supported on two resilient bearings on the basis of the transfer matrix method. He utilized the Timoshenko beam theory in the modeling of the

TH-2966_176103027

rotor system. Racic and Hidalgo (2007) reviewed balancing strategies utilizing *N* and *N*+2 number of balancing planes using ICs. They provided guidelines to use a suitable method for obtaining the best results in balancing problems. Wang (2007) developed an approach to balance a flexible rotor system based on the holospectrum method and ICs. Kang *et al*. (2008) described a finite element model to improve the efficiency and accuracy of balancing of rotor system by optimizing the locations of the balancing planes and sensors using ICs. Untaroiu *et al*. (2008) developed a Linear Matrix Inequality (LMI) balancing strategy based on ICs by considering constraints on the magnitude of correction weights and level of vibration reduction. Yu (2009) demonstrated the relation of ICs between multiplane and static couple methodology on two plane balancing of the rotor systems. Chatterton *et al*. (2010) introduced an automatic method for the estimation of the balancing masses based on the robust regression method. Zhang *et al*. (2011) proposed a balancing method for the rotors whose unbalance states have a continuous spatial distribution. They developed a FEM model and obtained balance masses on the basis of ICs. Deepthikumar *et al*. (2014) presented a procedure to reduce cycle time to balance the flexible rotors with a permanent bow by estimating the correction mass in a trial run. They also carried out experiments to verify the methods.

Khulief *et al*. (2014a) developed a hybrid analytical or experimental methodology to balance the flexible rotor system at high speeds. They combined the experimental modal analysis, FEM modeling, mathematical identification, and vibration measurements to balance the rotor system without trial weights. Khulief *et al*. (2014b) demonstrated a methodology to balance the high-speed rotors at low speed by combining both modal balancing and ICs. Ye *et al*. (2018) proposed a balancing strategy without using trial

TH-2966_176103027

weights based on a dynamic similitude scale model to balance the large-scale rotor system. The new methodology with ICs is also compared to the traditional ICM. However, as the ICM procedure is carried out experimentally, the measurement errors in the balancing procedure. Sufficient number of test runs are required to identify the required number of correction masses that require the computation of large data sets.

Moreover, the identification of the residual unbalances has been carried out in the rotor systems supported on conventional bearings through different identification techniques apart from ICM. Edwards *et al*. (2000) developed an identification algorithm to estimate the unbalance as well as the parameters corresponding to the support condition of the rotor system. They also successfully identified the bend present in the experimental test rig. Tiwari *et al*. (2002) developed an identification algorithm to identify the stiffness and damping parameters of the bearings in the flexible rotor system. They utilized the frequency domain displacement responses due to unbalances present in the system to predict the parameters. Lees *et al*. (2004) presented an identification algorithm to identify the unbalance as well the bearing model of the flexible rotor system. They obtained the fault parameter with the help of a single runup or rundown of the machine. El-Shafei *et al*. (2004) developed a balancing methodology for the flexible rotor system using complex vibration displacements and complex rotor modes. They performed several experiments on the developed test rig with the proposed methodology to balance the rotor system without trial weights. Liu and Qu (2008) developed an algorithm for balancing of the flexible rotor system by using the information from fusion of multiple sensors instead of single sensor with the help of holospectrum approach in traditional balancing methods. The performed computer simulations and the optimization based on genetic algorithms to simplify the

TH-2966_176103027

procedure involved in balancing of the rotor system. Saldarriaga *et al*. (2011) utilized optimization techniques based on the genetic algorithms to identify the unbalance distribution in the flexible rotor system. They adjusted the system parameters of the FEM model as per the experimental results and solved the inverse problem to obtain the correction weights for balancing. Yao *et al*. (2020) developed an optimization method with dual objectives to identify the balance masses for the dynamic balancing of the flexible rotor system. They developed a rotor bearing system model with two discs to validate the methodology through both numerical simulations and experiment results. Ahmed *et al*. (2020) used a combination of ICM and four-run method to balance both rigid and flexible rotor system without measurement of the phase of the vibration response. They implemented centroid concept to locate the position of the unbalance masses and verified their results experimentally.

Few researchers have also studied the dynamics as well as balancing methodology of the complex rotor systems, such as the dual rotors that are used in the aero engines. Yang *et al*. (2004) demonstrated a method to balance a dual rotor system without separating the composite vibration signal from both the rotors in the form of beat as done in the conventional method. For the balancing of inner and outer rotors, they utilized reciprocity ICs. Yang *et al*. (2016) investigated the fixed point rubbing of the dual rotor system by utilizing the vibrational response of the system. The beat phenomenon was observed for a particular speed ratio in the system and also showed various combination frequencies present in the displacement response due to fixed-point rubbing. Zhang *et al*. (2018) proposed an identification algorithm to balance the dual rotor system by adding the trial weights on the outer rotor system. Wang and Jiang (2018) showed the effect of unbalance

TH-2966_176103027

and the misalignment faults in the dual rotor system. The vibration characteristics of the outer rotor get transferred to the inner rotor due to the strong coupling effect generated by the inter shaft bearing. The 1X and 2X harmonics of the inner rotor are prominent in the unbalanced and misaligned dual-rotor system. Wang *et al*. (2019) analyzed the dynamics of a dual rotor system using both finite element model and experimental results. The finite element model showed accurate results in predicting the critical speeds of the system in comparison to the experimental setup.

As the level of unbalances is unknown in the rotating machinery, the system cannot be operated at high speeds for response measurements, which limits the balancing procedures. The high amplitude of vibration near critical speed may damage the proximity sensors or any attached components of the machinery. Therefore, there is a requirement for a device that can control the level of vibration of the system within specified levels and also allows the rotor system to accelerate above the critical speeds without any damage to the machinery. In order to overcome the difficulty, AMBs are utilized to identify the faults present in the rotor system and is discussed in the next section.

1.5.2. Online balancing techniques with AMB control

With the recent advancement in technology, AMBs are now implemented in the rotating machinery to actively control the level of vibration in the system. The rotor system equipped with AMBs should operate with vibration displacement and actuator current as per ISO 14839 standard series. A lot of research work has been done to estimate the faults present in the rotor-AMB system. Lum *et al*. (1998) performed single plane balancing of the rigid rotor system supported on AMBs by utilizing the measurement responses at a particular operating speed. They presented an adaptive control law utilizing ICM for a

TH-2966_176103027

single plane active balancing of the rotor system. Dyer *et al*. (2002) developed a strategy for the multi-plane active balancing control using influence coefficients (IC) to improve the robustness of control against modeling and errors in estimation. Setiawan *et al*. (2002) identified unbalances and synchronous runout in the rotor system supported on magnetic bearings at constant operating speed by varying the bias current. Mitenkov *et al*. (2007) presented an algorithm for the identification of the unbalance of a non-uniform flexible rotor on AMBs. The algorithm is based on the solution of the inverse problem of the rotor dynamics utilizing displacement data of the rotor system and the electromagnetic forces. Inoue *et al*. (2009) estimated unbalance in the rotor-AMB system using a disturbance observer. They showed that the nonlinear terms in the displacement responses due to bearing nonlinearities are reduced with the suppression of vibration response through AMB control. After the reduction of nonlinear components, the unbalance in the system is identified. Tiwari *et al*. (2012) developed an extended influence coefficient method to balance the flexible rotor system supported on magnetic bearings. They utilized the displacement responses as well as magnetic forces to predict the corresponding influence coefficients of the rotor system, which are further used to estimate the balance masses.

Beltran-Carbajal *et al*. (2013) proposed an active control method to balance rotating machinery based on the compensation of a perturbation force signal with variable operational speed and unknown system parameters. Fang *et al*. (2013) presented a balancing methodology for a magnetically levitated rotor (MLR) system without trial weights. Coil currents of AMBs are used instead of a vibrational response to estimate the correction masses. Dohnal and Sekhar (2014) described the use of bearing control current for unbalance fault diagnostics of a flexible rotor levitated on AMBs. Wang *et al*. (2014)

TH-2966_176103027

proposed a balancing method of high efficiency and precision based on virtual trial weight for a flexible rotor system levitated on AMBs. Tiwari and Chougale (2014) described an identification algorithm to estimate the bearing dynamic parameters (force-current and force-displacement coefficients) and rotor residual unbalances in a flexible rotor-AMB system supported by AMBs. Kejian *et al.* (2015) proposed a method that is based on the seeking unbalance mass position that produces the control signal according to the real-time position of the rotor's unbalance mass. Xu and Chen (2015) identified the unbalances present in the rotor system using a synchronous current reduction procedure using a variable phase notch feedback. The balancing of the rotor system is performed by adding the balance masses in the rotor system. Xu *et al*. (2016) presented an adaptive automatic balancing control method to overcome the synchronous compensation error, which is due to parameter errors and variation of power amplifiers in the AMB systems. Prasad and Tiwari (2019) developed an identification algorithm to estimate AMBs speed-dependent dynamic parameters and residual unbalances in a flexible rotor system at high speeds. However, instead of supporting the whole system through AMBs (fully levitated system), they utilized AMBs in the system only for the suppression of vibration through controlling magnetic force as partially levitated or controlled rotor-AMB system. Li *et al*. (2021) discussed a field balancing technique to dynamically balance the rotor system supported on AMB. They utilized an extended state observer to estimate the unbalance present in the system and showed the accuracy of the algorithm with simulations and experiments.

These advanced techniques to identify the unbalances in the rotor system with AMB as exciter or as a controller requires complicated control structures and identification algorithms. The identification techniques can be further improved with the simultaneous

TH-2966_176103027

application of AMB as a controller and exciter with the application of simple identification algorithms, such as ICM, as discussed in the literature.

1.6. Multiple fault estimation in the cracked rotor with unbalances

The presence of a crack in the rotor system affects the health of the rotating machinery to a greater extent. The increase in the vibrational response of the rotor system with the propagation of the cracks with time increases the chance of the failure of machinery. The reduction of shaft stiffness due to the opening and closure of the crack's faces depends on the interaction of unbalance forces and the static weight. Therefore, early detection of the severity of cracks in the rotor system is an important requirement for maintaining the health of rotating machinery. Sekhar (2003, 2004) demonstrated an online identification procedure of cracks present in the rotor system using wavelet transform. He developed a FEM model and implemented crack as a change in local flexibility. He further utilized fast Fourier transform for the identification of crack parameters. Darpe *et al*. (2004b, 2006) introduced external excitation in the cracked rotor system to identify the specific signatures of the crack. They considered a Timoshenko beam element with a breathing crack model. The differences and addition of frequencies near the excitation frequencies are found to be useful in the identification of rotor cracks. They further demonstrated the effect of the shaft bow on the dynamics of the rotor system with a transverse crack. Sinou and Lees (2005) analyzed the rotor system with transverse cracks. They investigated the orbit response of the rotor system with breathing crack operating at half of the first critical speed. Pennacchi *et al*. (2006) developed a model-based procedure to identify the transverse cracks in industrial rotor systems. They considered different types of cracks, such as a small crack, a

TH-2966_176103027

deep crack, and a slot, for their work and identified the depth and opposition of the cracks with excellent accuracy.

Zhou *et al*. (2005) confirmed experimentally that the effect of crack could be seen in the orbit plot and spectrum in the case of a deep crack. Guo and Peng (2007) utilized Hilbert-Huang transform to investigate the transient response of a transverse crack in the rotor system. They studied the 1X, 2X, and 3X harmonics components in the response of the rotor system. Arem and Maitournam (2008) developed a 3-dimensional finite element model to identify additional flexibility due to cracks. They also utilized Floquet theory to analyze the stability of the cracked shaft. Kumar and Rastogi (2009) presented a review work on the methodology developed by the researchers to investigate the crack present in the rotor system. They also discussed an extended Lagrangian methodology to study the dynamics of the cracked rotor system. Al-Shudeifat and Butcher (2011) developed a breathing function for the transverse crack in the rotor system. They demonstrated that their present model of crack provides more accurate results than the approximated models used in the previous literature. Kulesza and Sawicki (2012) utilized the rigid finite element method to develop a mathematical model of the cracked rotor system. They also performed experiments to show the effectiveness of the methodology. Shravankumar and Tiwari (2013) described an identification procedure to obtain the coefficients of switching cracks present in the rotor system along with the residual unbalances. They also introduced measurement noise in the displacement responses to verify the robustness of the algorithm. Han and Chu (2013) subjected time-dependent base motions to the cracked rotor system and observed its effects on the dynamics of the system. Fu (2015) examined the behavior of switching crack on the bridge subjected to dynamic loading due to running vehicles.

TH-2966_176103027

They found out that the switching behavior of the cracks can reduce the first mode of resonance and increase the next mode.

Chandra and Sekhar (2016) compared the effectiveness of different signal processing methods, such as the Hilbert-Huang transform, wavelet transform, and short-time Fourier transform, in the detection of different faults present in the rotor system. Spagnol *et al*. (2018) studied the rotor system with breathing crack without considering the weight dominance effect in the system. They found out that the unbalance magnitude and orientation greatly influence the breathing behavior of the fatigue crack.

Apart from generating different stiffness properties in the shaft, the rubbing of crack surfaces at the time of opening and closure develops internal damping in the system. The internal damping force direction changes with the rotation of the shaft and, therefore, is considered as rotating damping. It causes instability in the system when the system rotates above critical speeds, and hence, it is required to be investigated. Dimentberg (2005) estimated the mean and standard deviation value of the internal damping coefficient by the measured response of the rotor system. He utilized a Jeffcott rotor model with variations of the internal damping coefficient. Fischer and Strackeljan (2006) analyzed different models of the internal damping, and numerical and analytical estimation of parameters, which affects the stability of the lab centrifuges at high speeds, is carried out. Peng *et al*. (2017) discussed the effects of stationery damping and anisotropic internal damping on the stability condition of the rotor system. They showed the root locus plot, decay rate plot, and Campbell diagram to show the instability generated by varying the anisotropic ratio of the rotating damping. Roy and Tiwari (2019) estimated residual unbalance, internal (rotating), and external damping in the rotor-bearing system with the cracked shaft. They

TH-2966_176103027

assumed a switching crack model in the Jeffcott rotor system to examine the influence of crack in the dynamics of the rotor.

With the advancement of technology, Active Magnetic Bearings (AMBs) are being utilized as the replacement of conventional bearings (Maslen and Schweitzer, 2009). The AMBs reduce the vibration generated in the system and help in the condition monitoring of the cracked rotor system. AMBs can be utilized as an exciter without any physical contact to generate external excitation for the identification of the fault signatures. Few researchers have worked on the identification of fault parameters with the help of AMB as an exciter or damper. Aenis *et al*. (2002) discussed the comparison of measured force utilizing different measurement methods over a large speed range. They also developed a state-space model to diagnose the rotor-AMB system. Zhu *et al*. (2003) discussed the analysis of the cracked rotor system controlled with the help of an active magnetic bearing. They showed that the diagnosis of such a system depends on the control strategy employed in the system. Quinn *et al*. (2005) identified the time-dependent stiffness because of the presence of the breathing nature of the cracks. The external forcing is applied to the system with the help of AMB located at the mid-span of the shaft.

Sawicki *et al*. (2011) applied sinusoidal excitations to the cracked rotor through the magnetic bearing for the detection of the cracks. Morais *et al*. (2012) studied the control of the dynamic behavior of a rotor system by the use of an electromagnetic actuator. They carried out a simulation to determine the possibility of controlling the vibration generated due to the breathing nature of the cracks. Xu *et al*. (2017) demonstrated a methodology to identify the stiffness and damping coefficients of the AMB based on the unbalance response of the system. They verified the estimated parameters through experimentation,

TH-2966_176103027

which were found to be highly accurate. Ebrahimi *et al*. (2018) studied vibration control of the rotor system with open edge crack with the help of an electromagnetic actuator. They formulated a control law to reduce the stresses at the crack section by introducing two cost functions. Sarmah and Tiwari (2020) proposed an identification algorithm to identify the multiplicative and additive faults in the cracked rotor-AMB, such as residual unbalances, additive crack stiffness, shaft bow, and internal damping.

The research work done in the identification of the residual unbalances as well as different faults in the rotor system is quite extensive. However, the techniques can still be redesigned to obtain an optimum approach for the reduction of vibration that would require less computation and skilled human effort. For diagnosis of fault in rotating machinery and in correlation to the literature survey, some new methodologies are designed in the present work to estimate the residual unbalances in the rotor-AMB system.

1.7. Gaps in the literature survey

The reduction of residual unbalances in the rotor system has been a challenge to researchers over a long period of time. To operate in the limited range of vibrational disturbance, the rotating machinery is required to be balanced by estimating the accurate magnitude and orientation of the unbalances. A lot of research works have been reported that include various identification techniques for fault estimation as well as active control techniques for vibration suppression. Still, there is always a requirement to develop a balancing methodology that would reduce the utilization of computational time and skilled human effort. As per the literature survey done in the present work, the scope of improvement lies in the topics discussed as follows:

TH-2966_176103027

1. *Difficulty in operating above critical speeds*: As the level of unbalances is unknown in the rotor system, accelerating the system above critical speed, for its response measurement to be used in available balancing techniques, may result in damage to the machinery due to the large amplitude of vibration. For high-speed balancing of the rotor system, there is always a requirement of some control devices to maintain the level of vibration within the desired limit. Apart from utilizing AMB as a support bearing in a different rotating system, it can be integrated as a controlling device while the system can remain supported on convention bearings.

2. *Complexity in active control approaches*: A lot of research works have been reported to suppress the vibration using different controller designs and filters. The use of complex control structures requires high skilled engineers, a lot of computational effort, and energy consumption for the continuous operation of the machinery. Therefore, apart from continuous suppression of undesired vibration, it would be beneficial to balance the system at high-speed using a simple control algorithm (PI, PD or PID) within a limited operation time.

3. *Modelling errors*: In most of the model-based identification techniques, knowledge of the physical properties of the rotor system is required. With the complexity in the design of the rotating components, the development of approximate models using lumped mass approach or FEM gets difficult. The deviation of the designed models from the real systems results in an error in the identified faults parameters, which may further result in the inadequate balancing of the systems. To overcome this problem, methodology such as ICM can be implemented with AMB control, which requires less information about the system to estimate the residual unbalances at different balancing planes.

TH-2966_176103027

4. *Manual addition of trial unbalances*: Several field balancing techniques requires manual addition of trial unbalances to identify the unbalances in the system. This results in the wastage of time and contamination of the components while opening and closure the rotor's casing. The use of AMB as an exciter to generate the virtual trial unbalances (VTUs) as magnetic excitation is required. The AMB has been utilized to excite the rotor system with different frequencies but the introduction of synchronized magnetic excitation (as VTUs) to imitate the behavior of manually added unbalances in the rotor while crossing critical speed has not been carried out. The utilization of VTUs in the field balancing techniques for balancing high-speed machinery is still required to be investigated.

5. *Large number of trial runs*: The increase in the number of trial runs increases the computational time and effort in fault identification of the rotor system. The identification algorithm is required to be optimized to utilize the minimum number of trial runs.

6. *Requirement of periodic flexible rotor balancing at high speed*: With the deposition of the foreign particles and the addition or removal of the rotating components, the unbalance distribution of the system may change. It is difficult to operate the rotor system above critical speeds for balancing the rotor system repetitively without knowing the level of unbalance. To overcome the problem, there is a requirement to develop an identification algorithm that would predict the correction masses for flexible rotor balancing while operating at low speed.

7. *Multi-fault identification*: As the number of faults increases in the system, the complexity of the identification algorithm increases to estimate the fault parameters. The identification of unbalances using various techniques for rigid and flexible rotors may result in incorrect estimation in the presence of other faults such as cracks and

TH-2966_176103027

misalignment. The extension of balancing techniques to estimate the unbalances along with various rotor faults with the application of VTUs through AMB is required to be studied.

1.8. Proposed work

The objectives of the present work have been defined to identify the residual unbalances in the high-speed rotor system with the application of AMB as a controller as well as exciter. The analysis is to be carried out both analytically using the FEM model of the rotor systems as well as experimentally in the developed rotor test rigs. The emphasis is to be given to develop an identification algorithm that can be utilized for on-site estimation of the multiple faults in the rotor system with minimum information of the dynamics of the system.

1. Integration of AMB in the rotor system

(a) To minimize the vibration of the rotor system with accepted level, The AMB is to be integrated into the rotor system supported on conventional bearings.

(b) The FEM model of the rotor-AMB system is to be developed to study the dynamics of the system during run-up above critical speed with the PID control.

(c) An experimental test rig is to be developed with a rotor supported on conventional bearings and integrated with AMB is to be utilized to suppress the vibration at high speeds.

TH-2966_176103027

2. Application of ICM and VTUs for flexible rotor balancing

(a) Instead of manually added trial unbalances, AMB is to be utilized to generate virtual trial unbalances (VTUs) as magnetic excitations with simultaneous vibration control.

(b) Modification of ICM to estimate the residual unbalances with two trial runs using VTUs is to be carried out.

(c) Estimation of appropriate location of AMB in rotor system to be done to obtain the maximum vibration reduction with balancing above critical speeds.

(d) Experimental validation of the developed balancing procedure is to be carried out with AMB control during the run-up of the system above its 1^{st} critical speed.

3. High speed balancing at low operating speed

(a) A FEM model of flexible rotor system is to be developed integrated with the AMBs for repetitive high-speed balancing using unbalance estimates at low speeds.

(b) A novel Virtual Excitation at Low-Speed for High-Speed Balancing (VELSHSB) method is to be developed for unbalance estimation using VTUs that requires a one-time estimation of the influence coefficients at high speeds (greater than critical speeds) and periodic estimated values of the residual unbalances at low speeds to predict the balance masses utilized for flexible rotor balancing.

(c) Balancing of the system is to be carried out to show the reduction of the vibration response on the addition of the estimated balance masses while crossing different critical speeds.

TH-2966_176103027

4. Balancing of dual rotor system with VTUs

(a) A FEM model of the dual rotor system supported on conventional bearings is to be developed with AMB integrated into the inner rotor and the effective suppression of vibration in both rotors is to be studied.

(b) Balancing of both inner and outer rotors is to be performed using VTUs as Multiple Virtual Excitation for Dual rotor Balancing (MVEDRB).

5. Multi fault identification in the cracked rotor-AMB system with multi-harmonic VTUs

(a) A FEM model of the cracked rotor-AMB system supported on conventional bearings is to be developed with switching transverse crack.

(b) An identification algorithm is to be developed to estimate fault parameters in the cracked rotor system by utilizing influence coefficients of the system and full spectrum response of the rotor system at multiple harmonics.

(c) A virtual multi-harmonic excitation force is to be introduced at the AMB location to estimate the fault parameters such as additive crack stiffness and internal damping due to rubbing of crack faces along with unbalances.

(d) Experimental identification of the cracked rotor faults with AMB control and multi-harmonic influence coefficient method is to be carried out.

1.9. Outline of the thesis

The present work focuses on the utilization of AMB to control the level of vibration as well as to generate external magnetic excitation to identify the faults present in the rotor-

TH-2966_176103027

AMB systems. The identification algorithm based on the ICM is required to be developed to estimate the faults with minimum information of the rotor system. The effectiveness of the developed identification methodology is verified by utilizing the vibration responses from the finite element model of the different rotor-AMB systems as well as from the experimental test rigs. The thesis consists of seven chapters, out of which the main contribution of the work is depicted in Chapters 2 to 6. The chapters in the thesis are organized as follows.

Chapter 1 gives the introduction to the faults present in the rotating machinery and various identification techniques to predict the nature and level of faults in the system. The balancing methodologies implemented to reduce the level of unbalances present in the rotor systems with and without AMB control are also discussed.

Chapter 2 presents the development of the identification algorithm to predict the magnitude and phase of the residual unbalances for balancing the flexible rotor system supported on conventional bearings and integrated with AMB. The AMB is utilized to suppress the vibration of the rotor system while crossing critical speeds as well as generate virtual trial unbalances as magnetic excitations to identify the unbalances. The balancing methodology is developed based on ICM that utilizes VTUs instead of manually added trial unbalances and a lesser number of rotor runs than the conventional method to estimate the balance masses for flexible rotor balancing.

Chapter 3 describes the balancing methodology developed to balance the flexible rotor system periodically using VTUs while operating the rotor-AMB system at low speeds. The identification algorithm requires a one-time estimation of the influence coefficients at high speeds (greater than critical speeds), and periodic estimated values of

TH-2966_176103027

the residual unbalances at low speeds to predict the balance masses utilized for flexible rotor balancing. The effectiveness of the present algorithm is verified with the developed finite element model of the rotor-AMB system.

Chapter 4 illustrates the identification algorithm developed to estimate the unbalances present in the complex rotor system, such as the dual rotor system. The estimation procedure of balance masses at both inner and outer rotor systems with the application of low and high pressure rotor frequency excitations from the AMB present in the inner rotor system is described. This strategy allows balancing of the dual rotor system with minimum information of the rotor system and less manual effort. The effectiveness of the present algorithm is verified with the utilization of displacement responses from the developed finite element model of dual rotor-AMB system supported on conventional bearings.

Chapter 5 describes the experimental validation of the identification algorithm developed based on ICM and with the utilization of VTUs as magnetic excitations. The experimental rotor test rig integrated with AMB is developed to operate the system above its critical speed with a PID controller. The experimental difficulty in synchronizing the excitation frequency of the VTUs and the operating frequency of the system is explained in the chapter. The optimization of the power consumption of the system with the variation of the bias current at high and low amplitude of vibration in the rotor-AMB system is shown. The balancing of the rotor system is performed using the developed identification that requires two trial runs and less manual effort than conventional ICM.

Chapter 6 discusses the extension of the developed identification algorithm defined in chapter 2 to estimate the other multi-harmonic rotor faults such as cracks and

TH-2966_176103027

misalignment along with residual unbalances in the system. The identification of the fault parameters in the cracked rotor-AMB system is carried out based on the estimated influence coefficients corresponding to the different harmonics of the displacement responses. The application of AMB to control the vibration of the system as well as to generate multi-harmonic excitation force is described in the chapter. The change in stiffness of the rotor system due to the presence of transverse fatigue crack is analyzed in the present chapter with the utilization of AMB and displacement responses from the system. The effectiveness of the algorithm in the estimation of characteristics and magnitude of cracked rotor faults is described through both numerical simulation and experimental results.

Chapter 7 summarizes the contributions of the research work and provides some recommendations for potential in further research topics as an extension of this work.

TH-2966_176103027

CHAPTER 2

IN-SITU BALANCING OF FLEXIBLE ROTOR-BEARING SYSTEM INTEGRATED WITH ACTIVE MAGNETIC BEARING USING VIRTUAL TRIAL UNBALANCES

This chapter deals with the development of the identification algorithm to estimate the residual unbalances in the rotor system supported on the conventional bearings and integrated with the AMB. The modifications made in the conventional ICM with the implementation of AMB to reduce manual effort, computational effort, and the number of rotor runs are discussed. The utilization of AMB in the rotor system as a controller for suppression of the vibration above critical speeds and as an exciter for generation of VTUs as magnetic excitation is described. The finite element modelling of the rotor-AMB system is carried out to obtain the displacement responses for validation of the developed algorithm. The effect of the location of AMB in the estimation of residual unbalances and balancing of the rotor system is also discussed. The robustness of the algorithm in the presence of the measurement noise is shown to determine its applicability in the balancing of the practical rotor systems.

2.1. Introduction

Apart from suppressing the vibrational response in real-time through various complex control strategies discussed in the literature survey, it is beneficial to estimate the unbalances and balance the rotor system. This reduces the excessive power consumption by the Active Magnetic Bearing (AMB) in the suppression of vibration. The conventional

TH-2966_176103027

Influence Coefficient Method (ICM) is being widely utilized for on-site balancing of the rotor system (Tiwari, 2017). For the balancing of the flexible rotor, the system is required to be operated above critical speeds for measuring responses, which is very difficult in the presence of residual unbalance. The problem can be solved by introducing AMB as a controller in the system to suppress the vibration responses within an appreciable range while crossing critical speeds during response measurement. Also, repetitive opening and closure of the casing of rotor system for manual addition of trial unbalances, the system may get contaminated with foreign particles present in the environment and is time-consuming. The Virtual Trial Unbalances (VTUs) as magnetic excitations through AMB that can imitate the behavior of manual trial unbalances can be utilized without affecting the condition of the system. The excitation frequency of the VTUs is required to be synchronized with the operating speed to the system while crossing critical speed to imitate the behavior of the manually added unbalances. This concept of generating magnetic excitations as VTUs through AMB is a novel contribution in the development of balancing strategy for high-speed machinery. The VTUs can be generated in the rotor system while AMB controls the vibration response so that the vibration due to residual unbalances and the excitation force can be kept under control. The utilization of VTUs with the application of the balancing strategy based on ICM can be beneficial to monitor the level of unbalances in the system during the operating condition of the rotor system.

Therefore, in this chapter, a new balancing method has been discussed using the Virtual Trial Excitation Influence Coefficient Method (VTEICM) for a flexible rotor system supported on conventional bearings and integrated with AMB. Apart from the utilization of manual trial unbalances in the conventional influence coefficient method, in

TH-2966_176103027

VTEICM, VTUs are utilized as magnetic excitations to obtain the residual unbalances. The present balancing strategy reduces the computational effort by reducing the number of rotor runs as required in the unbalance estimation using conventional ICM. The effectiveness of the present algorithm is shown through the balancing of the rotor-AMB system developed using FEM. In the numerical model, the discrete unbalances are considered at the disc locations along with the randomly distributed unbalances in the shaft. The resultant unbalances are identified at the balancing planes based on the vibration responses obtained from the numerical model, and the balancing of the system is performed.

2.2. Assumption and descriptions of the rotor-AMB system

A flexible rotor-bearing system supported on the conventional bearings and integrated with AMB is considered in the present work, as shown in Fig. 2.1. The addition of AMB to the system allows safe traversal of the system above critical speed and generates additional magnetic excitations for the identification of the residual unbalances utilizing VTEICM. The shafts considered are flexible in nature on which rigid discs (D) are mounted as balancing planes.

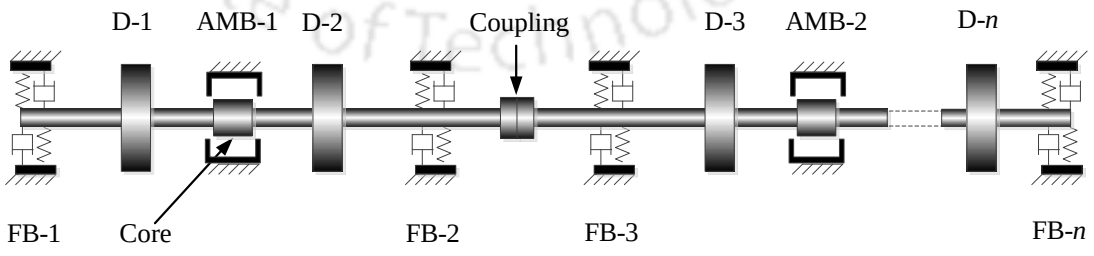


Fig. 2. 1. An illustrative representation of a flexible rotor-bearing system integrated with AMBs.

TH-2966_176103027

AMBs introduced in the present system generate linearized magnetic forces to control as well as excite the system as per requirement. This means that the rotor displacements relative to the magnetic gap are comparatively small, and the control currents never exceed the bias. The conventional bearings are considered to support the rotor system are assumed to behave linearly with respect to the displacement responses. The non-linearities present in the rotor system may affect the balancing estimates obtained using ICM if unbalance level is high. As the vibration is minimized with the implementation of the AMB in the system, the nonlinear forces generated at the bearing locations are minimized and, therefore, can be neglected for unbalance identification. The application of the ICM for the on-site balancing of the industrial rotor systems is described in literatures (Zhou *et al.* (2004); Kang *et al.* (2008); Inoue *et al.*, 2009; Levecque *et al.*, (2011); Tiwari *et al.* (2012)). A PID controller is considered to perform closed-loop controlling action through AMBs**.**

2.3. Description of the Conventional and Virtual Trial Excitation Influence Coefficient Method

For the field (or in-situ) balancing of rotating machinery, Conventional Influence Coefficient Method (Ferraris *et al*., 2006; Levecque *et al*., 2011) is widely being used in the industries. This method is quite easy to be utilized and requires lFess information regarding the rotor system as compared to modal balancing (Li *et al*., 2013). In conventional ICM, to obtain residual unbalances, the displacement responses of vibration at different measurement planes are required, along with the manual addition of trial unbalances at the balancing planes. The problem arises in the flexible rotor balancing,

TH-2966_176103027

which requires the rotor system to achieve rotating speed above the critical speeds in presence of residual unbalances, which is difficult to achieve without any suppression force. Also, manual addition of trial unbalances is difficult in a practical rotor system and time consuming.

2.3.1. Conventional Influence Coefficient Method

The conventional ICM is the field balancing technique, using which the balancing can be performed at the site of rotating machinery without removal of the rotating components from the system. It involves the utilization of influence coefficients of the rotor system (as shown in Fig. 2.2) to estimate the unbalances in the system by using displacement responses at different measurement planes. The influence coefficients are obtained from the vibrational response of the rotor system. In conventional ICM, at first, the displacement responses are obtained for the system with residual unbalances and then after adding trial unbalances along with the residual unbalances at the different balancing planes

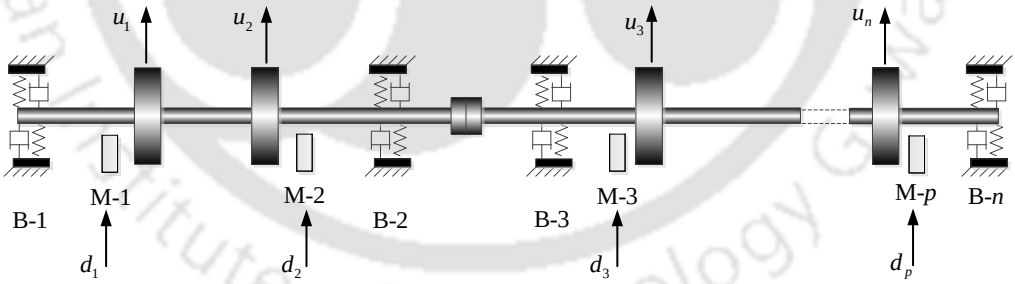


Fig. 2. 2. A line diagram of a flexible rotor-bearing system with residual unbalances and measurement locations.

In conventional ICM, '*n'* number of discs are considered as the balancing planes, and '*p'* number of measurement planes (M) are considered, then the residual unbalances are related to the vibrational displacements and influence coefficients as

TH-2966_176103027

$$\mathbf{d}_1(\omega) = \mathbf{B}_I(\omega)\mathbf{u}_1 \tag{2.1}$$

with, $\mathbf{d}_1(\omega) = \{d_1(\omega) \quad d_2(\omega) \quad \cdots \quad d_p(\omega)\}^T$; $\mathbf{B}_I(\omega) = [\boldsymbol{\beta}_1(\omega) \quad \boldsymbol{\beta}_2(\omega) \quad \ldots \quad \boldsymbol{\beta}_n(\omega)]_{p\times n}$

$\mathbf{u}_1 = \{u_1 \quad u_2 \quad \cdots \quad u_n\}^T$; $u_n = m_n e_n e^{(j\phi_n)}$

where, d_1, d_2, …, d_p represent the displacement of the rotor system at the different measurement planes; u_1, u_2, …, u_n represent residual unbalances at different balancing plane locations; m_n is the mass of the disc, e_n is eccentricity, and ϕ_n is the phase of the center of mass of the disc with respect to a reference axis; $\boldsymbol{\beta}_n$ represents the column vector of influence coefficients corresponding to each unit unbalance force (u_n) at each measurement location (d_p). Eq. (2.1) is applicable under the assumption that the system is linear and considering the synchronous unbalance response of the rotor. A detailed description of $\mathbf{B}_I$ matrix is given by Eq. A.1 in Appendix A. At first, the displacement responses are obtained with only residual unbalances in the system. Then considering trial unbalance (T_R) on the first balancing plane along with residual unbalances as shown in Fig. 2.3, displacement responses are obtained as

$$\mathbf{d}_2(\omega) = \mathbf{B}_I(\omega)\mathbf{u}_2 \tag{2.2}$$

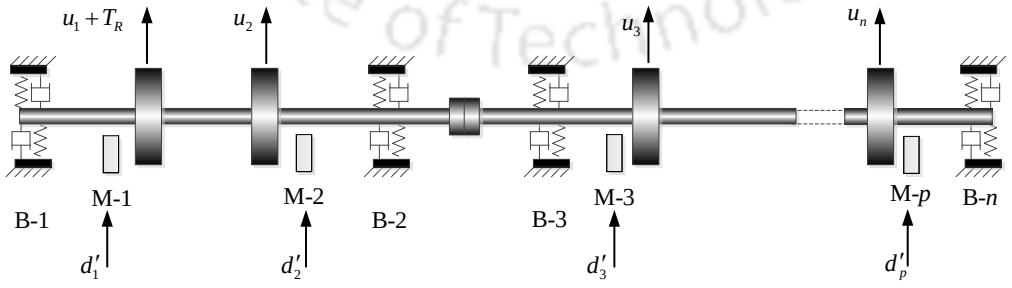


Fig. 2. 3. A line diagram of a flexible rotor-bearing system with additional trial unbalance at the disc (D-1).

TH-2966_176103027

with, $\mathbf{u}_2 = \{u_1 + T_R \quad u_2 \quad \cdots \quad u_n\}^T$; $\mathbf{d}_2(\omega) = \{d_1'(\omega) \quad d_2'(\omega) \quad \cdots \quad d_p'(\omega)\}^T$;

$T_R = m_R e_R \mathrm{e}^{(\mathrm{j}\phi_R)}$

where, m_R is mass, e_R is eccentricity, and ϕ_R is a phase of the trial mass introduced. $\mathbf{d}_2$ is the displacement responses obtained at the measurement plane locations after introducing trial unbalance in the system. On subtracting displacement responses of both the cases, i.e., Eq. (2.1) from Eq. (2.2), influence coefficients are obtained for different measurement planes corresponding to the first balancing plane where the trial mass was applied, as

$$\mathbf{d}_2(\omega) - \mathbf{d}_1(\omega) = \mathbf{B}_I(\omega)\mathbf{u}_T; \qquad \mathbf{u}_T = \{T_R \quad 0 \quad \cdots \quad 0\}^T \tag{2.3}$$

The influence coefficients in the first column ($\boldsymbol{\beta}_1$) are obtained from Eq. (2.4).

$$\boldsymbol{\beta}_1(\omega) = \{\mathbf{d}_2(\omega) - \mathbf{d}_1(\omega)\} / T_R \tag{2.4}$$

Similarly, by considering trial unbalances at different balancing planes, the influence coefficient in other columns ($\boldsymbol{\beta}_2$, $\boldsymbol{\beta}_3$, …., $\boldsymbol{\beta}_n$) are also predicted. The above procedure has to be completed at a particular rotor speed. The influence coefficients for different spin speeds for flexible rotor balancing can also be obtained using the same procedure. Then, for different speeds, Eq. (2.1) will take form as

$$\mathbf{d}_c = \mathbf{P}\mathbf{u}_1 \tag{2.5}$$

with, $\mathbf{d}_c = \{\mathbf{d}_1(\omega_1) \quad \mathbf{d}_1(\omega_2) \quad \cdots \quad \mathbf{d}_1(\omega_t)\}^T$; $\mathbf{P} = \{\mathbf{B}_I(\omega_1) \quad \mathbf{B}_I(\omega_2) \quad \cdots \quad \mathbf{B}_I(\omega_t)\}^T$

where, ω_1 through ω_t are the spin speed of the ramp-up rotor system. Using Eq. (2.5), at different balancing planes, the residual unbalances can be obtained as

TH-2966_176103027

$$\mathbf{u}_1 = \left(\mathbf{P}^T\mathbf{P}\right)^{-1}\mathbf{P}^T\mathbf{d}_c \tag{2.6}$$

2.3.2. Formulation of Virtual Trial Excitation Influence Coefficient Method (VTEICM)

In the proposed VTEICM, an AMB is introduced in the rotor system to suppress the vibration while run-up above critical speeds. Also, virtual trial unbalances are introduced instead of manually added trial unbalances by varying the magnetic field through an AMB at one location of the shaft span. The rotor-bearing-AMB system consists of '*n*' number of discs (balancing planes) supported on the conventional bearings and integrated with AMBs and is shown in Fig. 2.1. The AMB is used as a controller as well as an exciter.

2.3.2.1. Introduction of virtual trial unbalance

The displacement of the rotor system is taken at the balancing planes and AMB location, as shown in Fig. 2.4, in both *x* and *y* directions. In VTEICM, the displacement signals in both the directions are combined to get a rotating response vector due to the rotating unbalance force vector given as

$$r(t) = x(t) + \mathrm{j}y(t) \tag{2.7}$$

where, $r(t)$ is the resultant radial displacement vector, and $x(t)$ and $y(t)$ are the displacements in *x* and *y*-direction, respectively. The complex displacement vector at the first balancing plane location ($r_{d,1}$), and the residual unbalance force vectors at different balancing plane locations are related to influence coefficients, as

$$r_{d,1}(\omega) = \alpha_{11}(\omega)u_{d,1} + \alpha_{12}(\omega)u_{d,2} + \cdots + \alpha_{1n}(\omega)u_{d,n} \tag{2.8}$$

with, $u_{d,n} = m_{d,n}e_{d,n}\mathrm{e}^{\,\mathrm{j}\phi_{d,n}}$

TH-2966_176103027

where, $m_{d,n}$ is the mass, $e_{d,n}$ is the eccentricity, and $\phi_{d,n}$ is the phase of unbalance at n^{th} balancing plane location. $\alpha_{1,1}$, …., $\alpha_{1,n}$ are influence coefficients, which are defined as the displacement at the first balancing plane location, per unit residual unbalances at the 1^{st}, 2^{nd}, …, n^{th} balancing plane locations, respectively. The second subscript '1' in the response represents the run-up of the rotor system considering the only residual unbalances in the system with controlling magnetic force through an AMB and $u_{d,1}$, $u_{d,2}$,..., $u_{d,n}$ are the complex equivalent residual unbalances at the 1^{st}, 2^{nd} , …, n^{th} balancing plane locations, respectively. Similarly, complex displacement vectors at the other balancing plane locations and AMB locations along with the residual unbalance force vectors are related to the influence coefficients as

$$\mathbf{r}_1 = \mathbf{A}(\omega)\mathbf{u}_1 \tag{2.9}$$

with, $\mathbf{r}_1 = \{r_{d,1}(\omega) \quad r_{d,2}(\omega) \quad \cdots \quad r_{d,n}(\omega) \quad r_m(\omega)\}$;

$\mathbf{A} = [\boldsymbol{\alpha}_1(\omega) \quad \boldsymbol{\alpha}_2(\omega) \quad \cdots \quad \boldsymbol{\alpha}_n(\omega) \quad \boldsymbol{\alpha}_m(\omega)]$; $\mathbf{u}_1 = \{u_{d,1} \quad u_{d,2} \quad \cdots \quad u_{d,n} \quad 0\}^T$

where, r_{d_n} and r_m are the displacements at the n^{th} balancing plane location and the AMB location, respectively. $\boldsymbol{\alpha}_m$ is the influence coefficients corresponding to the displacement responses at the discs locations due to unit load at the AMB location.

TH-2966_176103027

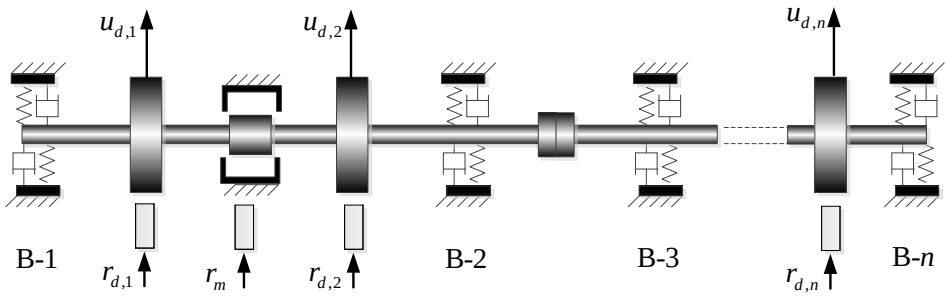


Fig. 2. 4. A line diagram of a flexible rotor-AMB system with residual unbalances and measurement locations.

In this methodology, the measurement planes are not at separate locations than balancing planes as considered in the conventional ICM for the estimation of $\mathbf{B}_I$ matrix mentioned in Eq.(2.1). The detailed description of **A** matrix is given by Eq. A.1 in Appendix A. As discussed earlier, in ICM, the trial unbalances are required to be introduced manually in the system for the calculation of respective influence coefficients. The method is time-consuming and requires a lot of mechanical effort. So, in the proposed VTEICM, for the calculation of influence coefficients of the system, a known virtual trial unbalance in the form of magnetic force is introduced along with the controlling force in the AMB system. In conventional ICM, the mechanical trial unbalances need to be given at balancing planes one by one, whereas in the present method, virtual trial unbalance is used only at AMB location and not a balancing plane location. So, there is no need either to keep AMBs at all balancing plane locations to give virtual trial unbalances, which is not a practical solution. The trial unbalance is expressed as

$$f_T = m_T e_T \mathrm{e}^{\,\mathrm{j}\phi_T} \tag{2.10}$$

where, m_T is the mass, e_T is the eccentricity and ϕ_T is the phase of virtual trial unbalance to be introduced. The equivalent magnetic force is given as

TH-2966_176103027

$$f_{mT} = k_i I_T \mathrm{e}^{\,\mathrm{j}\varphi_T} \tag{2.11}$$

where, k_i is the current force factor of the AMB, I_T and φ_T are the amplitude and phase of trial current to be introduced in the AMB. Eq. (2.11) is applicable if the AMB system behaves linearly. Additionally, the same equation is applicable if the phase lag introduced by the AMB power amplifier is negligibly small. However, if current mode control is applied through the amplifier, it removes the phase lag introduced in the circuit. In order to get a similar effect as trial unbalance, the magnitude and phase of the equivalent magnetic force should be equal to that of the trial unbalance. So, on comparing Eq. (2.10) with Eq. (2.11), we obtain the trial current signal (which generate excitation force) to be subtracted from the controlling current (which generate controlling force) in order to obtain the effect of trial unbalance force, as

$$i_T = I_T \mathrm{e}^{\,\mathrm{j}\varphi_T} \tag{2.12}$$

with, $I_T = \left(m_T e_T\right)/k_i$ and $\varphi_T = \phi_T$

2.3.2.2. Identification of force current factor (k_i)

The magnetic force introduced in the differential control mode is mentioned in Eq. (1.9). On the addition of a constant load (f_l) at the AMB location, the shaft shifts from its position, which is compensated by a constant control current i_l. As the equilibrium position is achieved, then $x = 0$ and $i_c = i_l$. The equilibrium equation can be developed as

$$f_m = \left\{c_1\left(i_b + i_c\right)^2 / l_g^2\right\} - \left\{c_1\left(i_b - i_c\right)^2 / l_g^2\right\} \tag{2.13}$$

$$f_l = \left(4c_1 i_b i_l\right)/l_g^2; \qquad f_l = k_i i_l \tag{2.14}$$

TH-2966_176103027

$$k_i = f_l / i_l \tag{2.15}$$

The AMB force current factor can be estimated using Eq. (2.15) and is utilized to generate virtual trial unbalances. Also, for displacement $x(t) << l_g$ and $y(t) << l_g$, the magnetic force introduced along the x and y axes for controlling the vibration is given as

$$f_{m_y,1}(t) = -k_s y_{m,1}(t) + k_i \left\{ k_P y_{m,1}(t) + k_I \bar{y}_{m,1}(t) + k_D \dot{y}_{m,1}(t) \right\} \tag{2.16}$$

$$f_{m_x,1}(t) = -k_s x_{m,1}(t) + k_i \left\{ k_P x_{m,1}(t) + k_I \bar{x}_{m,1}(t) + k_I \dot{x}_{m,1}(t) \right\} \tag{2.17}$$

where, $f_{m_x,1}$ and $f_{m_y,1}$ are the magnetic forces generated in x and y directions for the first run-up of the system. $y_m(t)$ and $x_m(t)$ are displacements of the rotor in y and x-direction at the AMB location, respectively. Therefore, the total magnetic force generated after introducing trial current (i_T) along with controlling current (from PID controller) in the time domain is given as,

$$f_{m_y,2}(t) = -k_s y_{m,2}(t) + k_i \left\{ k_P y_{m,2}(t) + k_I \bar{y}_{m,2}(t) + k_D \dot{y}_{m,2}(t) - I_T \omega^2 \sin(\omega t + \varphi_T) \right\} \tag{2.18}$$

$$f_{m_x,2}(t) = -k_s x_{m,2}(t) + k_i \left\{ k_P x_{m,2}(t) + k_I \bar{x}_{m,2}(t) + k_D \dot{x}_{m,2}(t) - I_T \omega^2 \cos(\omega t + \varphi_T) \right\} \tag{2.19}$$

where, $f_{m_y,2}(t)$ and $f_{m_x,2}(t)$ are the total magnetic forces acting in the y and x-directions, respectively. The subscript '2' represents the run-up of the rotor system considering the trial magnetic unbalance force along with the controlling magnetic force.

TH-2966_176103027

2.3.2.3. Estimation of influence coefficients and residual unbalances

Now, after introducing trial magnetic unbalance force along with the controlling magnetic force as shown in Fig. 2.5, the new complex displacement vectors and complex force vectors are related with influence coefficients, as

$$\mathbf{r}_2 = \mathbf{A}(\omega)\mathbf{u}_2 \tag{2.20}$$

with, $\mathbf{u}_2 = \left\{u_{d,1} \quad u_{d,2} \quad \cdots \quad u_{d,n} \quad f_T\right\}^T$; $\mathbf{r}_2 = \left\{r'_{d,1}(\omega) \quad r'_{d,2}(\omega) \quad \cdots \quad r'_{d,n}(\omega) \quad r'_m(\omega)\right\}$

where, $r'_{d,n}$ is the displacement response at the n^{th} balancing plane due to the combined effect of residual unbalances and the additional magnetic excitation. In the VTEICM, the value of trial unbalance considered in Eq. (2.10) for generating trial magnetic force is taken in Eq. (2.20). So, the value of the trial magnetic force is not required to be measured. This is true for the case the magnetic bearings behave linearly, and their force constant k_i is known. This usually requires an experimental characterization. It should be noted that influence coefficients in the presence of AMB as the controller (or suppression force) are different as compared to without its presence. With the addition of virtual trial unbalance at AMB location, influence coefficients are expected not to change influence coefficients among balancing planes. However, we have some more influence coefficients relating between AMB locations and balancing planes. This is similar to conventional ICM, in which trial unbalances at different balancing planes are expected not to change influence coefficients under the assumption of linearity due to a small change in displacement. Now, the required influence coefficients of the system are obtained by subtracting Eq. (2.9) from Eq.(2.20), as

$$\mathbf{r}_2 - \mathbf{r}_1 = \mathbf{A}(\omega)\mathbf{u}_T \tag{2.21}$$

TH-2966_176103027

with, $\mathbf{u}_T = \{0 \quad 0 \quad \cdots \quad 0 \quad f_T\}^T$

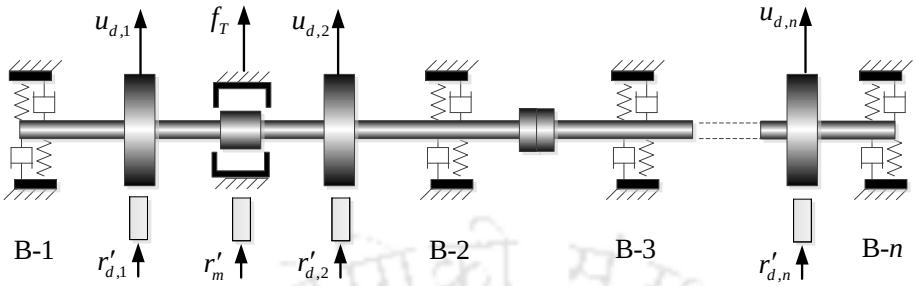


Fig. 2. 5. A line diagram of a flexible rotor-AMB system with additional virtual trial unbalances at the AMB location.

From above, influence coefficients in the last column of **A** matrix corresponding to the virtual trial unbalance f_T are expressed as,

$$\boldsymbol{\alpha}_m(\omega) = \{\mathbf{r}_2 - \mathbf{r}_1\} / f_T \tag{2.22}$$

Unlike conventional ICM, in VTEICM, only one trial unbalance is required to obtain all the influence coefficients required in the prediction of residual unbalances present in the system. As the influence coefficient matrix is assumed to be symmetrical, the column vector $\boldsymbol{\alpha}_m$ is equivalent to the row vector corresponding to the displacement at magnetic bearing (r_m) as shown in Appendix A and is given as

$$\alpha_{1m} = \alpha_{m1}; \quad \alpha_{2m} = \alpha_{m2}; \quad \ldots; \quad \alpha_{nm} = \alpha_{mn} \tag{2.23}$$

The residual unbalances can be estimated using the displacement at the AMB location for the system from Eq. (2.9) and is given as

$$r_m(\omega) = \boldsymbol{\alpha}_r(\omega)\mathbf{u}_r \tag{2.24}$$

with, $\boldsymbol{\alpha}_r = \{\alpha_{m1}(\omega) \quad \alpha_{m2}(\omega) \quad \cdots \quad \alpha_{mn}(\omega)\}$; $\mathbf{u}_r = \{u_{d,1} \quad u_{d,2} \quad \cdots \quad u_{d,n}\}^T$

TH-2966_176103027

Similarly, for the different spin speed of the rotor, the influence coefficients, which is speed-dependent, mentioned in the equations between Eq. (2.9) and Eq. (2.23), are obtained, and then Eq. (2.24) for different speeds are assembled to estimate the residual unbalances as

$$\mathbf{r} = \mathbf{H}\mathbf{u}_r \tag{2.25}$$

with, $\mathbf{r} = \{r_m(\omega_1) \quad r_m(\omega_2) \quad \cdots \quad r_m(\omega_t)\}^T$; $\mathbf{H} = [\boldsymbol{\alpha}_r(\omega_1) \quad \boldsymbol{\alpha}_r(\omega_2) \quad \cdots \quad \boldsymbol{\alpha}_r(\omega_t)]^T$

which can be solved to get unbalances, as

$$\mathbf{u}_r = \left(\mathbf{H}^T\mathbf{H}\right)^{-1}\mathbf{H}^T\mathbf{r} \tag{2.26}$$

The residual unbalances '$\mathbf{u}_r$' obtained from Eq. (2.26) are used as balancing mass with opposite phase (+180°) for the reduction of vibration response. Herein, influence coefficients related to the AMB location and balancing plane location are only required. In the present methodology, the locations of virtual trial unbalances are different from balancing planes. In fact, they are at the same location as the AMB, and the measurement planes are at the balancing planes and AMB locations. In previous procedures, the trial unbalances, and measuring planes may be different. The major advantage of the present method is that a single trial unbalance will be required at AMB location in the form of virtual trial unbalance to estimate the necessary influence coefficients, and then it can be used for obtaining all residual unbalances.

For the numerical testing and the effectiveness of the proposed balancing method over conventional ICM, finite element modelling of the rotor-AMB system with residual unbalances is done as described in the next section. The displacement responses obtained

TH-2966_176103027

from the developed model and the magnitude and phase of the VTU are to be utilized to predict the resultant residual unbalances at the balancing planes.

2.4. Finite Element Modelling of Rotor-AMB system

The FEM model of the present rotor-AMB system consists of shaft elements with two rotational and two translational DOFs at the respective nodes. The system is oriented with the axis of the shaft, i.e., along the horizontal *z*-axis and external forces along transverse *x* and *y*-axes, as shown in Fig. 2.6. The model is subjected to forces, such as the inertia and residual unbalance of the rotor, the damping and stiffness forces of the support bearings, magnetic forces of the AMBs, along with gyroscopic couples on discs. The rotor system consists of both randomly distributed shaft unbalances and discrete disc unbalances. The system of equations of each model component is discussed below.

2.4.1 Flexible shaft

Euler-Bernoulli's beam model is considered for the development of the equations of motion of the flexible shafts. The effects of shear deformation and rotary inertia are higher in the circular shaft with a large cross-sectional area, so for the slender shaft considered in the present work, those effects have been neglected. The gyroscopic effect is considered for discs only. The rotating machinery experiences a very large amplitude of vibration as the system approaches the critical speed due to the presence of residual unbalances. With the deposition of the oil and foreign particles, manufacturing error, and thermal distortion, the mass distribution of the system changes. As a result of the change in position of the center of mass from the rotating axis, the level of unbalances changes in the rotating

TH-2966_176103027

components. In order to incorporate the effect of unbalances dispersed throughout the system, randomly distributed shaft unbalances are incorporated in the system at the different node locations in the shafts. The elements of the shaft are further divided into various segments and are considered as discs with a different eccentricity and phase, as shown in Fig. 2.6. The length of the segments is equal, and the unbalance forces developed at k^{th} segment for n^{th} element is given as

$$f_{s,k} = \rho A_L l_k e_{s,k} \mathrm{e}^{\mathrm{j}\phi_{s,k}} \tag{2.27}$$

with, k = 1, 2, 3, …, p is the number of segments in n^{th} element, ρ is the density of the shaft, A_L is the area of cross-section, and l_k is the length of the k^{th} segment, $e_{s,k}$ and $\phi_{s,k}$ are the eccentricity and phase of the unbalance assumed at the k^{th} segment. The overall unbalance ($\mathbf{f}_{e,n)}$ force in n^{th} element corresponding to the four degrees of freedom are estimated at the node n and n+1 locations as

$$\mathbf{f}_{e,n} = \int_0^{l_{e,n}} \sum_{k=1}^{p} f_{s,k}(t)\,\delta(z - z_k)\mathbf{p}(z)\,dz \tag{2.28}$$

with, $\mathbf{p}(z) = \left\{ \left(1 - 3\frac{z^2}{l_{e,n}^{\ 2}} + 2\frac{z^3}{l_{e,n}^{\ 3}}\right) \quad \left(z - 2\frac{z^2}{l_{e,n}} + \frac{z^3}{l_{e,n}^{\ 2}}\right) \quad \left(3\frac{z^2}{l_{e,n}^{\ 2}} - 2\frac{z^3}{l_{e,n}^{\ 3}}\right) \quad \left(-\frac{z^2}{l_{e,n}} + \frac{z^3}{l_{e,n}^{\ 2}}\right) \right\}^T$

where, z_k is the location of the k^{th} segment from node 1 of the element-1 along the z-axis, as shown in Fig. 2.6, $l_{e,n}$ is the length of the n^{th} element, 'δ' is the Dirac delta function that represents the unbalance force as a distributed force in the form of integral and **p**(z) is the shape function vector corresponding to the different degree of freedom of the system.

TH-2966_176103027

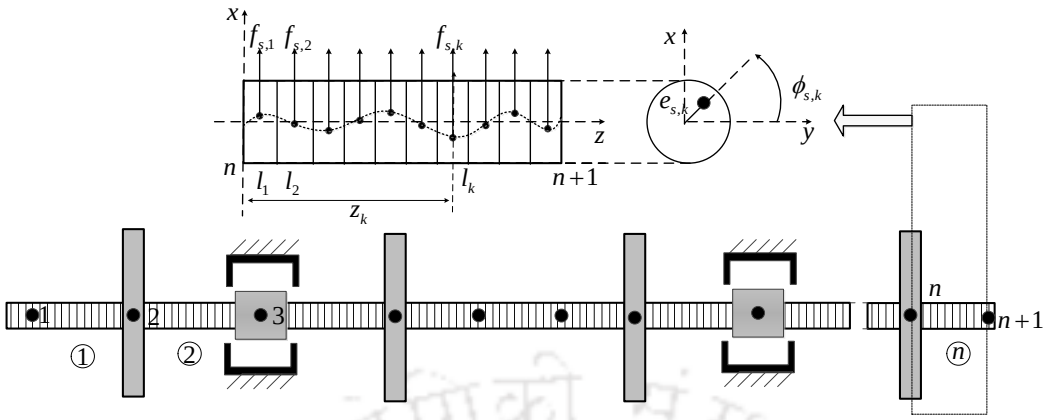


Fig. 2. 6. The flexible shaft presenting different segments with randomly distributed unbalance forces.

Equation of Motion (EOM) for n^{th} element of the shaft is given as

$$\mathbf{M}_s^e \ddot{\boldsymbol{\eta}}^e(t) + \mathbf{K}_s^e \boldsymbol{\eta}^e(t) = \mathbf{f}_{e,n}(t) \tag{2.29}$$

where, $\mathbf{M}_s^e$ and $\mathbf{K}_s^e$ are the mass and stiffness matrices of the shaft; $\boldsymbol{\eta}^e$ and $\mathbf{f}_{e,n}$ are the shaft displacement vector and the randomly distributed unbalance force vector. The matrices and vectors are required in the FEM modeling of the flexible shaft in the rotor system (Tiwari, 2017).

$$\mathbf{M}_s^e = \frac{\rho A l_{e,n}}{420}\begin{bmatrix} 156 & 22l_{e,n} & 54 & -13l_{e,n} \\ & 4l_{e,n}^2 & 13l_{e,n} & -3l_{e,n}^2 \\ & & 156 & -22l_{e,n} \\ sym & & & 4l_{e,n}^2 \end{bmatrix};\quad \mathbf{K}_s^e = \frac{EI}{l_{e,n}^3}\begin{bmatrix} 12 & 6l_{e,n} & -12 & 6l_{e,n} \\ & 4l_{e,n}^2 & -6l_{e,n} & 2l_{e,n}^2 \\ & & 12 & -6l_{e,n} \\ sym & & & 4l_{e,n}^2 \end{bmatrix} \tag{2.30}$$

$$\boldsymbol{\eta}_x(t) = \begin{Bmatrix} x_1 & \phi_{y_1} & x_2 & \phi_{y_2} \end{Bmatrix}^T;\qquad \boldsymbol{\eta}_y(t) = \begin{Bmatrix} y_1 & \phi_{x_1} & y_2 & \phi_{x_2} \end{Bmatrix}^T \tag{2.31}$$

where, ρ and E are the density and Young's modulus of the shaft material; l_e and A are the length and cross-section of the shaft; $\boldsymbol{\eta}_x$ and $\boldsymbol{\eta}_y$ are the system responses along x and y axes, respectively.

TH-2966_176103027

2.4.2 Rigid discs

Mountings that are present in various rotating machinery, such as the turbine, flywheel, and gears, are modeled as rigid discs (D-*n*). The inertia and gyroscopic effects of the rigid discs are considered in the present work, along with discrete unbalances. The unbalances arise mainly due to assembly and manufacturing errors. The EOM of the discs for the n^{th} element is given as

$$\mathbf{M}_d^e \ddot{\boldsymbol{\eta}}^e(t) + \omega \mathbf{G}_d^e \dot{\boldsymbol{\eta}}^e(t) = \mathbf{f}_d^e(t) \tag{2.32}$$

where, $\mathbf{M}_d^e$ and $\mathbf{G}_d^e$ are the mass and gyroscopic matrices of the discs for each element; $\mathbf{f}_d^e$ is the discrete unbalance force considered at the disc location; ω is the spin speed of the rotor. The unbalance force corresponding to the n^{th} element in the *x*-*y* plane is given as

$$\mathbf{f}_d^e(t) = m_n e_n \omega^2 e^{\mathrm{j}(\omega t + \phi_n)} \mathbf{q}_n \tag{2.33}$$

with, $\mathbf{q}_n = \{1 \quad 0 \quad 0 \quad 0\}^T$

where, *n* is the number of rigid discs; m_n, e_n, and ϕ_n are the mass, eccentricity, and phase of the unbalance at the n^{th} disc location; $\mathbf{q}_n$ is the position vector in the *x*-*y* plane, and entry '1' in the vector is the location of the translational node corresponding to the n^{th} disc.

2.4.3 Support bearings

The rotor system is supported by flexible bearings (FB) that introduce the damping and stiffness forces in the system. The forces are applied at the respective node location in the FEM model and are given as

TH-2966_176103027

$$\mathbf{f}_b(t) = \left(\sum_{j=1}^{n} k_{b,j} \mathbf{B}_j \right) \boldsymbol{\eta}(t) + \left(\sum_{j=1}^{n} c_{b,j} \mathbf{B}_j \right) \dot{\boldsymbol{\eta}}(t) \tag{2.34}$$

$$\mathbf{f}_b(t) = \mathbf{K}_b \boldsymbol{\eta}(t) + \mathbf{C}_b \dot{\boldsymbol{\eta}}(t) \tag{2.35}$$

with, $$\mathbf{B}_j = \begin{bmatrix} \ddots & 0 & 0 & 0 & 0 \\ & 1 & 0 & 0 & 0 \\ & & 0 & 0 & 0 \\ & & & \ddots & 0 \\ sym & & & & 0 \end{bmatrix}$$

where, $\mathbf{f}_b$ is the bearing force at the respective node location; $\boldsymbol{\eta}(t)$ is the displacement vector corresponding to different node locations in the rotor system; $c_{b,j}$ and $k_{b,j}$ are the bearing damping and stiffness coefficients corresponding to the j^{th} flexible bearing, respectively; $\mathbf{B}_j$ is position matrix for the bearing locations, and '1' represents the node location corresponding to the j^{th} conventional bearing; $\mathbf{K}_b$ and $\mathbf{C}_b$ are the bearing stiffness and mass matrices, respectively.

2.4.4 Active Magnetic Bearings (AMBs)

The AMB is additionally introduced in the present work, apart from conventional bearings, to allow the rotor system to successfully cross its critical speeds with a minimum amount of vibration by applying controlling magnetic forces. Also, the AMB is utilized to generate virtual trial unbalances for the identification of residual unbalances, which does not require the stopping of the machine during its operation. The controlling magnetic forces are applied through differential control mode, as shown in Fig. 1.13. A PID controller is incorporated to supply the control current and accordingly generate control forces. In control, the structure of the PID controller is simpler than the other controllers. The steady-state error is comparatively lower, and it has better performance while operating the system

TH-2966_176103027

closer to the design conditions. On the other hand, the tuning of the PID controller gains with the changing environmental and operating conditions is difficult. Also, it takes a longer response time for a step-change. Polajžer *et al*. (2006) decentralized the closed-loop controller for the AMB using a combination of PD and PI controllers. They showed that the proposed controller provides high stiffness and damping property than the conventionally used PID controllers. Sabirin *et al*. (2007) designed two controllers, i.e., a PID controller and state-space controller, and analyzed their effectiveness in levitation of the rotor and unbalance compensation. They also developed the rotor-AMB system model with a detailed description of PWM in the control algorithm. Chen and Knospe (2007) considered three control approaches, i.e., the speed specified control, speed interval control, and speed independent control, to actively suppress the machining chatter in the machines. They showed that the designed control approaches give better results than the conventional PID controller. Zhong and Zhu (2013) designed a 2 degree of freedom PID controller to suppress the vibrational response of the flexible rotor system passing through its first critical speed. Psonis *et al*. (2015) designed a linearized model magnetic bearing system using a PID controller. They studied the stability of the system using the characteristics equation and Routh-Hurwitz criteria.

The control current, mentioned in Eq. (1.4), is applied through a PID controller, which is given as

$$i_c(t) = k_P r_m(t) + k_I \bar{r}_m(t) + k_D \dot{r}_m(t) \tag{2.36}$$

where, the symbols dot (·) and bar (-) represent the derivative and integration of the variable, respectively. The AMB force $\mathbf{f}_m(t)$ is applied at the respective node locations in the present system as

TH-2966_176103027

$$\mathbf{f}_m(t) = -k_s\mathbf{S}\boldsymbol{\eta}(t) + k_i(k_P\mathbf{S}\boldsymbol{\eta}(t) + k_I\mathbf{S}\bar{\boldsymbol{\eta}}(t) + k_D\mathbf{S}\dot{\boldsymbol{\eta}}(t)) \tag{2.37}$$

with, $\mathbf{S} = \begin{bmatrix} \ddots & 0 & 0 & 0 & 0 \\ & 1 & 0 & 0 & 0 \\ & & 0 & 0 & 0 \\ & & & \ddots & 0 \\ sym & & & & 0 \end{bmatrix}$

where, **S** is the position matrix of AMB and '1' represents the node location corresponding to the AMB location.

2.4.5. Equations of motion of the overall system

Equations of motion of various components along with external force equations are assembled together to get the systems' global equations of motion and is given as

$$\left(\mathbf{M}_s + \mathbf{M}_d\right)\ddot{\boldsymbol{\eta}}(t) + \mathbf{C}_b - \omega\mathbf{G}_d\dot{\boldsymbol{\eta}}(t) + \left(\mathbf{K}_s + \mathbf{K}_b\right)\boldsymbol{\eta}(t) = \mathbf{f}_u(t) - \mathbf{f}_m(t) \tag{2.38}$$

with, $\mathbf{f}_u(t) = \mathbf{f}_s(t) + \mathbf{f}_d(t)$

where, $\mathbf{M}_s$ and $\mathbf{M}_d$ are the assembled mass matrices of the shaft and the discs and $\mathbf{K}_s$ and $\mathbf{K}_d$ are the assembled stiffness matrices for the shaft and conventional bearings, respectively; $\mathbf{G}_d$ is the assembled gyroscopic matrix for the discs; $\mathbf{f}_s$ and $\mathbf{f}_d$ are the assembled unbalance force vectors corresponding to shaft and discs, respectively; $\boldsymbol{\eta}$ and $\mathbf{f}_m$ are the overall displacements and AMB force vector corresponding to different node locations. Now, substituting AMB force equation Eq. (2.37) in Eq. (2.38) we get

$$\left(\mathbf{M}_s + \mathbf{M}_d\right)\ddot{\boldsymbol{\eta}}(t) + \left(\mathbf{C}_b - \omega\mathbf{G}_d\right)\dot{\boldsymbol{\eta}}(t) + \left(\mathbf{K}_s + \mathbf{K}_b\right)\boldsymbol{\eta}(t) = \mathbf{f}_u(t) + k_s\mathbf{S}\boldsymbol{\eta}(t) - k_i\mathbf{S}(k_P\boldsymbol{\eta}(t) + k_I\bar{\boldsymbol{\eta}}(t) + k_D\dot{\boldsymbol{\eta}}(t)) \tag{2.39}$$

or,

TH-2966_176103027

$$\left(\mathbf{M}_s+\mathbf{M}_d\right)\ddot{\boldsymbol{\eta}}(t)+\left(\mathbf{C}_b-\omega\mathbf{G}_d+k_ik_D\mathbf{S}\right)\dot{\boldsymbol{\eta}}(t)+\left(\mathbf{K}_s+\mathbf{K}_b-k_s\mathbf{S}+k_ik_P\mathbf{S}\right)\boldsymbol{\eta}(t)+k_ik_I\mathbf{S}\bar{\boldsymbol{\eta}}(t)=\mathbf{f}_u(t) \tag{2.40}$$

The response of the system and the unbalance force can be given as

$$\boldsymbol{\eta}(t)=\mathbf{r}\mathrm{e}^{\mathrm{j}\omega t};\quad \mathbf{f}_u(t)=\mathbf{f}_p\mathrm{e}^{\mathrm{j}\omega t} \tag{2.41}$$

where, $\mathbf{f}_p$ and $\mathbf{r}$ are the complex force and displacement vectors, respectively. Substituting, Eq. (2.41) in Eq. (2.40) we get

$$\left\{-\omega^2\left(\mathbf{M}_s+\mathbf{M}_d\right)+\mathrm{j}\omega\left(\mathbf{C}_b-\omega\mathbf{G}_d+k_ik_D\mathbf{S}\right)+\left(\mathbf{K}_s+\mathbf{K}_b-k_s\mathbf{S}+k_ik_P\mathbf{S}\right)+\frac{k_ik_I}{\mathrm{j}\omega}\mathbf{S}\right\}\mathbf{r}=\mathbf{f}_p \tag{2.42}$$

or,

$$\mathbf{r}=\left\{-\omega^2\left(\mathbf{M}_s+\mathbf{M}_d\right)+\mathrm{j}\omega\left(\mathbf{C}_b-\omega\mathbf{G}_d+k_ik_D\mathbf{S}\right)+\left(\mathbf{K}_s+\mathbf{K}_b-k_s\mathbf{S}+k_ik_P\mathbf{S}\right)+\frac{k_ik_I}{\mathrm{j}\omega}\mathbf{S}\right\}^{-1}\mathbf{f}_p \tag{2.43}$$

or,

$$\mathbf{r}=\boldsymbol{\alpha}\mathbf{f}_p \tag{2.44}$$

with, $\boldsymbol{\alpha}=\left\{-\omega^2\left(\mathbf{M}_s+\mathbf{M}_d\right)+\mathrm{j}\omega\left(\mathbf{C}_b-\omega\mathbf{G}_d+k_ik_D\mathbf{S}\right)+\left(\mathbf{K}_s+\mathbf{K}_b-k_s\mathbf{S}+k_ik_P\mathbf{S}\right)+\frac{k_ik_I}{\mathrm{j}\omega}\mathbf{S}\right\}^{-1}$

where, $\boldsymbol{\alpha}$ is defined as the influence coefficient matrix, i.e., to be utilized in the identification algorithm proposed to obtain residual unbalances present in the system. Then, the predicted balance masses are utilized in the present system to inspect the level of vibration reduction.

TH-2966_176103027

2.5. Numerical Simulation of the Proposed Balancing Method

The rotor system consists of a flexible shaft supported on two conventional bearings, three rigid discs as balancing planes, and an AMB for controlling as well as generating virtual trial unbalance force (Model 1) as shown in Fig. 2.7. The properties of the shaft, conventional bearings (Tiwari, 2005), and the AMB is given in Table 2.1, 2.2, and 2.3, respectively. In the present work, both randomly distributed shaft unbalances, and the discrete unbalances at the location of the disc are considered, as shown in Fig. 2.8. The control gains of the PID controller are assumed as k_P = 4000 A/m, k_I = 2000 A/m-s and k_D = 3 A-s/m (Tiwari and Chougale, 2014) based on suitable tuning. The proposed procedure neglects the phase lag introduced by the power amplifier, which drives the AMB system. The magnitude and phase of virtual trial unbalance, as mentioned in Eq. (2.10) are taken as 1.6×10^{-5} kg-m and 0.3491 rad, respectively. In VTEICM, only one trial unbalance is utilized, whereas in conventional ICM minimum of three trial unbalances are required for estimation of unbalances for dynamic balancing of the flexible rotor system. The responses of the rotor-bearing system are obtained based on Eq. (2.38) using the SIMULINK model as shown in Fig. 2.9.

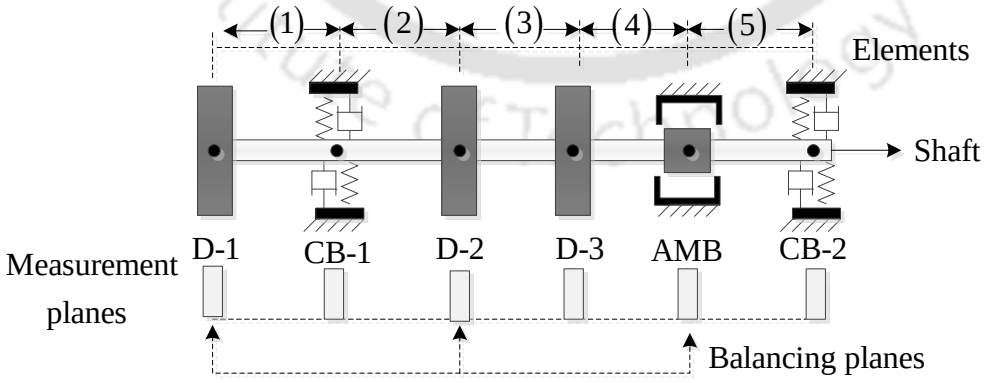


Fig. 2. 7. The flexible rotor-AMB system is supported on conventional bearings (Model 1).

TH-2966_176103027

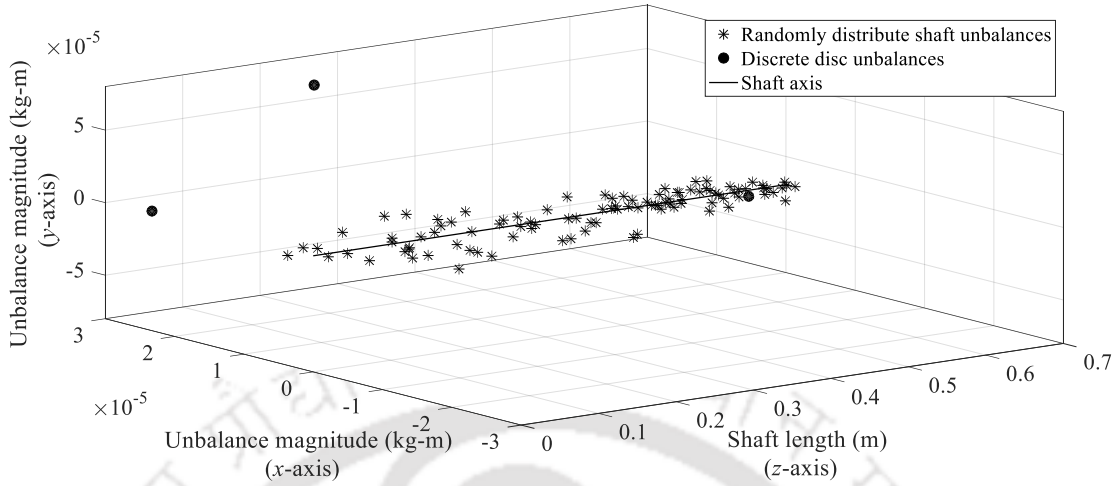


Fig. 2. 8. The distribution of the random shaft unbalances, and the discrete disc unbalances along the axis of the shaft.

The steps involved in the estimation of the residual unbalances at the balancing planes through the proposed identification algorithm are given in the flowchart, as shown in Fig. 2.10. The rotor system is accelerated with an angular acceleration of 23.17 rad/s^2 from the spin speed of 5 rad/s to 700 rad/s.

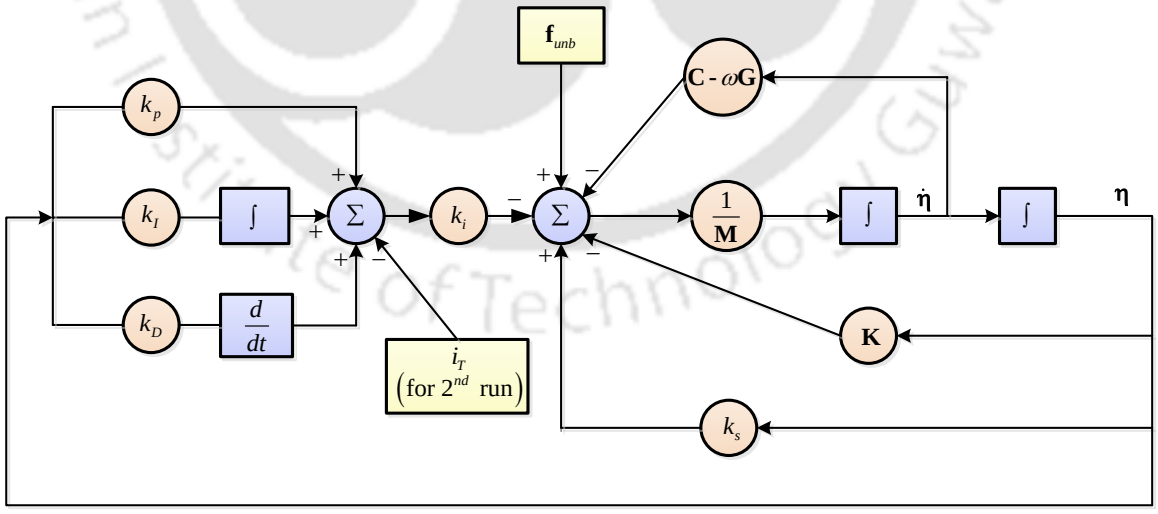


Fig. 2. 9. Diagram of the rotor-AMB system model in SIMULINK.

TH-2966_176103027

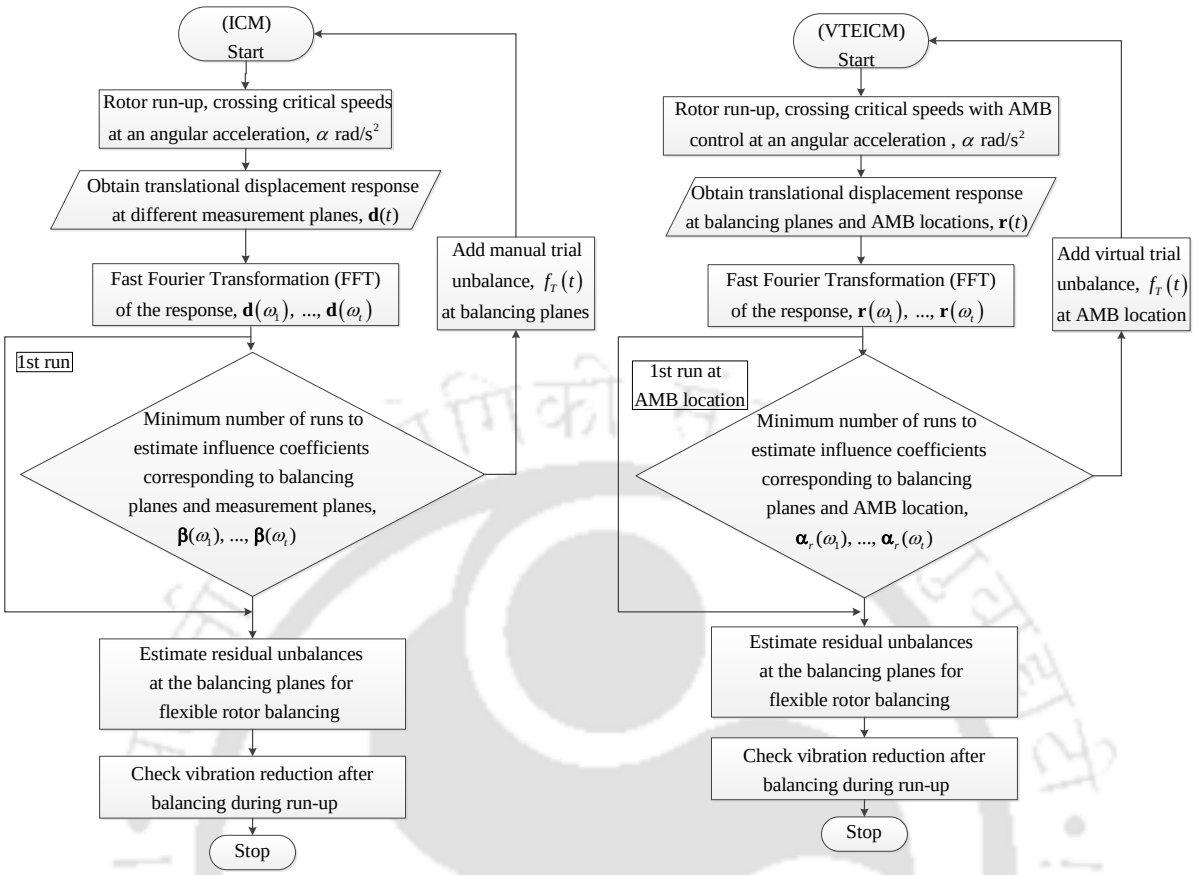


Fig. 2. 10. Flow chart of the balancing procedure using conventional ICM and VTEICM for the flexible rotor system.

The critical speed of the system, without AMB control, in the first three backward whirls is found out to be 110.5, 289.8, and 431.9 rad/s, and in the first three forward whirls is found out to be 114.0, 313.0, and 495.5 rad/s. Whereas with AMB control, as shown in Fig. 2.11, in the backward whirl is found out to be 140.3, 296.6, and 469.7 rad/s, and in the forward whirl is found out to be 145.2, 316.9, and 552.2 rad/s. In the first run, the rotor is allowed to rotate with the mentioned spin speed and acceleration to obtain displacements due to residual unbalances at discs and shaft in the presence of AMB as a controller. In the second run, the system is rotated considering trial unbalance at AMB as a magnetic force

TH-2966_176103027

along with existing residual unbalances to obtain the displacement response in the presence of AMB (also as a controller).

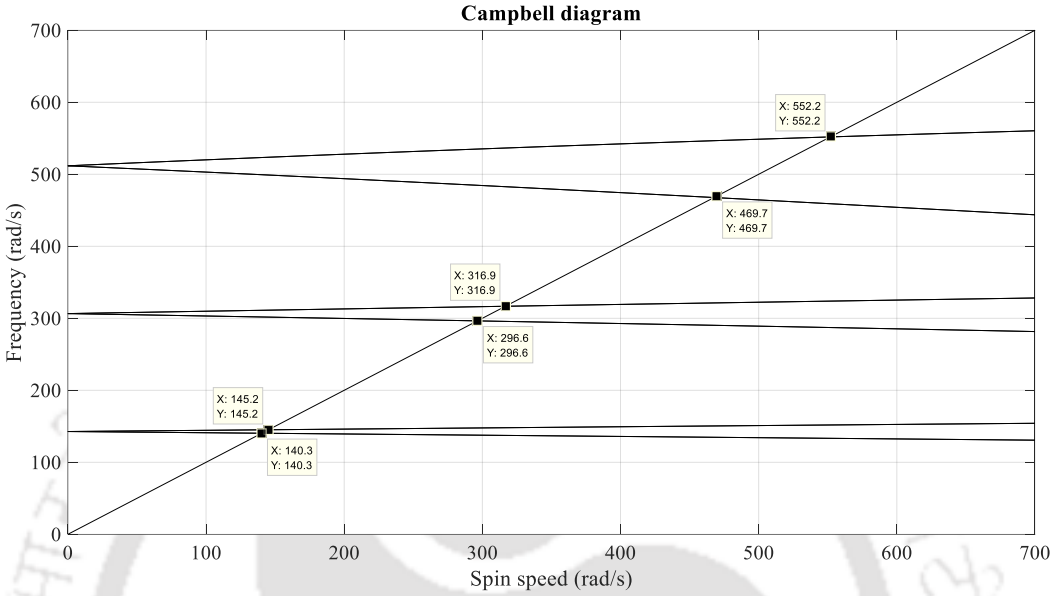


Fig. 2. 11. Campbell diagram of the rotor-AMB system depicting different forward and backward whirls.

Now, Fast Fourier Transformation (FFT) of the time domain displacement signals is carried out of the rotor system in order to obtain 1X amplitudes and phases of displacements against each frequency of rotation as described in Fig. 2.12.

TH-2966_176103027

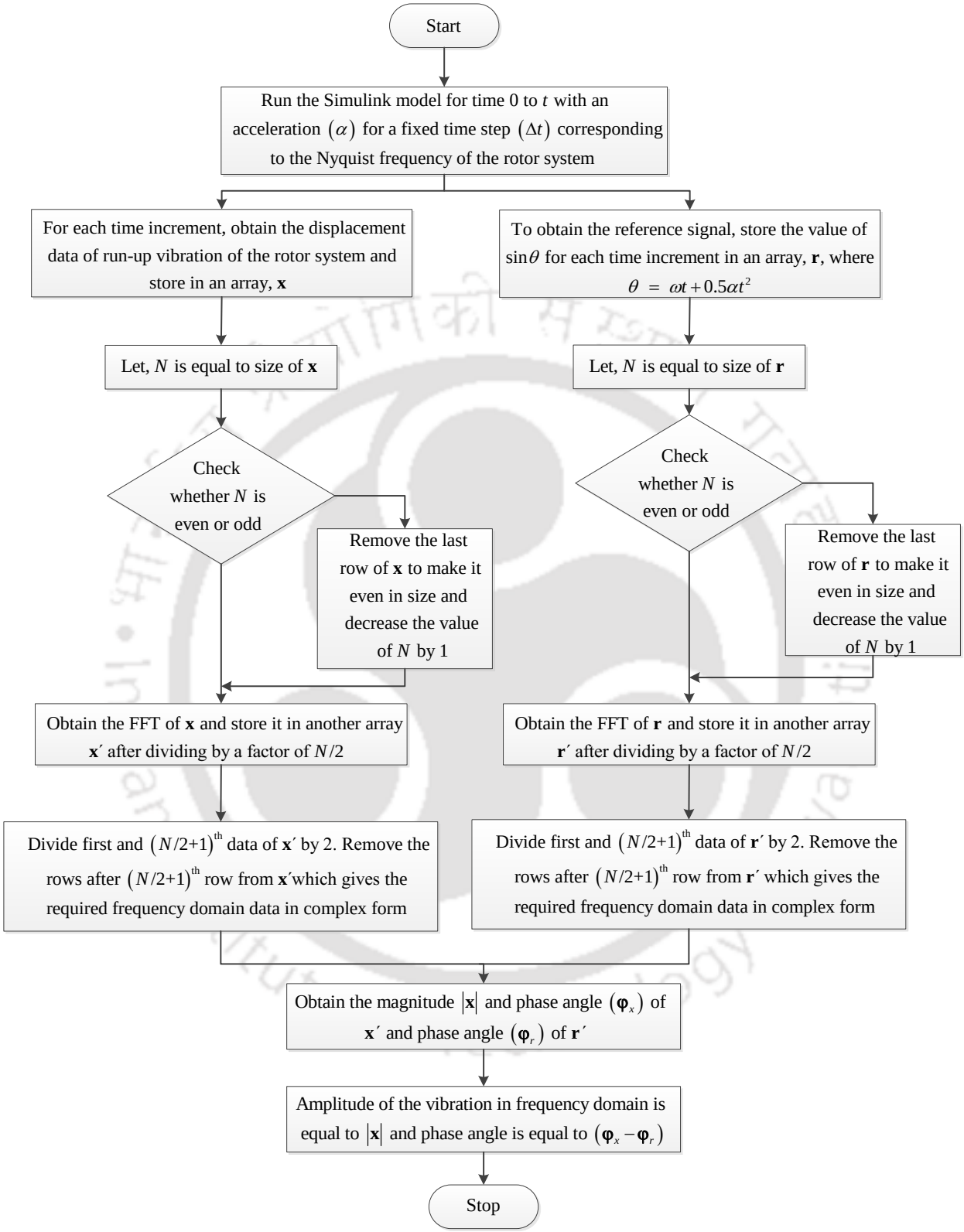


Fig. 2. 12. A process chart for the calculation of correct phase of displacement during rotor run–up using the FFT.

TH-2966_176103027

For this, a reference signal is assumed to estimate the desired phase of the displacement signals. The complex displacements for different frequencies are then utilized to obtain the residual unbalances at the balancing planes using the VTEICM. Also, a Hanning window function is applied to the time domain responses to get the desired level of amplitudes corresponding to the frequency with FFT. The window function reduces the spectral leakage in the signal and provides better frequency and amplitude resolution for the runup response of the rotor system. It has been utilized by various researchers such as Prabhakar *et al.* (2002); Su and Chong (2004); Roques *et al.* (2010); Tiwari and Chougale (2014); Xia *et al.* (2020) to analyze the ramp up vibration responses.

Table 2. 1. Parameters of the flexible rotor system.

Parameters	Values		
ρ (Shaft's density)	7850 kg/m^3		
E (Young's modulus of elasticity)	2.06 ×10^{11} N/m^2		
d (Shaft's diameter) and L (Shaft's length)	10 mm and 615 mm		
Elements' length in the rotor system	96, 139, 82, 183 and 115 mm		
Components	Mass (kg)	Moment of inertia (kg-m^2)	
		Diametral	Polar
Disc 1	0.78	4.44×10^{-4}	8.30×10^{-4}
Disc 2 and Disc 3	1.20	13.09×10^{-4}	27.39×10^{-4}
AMB core	0.88	5.17×10^{-4}	3.98×10^{-4}
Residual unbalance	Magnitude (kg-m)	Orientation (degree)	
Disc 1	2.34 ×10^{-5}	5.73^o	
Disc 2	7.20 ×10^{-5}	68.75^o	
Disc 3	3.60 ×10^{-5}	120.32^o	

TH-2966_176103027

Table 2. 2. Parameters of the conventional bearings

Parameters	Values
Bearing 1	
k_{b_1} (Stiffness coefficient)	4×10^5 N/m
c_{b_1} (Damping coefficient)	200 N-s/m
Bearing 2	
k_{b_2} (Stiffness coefficient)	5×10^5 N/m
c_{b_2} (Damping coefficient)	210 N-s/m

Normally, in the displacement signal, the noise is generated due to electrical disturbances, surface roughness, and environmental conditions. So, in complex displacement responses, 5% and 10% of random valued noise are also added to investigate the robustness of the proposed algorithm against measurement noise. After balancing, to see the amount of reduction in system response, the system is again rotated (without AMB). So, if AMB fails due to some electrical fault, then also the system can be rotated at higher speeds without much vibrational response.

Table 2. 3. Parameters of AMB system.

Parameter	Values
k_i (Direct force current factor)	42.10 N/A
k_s (Direct force displacement factor)	1.052×10^5 N/m

2.5.1 Vibration suppression with AMB

The AMB is included in the rotor system to allow the system to safely cross different critical speeds (on run-up) by suppressing the vibration caused due to residual unbalances

TH-2966_176103027

and obtaining the displacement responses. The acceleration of the system is kept low so that the transients are avoided. The run-up rate chosen ensures moderate acceleration. Too fast run-up gives transients and too slow leads to locked-up of rotor speed at resonance (if rotor speed stays for longer period around resonance, then amplitude built-up and rotor goes unstable). Numerical responses do not show much transients but in experiments choice of run-up rate is chosen by trial and error. As discussed in Hassenpflug *et al.* (1981), the effect of different values of acceleration is more prominent in systems with low damping. The slow run-up and fast run-up are discussed in the literature as per the ratio of the acceleration (α) and square of critical speed (ω_{cr}) as in Hassenpflug et al. (1981). The increment of acceleration values reduces amplitudes as well as shifts the critical speed based on the damping of the system. The beating phenomenon also increase in the low damped system. The displacement amplitudes of present rotor-AMB system with and without AMB control for different acceleration ratios in range of 1e-04 (slow) to 1e-02 (fast) are shown in Fig. 2.13 below. In the present rotor-AMB model, the change in acceleration value has less effect in the system's behavior and the beating effect as seen in without AMB case is reduced with the increment in damping through the AMB system. A moderate acceleration value of 23.17 rad/s2 is selected to allow the rotor system to cross the desired critical speeds in 30 s while maintaining the maximum amplitude of vibration within the limits of air gap of AMB system.

The suppressed displacement responses with AMB along with controlling currents are utilized for the prediction of residual unbalances in the system. So, it is necessary to see whether the assumed control gains of AMB are able to actively suppress the rotor vibration. Therefore, the displacement responses of the rotor system are obtained without

TH-2966_176103027

and with AMB control in the system at Disc 1 and AMB location for Model 1, as shown in Fig. 2.14 (a) and (b), respectively.

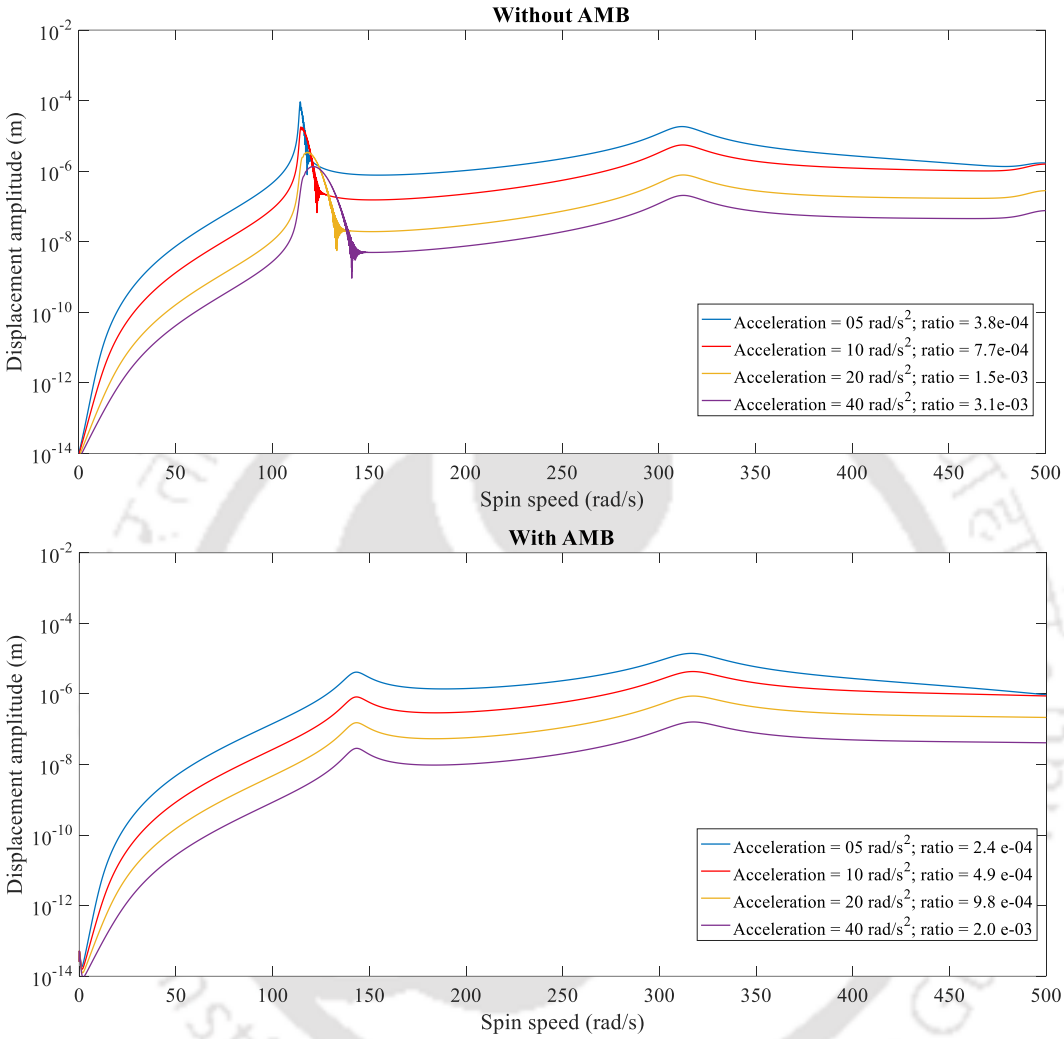


Fig. 2. 13. The displacement amplitude vs. frequency plots for different acceleration values without and with AMB control.

The FFT of displacement responses is carried out to obtain 1X amplitude and phase of displacements corresponding to each frequency of rotation. Fig. 2.14 (c) and (d) represent the frequency domain amplitudes of the run-up system corresponding to each spin speed without and with AMB control, respectively. Fig. 2.14 (e) and (f) represent the phases of the displacement response corresponding to each spin speed without and with

TH-2966_176103027

AMB control, respectively. The plots show that the vibration is effectively suppressed using AMB, and the system can easily run-up above critical speeds. It is also seen that the rotor system is able to cross the third critical speed, which is difficult to achieve in the real system. Therefore, in real conditions, the system is required to run-up with the AMB up to the safe working speed, which can go up to the second critical speed. The maximum percentage reduction with AMB control in the time domain along all the node locations is 60.02 %.

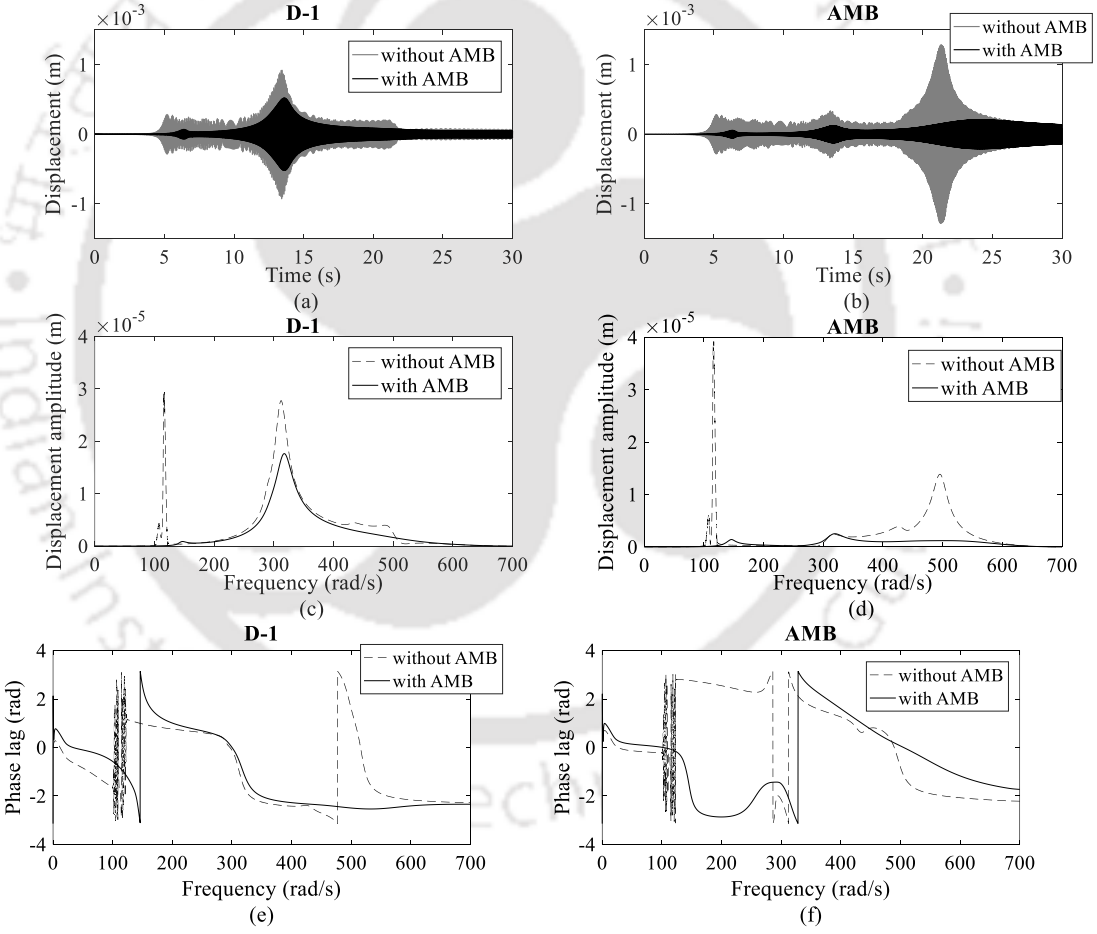


Fig. 2. 14. (a) and (b) rotor run-up time domain displacement response along *x*-axis, (c) and (d) rotor run-up frequency domain displacement amplitude vs. speed plot, (e) and (f) rotor run-up displacement phase (rad) vs. speed plot without and with AMB control at Disc 1 and AMB location respectively (Model 1).

TH-2966_176103027

2.5.2 Estimation of the force current factor (k_i)

The estimation of k_i is carried out as per Eq. (2.15) in the present rotor-AMB model. A constant force is introduced in the static condition ($\omega = 0$) at the AMB location along the x-axis. The controlling current introduced by the AMB to compensate for the displacement generated by the constant force (2 N) is shown in Fig 2.15 (a). The control current shifts the displacement of the shaft back to the equilibrium condition, as shown in Fig 2.15 (b). The additional static control current is obtained to estimate the value of k_i. The different magnitude of the constant force is applied along the x-axis, and the corresponding force current factor is estimated as shown in Table 2.4. As it is seen from Table 2.4, the assumed and the estimated values of k_i have a very small percentage variation of < 0.03%.

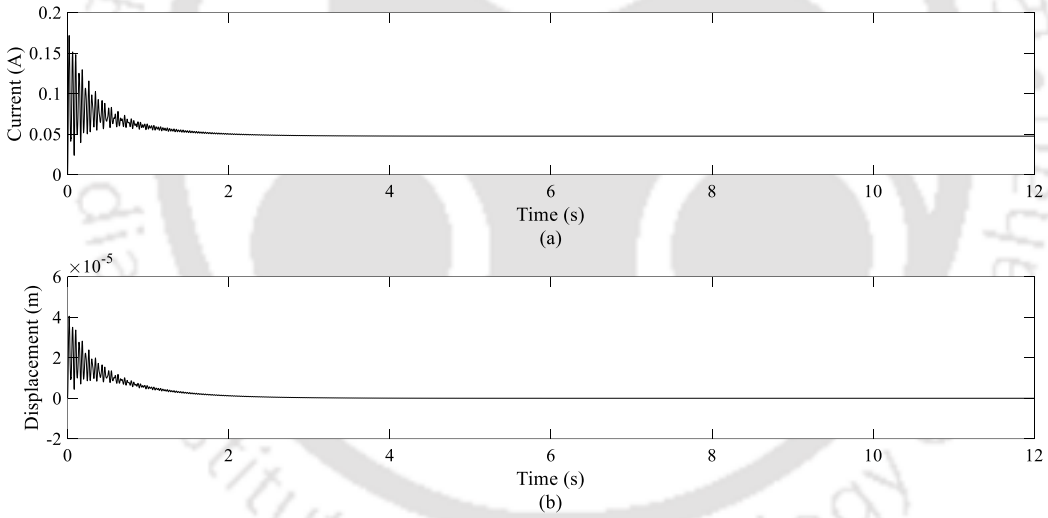


Fig. 2. 15. For a static load of 2 N at the AMB location (a) Control current (b) Shaft displacement at the AMB location.

TH-2966_176103027

Table 2. 4. Estimated value of the force current factor (k_i) in numerical model for different values of constant load (assumed value = 42.1 N/A).

Constant load (N)	Constant control current (A)	Force current factor (N/A)	Percentage variation (%)
1	2.375×10^{-2}	42.1053	0.0126
2	4.751×10^{-2}	42.0964	–0.0086
5	11.88×10^{-2}	42.0875	–0.0297
10	23.75×10^{-2}	42.1053	0.0126

2.5.3 Estimation of the discrete and distributed unbalances

The developed identification algorithm is tested by assuming discrete residual unbalance at disc locations and estimating their values using the VTEICM (Eqs. (2.9)- (2.26)) for the rotor Model 1. Both the magnitude and phase of estimated unbalance shown in Table 2.5 are found to be equivalent to assumed values up to 3 decimal places. It shows that the algorithm is able to correctly estimate the unbalances at the location of the discs. Now, the algorithm is checked for estimation of equivalent residual unbalances at balancing planes with the addition of randomly distributed unbalances in the shaft along with discrete unbalances at the discs. The equivalent unbalances are estimated at the location of the balancing planes, as shown in Table 2.6. To balance the system, the equivalent unbalances are identified added in the rotor system as balance masses with 180+ phases. After balancing the current consumption by the AMB in suppression of unbalance is compared with the condition before balancing as shown in Fig 2.16. The reduction in current consumption saves the overall energy requirement of the system through balancing, and then AMB can be utilized in the system to take care of the other faults/disturbances. The time domain displacement responses of the system before and after balancing with AMB

TH-2966_176103027

control at D-1 and AMB locations are shown in Fig. 2.17 (a) and (b), respectively. The frequency domain displacement amplitude of the system before and after balancing is shown in Fig. 2.17 (c) and (d), respectively. The phases of the displacement responses before and after balancing are shown in Fig. 2.17 (e) and (f), respectively. With AMB control, after balancing the rotor system, the maximum reduction in time domain displacement responses at all the node locations is found to be 94.76%.

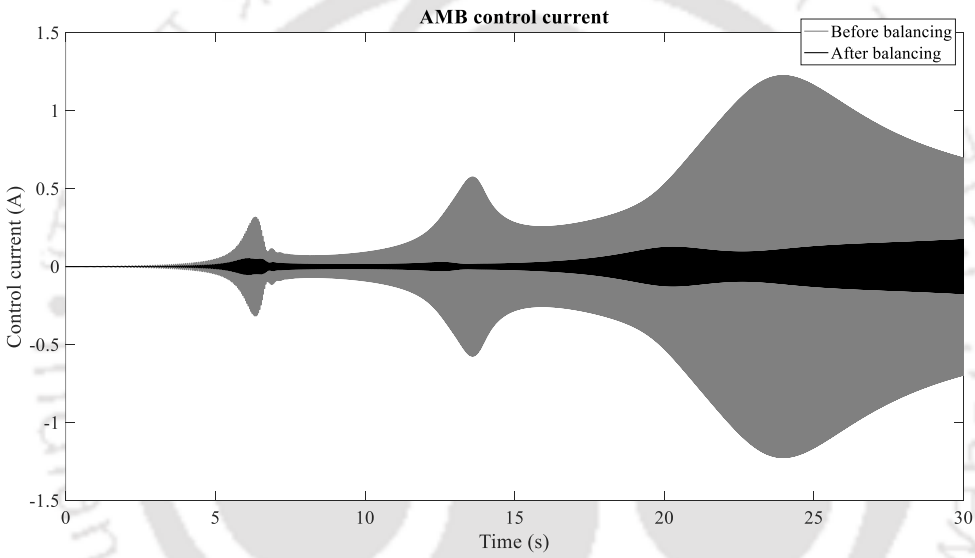


Fig. 2. 16. Control current vs. time plot before and after balancing along the *x*-axis (at AMB for Model 1).

It is also necessary to check whether the system can be operated at a higher spin speed in case the AMB fails due to some electrical faults. So, the FFT of the displacement responses (before and after balancing) is carried out for the rotor system, excluding AMB control to obtain 1X amplitude and phase of displacements corresponding to each frequency of rotation. The displacement amplitudes versus rotor run-up speeds are plotted for the rotor Model 1 with and without balancing and excluding AMB to show the

TH-2966_176103027

reduction in vibration with balancing at all three balancing planes in a horizontal direction (*x*-axis). In Fig. 2.18 (a) and (b), the plot represents time-domain displacements of the rotor system Model 1 at Disc 1 and AMB location while crossing different critical speeds before and after balancing, respectively. Figs. 2.18 (c) and (d) represent the frequency domain amplitudes of the run-up system corresponding to each spin speed before and after balancing, respectively. Figs. 2.18 (e) and (f) represent the phases of the displacement responses corresponding to each spin speed before and after balancing, respectively.

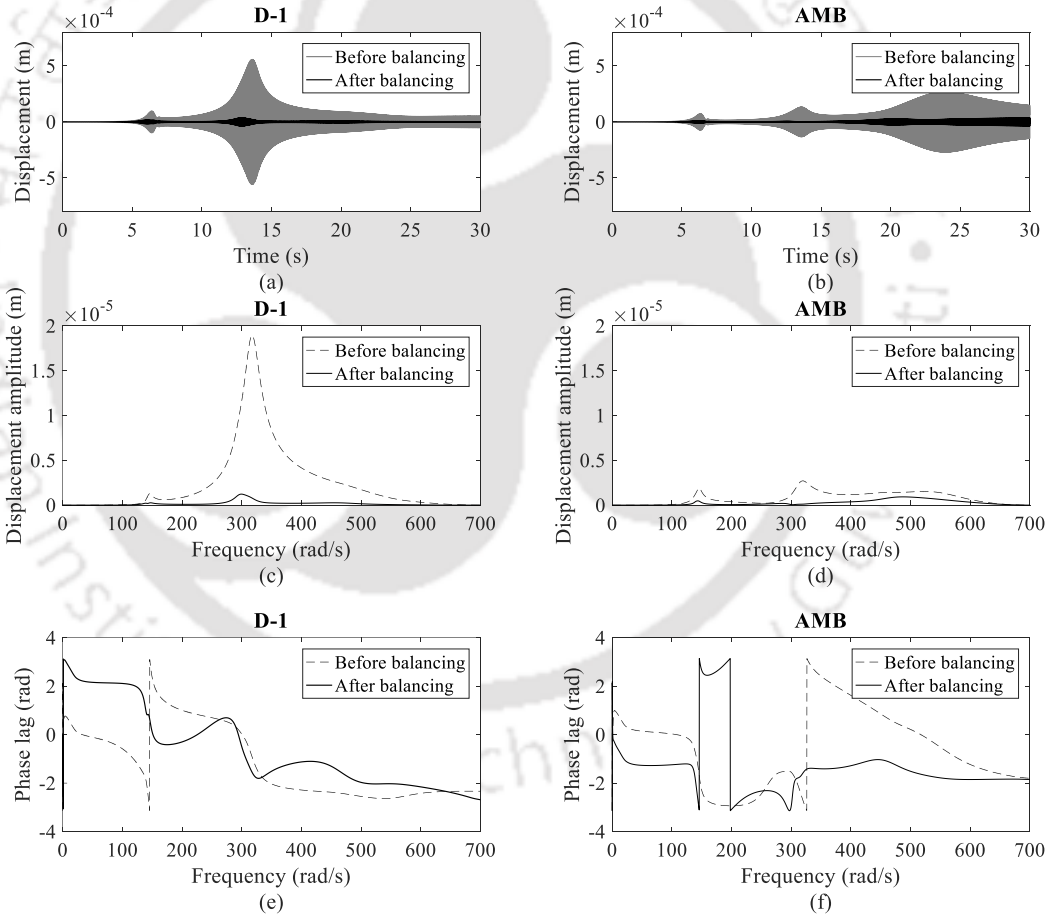


Fig. 2. 17. (a) and (b) rotor run-up time domain displacement response along *x*-axis, (c) and (d) rotor run-up frequency domain displacement amplitude vs. speed plot, (e) and (f) rotor run-up displacement phase (rad) vs. speed plot before and after balancing at Disc 1 and AMB location respectively (Model 1, including AMB control).

TH-2966_176103027

Excluding AMB control, after balancing the rotor system, the maximum reduction in time domain displacement responses at all the node locations is found to be 89.84%. The plots show that the vibration response of the rotor system has been greatly reduced throughout the run-up after balancing. It shows that after balancing, the utilization of control current in AMB is reduced due to less vibrational response, and the system can also be rotated at higher spin speeds in the case if AMB fails due to electrical faults.

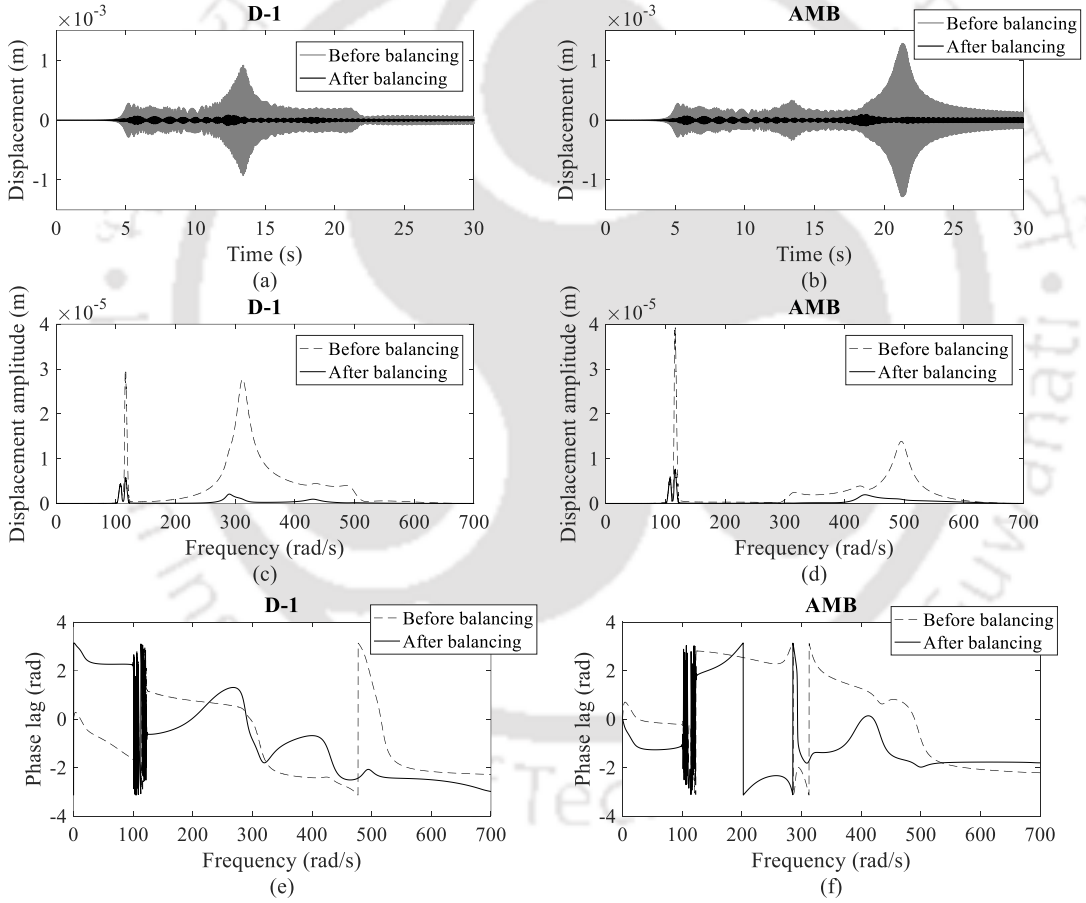


Fig. 2. 18. (a) and (b) rotor run-up time domain displacement response along *x*-axis, (c) and (d) rotor run-up frequency domain displacement amplitude vs. speed plot, (e) and (f) rotor run-up displacement phase (rad) vs. speed plot before and after balancing at Disc 1 and AMB location respectively (Model 1, excluding AMB control).

TH-2966_176103027

2.5.4 Comparison of percentage reduction in displacement amplitude obtained using different methods

In order to check the effectiveness of the developed method, the residual unbalances are also obtained using conventional ICM without AMB control using manually added trial unbalances (Eqs. (2.1) – (2.6)) for Model 1. In the conventional ICM, along with the displacements of the shaft at conventional bearing locations, the displacement at node position of AMB is also utilized (AMB forces are not considered).

Table 2. 5. Comparison of the unbalance magnitudes and phases estimated using VTEICM from assumed values considering residual unbalances only at discs for a rotor with 0% noise.

Disc	Assumed values of unbalances		Estimated values of unbalances 0% Noise			
	Magnitude (kg-m)	Phase (rad)	Magnitude (kg-m)	% error	Phase (rad)	% error
Disc-1	2.340×10^{-5}	0.100	2.339×10^{-5}	–0.05	0.1000	–0.04
Disc-2	7.200×10^{-5}	1.200	7.200×10^{-5}	0.01	1.1999	–0.01
Disc-3	3.600×10^{-5}	2.100	3.600×10^{-5}	0.01	2.1005	0.02

The residual unbalances, as shown in Table 2.6, are then utilized as balance masses with 180°+ phase to check the level of reduction obtained using the two methods. After balancing, the displacement response at Disc 1 location is obtained for the two methods. The frequency domain amplitudes and phases after balancing with the estimates obtained using conventional ICM are shown in Fig. 2.19. The level of vibration reduction achieved after the addition of the correction masses estimated using conventional ICM is found out to be 87.92%, which is similar to that obtained using VTEICM (89.84%). But VTEICM has the advantage of using AMB that allows the safe traversal above the critical speed of

TH-2966_176103027

the rotor system during ramp-up. Also, generating trial unbalances through the AMB reduces the mechanical effort and the number of trial runs for the balancing. So, overall VTEICM suits better for the balancing of the flexible rotor while crossing various critical speeds.

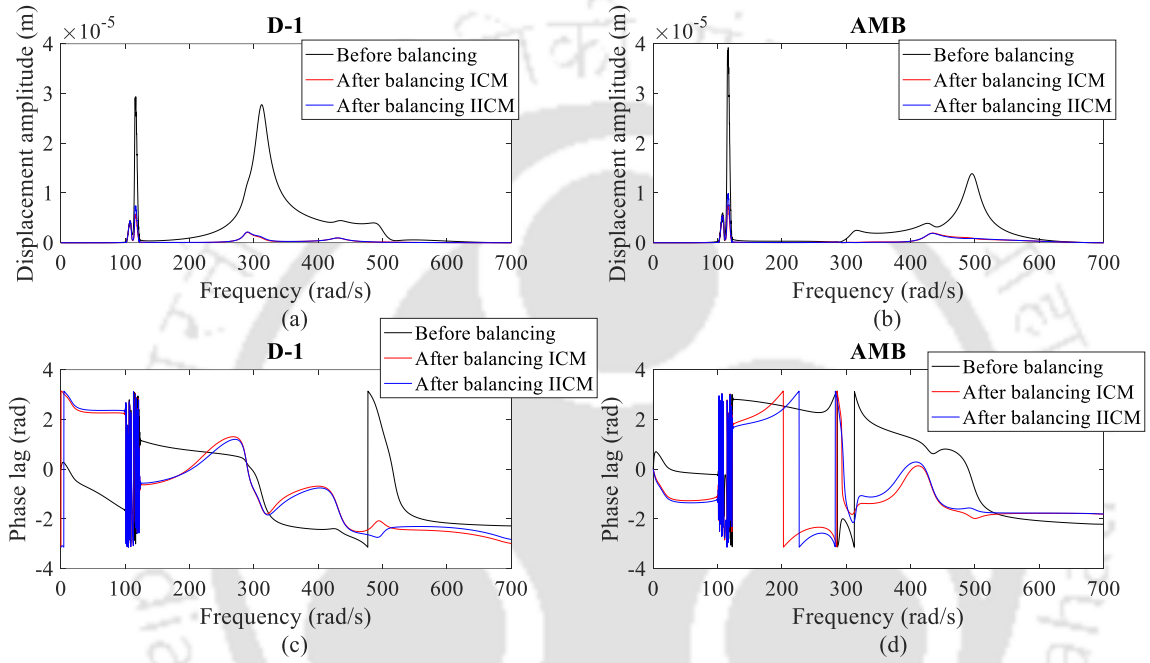


Fig. 2. 19. (a) and (b) rotor run-up frequency domain displacement amplitude vs. speed plot, (c) and (d) rotor run-up displacement phase (rad) vs. speed plot before and after balancing at Disc 1 and AMB location respectively using balance estimates of conventional ICM and VTEICM (Model 1, excluding AMB control).

Table 2. 6. Comparison of the unbalance magnitudes and phases estimated using conventional ICM and VTEICM from assumed values considering residual unbalances at both shaft and discs for Model 1.

Disc	Conventional ICM		VTEICM	
	Magnitude (kg-m)	Phase (rad)	Magnitude (kg-m)	Phase (rad)
Disc-1	2.250×10^{-5}	0.6728	2.236×10^{-5}	0.6821
Disc-2	13.162×10^{-5}	2.8504	13.350×10^{-5}	2.8548
Disc 3	11.284×10^{-5}	0.0476	11.694×10^{-5}	0.0391

TH-2966_176103027

2.5.5 Identification of suitable AMB location

Apart from Model 1, two other models (Model 2 and Model 3), as shown in Fig. 2.20 and 2.21, respectively, are also considered to obtain the suitable position of the magnetic bearing in the rotor system for the maximum reduction of the unbalances. The equivalent unbalances (both shaft and discs) are estimated for both the models using the VTEICM, as given in Table 2.7. Then, the estimated unbalances are taken as balancing masses at the location of the disc with opposite orientation to the unbalances. The displacement amplitudes and phases are obtained for the system with and without balancing in the time domain (excluding AMB control), as shown in Fig. 2.22 for Model 2 and Fig. 2.23 for Model 3, respectively, at Disc 1 and AMB location.

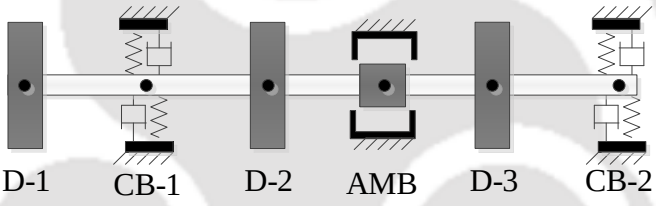


Fig. 2. 20. The flexible rotor-AMB system supported on conventional bearings (Model 2).

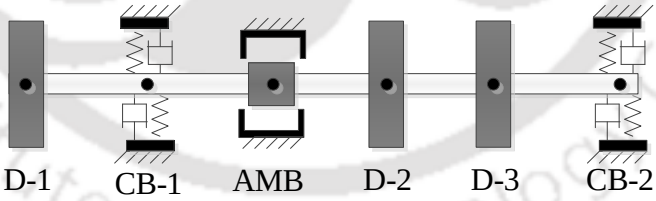


Fig. 2. 21. The flexible rotor-AMB system supported on conventional bearings (Model 3).

After balancing, the maximum percentage reduction of time domain displacement responses is obtained for all the node locations without AMB control, as shown in Fig. 2.24. Model-2 and Model-3 show a percentage reduction of 82.89% and 82.32%, respectively, which is nearer to the reduction achieved for Model-1. Also, the displacement

TH-2966_176103027

responses at the discs and AMB locations are analyzed to estimate the percentage reduction in vibrational responses of the system. The maximum amplitude of vibration at all the discs and AMB locations are compared, and the overall maximum amplitude of the system is utilized to estimate the reduction percentage in Fig. 2.24.

Table 2. 7. Comparison of the unbalance magnitudes and phases estimated using VTEICM from assumed values considering residual unbalances at both shaft and discs for all the proposed models as shown in Figs. 2.7, 2.19, and 2.20.

Disc	Model-1		Model-2		Model-3	
	Magnitude (kg-m)	Phase (rad)	Magnitude (kg-m)	Phase (rad)	Magnitude (kg-m)	Phase (rad)
Disc-1	2.236×10^{-5}	0.6821	2.429×10^{-5}	0.6776	2.713×10^{-5}	0.7202
Disc-2	13.350×10^{-5}	2.8548	1.707×10^{-5}	1.4984	2.243×10^{-5}	0.9526
Disc 3	11.694×10^{-5}	0.0391	3.928×10^{-5}	0.5564	6.103×10^{-5}	0.7614

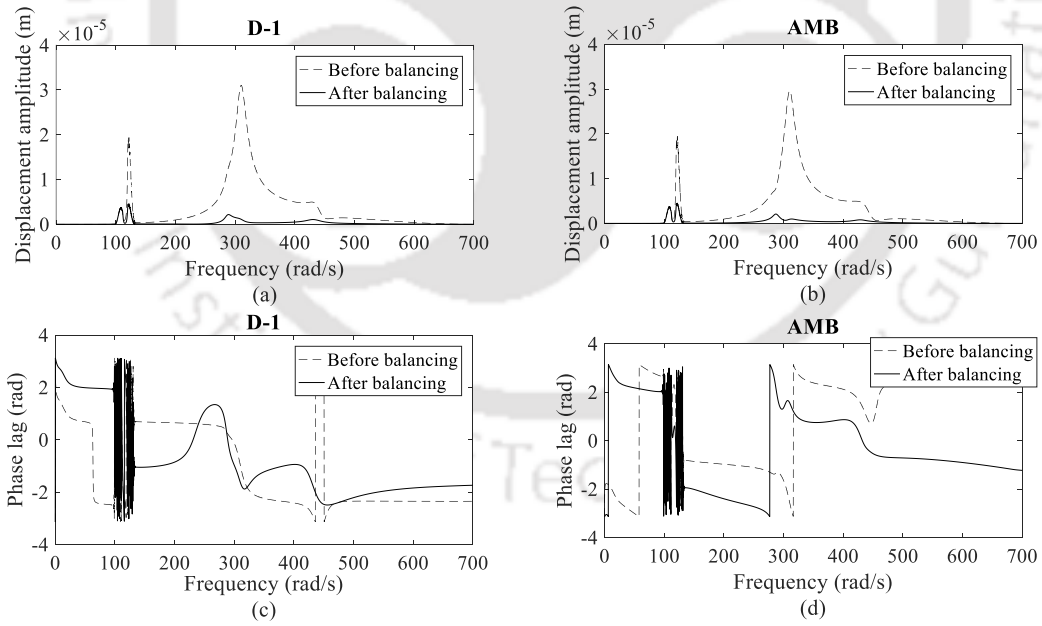


Fig. 2. 22. (a) and (b) rotor run-up frequency domain displacement amplitude vs. speed plot, (c) and (d) rotor run-up displacement phase (rad) vs. speed plot before and after balancing at Disc 1 and AMB location respectively (Model 2, excluding AMB control).

TH-2966_176103027

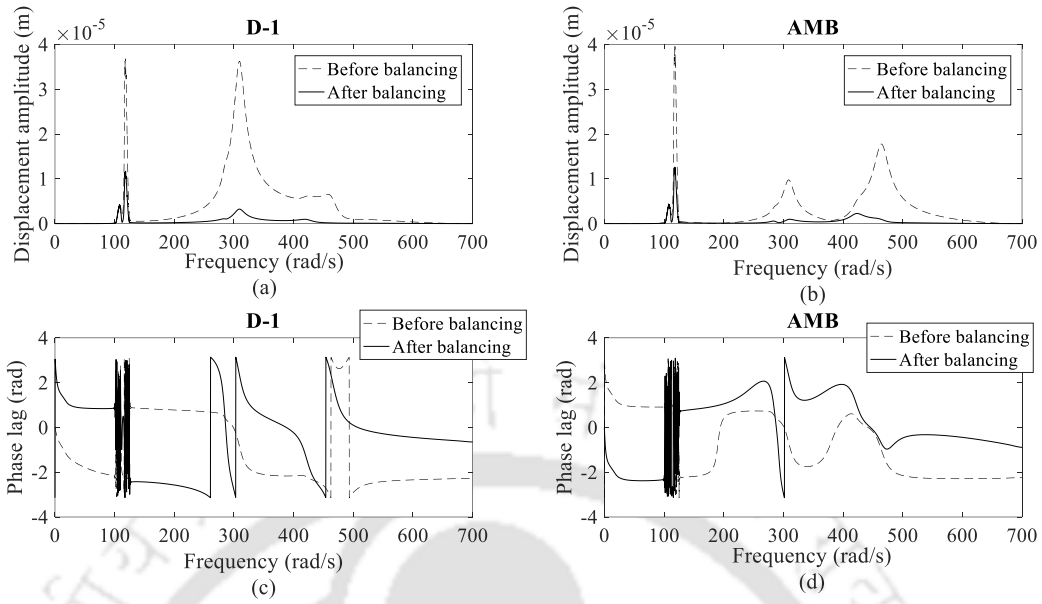


Fig. 2. 23. (a) and (b) rotor run-up frequency domain displacement amplitude vs. speed plot, (c) and (d) rotor run-up displacement phase (rad) vs. speed plot before and after balancing at Disc 1 and AMB location respectively (Model 3, excluding AMB control).

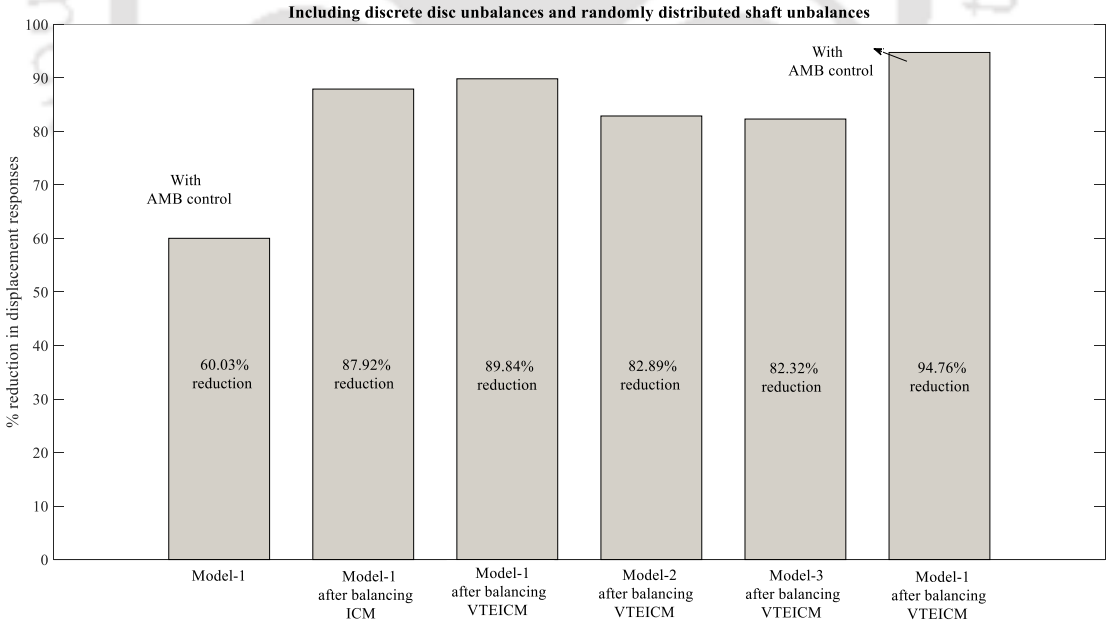
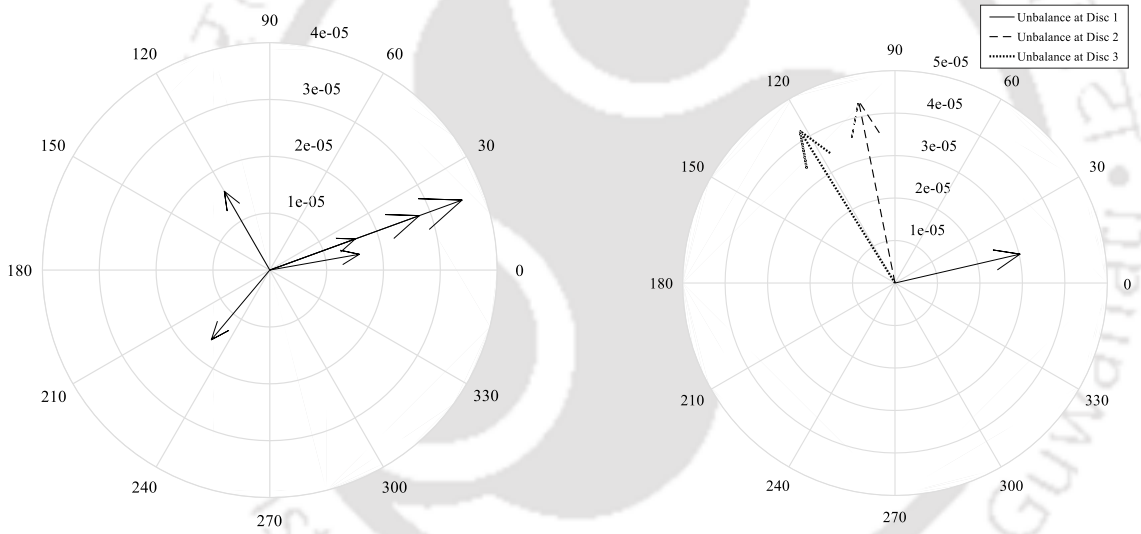


Fig. 2. 24. Percentage reduction in vibrational response of the rotor system without and with AMB control after balancing using conventional ICM and VTEICM.

TH-2966_176103027

The locations at which maximum reduction occurs may change for different models of the rotor-AMB system. Therefore, the overall reduction in maximum amplitude from different measurement locations is considered to maintain uniformity in the calculations for all the three models. So, the present balancing approach can be utilized for all the three different models considered in the present work.

Since the virtual trial unbalance is introduced as a magnetic force in the system, the equivalent unbalances are also obtained considering different amplitudes and phases from the virtual trial unbalance, as shown in Fig. 2.25.



(a) (b)

Fig. 2. 25. (a) Polar representation of magnitude and phase for different trial unbalances generated through AMB as magnetic forces (b) Polar representation of magnitude and phase for different residual unbalances at the three discs locations, obtained using trial unbalances.

It shows that there is no change in estimation with variation in values of trial unbalances. Also, 5%, 8%, and 10% random noise have been introduced in the time domain displacement responses to check the robustness of the algorithm. The percentage deviation

TH-2966_176103027

in the magnitude and phase of unbalances with the addition of noise is shown in Table 2.8. It shows that the percentage variation in the value of estimated unbalances is less than 1% for amplitude and for phase with 10% of noise. This illustrates the robustness of the proposed identification algorithm against measurement noise.

Table 2. 6. Percentage change in the value of unbalance magnitude and phase of the estimated with variation in the level of noise.

Disc	5% Noise		8% Noise		10% Noise	
	Magnitude	Phase	Magnitude	Phase	Magnitude	Phase
Disc-1	–0.07	0.03	–0.09	0.09	–0.11	0.13
Disc-2	–0.03	–0.01	–0.07	–0.01	–0.11	–0.02
Disc-3	–0.01	–0.02	–0.01	–0.09	–0.02	–0.15

2.6 Remarks

In the present chapter, a new balancing methodology has been introduced for a flexible rotor-bearing-AMB system supported on conventional bearings using an VTEICM. Along with the generation of the controlling current for suppression of vibration and for a safe traversal of the system, while crossing different critical speeds, the AMB also generates virtual trial unbalances as a magnetic force to be utilized in VTEICM. The main advantage of generating trial unbalance from AMB is that the mechanical effort and execution time for balancing is greatly reduced than the convention method, where trial unbalances have to be introduced mechanically at the balancing planes. Also, only one virtual trial unbalance is required to estimate the unbalances at the balancing planes, which is more beneficial than conventional ICM, which requires a minimum of three trial unbalances for the flexible rotor balancing. One more important advantage of this methodology is that

TH-2966_176103027

after balancing, the current consumption of the AMB in suppression of unbalance is greatly reduced, and then it can be taken care of any unexpected rise in response at higher speeds. The plots obtained show that after balancing (also excluding AMB), the displacement responses of the rotor system have been greatly reduced, which allows the rotor system to safely cross different critical speeds while being supported on the conventional bearings if AMB fails. This reduces the power consumption and computational effort utilized by the AMB for the suppression of residual unbalance forces and also avoids saturation of magnetic field at the higher speed due to large amplitude of unbalance force. Also, the robustness of the algorithm has been shown with the addition of a different level of random measurement noises in the time domain displacement signals. It has been seen from the plots the present algorithm is efficient in balancing the rotor system despite the location of AMB in the system. The present algorithm can be extended to identify the unbalances present in the rotor system for flexible rotor balancing while operating the system at low speed. This may reduce the chances of the system getting damaged while operating above critical speed without knowing the level of unbalances, which is discussed in detail in the next chapter.

TH-2966_176103027

CHAPTER 3

IN-SITU BALANCING OF FLEXIBLE ROTOR-BEARING-AMB SYSTEM USING VIRTUAL TRIAL UNBALANCES AT SLOW RUN

The present chapter deals with the formulation of the identification algorithm to estimate the residual unbalances in the rotor-AMB system for high-speed balancing while operating the system at low speeds. The mathematical model developed using FEM, as explained in the previous chapter, is modified and utilized to generate the displacement responses and verify the effectiveness of the identification algorithm. The percentage reduction in the displacement response with the balancing of the rotor system using the present methodology is shown. In this chapter, the identification algorithm is extended with the utilization of VTUs from more than one AMB location in the estimation of the residual unbalances.

3.1. Introduction

The level of unbalance is required to be estimated periodically in the rotating machinery to prevent any damage to the system while operating above critical speed. The estimation procedures for high-speed balancing require the system to be operated above critical speed with an unknown level of unbalances. Though AMB present in the system controls the level of vibration while crossing critical speed, but the increment in the level of unbalance responses may sometimes be difficult to control. Therefore, we require a new identification algorithm that would make the flexible rotor balancing to be possible at low speeds (below

TH-2966_176103027

critical speed). Since the influence coefficient of the system does not change with the severity of the unbalance forces. Therefore, in the present chapter, a new balancing method, i.e., Virtual Excitation at Low-Speed for High-Speed Balancing (VELSHSB) method for unbalance estimation is described that requires a one-time estimation of the influence coefficients at high speeds (greater than critical speeds) and periodic estimated values of the residual unbalances at low speeds to predict the balance masses utilized for flexible rotor balancing. The unbalances estimated using VELSHSB is compared with the VTEICM, where the estimation of unbalances and influence coefficients are required to be carried out simultaneously at high speeds, every time. In VELSHSB, the system is ramp-up at high-speed to obtain influence coefficients corresponding to different spin speeds at measurement planes. In the next run, the system is rotated at a spin speed lower than the first critical speed. The unbalance at the lower speed is estimated at different node locations, which are then utilized along with high-speed influence coefficients to obtain balance masses required for the high-speed balancing. Therefore, the proposed algorithm focuses on utilizing minimum information of the rotor system as well as emphasizes the reduction of quality time involved in condition monitoring of the rotor system.

3.2. Estimation of influence coefficients at high speeds (One-time estimates)

In the proposed algorithm, '*n'* number of balancing planes are assumed for positioning and prediction of the balance masses, i.e., at the location of discs as shown in Fig. 3.1. The translational displacements measurement is to be carried out at discs, 'q' number of bearings as well as 'k' number of AMB locations, i.e., at '$p = (n+k+q)$' number of

TH-2966_176103027

measurement planes along the shaft axial positions. As compared to the VTEICM, in VELSHSB, more AMB planes are introduced (Eq. (3.1)) to control the system and generate VTUs in order to show the effectiveness of the algorithm in the presence of several AMBs. Since VELSHSB aims to estimate the unbalances at low speeds for flexible rotor balancing, so to incorporate the effect of change in unbalance distribution at the limited number of balancing planes at high speed, the influence coefficients are estimated at a greater number of measurement planes than that utilized in conventional ICM (Eq. (2.1)) or VTEICM (Eq. (2.9)). The influence coefficients are related to the displacement and unbalance forces at the corresponding measurement locations as

$$\mathbf{r}(\omega)_{(p\times 1)} = \boldsymbol{\gamma}(\omega)_{(p\times p)}\,\mathbf{f}_{u(p\times 1)} \tag{3.1}$$

with, $\mathbf{r} = \left\{ r_{d,1} \quad \cdots \quad r_{d,n} \quad r_{m,1} \quad \cdots \quad r_{m,k} \quad r_{b,1} \quad \cdots \quad r_{b,q} \right\}^T$;

$\mathbf{f}_u = \left\{ f_{u,1} \quad f_{u,2} \quad f_{u,3} \quad \cdots \quad f_{u,p} \right\}^T$; $\quad f_{u,p} = m_{d,p} e_{d,p} \mathrm{e}^{\,\mathrm{j}\phi_{d,p}}$

$$\boldsymbol{\gamma}(\omega) = \left[\boldsymbol{\gamma}_1(\omega) \quad \boldsymbol{\gamma}_2(\omega) \quad \cdots \quad \boldsymbol{\gamma}_p(\omega) \right] \tag{3.2}$$

where, ($r_{d,1}$, $r_{d,2}$, ..., $r_{d,n}$); ($r_{m,1}$, $r_{m,2}$, ..., $r_{m,k}$); ($r_{b,1}$, $r_{b,2}$, ..., $r_{b,q}$) are displacements obtained at balancing planes, and the AMB and support bearing locations, respectively. $f_{u,1}$, $f_{u,2}$, ..., $f_{u,p}$ are residual unbalances present in the shaft as well as discs. $\boldsymbol{\gamma}_1$, $\boldsymbol{\gamma}_2$, …, $\boldsymbol{\gamma}_p$ are column vectors of influence coefficients corresponding to different node locations. The subscript '*T*' represents the transpose of the matrix or vector. To obtain influence coefficients, a virtual trial unbalance as a magnetic force (f_T) is introduced at the k^{th} AMB location, as shown in Fig. 3.2.

TH-2966_176103027

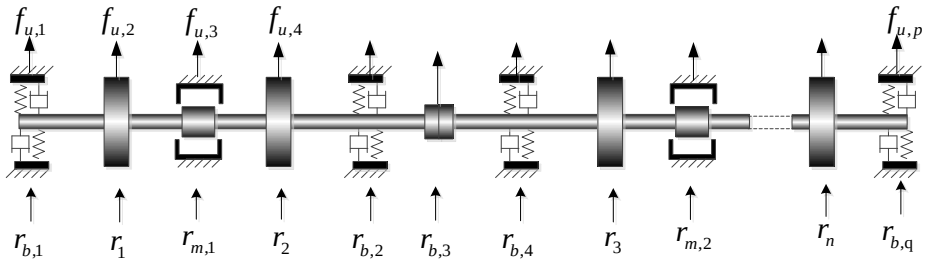


Fig. 3. 1. The rotor-AMB model with unbalance forces ($f_{u,1}$ to $f_{u,p}$) at different node locations.

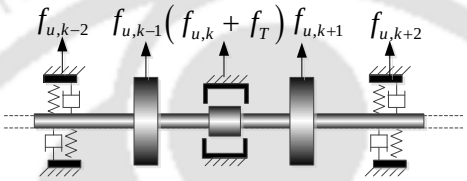


Fig. 3. 2. The rotor-AMB model with unbalance forces and virtual trial unbalances (f_T).

This excitation force is generated along with the controlling force to obtain a change in displacement at different node locations as given in Eqs. (2.16) and (2.17). With the addition of the trial magnetic force at the k^{th} AMB location, the displacement at the respective measurement planes changes and is given as

$$\mathbf{r}'(\omega)_{(p\times 1)} = \boldsymbol{\gamma}(\omega)_{(p\times p)}\,\mathbf{f}'_{u(p\times 1)} \tag{3.3}$$

with, $\mathbf{f}'_u = \left\{ f_{u,1} \quad f_{u,2} \quad \cdots \quad f_{u,k}+f_T \quad \cdots \quad f_{u,p} \right\}^T$

On subtracting, Eq. (3.1) from Eq. (3.3), influence coefficients are obtained as

$$\mathbf{r}'(\omega) - \mathbf{r}(\omega) = \boldsymbol{\gamma}(\omega)\mathbf{f}_r \tag{3.4}$$

with, $\mathbf{f}_r = \{0 \quad 0 \quad \cdots \quad f_T \quad \cdots \quad 0\}^T$

TH-2966_176103027

$$\boldsymbol{\gamma}_k(\omega) = \left(\mathbf{r}'(\omega) - \mathbf{r}(\omega)\right) / f_T \tag{3.5}$$

with, $\boldsymbol{\gamma}_k(\omega) = \left\{\gamma_{1,k}(\omega) \quad \gamma_{2,k}(\omega) \quad \gamma_{3,k}(\omega) \quad \cdots \quad \gamma_{p,k}(\omega)\right\}^T$

The obtained influence coefficient vector, $\boldsymbol{\gamma}_k$ at different measurement planes corresponding to a unit force at the AMB location, is considered for the estimation of residual unbalances. From Eq.(3.1), the column matrix $\boldsymbol{\gamma}_k$ is equivalent to the row matrix of influence coefficient corresponding to the AMB location for the unit force at different nodes. Influence coefficients are related to the AMB displacement and unbalance forces, as

$$r_{m,k}(\omega) = \boldsymbol{\gamma}_s(\omega)\mathbf{f}_u \tag{3.6}$$

with, $\boldsymbol{\gamma}_s(\omega) = \left\{\gamma_{k,1}(\omega) \quad \gamma_{k,2}(\omega) \quad \gamma_{k,3}(\omega) \quad \cdots \quad \gamma_{k,p}(\omega)\right\}$

Similarly, the AMB displacements at different locations are related to influence coefficients as

$$\mathbf{r}_m(\omega) = \boldsymbol{\gamma}_r(\omega)\mathbf{f}_u \tag{3.7}$$

with, $\mathbf{r}_m(\omega) = \left\{r_{m,1}(\omega) \quad r_{m,2}(\omega) \quad \cdots \quad r_{m,k}(\omega)\right\}^T$

The detailed description of the $\boldsymbol{\gamma}_r$ matrix is given by Eq. A.2 in Appendix A. Now, influence coefficients mentioned in Eq. (3.7) are obtained for different spin speeds during run-up of the system surpassing its critical speeds and is given as

$$\mathbf{Z}_h = \left[\boldsymbol{\gamma}_r(\omega_1) \quad \boldsymbol{\gamma}_r(\omega_2) \quad \cdots \quad \boldsymbol{\gamma}_r(\omega_h)\right]^T \tag{3.8}$$

TH-2966_176103027

where, $\mathbf{Z}_h$ is the high-speed influence coefficient matrix, and $\boldsymbol{\gamma}_r$ (ω_h) is the influence coefficient matrix for the h^{th} spin speed of the rotor system since it is speed-dependent.

3.3. Formulation of Virtual Excitation at Low-Speed for High-Speed Balancing (VELSHSB) method

The residual unbalances in the rotor system are considered as randomly distributed shaft unbalances and discrete disc unbalances, and their equivalence is estimated at the limited number of balancing planes. The contribution of residual shaft unbalances is different at balancing planes for spin speeds below and above critical speeds due to the formation of mode shapes and the increasing magnitude of effective shaft unbalances. As a result of this, the complete balancing of the flexible rotor systems is difficult to achieve. However, the estimation of balance masses using the VTEICM over a specified range of spin speeds provides an acceptable level of balancing. Also, it is difficult to rotate the rotor system above its critical speeds after every overhaul to estimate the balance masses periodically without knowing the level of residual unbalances. So, VELSHSB is introduced that utilizes residual unbalances obtained at different measurement locations at low spin speeds and the high-speed influence coefficients to estimate the balance masses for the high-speed balancing. In VELSHSB, at first, the residual unbalances are obtained at different measurement planes while operating the rotor system at a slow speed. Then using the low speed and the influence coefficients obtained at high speeds, the resultant unbalances are obtained at the limited number of the balancing planes.

TH-2966_176103027

Residual unbalances at different measurement locations are identified using Eqs. (3.1) through (3.8) at spin speeds lower than the first critical speed. Influence coefficients are related to residual unbalances at different measurement locations and displacements as

$$\mathbf{r}_l = \mathbf{Z}_l \mathbf{f}_u \tag{3.9}$$

with, $\mathbf{r}_l = \left\{ \mathbf{r}_m(\omega_1) \quad \mathbf{r}_m(\omega_2) \quad \cdots \quad \mathbf{r}_m(\omega_l) \right\}^T$; $\mathbf{Z}_l = \left[\boldsymbol{\gamma}_r(\omega_1) \quad \boldsymbol{\gamma}_r(\omega_2) \quad \cdots \quad \boldsymbol{\gamma}_r(\omega_l) \right]^T$

Eq. (3.9) gives

$$\mathbf{f}_u = \left(\mathbf{Z}_l^T \mathbf{Z}_l \right)^{-1} \mathbf{Z}_l^T \mathbf{r}_l \tag{3.10}$$

where, $\mathbf{Z}_l$ is the low-speed influence coefficient matrix, and $\boldsymbol{\gamma}_r$ (ω_l) is the influence coefficient matrix for l^{th} spin speed of the rotor system. The residual unbalance obtained from Eq. (3.10) is utilized with the high-speed influence coefficient, obtained using Eq. (3.8), to estimate displacement responses at AMB locations for higher spin speeds, as

$$\mathbf{r}_b = \mathbf{Z}_h \mathbf{f}_u \tag{3.11}$$

with, $\mathbf{r}_b = \left\{ \mathbf{r}_m(\omega_1) \quad \mathbf{r}_m(\omega_2) \quad \cdots \quad \mathbf{r}_m(\omega_h) \right\}^T$

On substituting Eq. (3.10) into Eq. (3.11), we get

$$\mathbf{r}_b = \mathbf{Z}_h \left(\mathbf{Z}_l^T \mathbf{Z}_l \right)^{-1} \mathbf{Z}_l^T \mathbf{r}_l \tag{3.12}$$

Now, obtained displacement responses are utilized with influence coefficients at high-speed speeds corresponding to balancing planes to estimate the unbalances, as

$$\mathbf{r}_b = \mathbf{Z}_b \mathbf{f}_n \tag{3.13}$$

TH-2966_176103027

with, $\mathbf{Z}_b = \left[\boldsymbol{\gamma}_b(\omega_1) \quad \boldsymbol{\gamma}_b(\omega_2) \quad \cdots \quad \boldsymbol{\gamma}_b(\omega_h)\right]^T$;

$$\boldsymbol{\gamma}_b(\omega)_{(k\times n)} = \left[\boldsymbol{\gamma}_{b,1}(\omega) \quad \boldsymbol{\gamma}_{b,2}(\omega) \quad \boldsymbol{\gamma}_{b,3}(\omega) \quad \cdots \quad \boldsymbol{\gamma}_{b,n}(\omega)\right]$$

where, $\boldsymbol{\gamma}_{b,n}$ is the influence coefficient vector corresponding to AMB locations for a unit load at n^{th} balancing plane as given by Eq. A.2 in Appendix A. $\mathbf{f}_n$ vector is the resultant residual unbalances at different balancing planes. Eq. (3.13) gives

$$\mathbf{f}_n = \left(\mathbf{Z}_b{}^T\mathbf{Z}_b\right)^{-1}\mathbf{Z}_b{}^T\mathbf{r}_b \tag{3.14}$$

Substituting Eq. (3.12) in Eq.(3.14), the residual unbalances are obtained as

$$\mathbf{f}_n = \left(\mathbf{Z}_b{}^T\mathbf{Z}_b\right)^{-1}\mathbf{Z}_b{}^T\mathbf{Z}_h\left(\mathbf{Z}_l{}^T\mathbf{Z}_l\right)^{-1}\mathbf{Z}_l{}^T\mathbf{r}_l \tag{3.15}$$

The estimated residual unbalances at balancing planes are to be applied at opposite orientations as balancing masses to observe the level of reduction in unbalance responses.

3.4. Numerical simulations of the proposed balancing method

For the purpose of simulations, a FEM model of the flexible rotor-AMB system is developed in MATLAB-SIMULINK interface that consists of three rigid discs mounted on a flexible shaft and is supported by two conventional bearings, as shown in Fig. 3.3. The system is divided into five elements with two translational and two rotational DoFs at each node location. Disc locations are considered as balancing planes, whereas measurement planes are considered at the node locations shown in Fig. 3.3. AMBs are also incorporated in the system to reduce the vibrational response as well as to generate virtual trial unbalances required to estimate the balance masses.

TH-2966_176103027

Table 3. 1. Physical parameters of the rotor-AMB system

Parameters	Values
Total flexible shaft's length, l	615 mm
Elements' length, l_s	48, 48, 139, 82, 83 and 215 mm
Shaft's diameter, d	10 mm
Shaft's density, ρ	7850 kg/m^3
Young's modulus of elasticity, E	2.06×10^{11} N/m^2
Rigid discs' (D-1, D-2, and D-3) and AMB core's mass	0.78, 1.2, 1.2 and 0.88 kg
Diametral moment of inertia of discs and core	$(4.44, 13.09, 13.09, 5.17)\times10^{-4}$ kg-m^2
Polar moment of inertia of discs and core	$(8.30, 27.39, 27.39, 3.98)\times10^{-4}$ kg-m^2
Numbers of random unbalances in each element of shaft	5, 5, 20, 20, 30 and 20
Magnitude of unbalances at discs (D-1, D-2, and D-3)	$(2.34, 7.2, \text{and } 3.6)\times10^{-5}$ kg-m
Phase of unbalances at discs (D-1, D-2, and D-3)	5.73°, 68.75°, and 120.32°
Support bearing stiffness (CB-1 and CB-2)	4.5×10^5 and 5×10^5 N/m
Support bearing damping coefficient (CB-1 and CB-2)	210, 200 N-s/m
AMB-1 and AMB-2, current stiffness factor, k_i	42.1, 43 N/A
AMB-1 and AMB-2, displacement stiffness factor, k_x	105210, 107210 N/m

A PID controller is introduced in the rotor-AMB system, with tuned controller gains as k_P = 4200 A/m, k_D= 1 A-s/m and k_I = 2000 A/m-s (Tiwari and Chougale, 2014). Residual unbalances are assumed both at discs (D-1, D-2, and D-3) as well as in the shaft, as shown in Fig. 3.4. The physical properties of components of the rotor system are mentioned in Table 3.1. The system of equations is solved using SIMULINK model as shown in Fig. 3.5 utilizing the Runge-Kutta solver with a time step of $1/2^{14}$. Critical speeds of the rotor system are determined by estimating eigenvalues for the free vibration case with the AMB control. A Campbell diagram shown in Fig. 3.6 displays critical speeds of the system, i.e.,

TH-2966_176103027

186, 308, and 540 rad/s for the forward whirl and 179, 288, and 468 rad/s for the backward whirl condition. Critical speeds of the system without AMB control are obtained as 105, 268, and 537 rad/s for the forward whirl and 101, 251, and 464 rad/s for the backward whirl. In order to check the vibration reduction achieved through the AMB control, the system is accelerated from a spin speed of 5 rad/s to 700 rad/s with an angular acceleration of 23.17 rad/s^2. Shaft displacements are obtained at different measurement locations based on Eq. (2.38) with and without consideration of AMB in the system.

In Fig. 3.7 (a), (b), (c), and (d), the time-domain response of the system along the *x*-axis at discs and AMB-2 locations is plotted without and with AMB control. It is clearly seen that the AMBs successfully reduce the vibration that will allow the safe traversal of the rotor system to surpass its critical speeds.

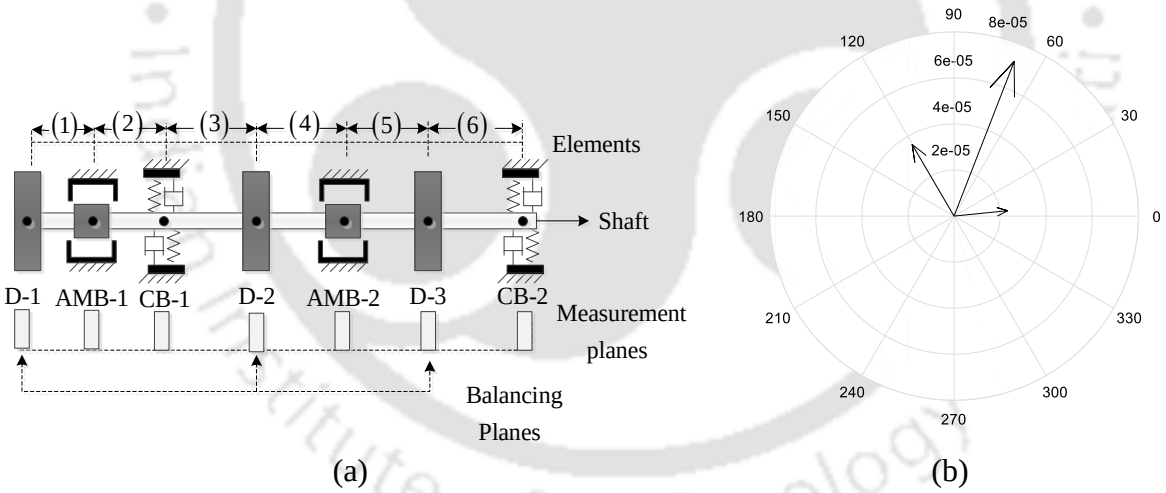


Fig. 3. 3 (a) An illustrative representation of the rotor-AMB model supported on two conventional bearings with three balancing planes as rigid discs and (b) A pictorial representation of disc unbalances on the *x*-*y* plane, the orientation and magnitude of the unbalance is shown in degree and kg-m.

TH-2966_176103027

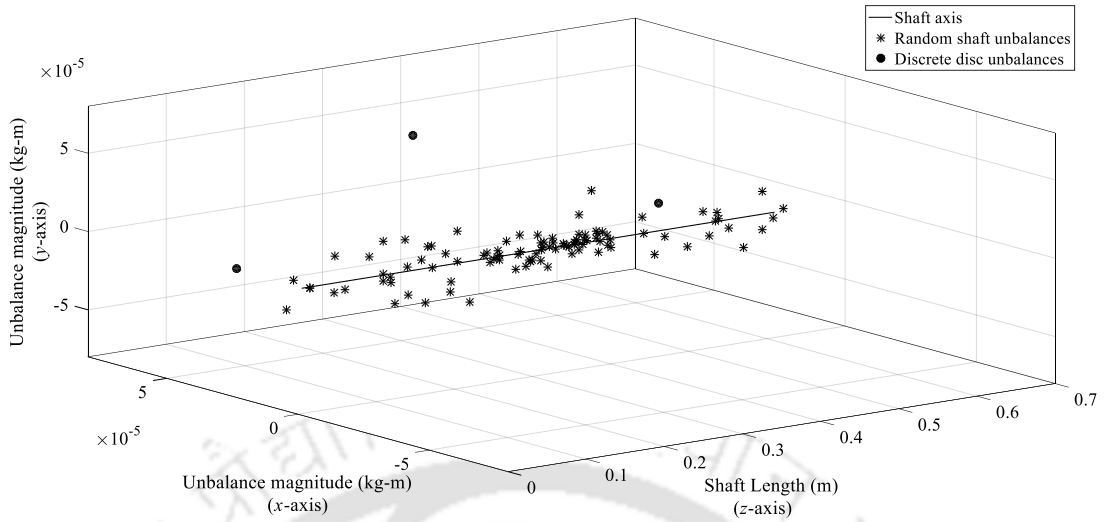


Fig. 3. 4. The magnitude of random shaft unbalances (‘*’) and discrete disc unbalances (‘•’) in kg-m is represented at different orientations in *x*-*y* plane along the *z*-axis.

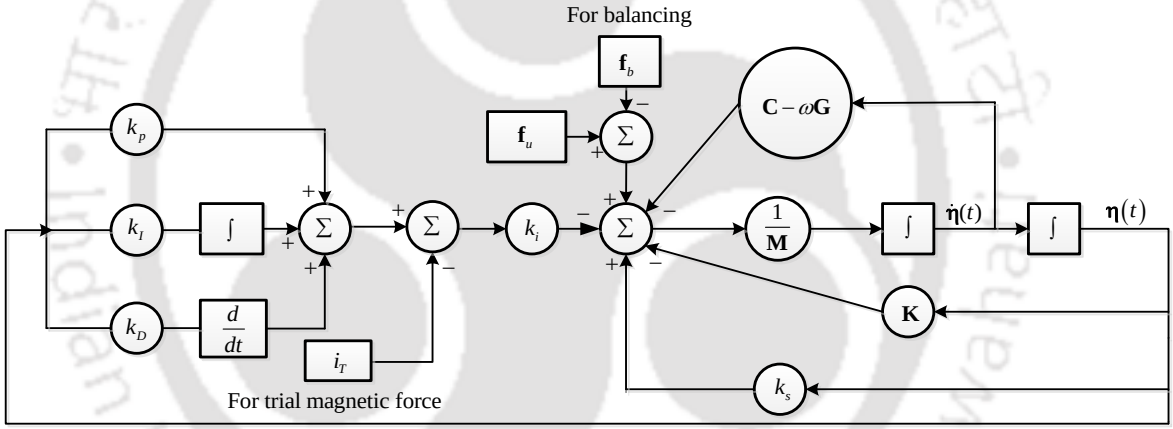


Fig. 3. 5. A pictorial representation of the SIMULINK model developed to solve the differential equation in MATLAB platform using Runge-Kutta solver.

Now, the Fast Fourier Transformation (FFT) of the time domain signal is carried out to obtain the half-spectrum displacement amplitudes corresponding to different spin speeds during the runup of the rotor as shown in Fig. 3.8. The phase of the frequency domain signal is compensated with respect to the phase of a reference signal.

TH-2966_176103027

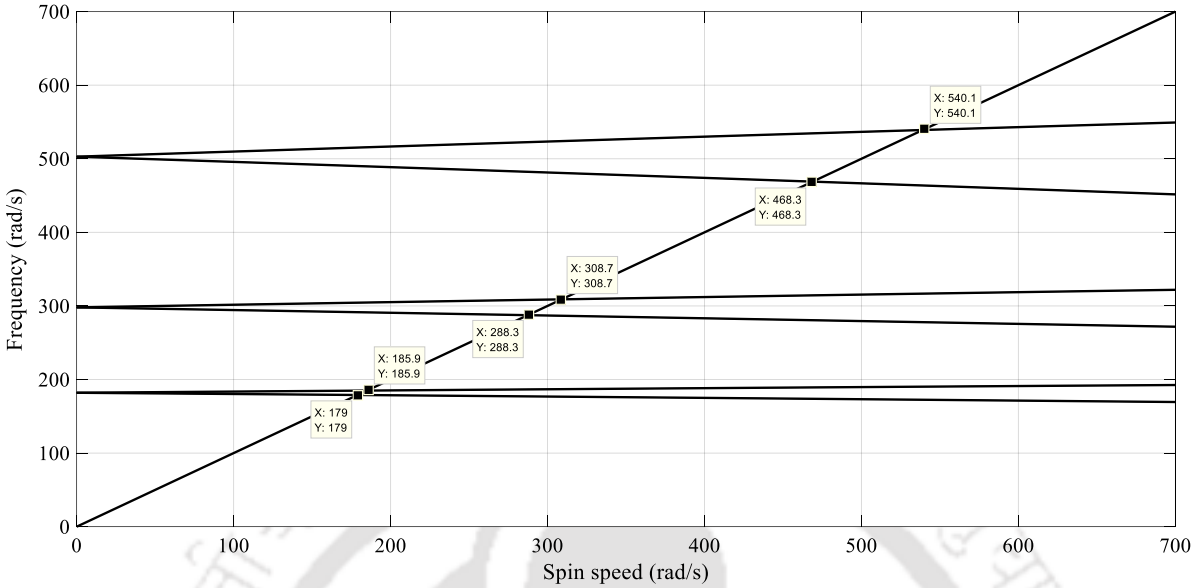


Fig. 3. 6. The Campbell diagram of the rotor system under AMB control for a spin speed of 0-700 rad/s displaying both forward and backward whirls.

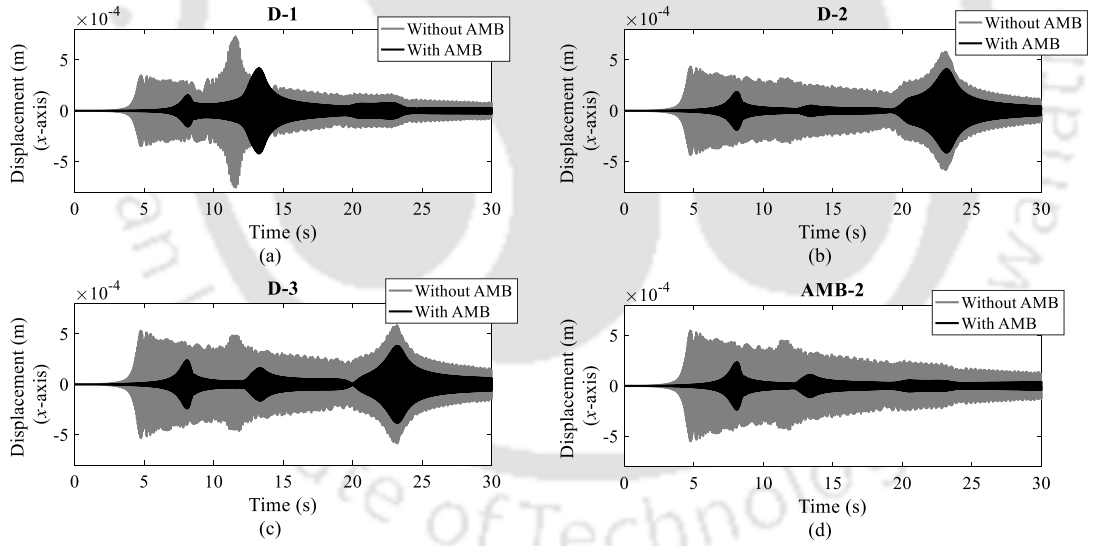


Fig. 3. 7. Shaft translational displacement (in meters) along *x*-axis vs. time (in seconds) plot at (a) disc D-1, (b) disc D-2, (c) disc D-3 (d) AMB-2 locations without and with AMB control as represented by grey and black lines (same line width) respectively; reduction in amplitude is achieved with AMB control; ramp-up speed 5-700 rad/s.

TH-2966_176103027

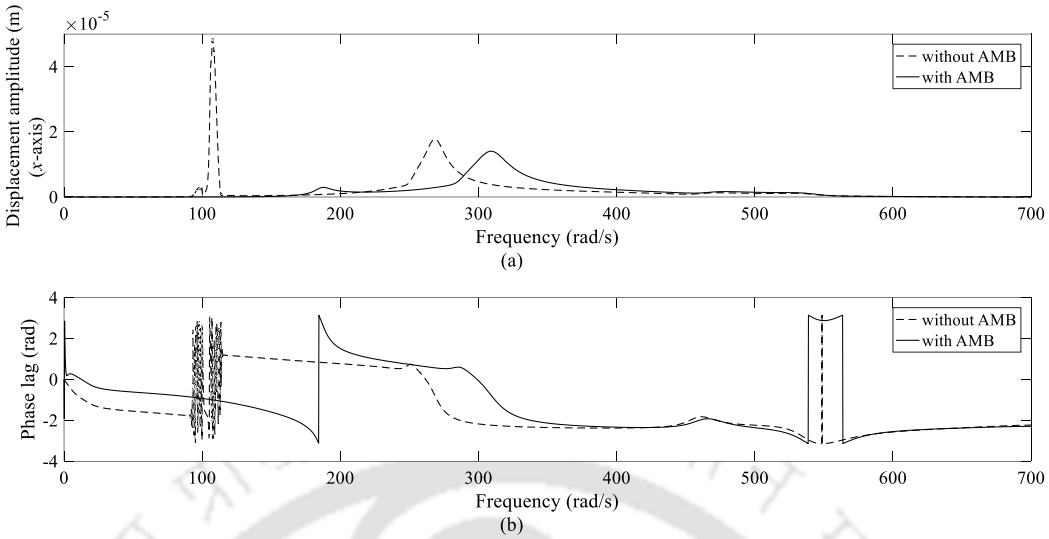


Fig. 3. 8. (a) Shaft translational displacement amplitude along *x*-axis vs. frequency plot and (b) phase vs frequency plot at the disc (D-1) location with and without AMB control as represented by solid and dotted lines; amplitude reduction is achieved throughout the ramp-up speed.

The plot between displacement amplitude at different frequencies (1X harmonic) is shown in Fig. 3.8 (a) and Fig. 3.8 (b) shows the corresponding phase at different frequencies, with and without AMB control. With AMB control, the maximum time domain displacement of the system at all node locations gets reduced by 44 %.

3.4.1. Evaluation of the mode shapes

The application of AMBs in the rotor system affects the normal modes of the system at different natural frequencies. Due to change in mode shapes, the balance masses estimated for the flexible rotor balancing with the AMB control may not be effective if utilized in the system without AMB control. So, in order to check the effectiveness of the present work in balancing the rotor system, the mode shapes are obtained at the first three natural frequencies. The eigenvectors (V) corresponding to the present system with and without AMB control are estimated for two different configurations (spin speed, $\omega = 0$ rad/s) as

TH-2966_176103027

shown in Fig. 3.9. For the case of AMB, the AMB stiffness value, i.e., $k_i k_P$-k_x, is added to the shaft and bearing stiffness at the respective AMB locations. In Fig 3.9 (a), for configuration-1, the AMB-2 is positioned in between two discs D-2 and D-3, near to the mid-span of the rotor system. In Fig 3.9 (b), for configuration-2, the AMB-2 is positioned in between disc D-3 and support bearing CB-2. The normalized eigenvectors 'V^*' are estimated with respect to the maximum value of the eigenvector (V_{max}) to obtain the mode shape in the range −1 to 1. The mode shapes obtained for configuration-1 with and without AMB control are plotted in Fig. 3.10, corresponding to the different node locations along the *z*-axis. Similarly, for configuration-2, the obtained mode shapes are shown in Fig. 3.11, with and without AMB control corresponding to the first three natural frequencies. As it is seen in both Figs. 3.10 and 3.11, the addition of AMBs in the system does not cause much variation in the mode shapes. However, the variation is slightly greater in the case of configuration-2, where AMB-2 is located near the bearing support.

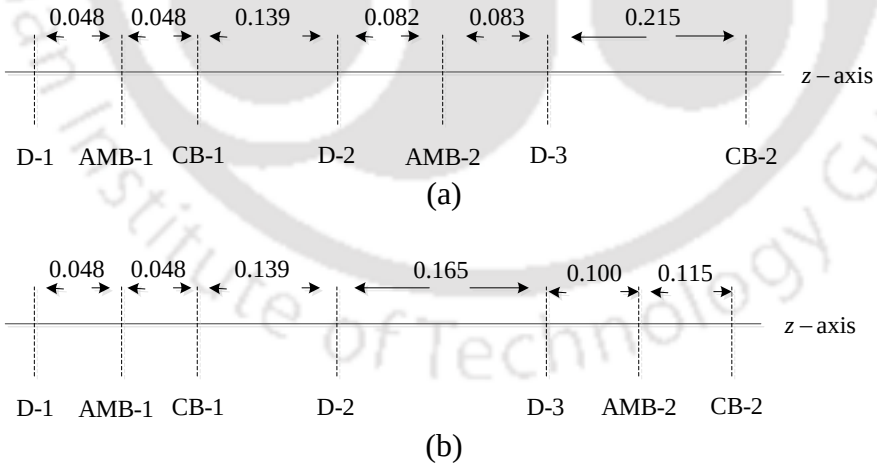


Fig. 3. 9. (a) Configuration-1 and (b) configuration-2 with distance between the rotor-AMB components in meters along *z*-axis.

TH-2966_176103027

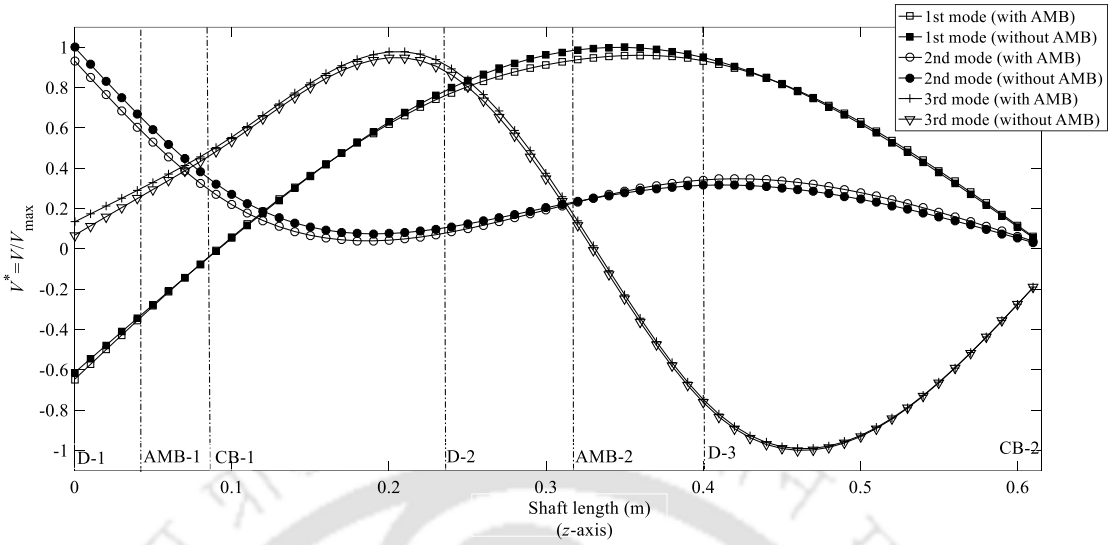


Fig. 3. 10. Mode shapes corresponding to the first three natural frequencies with and without consideration of AMBs in the system for configuration-1; symbols □, ○, and + represent 1st 2nd and 3rd bending modes with AMB control and symbols ■, ●, and ▽ represents respective mode shapes without AMB control.

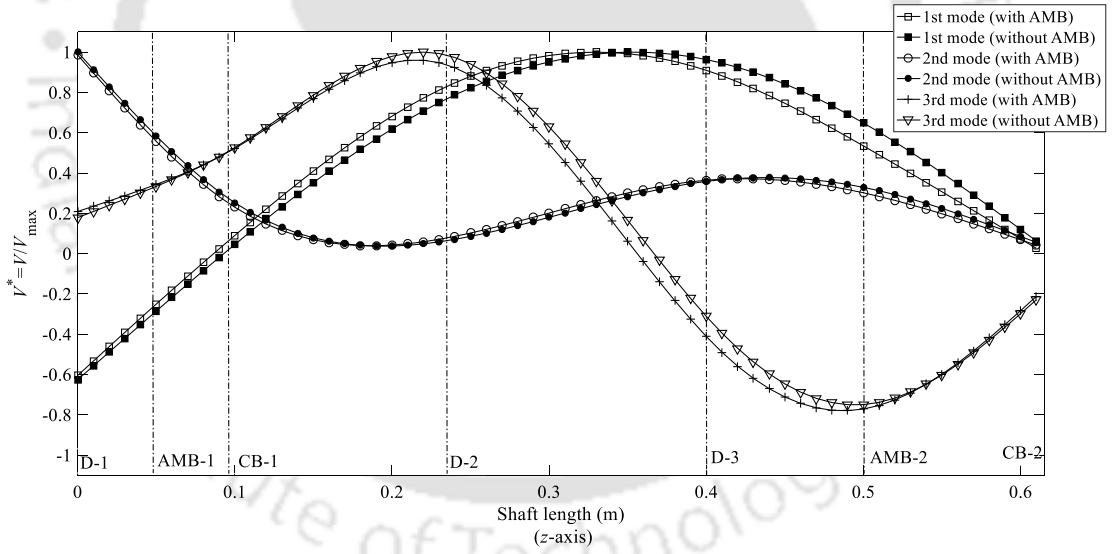


Fig. 3. 11. Mode shapes corresponding to the first three natural frequencies with and without consideration of AMBs in the system for configuration-2; symbols □, ○, and + represent 1st 2nd and 3rd bending modes with AMB control and symbols ■, ●, and ▽ represents respective mode shapes without AMB control.

TH-2966_176103027

So, the estimated balance masses in the present work using AMB control in the system can provide effective balancing of the system even if the AMBs are not in working condition.

3.4.2. Working of Virtual Excitation at Low-Speed for High-Speed Balancing (VELSHSB) method

The flexible rotor balancing is performed using both VTEICM and VELSHSB to show the effectiveness of the latter identification algorithm in balancing of flexible rotor system while operating at low speeds. Also, the latter method is more useful and focused as it requires the system to run-up above critical speeds only once, and the high-speed balancing of the system can be performed periodically by estimating the unbalances at different measurement locations at slow spin speeds whenever there is the maintenance of the rotor system. The comparison of both the identification algorithms developed to estimate balance masses at the balancing planes is shown in Fig. 3.12. The minimum number of runs are required to solve the equation as mentioned in Eq. 3.15. The solutions of the equations are checked to converge for given sets of amplitude and phases of displacement responses corresponding to different frequencies. Better estimation can be obtained by taking responses corresponding to a greater number of speeds. The VELSHSB utilizes the unbalances obtained at slow speeds and one-time estimates of high-speed influence coefficients similar to that obtained using VTEICM to repetitively estimate the balance masses for high-speed balancing as described in sub-sections 3.2 and 3.3. The virtual trial unbalance is required to be introduced to determine the residual unbalances in the system. So, the estimation of force current factor (k_i) is carried out that is required to generate the trial magnetic force by using Eq. (2.15). A constant load of 5 N is added at the AMB-1 location along the *x*-axis.

TH-2966_176103027

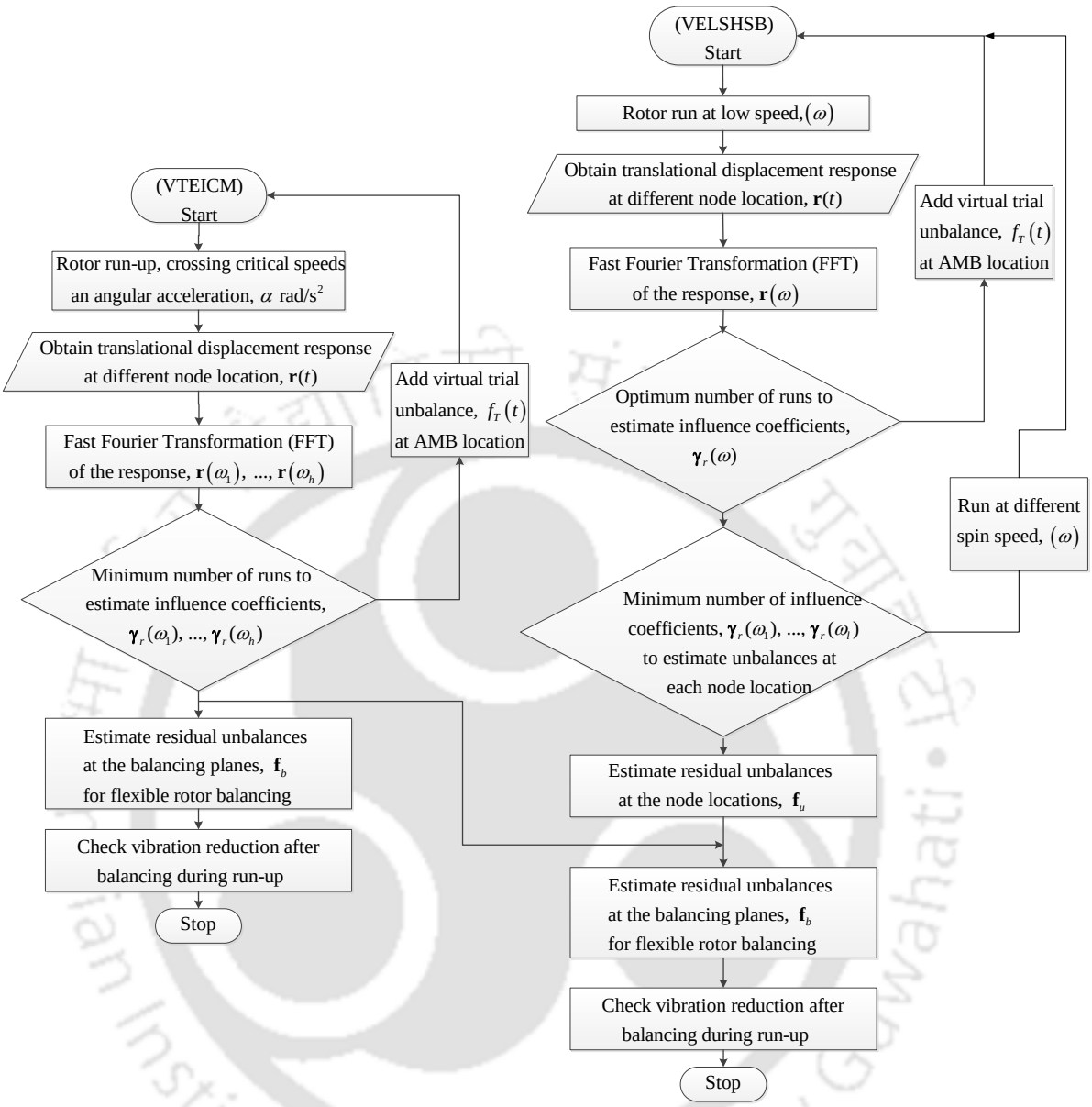


Fig. 3. 12. The comparative flow chart of the identification algorithms namely VTEICM and VELSHSB.

The constant control current obtained is equivalent to 0.1188 A, as shown in Fig 3.13 (a), which brings the shaft back to equilibrium position as shown in Fig. 3.13 (b). The value of k_i obtained is equal to 42.09 N/A, which has an error percentage of -0.024% from the assumed value. Similarly, for a constant load of 5 N at AMB-2, the current and displacement plots are shown in Fig. 3.13 (c) and (d), respectively. The value of k_i obtained

TH-2966_176103027

is equal to 43.07 N/A with an error percentage of 0.15%. The description of the two aforementioned methods utilized in the estimation of unbalances in the present rotor system is given in the following subsections.

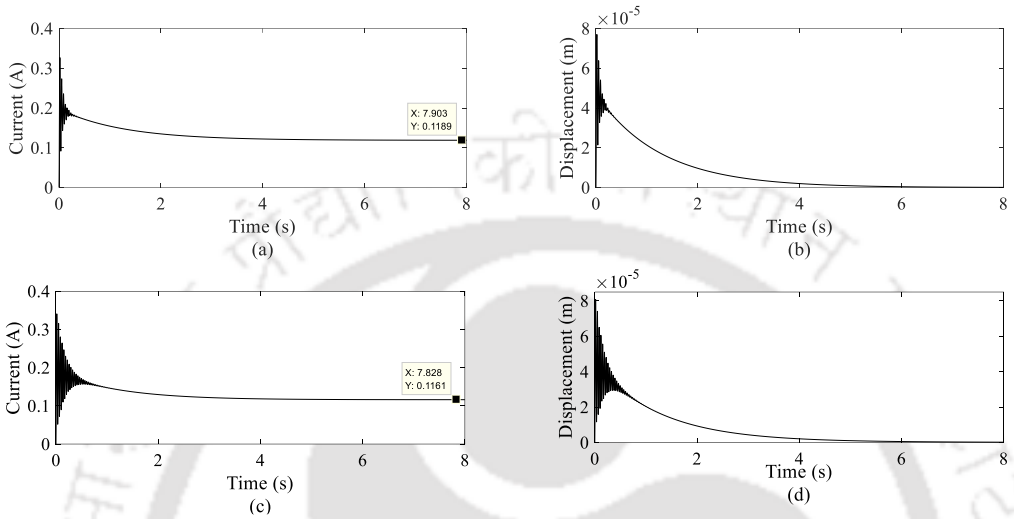


Fig. 3. 13. (a) Current (in Amperes) vs. time plot; the current increases and stabilizes after 6 seconds (b) Shaft's displacement (in meters) vs. time plot at the AMB-1 location; displacement diminishes after 6 seconds equilibrium location achieved and (c) Current vs. time plot, (d) Shaft's displacement vs. time plot at the AMB-2 location.

3.4.2.1. Unbalance estimation using VTEICM with multiple AMB

The system is accelerated to cross its critical speeds, i.e., from 5 to 700 rad/s, with the AMB control and displacement responses are obtained. A virtual trial unbalance as a magnetic force at the AMB-1 location is introduced with amplitude and phase equivalent to 1.6×10^{-5} kg-m and 20°, respectively. The system is again accelerated with an added trial unbalance to obtain the displacement response of the system at different node locations. The FFT of time-domain responses is carried out with respect to a reference signal for both rotor runs. Now, using Eq. (3.1)-(3.8) high-speed influence coefficients are estimated. The same process is repeated with virtual trial unbalance at the AMB-2 location. The

TH-2966_176103027

unbalances are estimated at balancing planes as per the algorithm shown in Fig. 3.12. The comparison of assumed and the estimated values are shown in Table 3.2.

3.4.2.2. Unbalance estimation using VELSHSB

The system is rotated at a spin speed lower than the first critical speed, i.e., at 80 rad/s, displacement responses are obtained at each measurement location. Now, the virtual trial unbalance is added at the AMB-1 location, and displacement responses are obtained again. The same process is repeated for a spin speed of 80-110 rad/s with a step of 5 rad/s. The FFT of the time domain responses are carried out, and low-speed influence coefficients are estimated using Eqs. (3.1) through (3.8).

The same process is repeated with virtual trial unbalance at AMB-2 location. The unbalances estimated at low speeds at each of the node locations using Eqs. (3.9) through (3.10). Now, the residual unbalances for high-speed balancing are obtained by utilizing the obtained unbalances at low speeds and high-speed influence coefficients as mentioned in Eqs. (3.11) through (3.15). The comparison of assumed and the estimated values of unbalances obtained using VELSHSB are shown in Table 3.2.

3.4.3. Verification of the identification algorithm

To verify the correctness of the algorithm, a comparison between the assumed and estimated values of discrete disc unbalances are shown in Table 3.2. As the unbalances present in the system may change after a certain period of time due to the addition of foreign particles or assembly defects, three sets of disc unbalances are considered. In the case of VTEICM, for every set of unbalances, high-speed influence coefficients are obtained operating the system above critical speed. Whereas, in the VELSHSB, for the 2nd and 3rd sets of the unbalances, the high-speed influence coefficients are not estimated

TH-2966_176103027

again. The residual unbalances are only estimated again at low speeds at chosen node locations, and high-speed influence coefficients of the 1st set are utilized to estimate the unbalances at balancing planes. As it can be seen from the table, both methods provide accurate results with a percentage of variations of less than 0.2 % in both magnitude and phases. However, the VELSHSB is more effective as it requires a one-time estimation of influence coefficients at high speeds. This reduces the probability of the rotor system getting damaged at high speeds after a maintenance schedule.

3.4.4. Unbalance estimation considering both discs and shaft unbalances

Now, the randomly distributed shaft unbalances are also included in the rotor system, as shown in Fig. 3.4. In the 1st set of unbalances, the disc unbalances are assumed, as mentioned in Table 3.1. For the 2nd, 3rd, and 4th sets, distributed shaft unbalances are increased in the system by 5%, 8%, and 10%, while disc unbalances remain the same as in the 1st set. As mentioned earlier, in the VELSHSB, the influence coefficient obtained at high speeds in 1st set is utilized in the estimation of unbalances for all the sets. The estimated unbalances for flexible rotor balancing are shown in Table 3.3. It is clearly visible that the VELSHSB estimates the unbalances effectively for different sets of both discs and shaft unbalances. To check the robustness of the VELSHSB, 5%, 8%, or 10% of random noise is added to the displacement amplitude of the rotor system for the 1st set of unbalances. The percentage variation in estimated unbalances in comparison to that obtained using VTEICM with 0% noise is shown in Table 3.4. With the introduction of shaft unbalances, the unbalances estimated at balancing planes changes for operating speeds below and above critical speeds.

TH-2966_176103027

Table 3. 2. Estimated disc unbalances at balancing planes using the VTEICM and VELSHSB methods.

		Assumed		VTEICM		VELSHSB	
Set	Discs	Magnitude (kg-m)	Phase (rad)	Magnitude (kg-m)	Phase (rad)	Amplitude (kg-m)	Phase (rad)
1	D-1	2.340×10^{-5}	0.1000	2.339×10^{-5}	0.0998	2.340×10^{-5}	0.1000
	% error			–0.04	0.20	0	0
	D-2	7.200×10^{-5}	1.2000	7.198×10^{-5}	1.2001	7.198×10^{-5}	1.2000
	% error			–0.03	0.08	–0.03	0
	D-3	3.600×10^{-5}	2.1000	3.600×10^{-5}	2.1000	3.600×10^{-5}	2.0999
	% error			0	0	0	0.01
2	D-1	4.680×10^{-5}	0.7000	4.680×10^{-5}	0.6996	4.680×10^{-5}	0.7000
	% error			0	–0.05	0	0
	D-2	1.080×10^{-4}	2.1000	1.080×10^{-4}	2.1000	1.080×10^{-4}	2.1001
	% error			0	0	0	0.01
	D-3	1.440×10^{-4}	1.0000	1.440×10^{-4}	1.0001	1.440×10^{-4}	1.0000
	% error			0	0.01	0	0
3	D-1	7.020×10^{-5}	–1.0000	7.017×10^{-5}	–1.0002	7.020×10^{-5}	–1.0000
	% error			–0.04	0.02	0	0
	D-2	3.600×10^{-5}	1.2000	3.601×10^{-5}	1.2007	3.598×10^{-5}	1.1998
	% error			0.03	0.06	–0.06	–0.02
	D-3	7.200×10^{-5}	1.8000	7.201×10^{-5}	1.8000	7.201×10^{-5}	1.8000
	% error			0.01	0	0.01	0

This is due to the change in resultant forces of shaft unbalances at high speeds and the formation of mode shapes corresponding to different critical speeds. So, using VELSHSB, the unbalances are estimated in the system for low operating speeds (80-110 rad/s) and high operating speeds (5-700 rad/s), as shown in Table 3.5. Both the magnitudes and phase of the estimated unbalances are different for both cases.

TH-2966_176103027

Table 3. 3. Estimated unbalances at balancing planes for the rotor system with both discrete disc and randomly distributed shaft unbalances.

		VTEICM		VELSHSB			
Set	Discs	Magnitude (kg-m)	Phase (rad)	Magnitude (kg-m)	% error	Phase (rad)	% error
1	D-1	2.049×10^{-5}	0.5667	2.049×10^{-5}	0	0.5671	0.07
	D-2	2.992×10^{-5}	1.9955	2.992×10^{-5}	0	1.9956	0.01
	D-3	4.345×10^{-5}	0.7443	4.346×10^{-5}	0.02	0.7443	0
2 (5%)	D-1	2.047×10^{-5}	0.5925	2.048×10^{-5}	0.08	0.5928	0.05
	D-2	2.901×10^{-5}	2.0842	2.901×10^{-5}	0	2.0843	0.01
	D-3	4.527×10^{-5}	0.7055	4.528×10^{-5}	0.02	0.7054	–0.01
3 (8%)	D-1	2.047×10^{-5}	0.6079	2.048×10^{-5}	0.05	0.6083	0.03
	D-2	2.858×10^{-5}	2.1399	2.858×10^{-5}	0	2.1400	0.10
	D-3	4.639×10^{-5}	0.6836	4.641×10^{-5}	0.04	0.6836	0
4 (10%)	D-1	2.047×10^{-5}	0.6182	2.048×10^{-5}	0.05	0.6186	0.06
	D-2	2.835×10^{-5}	2.1779	2.835×10^{-5}	0	2.1780	0
	D-3	4.715×10^{-5}	0.6697	4.717×10^{-5}	0.04	0.6697	0.01

The estimated unbalances with 5% of random noise are included as balance masses in the rotor system at an orientation opposite to that of estimated unbalances. The obtained responses before and after balancing using both the estimates of unbalances at slow speeds and high speeds are shown in Figs. 3.14 and 3.15, respectively. For slow speed estimates, in Fig. 3.14 (a), (b), (c), and (d), the time domain displacement response of the system is shown at the balancing planes and AMB-2 locations before and after balancing and exclusive of AMB control. In Fig. 3.15 (a), (b), (c), and (d), the time domain displacement response of the system is shown at the balancing planes and AMB-2 locations before and after balancing and exclusive of AMB control, for high-speed estimates. It is seen that the balancing with the unbalances estimated at high-speed using VELSHSB has a higher

TH-2966_176103027

reduction in vibration in comparison to that obtained at low speeds. In Fig. 3.16, the vibration of the system at balancing planes and AMB-2 locations gets reduced further after the application of AMB control in the system.

Table 3. 4. Estimated percentage change in unbalances at the balancing planes using VELSHSB with addition of different percentage of random noise.

Discs	5% noise		8% noise		10% noise	
	Magnitude	Phase	Magnitude	Phase	Magnitude	Phase
D-1	–2.97	–4.46	–1.71	–4.76	–1.41	–5.04
D-2	–12.33	8.86	–14.71	5.25	–15.64	4.30
D-3	8.95	4.76	6.35	7.04	5.72	7.88

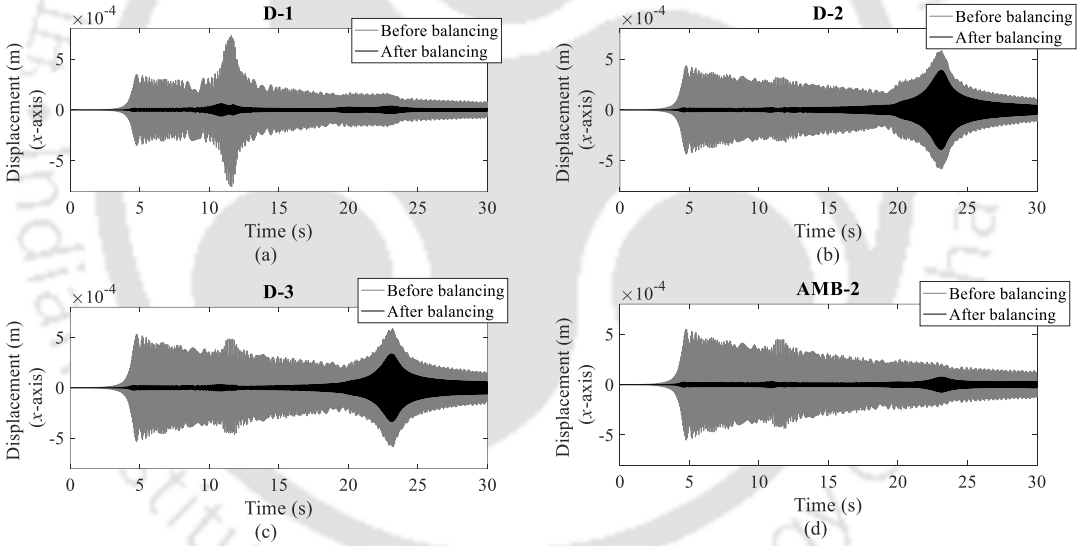


Fig. 3. 14. Displacement (in meters) vs. time (in seconds) plot at (a) disc D-1, (b) disc D-2, (c) disc D-3 and (d) AMB-2 before and after balancing using slow-speed estimates as represented by grey and black lines (same line width) respectively; moderate reduction in amplitude after balancing without AMB control.

TH-2966_176103027

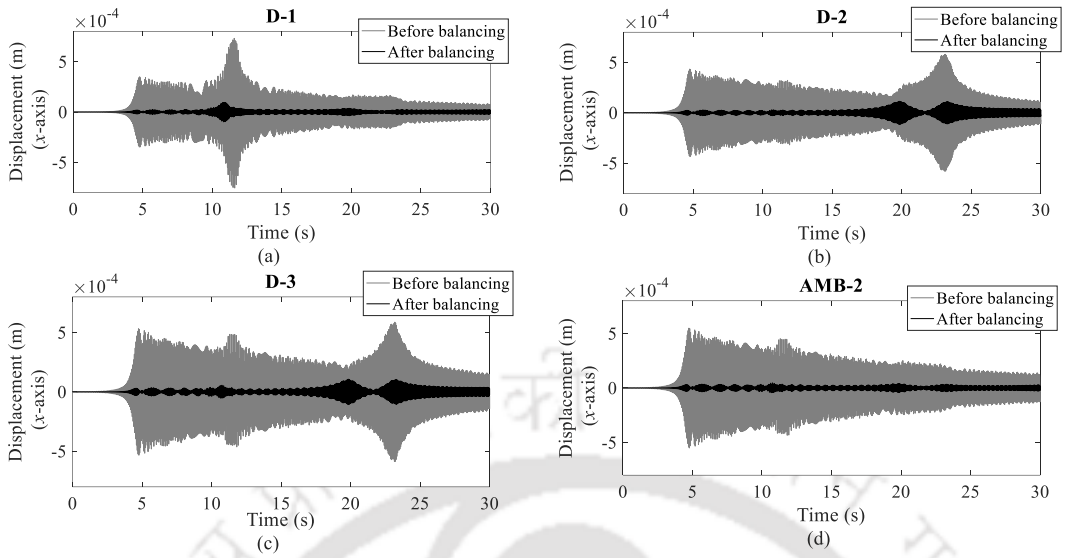


Fig. 3. 15. Displacement (in meters) vs. time (in seconds) plot at (a) disc D-1, (b) disc D-2, (c) disc D-3 and (d) AMB-2 before and after balancing using high-speed estimates as represented by grey and black lines (same line width) respectively; higher reduction in amplitude after balancing without AMB control.

Also, plots of displacement amplitudes are obtained in the frequency domain without AMB control at the disc 'D-1' location using FFT, as shown in Fig 3.17. In Fig. 3.17 (a) and (b), the displacement amplitudes and phases, respectively, at different run-up spin speeds are plotted before and after balancing. The amplitudes of the vibration responses corresponding to the different operating frequencies get reduced after balancing. Furthermore, in Fig. 3.18 (a) and (b), the AMB control is applied, and the displacement amplitudes and phases, respectively, are plotted at different run-up spin speeds without and with balancing, depicting the reduction in vibration. The percentage reduction in maximum time domain displacement throughout all the node locations in all the aforementioned cases after balancing is shown in Fig. 3.19. As it is seen in Fig. 3.19, the displacement reduction after the balancing with high-speed estimates and AMB control shows an 86 % reduction in the time domain vibrational response of the rotor system. The maximum amplitude of

TH-2966_176103027

vibration at all the measurement locations (discs and AMB) are compared and the overall maximum amplitude of the system is utilized to estimate the reduction percentage. After balancing the rotor system, the amount of control current required by the AMBs to suppress the vibration is greatly reduced. The control current generated at the AMB-1 and AMB-2 locations are plotted with respect to the run-up time as shown in Fig. 3.20 (a) and (b), respectively.

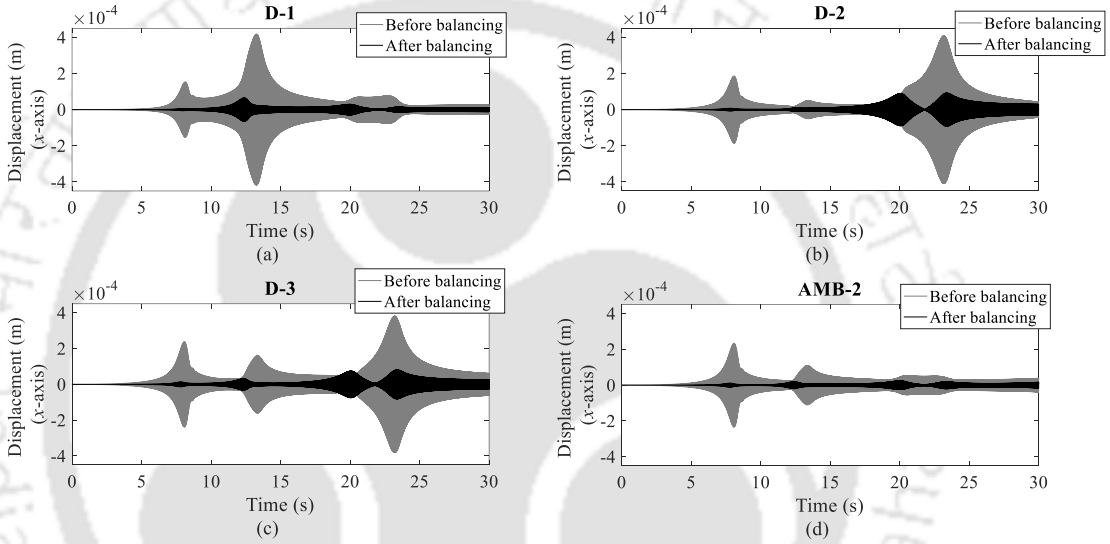


Fig. 3. 16. Displacement (in meters) vs. time (in seconds) plot at (a) disc D-1, (b) disc D-2, (c) disc D-3 and (d) AMB-2 before and after balancing using high-speed estimates as represented by grey and black lines (same line width) respectively; highest reduction in amplitude after balancing with AMB control. Spin speed varies from 5-700 rad/s.

Table 3. 5. Estimated unbalances at the balancing planes using VELSHSB and influence coefficients obtained at the slow and high speeds with 5% of random noise.

	Slow speed		High speed	
	Magnitude (kg-m)	Phase (rad)	Magnitude (kg-m)	Phase (rad)
Disc-1	1.894×10^{-5}	0.5897	1.988×10^{-5}	0.5418
Disc-2	1.535×10^{-5}	1.3368	2.623×10^{-5}	2.1725
Disc-3	4.292×10^{-5}	1.1106	4.735×10^{-5}	0.7798

TH-2966_176103027

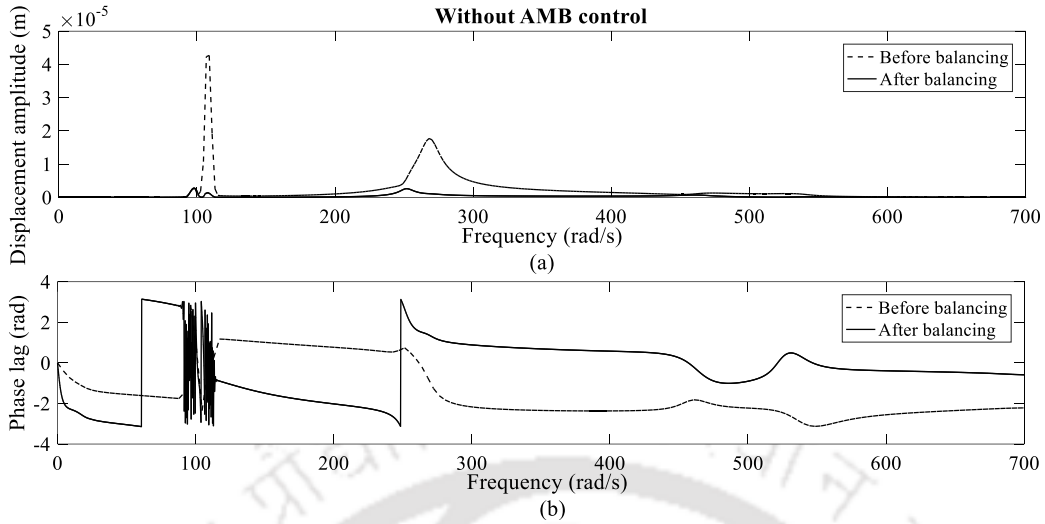


Fig. 3. 17. (a) Displacement amplitude vs run-up spin speeds, (b) Displacement phase vs. run-up spin speeds before and after balancing using high-speed estimates as represented by dotted and solid lines; amplitude reduction is achieved after balancing throughout the ramp-up speed at disc-1 location without AMB control.

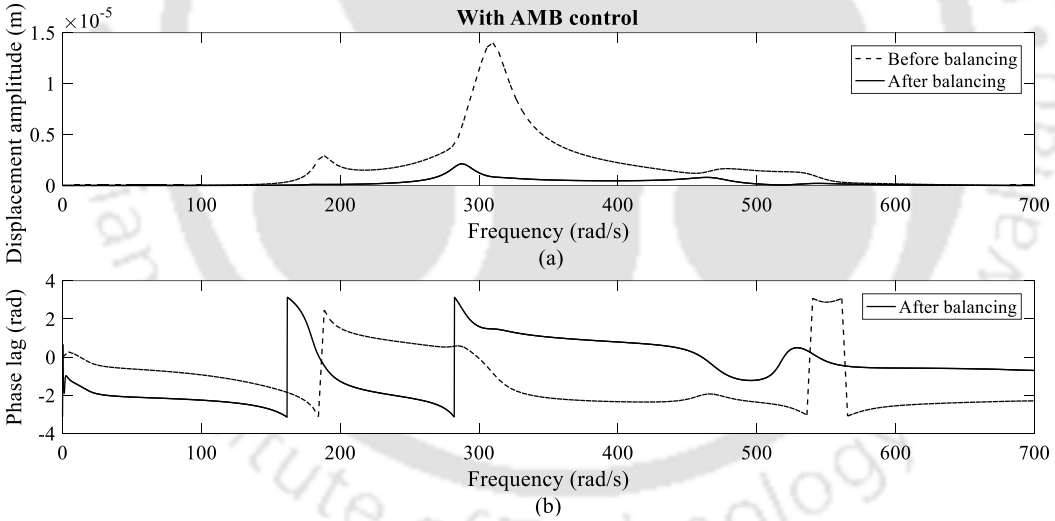


Fig. 3. 18 (a) Displacement amplitude vs run-up spin speeds, (b) Displacement phase vs. run-up spin speeds before and after balancing using high-speed estimates as represented by dotted and solid lines; amplitude reduction is achieved after balancing throughout the ramp-up speed at disc-1 location with AMB control.

TH-2966_176103027

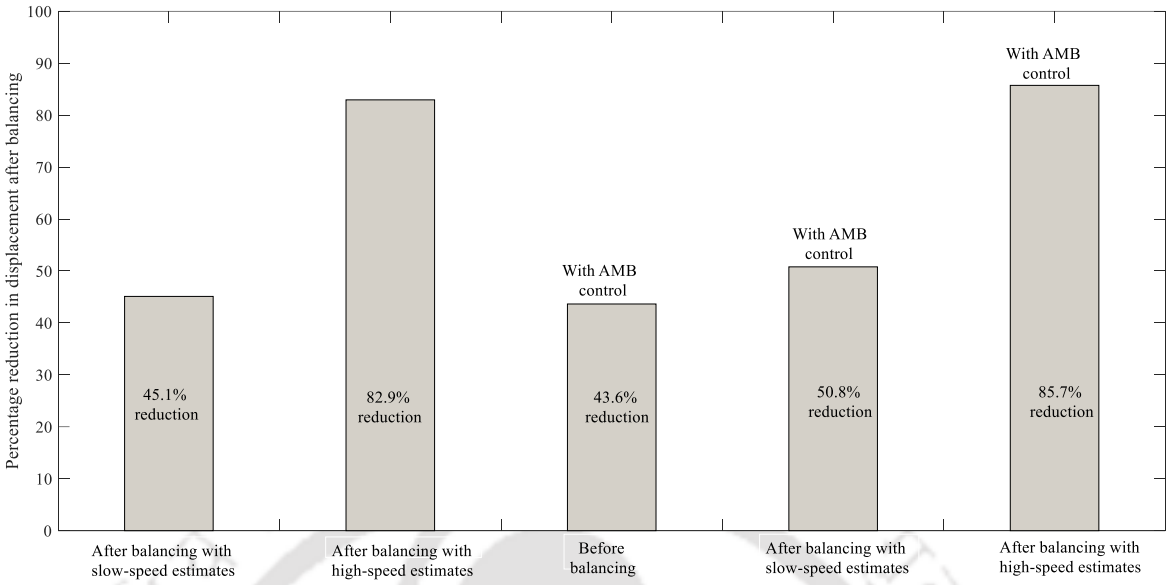


Fig. 3. 19. The percentage reduction in the maximum time domain displacement of the rotor system throughout all node locations after balancing of the rotor system with and without AMB control.

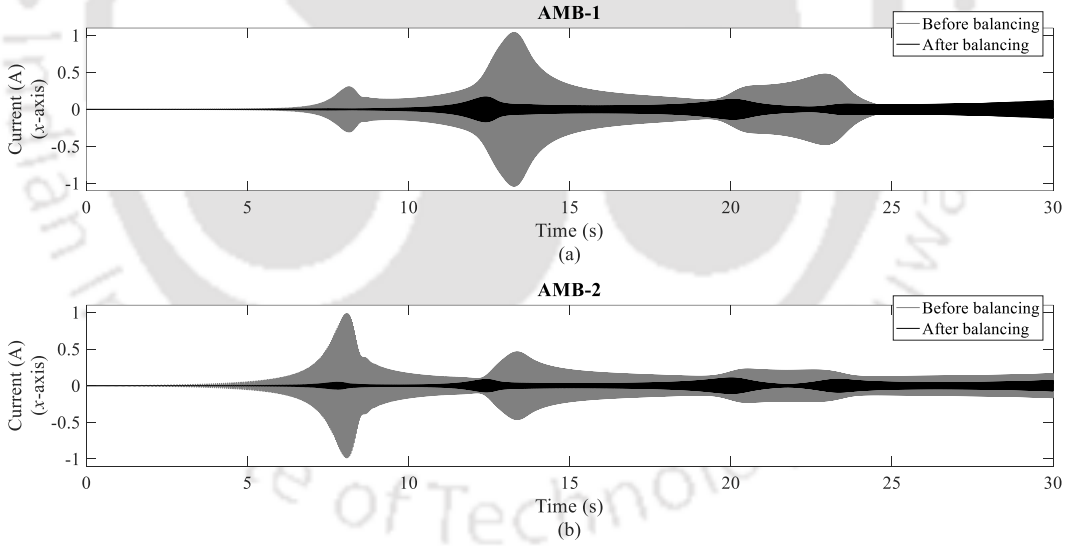


Fig. 3. 20. The current (in amperes) vs time (in seconds) plot along *x*-axis at (a) AMB-1, and (b) AMB-2 locations before and after balancing as represented by grey and black lines (same line width); reduction in control current is achieved after balancing.

TH-2966_176103027

The overall percentage reduction in current consumption at the AMB-1 and AMB-2 locations are found out to be 83.9% and 89.4%, respectively. This decreases the overall power consumption by the AMBs, i.e., approximately equal to 97% (Power $\propto$ current^2) in the rotor system. So, it is essential to balance the rotor system to improve the efficiency of the system by reduction of the energy consumption through AMBs at high speeds.

3.4.5. Unbalance estimation considering variation in properties of support bearing

Apart from the change of unbalances in the system with time, the support conditions also change with the change in lubrication condition, contamination of bearing parts, and wear and tear. Due to change in the bearing stiffness and damping properties, the influence coefficients of the system changes after a period of time. This affects the estimation done through the VELSHSB, where the influence coefficients at high speeds are obtained once. So, to verify the robustness of the VELSHSB, in the 1st set, the high-speed influence coefficients are obtained along with the estimated unbalances at balancing planes. For the next sets, the bearing properties are varied by 5% and 10% from its assumed values, and unbalances at slow speeds are obtained at different node locations. Now, influence coefficients obtained at high speeds in the 1st set are utilized to estimate the unbalances at the balancing planes for the other sets. Also, the unbalances are estimated using the VTEICM with the variation of support condition, as shown in Table 3.6. With the change in bearing properties, the estimated unbalances using the VTEICM change due to change in influence coefficients at high-speed for each set. Whereas in the case of VELSHSB, the influence coefficients at high-speed remain the same for each set, and no change in estimated unbalances occurs. The change in influence coefficients at low-speed does not affect the estimation as no mode shapes are formed. Also, the estimated unbalances using

TH-2966_176103027

VELSHSB do not vary much from that of the VTEICM, with a maximum variation of 3.7%. So, it is quite useful to perform periodic balancing of the flexible rotor system using the VELSHSB.

Table 3. 6. Estimated unbalances at the balancing planes using both methods with variations in support bearing's properties.

		VTEICM		VELSHSB			
Set	Discs	Magnitude (kg-m)	Phase (rad)	Magnitude (kg-m)	% error	Phase (rad)	% error
1	D-1	2.049×10^{-5}	0.5667	2.049×10^{-5}	0	0.5671	0.07
	D-2	2.992×10^{-5}	1.9955	2.992×10^{-5}	0	1.9956	0.01
	D-3	4.345×10^{-5}	0.7443	4.346×10^{-5}	0.02	0.7443	0
Variation in stiffness at conventional bearing (CB-1)							
2 (5%)	D-1	2.062×10^{-5}	0.5567	2.049×10^{-5}	–0.63	0.5671	1.87
	D-2	2.966×10^{-5}	1.9895	2.992×10^{-5}	0.87	1.9956	0.31
	D-3	4.345×10^{-5}	0.7459	4.346×10^{-5}	0.02	0.7443	–0.20
3 (10%)	D-1	2.074×10^{-5}	0.5472	2.049×10^{-5}	–1.21	0.5671	3.63
	D-2	2.940×10^{-5}	1.9835	2.992×10^{-5}	1.77	1.9956	0.61
	D-3	4.345×10^{-5}	0.7475	4.346×10^{-5}	0.02	0.7443	–0.43
Variation in damping coefficient at conventional bearing (CB-1)							
2 (5%)	D-1	2.053×10^{-5}	0.5681	2.049×10^{-5}	–0.19	0.5671	–0.18
	D-2	2.995×10^{-5}	1.9924	2.992×10^{-5}	–0.10	1.9956	0.16
	D-3	4.341×10^{-5}	0.7446	4.346×10^{-5}	0.12	0.7443	–0.04
3 (10%)	D-1	2.057×10^{-5}	0.5693	2.049×10^{-5}	–0.39	0.5671	–0.39
	D-2	2.998×10^{-5}	1.9892	2.992×10^{-5}	–0.20	1.9956	0.32
	D-3	4.337×10^{-5}	0.7449	4.346×10^{-5}	0.20	0.7443	–0.08

TH-2966_176103027

3.5. Remarks

In the present methodology, an identification algorithm is developed to estimate the unbalances in the flexible rotor-AMB system. The VELSHSB allows periodic estimation of the unbalances with the application of virtual trial unbalances as a magnetic force through AMBs. The unbalances estimated at the balancing planes provide an appreciable amount of vibration reduction in the flexible rotor system at high speeds. The VELSHSB utilizes the influence coefficients of the rotor system at high speeds and effectively estimates the unbalances with the change in unbalances after a period of time for flexible rotor balancing. The method requires a one-time estimation of the influence coefficients at high speeds and utilizes the unbalances estimated at the low speeds to balance the rotor system periodically. With the introduction of virtual trial unbalances, the effort and time are reduced as it is required in manual addition of trial unbalances. The reduction in the number of trial runs reduces the contamination of the rotor components with the opening and closure of the casing. Also, the change in support conditions of the system does not affect the unbalance estimation and amount of vibration reduction after balancing. The present balancing strategies are limited to the simple rotor system with all the rotating components operating at the same spin speeds. The identification algorithm is required to be extended to the balancing of the complex rotor system, where the inner and outer rotor system rotates at different operating frequencies, for example, a dual rotor. The next chapter considers this aspect.

TH-2966_176103027

CHAPTER 4

DYNAMIC BALANCING OF DUAL ROTOR-AMB SYSTEM THROUGH MULTIPLE VIRTUAL TRIAL UNBALANCES AS MAGNETIC EXCITATIONS

This chapter deals with the development of the identification algorithm based on influence coefficients for balancing complex rotor systems such as dual rotor systems. The implementation of AMB to control and generate virtual trial unbalances as magnetic excitations in compliance with the operating frequencies of the inner and outer rotor system is described. The finite element modelling of the dual rotor system supported on conventional bearings and integrated with AMB in the inner rotor system is discussed. In the present chapter, the utilization of displacement responses from the finite element model in the identification algorithm to estimate the residual unbalances in the dual rotor system is illustrated.

4.1. Introduction

The dual rotor systems are widely employed in aero engines due to their efficient performance in the complex structures (Yang *et al*., 2016; Jhang *et al*., 2018). The presence of a fault, such as the unbalance, may affect the efficiency of the machinery due to the large amplitude of vibration. Therefore, the implementation of the active vibration control devices in the dual rotor systems is required for monitoring the faults present in the machinery as well as to reduce the vibration response of the system. Due to the compact

TH-2966_176103027

structure of the system, it is difficult to balance the rotor system with manual addition of the trial unbalances as utilized in conventional ICM or by model-based identification techniques that require modelling of the complex rotor system. Therefore, a suitable balancing strategy is required to be developed that would reduce the manual effort as well as utilize only vibration responses to predict the unbalances in both the inner and outer rotor system. Also, in the case of active vibration control with AMBs, the control current applied in suppression of the vibration response consumes a lot of electrical energy. In order to address the above limitation in the efficient operation of a dual rotor system, a novel balancing strategy, i.e., Multiple Virtual Excitation for Dual rotor Balancing (MVEDRB) method, has been utilized to balance the dual rotor system with AMB control and excitation. The AMB is integrated into the inner rotor system (low pressure) supported on the conventional bearing to reduce the vibrational response of the system as well as to excite the rotor system at different operating frequencies to estimate the residual unbalances in both the inner and outer rotor system, simultaneously. The outer rotor system (high pressure) is supported on the conventional bearing and coupled with the inner rotor system with the intermediate flexible bearing. The virtual trial unbalances are excited in the form of magnetic force to generate the same effect in the rotor system as generated by manually added trial unbalances. The finite element modelling (FEM) of the dual rotor system is carried out to generate the displacement responses and virtual trial excitation forces for the validation of the developed balancing methodology.

TH-2966_176103027

4.2. Formulation of the Multiple Virtual Excitation for Dual rotor Balancing (MVEDRB) method

The dual rotor system supported on conventional bearing and integrated with AMB is shown in Fig. 4.1. The Low Pressure Rotor (LPR) or inner rotor system consists of two rigid discs and a flexible shaft with an AMB mounted on the shaft to control the vibration. The High Pressure Rotor (HPR) or outer rotor system consists of two rigid discs and a hollow shaft, which is coupled with the LPR system with the help of Intermediate Flexible Bearing (IFB). The vibrational displacement generated in the LPR system is transmitted to the HPR system due to the coupling effect of the IFB. With the utilization of external excitation through AMB in the LPR system, the residual unbalances are estimated in both LPR and HPR systems. The identification algorithm is based on the influence coefficient method, which utilizes the displacement responses of the rotor system at the discs and AMB locations and the value of external magnetic excitation subjected through AMB in the system. The resultant residual unbalances due to discrete disc unbalances and randomly distributed shaft unbalances are estimated at the balancing planes (rigid discs) for both the LPR and HPR systems. The procedure is performed in three rotor runs with the rotor system operating at different spin speeds. An additional magnetic excitation force is added to the system to estimate the influence coefficients of the system based on the displacement response at the discs and AMB locations. The influence coefficients are utilized along with the displacement response of the system to estimate the required residual unbalances in the system, as described below.

TH-2966_176103027

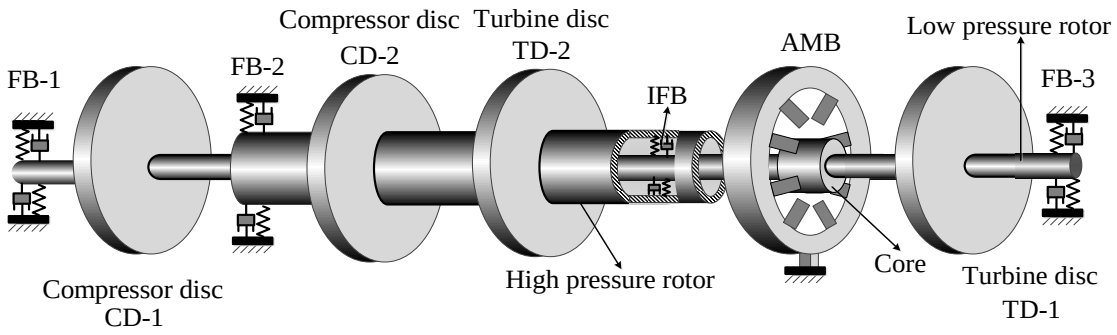


Fig. 4. 1 A pictorial representation of dual rotor-AMB system comprising of LPR and HPR supported on flexible bearings.

4.2.1. Initial run without additional excitation

First, the low pressure and high-pressure systems are rotated at a spin speed ω_L and ω_H. The displacement responses of the system are obtained at the respective measurement locations, which is due to the unbalance excitation force and are related to influence coefficients, and respective unbalances as

$$r_{a,L_1}(\omega_L) = \chi_{L_1,L_1}(\omega_L) f_{L_1} + \chi_{L_1,L_2}(\omega_L) f_{L_2} \tag{4.1}$$

$$r_{c,H_1}(\omega_H) = \kappa_{H_1,H_1}(\omega_H) f_{H_1} + \kappa_{H_1,H_2}(\omega_H) f_{H_2} \tag{4.2}$$

where, r_{a,L_1} and r_{c,H_1} are the complex displacement responses at the compressor discs (CD-1 and CD-2) of both LPR and HPR systems corresponding to their respective spin speeds as mentioned in Eqs. (4.1) and (4.2). χ and κ are the influence corresponding to the resultant unbalance forces in the LPR and HPR systems, respectively. f_{L_1} and f_{L_2} are the resultant residual unbalances at the compressor and turbine discs (CD-1 and TD-1) of LPR, respectively, and f_{H_1} and f_{H_2} are the resultant residual unbalances at the compressor and turbine discs (CD-2 and TD-2) of HPR, respectively. The relationship between the displacement responses obtained in different rotor systems and corresponding influence

TH-2966_176103027

coefficients is explained in detail in the FEM modelling in the following section. Similarly, the displacement responses at the other measurement locations are related to influence coefficients as

$$\mathbf{r}_L = \begin{bmatrix}\mathbf{a}_1 & \mathbf{a}_2 & \mathbf{a}_3\end{bmatrix}\mathbf{f}_L; \qquad \mathbf{r}_H = \begin{bmatrix}\mathbf{b}_1 & \mathbf{b}_2 & \mathbf{b}_3\end{bmatrix}\mathbf{f}_H \tag{4.3}$$

$$\mathbf{r}_L = \begin{Bmatrix} r_{a,L_1} & r_{a,L_2} & r_{a,m}\end{Bmatrix}^T; \qquad \mathbf{r}_H = \begin{Bmatrix} r_{c,H_1} & r_{c,H_2} & r_{c,m}\end{Bmatrix}^T; \qquad \mathbf{f}_L = \begin{Bmatrix} f_{L,1} & f_{L,2} & 0\end{Bmatrix}^T;$$

$$\mathbf{f}_H = \begin{Bmatrix} f_{H,1} & f_{H,2} & 0\end{Bmatrix}^T$$

where, $r_{a,m}$ and $r_{c,m}$ are the complex displacement responses at the AMB of LPR system corresponding to the spin speed of LPR and HPR systems. The detailed description of the influence coefficient matrices mentioned in Eq. (4.3) is given by Eq. A.3 in Appendix A.

4.2.2. Subsequent run with low-pressure rotor frequency (ω_L) excitation

In the second run, the influence coefficients corresponding to discs and AMB locations in the LPR system are identified. A magnetic excitation force in the form of virtual trial unbalance is generated with a frequency of ω_L at the AMB location and is given as

$$f_{T,L} = k_i i_{T,L} \mathrm{e}^{\mathrm{j}\varphi_T} \tag{4.4}$$

with, $i_{T,L} = \left(m_T e_T \omega_L^2\right)/k_i$

where, $i_{T,L}$ is the trial current, which is subtracted from the control current in order to generate a magnetic force equivalent to trial unbalance force, i.e., $m_T e_T \omega_L^2$. $\varphi_{T,L}$ is the phase of the trial current.

TH-2966_176103027

As the magnetic excitation frequency is equivalent to the operating speed of the LPR, the displacement responses corresponding to the operating speeds of the LPR change, and that of HPR remains constant. Therefore, the displacement responses are related to influence coefficients and the external forces as

$$\mathbf{r}'_L = \begin{bmatrix}\mathbf{a}_1 & \mathbf{a}_2 & \mathbf{a}_3\end{bmatrix}\mathbf{f}'_L; \qquad \mathbf{r}_H = \begin{bmatrix}\mathbf{b}_1 & \mathbf{b}_2 & \mathbf{b}_3\end{bmatrix}\mathbf{f}_H \tag{4.5}$$

with, $\mathbf{f}'_L = \begin{Bmatrix} f_{L,1} & f_{L,2} & f_{T,L}\end{Bmatrix}^T$; $\qquad \mathbf{r}'_L = \begin{Bmatrix} r'_{a,L_1} & r'_{a,L_2} & r'_{a,m}\end{Bmatrix}^T$

The influence coefficients corresponding to the AMB location due to external forces at the discs locations of the LPR system are estimated by subtracting Eq. (4.3) from Eq. (4.5) and are given as

$$\chi_{m,L_1} = \chi_{L_1,m} = \frac{r'_{a,L_1} - r_{a,L_1}}{f_{T,L}}; \quad \chi_{m,L_2} = \chi_{L_2,m} = \frac{r'_{a,L_2} - r_{a,L_2}}{f_{T,L}}; \quad \chi_{m,m} = \frac{r'_{a,m} - r_{a,m}}{f_{T,L}} \tag{4.6}$$

The influence coefficients identified in the Eq. (4.6) are utilized in the estimation of the residual unbalances at the LPR system.

4.2.3. Subsequent run with high-pressure rotor frequency (ω_H) excitation

In the third run, the magnetic excitation force is generated with ω_H frequency, and the third set of displacement responses are measured at the limited node locations. The displacement responses in the HPR system corresponding to the ω_H frequency are due to the residual unbalances and the additional excitation force at the AMB location and is given as

$$f_{T,L} = k_i i_{T,H} \mathrm{e}^{\mathrm{j}\varphi_T} \tag{4.7}$$

TH-2966_176103027

with, $i_{T,H} = \left(m_T e_T \omega_H^2 \right) / k_i$

In the third case, the frequency of the magnetic excitation force is equivalent to the frequency of the spin speed of the HPR. Therefore, the displacement response of the HPR system corresponding to its operating frequency is affected. The influence coefficients are related to the displacement responses, and both virtual and residual unbalances as

$$\mathbf{r}_L = \begin{bmatrix} \mathbf{a}_1 & \mathbf{a}_2 & \mathbf{a}_3 \end{bmatrix} \mathbf{f}_L ; \qquad \mathbf{r}'_H = \begin{bmatrix} \mathbf{b}_1 & \mathbf{b}_2 & \mathbf{b}_3 \end{bmatrix} \mathbf{f}'_H \tag{4.8}$$

with, $\mathbf{f}'_H = \begin{Bmatrix} f_{H,1} & f_{H,2} & f_{T,H} \end{Bmatrix}^T ; \qquad \mathbf{r}'_H = \begin{Bmatrix} r'_{c,H_1} & r'_{c,H_2} & r'_{c,m} \end{Bmatrix}^T$

The influence coefficients corresponding to the AMB location due to external forces at the discs locations of the HPR system are estimated by subtracting Eq. (4.3) from Eq. (4.8) and are given as

$$\lambda_{m,H_1} = \lambda_{H_1,m} = \frac{r'_{c,H_1} - r_{c,H_1}}{f_{T,H}}; \quad \lambda_{m,H_2} = \lambda_{H_2,m} = \frac{r'_{c,H_2} - r_{c,H_2}}{f_{T,L}}; \quad \lambda_{m,m} = \lambda_{m,m} \frac{r'_{c,m} - r_{c,m}}{f_{T,L}} \tag{4.9}$$

The influence coefficients identified in Eq. (4.9) are utilized in the estimation of the residual unbalances at the HPR system.

4.2.4. Estimation of the residual unbalances

The displacement responses of the rotor system at AMB location in the initial run case for both HPR and LPR rotor systems are related to their corresponding influence coefficients, and residual unbalance as

$$r_{a,m} = \chi_{m,L_1} f_{L_1} + \chi_{m,L_2} f_{L_2} \tag{4.10}$$

TH-2966_176103027

$$r_{c,m} = \lambda_{m,H_1} f_{H_1} + \lambda_{m,H_2} f_{H_2} \tag{4.11}$$

Now, the same relationship as shown in Eq. (4.10) and Eq. (4.11) are obtained for different spin speeds of the LPR and HPR system and are written as

$$\mathbf{r}_{a,m} = \begin{bmatrix} \boldsymbol{\chi}_{m,L_1} & \boldsymbol{\chi}_{m,L_2} \end{bmatrix} \mathbf{f}_{R,L}; \quad \mathbf{r}_{c,m} = \begin{bmatrix} \boldsymbol{\lambda}_{m,H_1} & \boldsymbol{\lambda}_{m,H_2} \end{bmatrix} \mathbf{f}_{R,H} \tag{4.12}$$

with, $\mathbf{r}_{a,m} = \left\{ r_{a,m}(\omega_{L,1}) \quad r_{a,m}(\omega_{L,2}) \quad \cdots \quad r_{a,m}(\omega_{L,t}) \right\}^T;$

$$\mathbf{r}_{c,m} = \left\{ r_{c,m}(\omega_{H,1}) \quad r_{c,m}(\omega_{H,2}) \quad \cdots \quad r_{c,m}(\omega_{H,t}) \right\}^T$$

$$\boldsymbol{\chi}_{m,i} = \left\{ \chi_{m,i}(\omega_{L,1}) \quad \chi_{m,i}(\omega_{L,2}) \quad \cdots \quad \chi_{m,i}(\omega_{L,t}) \right\}^T;$$

$$\boldsymbol{\lambda}_{m,j} = \left\{ \lambda_{m,j}(\omega_{H,1}) \quad \lambda_{m,j}(\omega_{H,2}) \quad \cdots \quad \lambda_{m,j}(\omega_{H,t}) \right\}^T; \qquad i = \{L_1, L_2\}; \qquad j = \{H_1, H_2\}$$

$$\mathbf{f}_{R,L} = \left\{ f_{L,1} \quad f_{L,2} \right\}^T; \qquad \mathbf{f}_{R,H} = \left\{ f_{H,1} \quad f_{H,2} \right\}^T$$

Now, combining Eq. (4.12), the residual unbalances in both HPR and LPR systems are obtained as

$$\begin{Bmatrix} \mathbf{r}_{a,m} \\ \mathbf{r}_{c,m} \end{Bmatrix} = \mathbf{D}_R \begin{Bmatrix} \mathbf{f}_{R,L} \\ \mathbf{f}_{R,H} \end{Bmatrix} \tag{4.13}$$

with, $\mathbf{D}_R = \begin{bmatrix} \boldsymbol{\chi}_{m,L_1} & \boldsymbol{\chi}_{m,L_2} & 0 & 0 \\ 0 & 0 & \boldsymbol{\lambda}_{m,H_1} & \boldsymbol{\lambda}_{m,H_2} \end{bmatrix}$

$$\begin{Bmatrix} \mathbf{f}_{R,L} \\ \mathbf{f}_{R,H} \end{Bmatrix} = \left(\mathbf{D}_R{}^T \mathbf{D}_R \right)^{-1} \mathbf{D}_R{}^T \begin{Bmatrix} \mathbf{r}_{a,m} \\ \mathbf{r}_{c,m} \end{Bmatrix} \tag{4.14}$$

TH-2966_176103027

The residual unbalances obtained in above Eq. (4.14) are added to the disc locations as balance masses with opposite orientation to check the level of reduction in vibration responses. The algorithm estimates the unbalances in both the rotor system simultaneously with external magnetic excitation applied at the AMB location in the LPR system. In the literature, the AMBs has been utilized as support bearing for the gas turbines and aero engines operating in the high temperature region with specially coated wires and ceramic potting. The AMBs have been designed to operate in extreme conditions without the needs of seals where traditional bearings could not function (Provenza *et al.* (2003); Takizuka *et. al* (2004); Eaton *et al.* (2010); Srinivas *et al.* (2018); Wang *et al.* (2019); Wang, Wang and Chen (2019)). However, the designed algorithm for the estimation of the unbalances in rotor-AMB systems is not affected with the position of AMB as it is discussed in Chapter 2, where different configuration of rotor-AMB system were considered. To verify the effectiveness of the algorithm, a finite element model of dual rotor system integrated with AMB is developed, and the displacement responses obtained from the model are utilized in the estimation of the residual unbalances.

4.3. Finite element modelling of the dual rotor-AMB system

A dual-rotor-AMB system supported on flexible bearings (FB) is modelled mathematically using the finite element method. Both the inner (low pressure) and outer (high pressure) rotors are divided into elements of different lengths with four degree-of-freedom at each node (two rotational and two translational). The rotors are coupled with the help of Intermediate Flexible Bearing (IFB) incorporated near the turbine disc of the high pressure rotor, as shown in Fig. 4.2. Discrete disc unbalances are assumed to be present at the disc

TH-2966_176103027

locations, and shaft unbalances are assumed to be distributed randomly over the span of both the rotors. The closed loop control of AMB is included by introducing a magnetic force in response to the vibration excitation of the rotor system. The linearized magnetic force model is utilized based on the differential control mode of the AMB system (Tiwari, 2017). The equations of motions of each component of the system (flexible shaft, discs, conventional bearings, and AMB) are discussed separately and then assembled together to obtain the overall equations of motion of the system.

4.3.1. Discretization of high pressure and low pressure rotors

The LPR and HPR systems are discretized into five and three elements, respectively, as shown in Fig. 4.2. The rigid discs comprising of compressors and turbines are incorporated at nodes 2 and 5 for LPR and 8 and 9 for the HPR system, respectively.

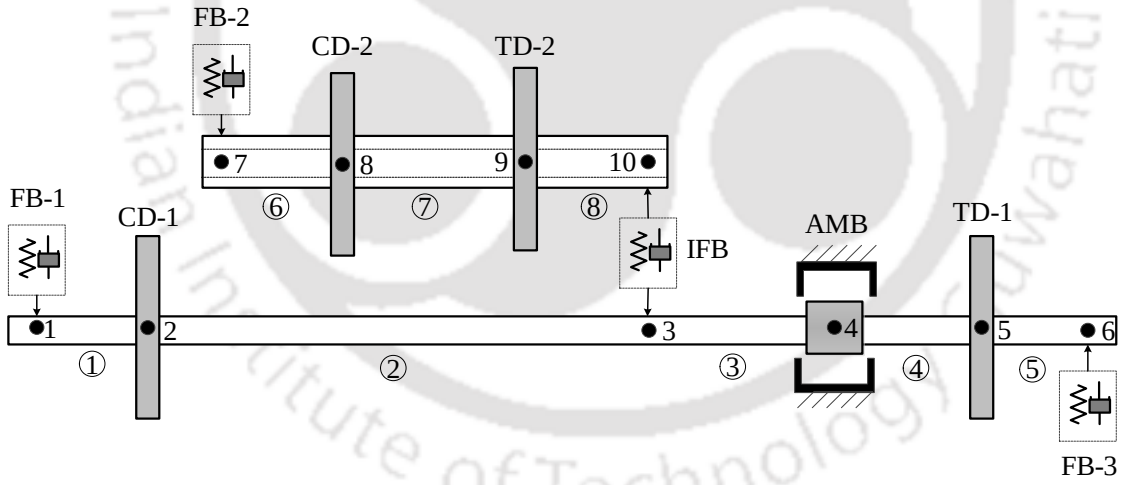


Fig. 4. 2. A finite element model considered for the dual-rotor AMB system with elements and node locations.

The flexible bearings are considered at nodes 1, 6, and 7 to support both the rotors, and the coupling between the rotors is established by the addition of the intermediate bearing in between the rotors at nodes 3 and 7. To reduce the substantial amount of vibrational

TH-2966_176103027

response in the system, an AMB is incorporated in the low pressure system at node 4. The detailed description of the equations of motion of the components of the dual rotor system is given in the sections below.

4.3.1.1. Flexible shafts with randomly distributed unbalances

Euler-Bernoulli's beam model is considered for the development of the equations of motion of the flexible shafts. Randomly distributed shaft unbalances are incorporated in the system at the different locations in the shafts. The elements of LPR are further divided into various segments and are considered as discs with a random eccentricity and phase, as shown in Fig. 4.3. The chosen unbalances are kept the same through the numerical simulation. The unbalance forces developed at k^{th} segment for element-1 is given as

$$f_{s,k} = \rho A_L l_k e_{s,k} \mathrm{e}^{\mathrm{j}\phi_{s,k}} \tag{4.15}$$

with, $k = 1, 2, 3, \ldots, n$ number of segments in element-1.

where, ρ is the density of the shaft in LPR, A_L is the area of cross-section, and l_k is the length of the k^{th} segment. $e_{s,k,}$ and $\phi_{s,k}$ are the eccentricity and phase of the unbalance assumed at the k^{th} segment. The overall unbalance forces at the different segments in element-1 are estimated at the node 1 and 2 locations as

$$\mathbf{f}_{e,1} = \begin{Bmatrix} f_{1,1} & M_{1,1} & f_{1,2} & M_{1,2} \end{Bmatrix}^T = \int_0^{l_{e,1}} \sum_{k=1}^{n} f_{s,k}(t)\,\delta(z - z_k)\,\mathbf{u}(z)\,dz \tag{4.16}$$

with, $\mathbf{u}(z) = \left\{ 1 - 3\frac{z^2}{l_{e,1}^{\,2}} + 2\frac{z^3}{l_{e,1}^{\,3}} \quad z - 2\frac{z^2}{l_{e,1}} + \frac{z^3}{l_{e,1}^{\,2}} \quad 3\frac{z^2}{l_{e,1}^{\,2}} - 2\frac{z^3}{l_{e,1}^{\,3}} \quad -\frac{z^2}{l_{e,1}} + \frac{z^3}{l_{e,1}^{\,2}} \right\}^T$

TH-2966_176103027

where, $f_{1,1}$, $f_{1,2}$, $M_{1,1}$, and $M_{1,2}$ are the unbalance forces and moments estimated at the node 1 and 2 locations, respectively, for the element-1. z_k is the location of the k^{th} segment from node 1 of the element-1 along the z-axis, as shown in Fig. 4.3.

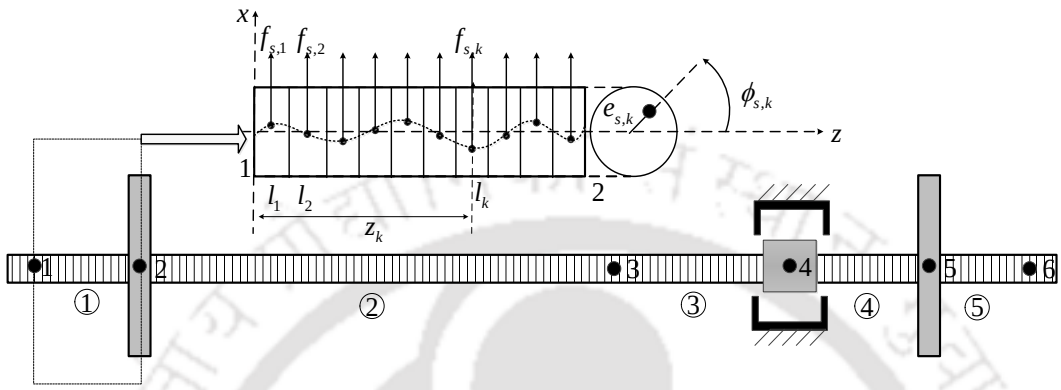


Fig. 4. 3. Random distribution of the residual unbalances throughout the span of the low pressure rotor

Similarly, for the elements 2, 3, 4, and 5, the unbalance forces in the flexible shaft are estimated at their respective node locations and are assembled together to estimate the overall shaft unbalance force corresponding to different node locations as shown in Eq. (4.17). Similarly, for HPR, the overall randomly distributed shaft unbalance force vector is estimated in Eq. (4.18).

$$\mathbf{f}_{s,L} = \left\{ f_{1,1} \quad M_{1,1} \quad f_{1,2}+f_{2,2} \quad M_{1,2}+M_{2,2} \quad \dots \quad f_{5,6} \quad M_{5,6} \right\}^T \tag{4.17}$$

$$\mathbf{f}_{s,H} = \left\{ f_{6,7} \quad M_{6,7} \quad f_{6,8}+f_{7,8} \quad M_{6,8}+M_{7,8} \quad \dots \quad f_{8,10} \quad M_{8,10} \right\}^T \tag{4.18}$$

Using Eqs. (4.17) and (4.18) , the equations of motion for the flexible shaft in LPR and HPR are given as

$$\mathbf{M}_{s,L}\ddot{\boldsymbol{\eta}}_L + \mathbf{K}_{s,L}\boldsymbol{\eta}_L = \mathbf{f}_{s,L} \tag{4.19}$$

TH-2966_176103027

$$\mathbf{M}_{s,H}\ddot{\boldsymbol{\eta}}_H + \mathbf{K}_{s,H}\boldsymbol{\eta}_H = \mathbf{f}_{s,H} \tag{4.20}$$

with, $\boldsymbol{\eta}_L = \{r_1 \quad \varphi_1 \quad r_2 \quad \varphi_2 \quad \dots \quad r_6 \quad \varphi_6\}^T$; $\boldsymbol{\eta}_H = \{r_7 \quad \varphi_7 \quad r_8 \quad \varphi_8 \quad \dots \quad r_{10} \quad \varphi_{10}\}^T$

where, $\mathbf{M}_{s,L}$, $\mathbf{K}_{s,L}$ and $\mathbf{M}_{s,H}$, $\mathbf{K}_{s,H}$ are the overall assembled mass and stiffness matrices for the low pressure and high pressure shaft, respectively. (r_1, r_2, …, r_{10}) and (φ_1, φ_2, …, φ_{10}) are the complex translational and rotational displacements, respectively corresponding to the different node locations.

4.3.1.2. Rigid discs with discrete unbalances

The compressors and turbines of the rotating machinery are modelled as the rigid disc mountings on the flexible shaft. Discrete residual unbalances are incorporated at the disc locations in both the LPR and HPR systems.

$$\mathbf{f}_{d,L} = \omega_L^2 \{0 \quad 0 \quad f_{C,1} \quad 0 \quad \dots \quad f_{T,1} \quad 0 \quad 0 \quad 0\}_{12\times1}^T \tag{4.21}$$

$$\mathbf{f}_{d,H} = \omega_H^2 \{0 \quad 0 \quad f_{C,2} \quad 0 \quad \dots \quad f_{T,2} \quad 0 \quad 0 \quad 0\}_{8\times1}^T \tag{4.22}$$

with, $f_{C,1} = m_{C,1}e_{C,1}e^{j\phi_{C,1}}$; $f_{T,1} = m_{T,1}e_{T,1}e^{j\phi_{T,1}}$; $f_{C,2} = m_{C,2}e_{C,2}e^{j\phi_{C,2}}$ and $f_{T,2} = m_{T,2}e_{T,2}e^{j\phi_{T,2}}$

where, $\mathbf{f}_{d,L}$ and $\mathbf{f}_{d,H}$ are discrete unbalance force vectors for low pressure and high pressure shaft, respectively. $f_{C,1}$, $f_{T,1}$, $f_{C,2}$, and $f_{T,2}$ are the residual unbalances at compressor and turbines discs for low pressure and high pressure shafts, respectively. The gyroscopic effects of the discs are considered that affect the dynamics of the system at high operating speeds. The equations of motion of the turbine and compressor discs for both the shafts are given as

TH-2966_176103027

$$\mathbf{M}_{d,L}\ddot{\boldsymbol{\eta}}_L - \omega_L \mathbf{G}_{d,L}\boldsymbol{\eta}_L = \mathbf{f}_{d,L} \tag{4.23}$$

$$\mathbf{M}_{d,H}\ddot{\boldsymbol{\eta}}_H - \omega_H \mathbf{G}_{d,H}\boldsymbol{\eta}_H = \mathbf{f}_{d,H} \tag{4.24}$$

where, $\mathbf{M}_{d,L}$, $\mathbf{M}_{d,H}$, $\mathbf{G}_{d,L}$, and $\mathbf{G}_{d,H}$ are the mass and gyroscopic matrices for the low pressure and high pressure shafts, respectively.

4.3.1.3. Support bearings and intermediate flexible bearings

The flexible support bearings are provided at node locations 1 and 6 for the LPR and at node location 7 for HPR. The stiffness and damping forces of the bearing are assumed to be linearly related to the displacement of the system at the respective node locations and are given as

$$\mathbf{f}_{L,1} = k_{L,1}\mathbf{L}_1\boldsymbol{\eta}_L + c_{L,1}\mathbf{L}_1\dot{\boldsymbol{\eta}}_L \tag{4.25}$$

$$\mathbf{f}_{L,2} = k_{L,2}\mathbf{L}_2\boldsymbol{\eta}_L + c_{L,2}\mathbf{L}_2\dot{\boldsymbol{\eta}}_L \tag{4.26}$$

$$\mathbf{f}_H = k_H\mathbf{H}\boldsymbol{\eta}_H + c_H\mathbf{H}\dot{\boldsymbol{\eta}}_H \tag{4.27}$$

with, $\mathbf{L}_1 = \text{diag}\{1 \quad 0 \quad \cdots \quad 0 \quad 0\}_{12\times12}$; $\mathbf{L}_2 = \text{diag}\{0 \quad 0 \quad \cdots \quad 1 \quad 0\}_{12\times12}$;

$\mathbf{H} = \{1 \quad 0 \quad \cdots \quad 0 \quad 0\}_{8\times8}$

where, $\mathbf{f}_{L,1}$, $\mathbf{f}_{L,2}$ and $\mathbf{f}_H$ are the overall bearing force at the node 1, 6, and 7 locations due to both stiffness and damping effect of the bearing. $k_{L,1}$, $k_{L,2}$, and k_H are the bearing coefficients, and $c_{L,1}$, $c_{L,2}$ and c_H are the damping coefficients at the respective node locations. The intermediate flexible bearing is included in between the high pressure and low pressure rotors at nodes 3 and 10. The relative displacement responses developed at the mentioned node location are utilized in generating the bearing forces at the IFB. The

TH-2966_176103027

IFB couples both the shafts, and the bearing force developed for both low pressure and high pressure shaft is given as

$$\mathbf{f}_{I,L} = k_f \left(\mathbf{q}_L \boldsymbol{\eta}_L - \mathbf{q}_H \boldsymbol{\eta}_H\right)\mathbf{q}_L^T + c_f \left(\mathbf{q}_L \dot{\boldsymbol{\eta}}_L - \mathbf{q}_H \dot{\boldsymbol{\eta}}_H\right)\mathbf{q}_L^T \tag{4.28}$$

$$\mathbf{f}_{I,H} = k_f \left(\mathbf{q}_H \boldsymbol{\eta}_H - \mathbf{q}_L \boldsymbol{\eta}_L\right)\mathbf{q}_H^T + c_f \left(\mathbf{q}_H \dot{\boldsymbol{\eta}}_H - \mathbf{q}_L \dot{\boldsymbol{\eta}}_L\right)\mathbf{q}_H^T \tag{4.29}$$

with, $\mathbf{q}_L = \{0 \quad 0 \quad 0 \quad 0 \quad 1 \quad 0 \quad 0 \quad 0 \quad 0 \quad 0 \quad 0 \quad 0\}$;

$\mathbf{q}_H = \{0 \quad 0 \quad 0 \quad 0 \quad 0 \quad 0 \quad 1 \quad 0\}$

where, k_f and c_f are the stiffness and damping coefficients of the IFB; $\mathbf{q}_L$ and $\mathbf{q}_H$ are the positional vectors of the IFB corresponding to the respective node locations.

4.3.1.4. Active magnetic bearing (AMB)

The AMB plays an important role in the safe operation of the rotor system by suppressing the vibrational response of the system within the desired level. An 8-pole AMB system is implemented in the present work with differential mode control and PID controller in the low pressure shaft of the system at node 4 location as shown in Fig. 4.2. The AMB force is introduced at the node location with the removal of the nonlinear terms and is given as

$$\mathbf{f}_m = -k_s \mathbf{P}\boldsymbol{\eta}_L + k_i \mathbf{i}_c \tag{4.30}$$

with, $\mathbf{P} = \text{diag}\{0 \quad 0 \quad 0 \quad 0 \quad 0 \quad 0 \quad 1 \quad 0 \quad 0 \quad 0 \quad 0 \quad 0\}$;

$\mathbf{i}_c = k_P \mathbf{P}\boldsymbol{\eta}_L + k_D \mathbf{P}\dot{\boldsymbol{\eta}}_{L,4} + k_I \int \mathbf{P}\boldsymbol{\eta}_L dt$

TH-2966_176103027

4.3.2. Assembled equation of motion of the rotor system

The equations of motion of the components of the rotor system are assembled together to form the final equation of motion as

$$\left(\mathbf{M}_{s,L}+\mathbf{M}_{d,L}\right)\ddot{\boldsymbol{\eta}}_L+\omega_L\mathbf{G}_{d,L}\dot{\boldsymbol{\eta}}_L+\mathbf{K}_{s,L}\boldsymbol{\eta}_L=\mathbf{f}_{s,L}+\mathbf{f}_{d,L}-\mathbf{f}_{L,1}-\mathbf{f}_{L,2}-\mathbf{f}_{I,L}-\mathbf{f}_m \tag{4.31}$$

$$\left(\mathbf{M}_{s,H}+\mathbf{M}_{d,H}\right)\ddot{\boldsymbol{\eta}}_H+\omega_H\mathbf{G}_{d,H}\dot{\boldsymbol{\eta}}_H+\mathbf{K}_{s,H}\boldsymbol{\eta}_H=\mathbf{f}_{s,H}+\mathbf{f}_{d,H}-\mathbf{f}_H-\mathbf{f}_{I,H} \tag{4.32}$$

Substituting, Eqs.(4.25), (4.26), (4.28) and (4.30) in Eq. (4.31) for the LPR system and Eqs. (4.27) and (4.29) in Eq. (4.32) for HPR system, we get

$$\begin{Bmatrix}\left(\mathbf{M}_{s,L}+\mathbf{M}_{d,L}\right)\ddot{\boldsymbol{\eta}}_L\\+\omega_L\mathbf{G}_{d,L}\dot{\boldsymbol{\eta}}_L+\mathbf{K}_{s,L}\boldsymbol{\eta}_L\end{Bmatrix}=\begin{Bmatrix}\mathbf{f}_{s,L}+\mathbf{f}_{d,L}-k_{L,1}\mathbf{L}_1\boldsymbol{\eta}_L-c_{L,1}\mathbf{L}_1\dot{\boldsymbol{\eta}}_L-k_{L,2}\mathbf{L}_2\boldsymbol{\eta}_L-c_{L,2}\mathbf{L}_2\dot{\boldsymbol{\eta}}_L\\-k_f\left(\mathbf{q}_L\boldsymbol{\eta}_L-\mathbf{q}_H\boldsymbol{\eta}_H\right)\mathbf{q}_L^T-c_f\left(\mathbf{q}_L\dot{\boldsymbol{\eta}}_L-\mathbf{q}_H\dot{\boldsymbol{\eta}}_H\right)\mathbf{q}_L^T-\left(-k_s\mathbf{p}\boldsymbol{\eta}_L+k_i\mathbf{i}_c\right)\end{Bmatrix} \tag{4.33}$$

$$\begin{Bmatrix}\left(\mathbf{M}_{s,H}+\mathbf{M}_{d,H}\right)\ddot{\boldsymbol{\eta}}_H\\+\omega_H\mathbf{G}_{d,H}\dot{\boldsymbol{\eta}}_H+\mathbf{K}_{s,H}\boldsymbol{\eta}_H\end{Bmatrix}=\begin{Bmatrix}\mathbf{f}_{s,H}+\mathbf{f}_{d,H}-k_H\mathbf{H}\boldsymbol{\eta}_H-c_H\mathbf{H}\dot{\boldsymbol{\eta}}_H\\-k_f\left(\mathbf{q}_H\boldsymbol{\eta}_H-\mathbf{q}_L\boldsymbol{\eta}_L\right)\mathbf{q}_H^T-c_f\left(\mathbf{q}_H\dot{\boldsymbol{\eta}}_H-\mathbf{q}_L\dot{\boldsymbol{\eta}}_L\right)\mathbf{q}_H^T\end{Bmatrix} \tag{4.34}$$

Rearranging Eqs. (4.33) and (4.34), with displacement dependent terms on the left-hand side and unbalance forces on the right-hand side, we get

$$\begin{Bmatrix}\left(\mathbf{M}_{s,L}+\mathbf{M}_{d,L}\right)\ddot{\boldsymbol{\eta}}_L+\left(\omega_L\mathbf{G}_{d,L}+c_{L,1}\mathbf{L}_1+c_{L,2}\mathbf{L}_2+k_ik_D\mathbf{P}\right)\dot{\boldsymbol{\eta}}_L+c_f\mathbf{q}_L\dot{\boldsymbol{\eta}}_L\mathbf{q}_L^T\\+\left(\mathbf{K}_{s,L}+k_{L,1}\mathbf{L}_1+k_{L,2}\mathbf{L}_2+k_ik_P\mathbf{P}-k_s\mathbf{P}\right)\boldsymbol{\eta}_L+k_f\mathbf{q}_L\boldsymbol{\eta}_L\mathbf{q}_L^T+k_ik_I\mathbf{P}\int\boldsymbol{\eta}_L dt\\-c_f\mathbf{q}_H\dot{\boldsymbol{\eta}}_H\mathbf{q}_L^T-k_f\mathbf{q}_H\boldsymbol{\eta}_H\mathbf{q}_L^T\end{Bmatrix}=\mathbf{f}_{s,L}+\mathbf{f}_{d,L} \tag{4.35}$$

$$\begin{Bmatrix}\left(\mathbf{M}_{s,H}+\mathbf{M}_{d,H}\right)\ddot{\boldsymbol{\eta}}_H+\left(\omega_H\mathbf{G}_{d,H}+c_H\mathbf{H}\right)\dot{\boldsymbol{\eta}}_H+c_f\mathbf{q}_H\dot{\boldsymbol{\eta}}_H\mathbf{q}_H^T\\+\left(\mathbf{K}_{s,L}+k_H\mathbf{H}\right)\boldsymbol{\eta}_H+k_f\mathbf{q}_H\boldsymbol{\eta}_H\mathbf{q}_H^T-c_f\mathbf{q}_L\dot{\boldsymbol{\eta}}_L\mathbf{q}_H^T-k_f\mathbf{q}_L\boldsymbol{\eta}_L\mathbf{q}_H^T\end{Bmatrix}=\mathbf{f}_{s,H}+\mathbf{f}_{d,H} \tag{4.36}$$

Now, let us assume,

TH-2966_176103027

$$\mathbf{q}_L\boldsymbol{\eta}_L\mathbf{q}_L^T=\mathbf{A}_1\boldsymbol{\eta}_L;\quad \mathbf{q}_H\boldsymbol{\eta}_H\mathbf{q}_L^T=\mathbf{A}_2\boldsymbol{\eta}_H;\quad \mathbf{q}_H\boldsymbol{\eta}_H\mathbf{q}_H^T=\mathbf{A}_3\boldsymbol{\eta}_H \quad \text{and} \quad \mathbf{q}_L\boldsymbol{\eta}_L\mathbf{q}_H^T=\mathbf{A}_4\boldsymbol{\eta}_L \tag{4.37}$$

$$\mathbf{f}_L=\mathbf{f}_{s,L}+\mathbf{f}_{d,L};\quad \text{and } \mathbf{f}_H=\mathbf{f}_{s,H}+\mathbf{f}_{d,H} \tag{4.38}$$

Substituting Eqs. (4.37) and (4.38) in Eqs. (4.35) and (4.36), we get

$$\left.\begin{aligned}&\left(\mathbf{M}_{s,L}+\mathbf{M}_{d,L}\right)\ddot{\boldsymbol{\eta}}_L+\left(\omega_L\mathbf{G}_{d,L}+c_{L,1}\mathbf{L}_1+c_{L,2}\mathbf{L}_2+k_ik_D\mathbf{P}+c_f\mathbf{A}_1\right)\dot{\boldsymbol{\eta}}_L\\&+\left(\mathbf{K}_{s,L}+k_{L,1}\mathbf{L}_1+k_{L,2}\mathbf{L}_2+k_ik_P\mathbf{P}-k_s\mathbf{P}+k_f\mathbf{A}_1\right)\boldsymbol{\eta}_L+k_ik_I\mathbf{P}\int\boldsymbol{\eta}_L dt\\&-c_f\mathbf{A}_2\dot{\boldsymbol{\eta}}_H-k_f\mathbf{A}_2\boldsymbol{\eta}_H\end{aligned}\right\}=\mathbf{f}_L \tag{4.39}$$

$$\left.\begin{aligned}&\left(\mathbf{M}_{s,H}+\mathbf{M}_{d,H}\right)\ddot{\boldsymbol{\eta}}_H+\left(\omega_H\mathbf{G}_{d,H}+c_H\mathbf{H}+c_f\mathbf{A}_3\right)\dot{\boldsymbol{\eta}}_H\\&+\left(\mathbf{K}_{s,L}+k_H\mathbf{H}+k_f\mathbf{A}_3\right)\boldsymbol{\eta}_H-c_f\mathbf{A}_4\dot{\boldsymbol{\eta}}_L-k_f\mathbf{A}_4\boldsymbol{\eta}_L\end{aligned}\right\}=\mathbf{f}_H \tag{4.40}$$

The solution for the equation of motion can be given as

$$\boldsymbol{\eta}_L=\boldsymbol{\eta}_a\mathrm{e}^{\mathrm{j}\omega_L t}+\boldsymbol{\eta}_b\mathrm{e}^{\mathrm{j}\omega_H t} \tag{4.41}$$

$$\boldsymbol{\eta}_H=\boldsymbol{\eta}_c\mathrm{e}^{\mathrm{j}\omega_H t}+\boldsymbol{\eta}_d\mathrm{e}^{\mathrm{j}\omega_L t} \tag{4.42}$$

Substituting, Eqs. (4.41) and (4.42) in Eqs. (4.39) and (4.40), we get

$$\mathbf{Z}_1\boldsymbol{\eta}_a+\mathbf{Z}_2\boldsymbol{\eta}_d=\mathbf{f}_L;\qquad \mathbf{Z}_3\boldsymbol{\eta}_c+\mathbf{Z}_4\boldsymbol{\eta}_b=0 \tag{4.43}$$

$$\mathbf{Z}_5\boldsymbol{\eta}_c+\mathbf{Z}_6\boldsymbol{\eta}_b=\mathbf{f}_H;\qquad \mathbf{Z}_7\boldsymbol{\eta}_a+\mathbf{Z}_8\boldsymbol{\eta}_d=0 \tag{4.44}$$

$$\text{with, } \mathbf{Z}_1=\left.\begin{aligned}&-\omega_L^2\left(\mathbf{M}_{s,L}+\mathbf{M}_{d,L}\right)+\mathrm{j}\omega_L\left(\omega_L\mathbf{G}_{d,L}+c_{L,1}\mathbf{L}_1+c_{L,2}\mathbf{L}_2+k_ik_D\mathbf{P}+c_f\mathbf{A}_1\right)\\&+\left(\mathbf{K}_{s,L}+k_{L,1}\mathbf{L}_1+k_{L,2}\mathbf{L}_2+k_ik_P\mathbf{P}-k_s\mathbf{P}+\frac{k_ik_I}{\mathrm{j}\omega_L}\mathbf{P}+k_f\mathbf{A}_1\right)\end{aligned}\right\};$$

TH-2966_176103027

$$\mathbf{Z}_2 = -\mathrm{j}\omega_L c_f \mathbf{A}_2 - k_f \mathbf{A}_2 ; \qquad \mathbf{Z}_3 = -\mathrm{j}\omega_H c_f \mathbf{A}_2 - k_f \mathbf{A}_2 ;$$

$$\mathbf{Z}_4 = \left\{ \begin{array}{l} -\omega_H^2 \left(\mathbf{M}_{s,L} + \mathbf{M}_{d,L} \right) + \mathrm{j}\omega_H \left(\omega_L \mathbf{G}_{d,L} + c_{L,1} \mathbf{L}_1 + c_{L,2} \mathbf{L}_2 + k_i k_D \mathbf{P} + c_f \mathbf{A}_1 \right) \\ + \left(\mathbf{K}_{s,L} + k_{L,1} \mathbf{L}_1 + k_{L,2} \mathbf{L}_2 + k_i k_P \mathbf{P} - k_s \mathbf{P} + \dfrac{k_i k_I}{\mathrm{j}\omega_L} \mathbf{P} + k_f \mathbf{A}_1 \right) \end{array} \right\};$$

$$\mathbf{Z}_5 = \left\{ \begin{array}{l} -\omega_H^2 \left(\mathbf{M}_{s,H} + \mathbf{M}_{d,H} \right) + \mathrm{j}\omega_H \left(\omega_H \mathbf{G}_{d,H} + c_H \mathbf{H} + c_f \mathbf{A}_3 \right) \\ + \left(\mathbf{K}_{s,H} + k_H \mathbf{H} + k_f \mathbf{A}_3 \right) \end{array} \right\};$$

$$\mathbf{Z}_6 = -\mathrm{j}\omega_H c_f \mathbf{A}_4 - k_f \mathbf{A}_4$$

$$\mathbf{Z}_7 = -\mathrm{j}\omega_L c_f \mathbf{A}_4 - k_f \mathbf{A}_4 ;$$

$$\mathbf{Z}_8 = \left\{ \begin{array}{l} -\omega_L^2 \left(\mathbf{M}_{s,H} + \mathbf{M}_{d,H} \right) + \mathrm{j}\omega_L \left(\omega_H \mathbf{G}_{d,H} + c_H \mathbf{H} + c_f \mathbf{A}_3 \right) \\ + \left(\mathbf{K}_{s,H} + k_H \mathbf{H} + k_f \mathbf{A}_3 \right) \end{array} \right\}$$

Substituting, $\boldsymbol{\eta}_d$ from Eq. (4.44) in Eq. (4.43) and substituting $\boldsymbol{\eta}_b$ from Eq. (4.43) in Eq. (4.44), we get

$$\left(\mathbf{Z}_1 - \mathbf{Z}_2 \frac{\mathbf{Z}_7}{\mathbf{Z}_8} \right) \boldsymbol{\eta}_a = \mathbf{f}_L ; \qquad \left(\mathbf{Z}_2 - \mathbf{Z}_1 \frac{\mathbf{Z}_8}{\mathbf{Z}_7} \right) \boldsymbol{\eta}_d = \mathbf{f}_L ;$$

$$\left(\mathbf{Z}_5 - \mathbf{Z}_6 \frac{\mathbf{Z}_3}{\mathbf{Z}_4} \right) \boldsymbol{\eta}_c = \mathbf{f}_H ; \qquad \left(\mathbf{Z}_6 - \mathbf{Z}_5 \frac{\mathbf{Z}_4}{\mathbf{Z}_3} \right) \boldsymbol{\eta}_b = \mathbf{f}_H \tag{4.45}$$

$$\boldsymbol{\eta}_a = \boldsymbol{\chi}_D \mathbf{f}_L ; \quad \boldsymbol{\eta}_b = \boldsymbol{\gamma}_D \mathbf{f}_H ; \quad \boldsymbol{\eta}_c = \boldsymbol{\kappa}_D \mathbf{f}_H ; \quad \boldsymbol{\eta}_d = \boldsymbol{\lambda}_D \mathbf{f}_L \tag{4.46}$$

with, $\boldsymbol{\chi}_D = \left(\mathbf{Z}_1 - \mathbf{Z}_2 \dfrac{\mathbf{Z}_6}{\mathbf{Z}_7} \right)^{-1} ; \qquad \boldsymbol{\kappa}_D = \left(\mathbf{Z}_5 - \mathbf{Z}_6 \dfrac{\mathbf{Z}_3}{\mathbf{Z}_4} \right)^{-1} ;$

TH-2966_176103027

$$\boldsymbol{\gamma}_D = \left(\mathbf{Z}_6 - \mathbf{Z}_5 \frac{\mathbf{Z}_4}{\mathbf{Z}_3} \right)^{-1} \quad \text{and} \quad \boldsymbol{\lambda}_D = \left(\mathbf{Z}_2 - \mathbf{Z}_1 \frac{\mathbf{Z}_8}{\mathbf{Z}_7} \right)^{-1}$$

where, $\boldsymbol{\chi}_D$ and $\boldsymbol{\kappa}_D$ are the influence coefficient matrices that describes the relationship of the unbalance forces in the low pressure and high-pressure rotor system with their corresponding responses. The influence coefficient matrix $\boldsymbol{\gamma}_D$ relates the displacement response in the LPR due to forces in HPR, and $\boldsymbol{\lambda}_D$ relates the displacement response in HPR due to forces in LPR. For the same frequencies in LPR and HPR, the matrices $\boldsymbol{\gamma}_D$ and $\boldsymbol{\lambda}_D$ are equivalent. The FEM model is developed to generate the displacement responses, which are utilized in the identification algorithm along with the introduction of virtual trial unbalances at the AMB location in the low-pressure shaft to justify the effectiveness of the estimation procedure.

4.4. Simulation results

The physical parameters utilized to describe the dual-rotor system are shown in Table 4.1. The stiffness coefficients of the integrated AMB system with the PID controller gains are listed in Table 4.2. The distribution of the random shaft unbalances in both HPR and LPR systems is shown in Fig. 4.4. The orientation and magnitude of the discrete disc unbalances introduced at the disc locations are mentioned in Table 4.1. The differential equation developed are solved in the MATLAB-SIMULINK platform using Runge-Kutta solver. The sampling frequency considered for the present system is equal to 2^{16} samples per sec. The natural frequencies of the system and the corresponding mode shapes are identified for the free vibration case without and with the application of AMB control forces, as shown in Fig. 4.5. The overall stiffness gain ($k_i k_P - k_s$) applied in the rotor system with AMB

TH-2966_176103027

control is added to the free vibration condition at the appropriate node location. Similarly, the overall derivative gain generated due to AMB control i.e., $k_i k_D$ is added to the system, which increases the overall damping of the system. The overall stiffness and the mass matrices are utilized to obtain the first three mode shapes of the rotor system as shown in Fig. 4.5 (a), (b), and (c), respectively, along the shaft axis. The modes of vibration with AMB control are found out to be similar to the modes of vibration without AMB control with slight variations at 2nd and 3rd mode for both HPR and LPR systems. This shows that the AMB integrated into the system introduces a trivial change in the dynamic behavior of the system but, on the other hand, can allow the rotor system to operate safely with a limited amount of vibration.

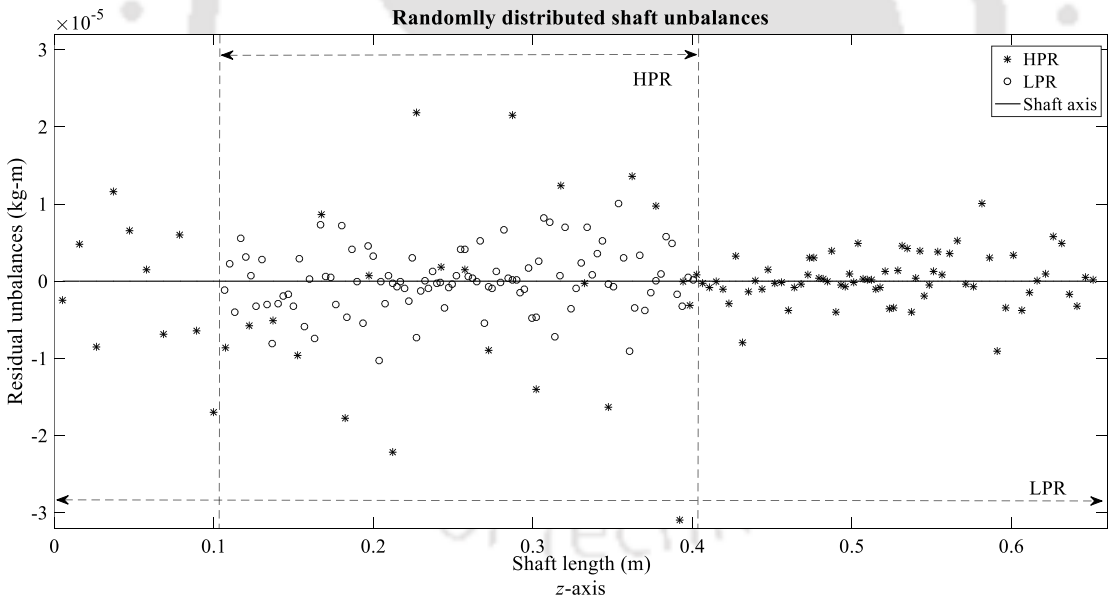


Fig. 4. 4. Randomly distributed residual shaft unbalances along the z-axis in both low-pressure rotor and high-pressure rotor systems.

TH-2966_176103027

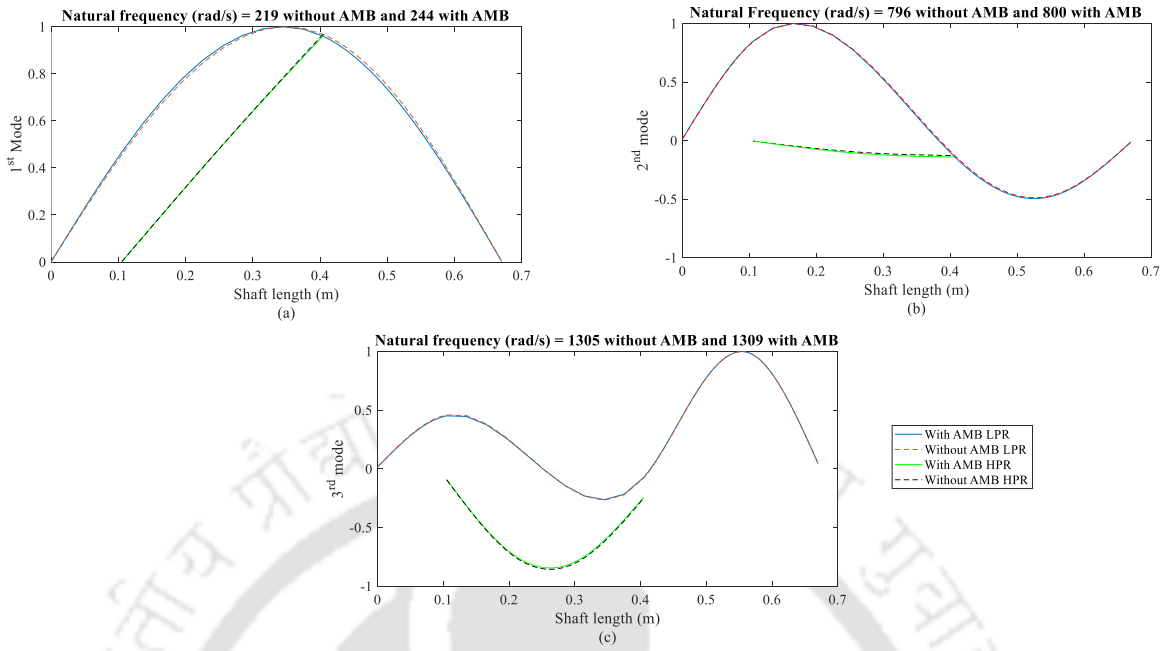


Fig. 4. 5. First three modes of the free vibration in both HPR and LPR systems along the shaft axis (*z*-axis).

The forward and backward whirls of the rotor system are identified inclusive of AMB control to identify the critical speed of the system due to the gyroscopic effects of discs in both HPR and LPR systems, as shown in Fig.4.6.

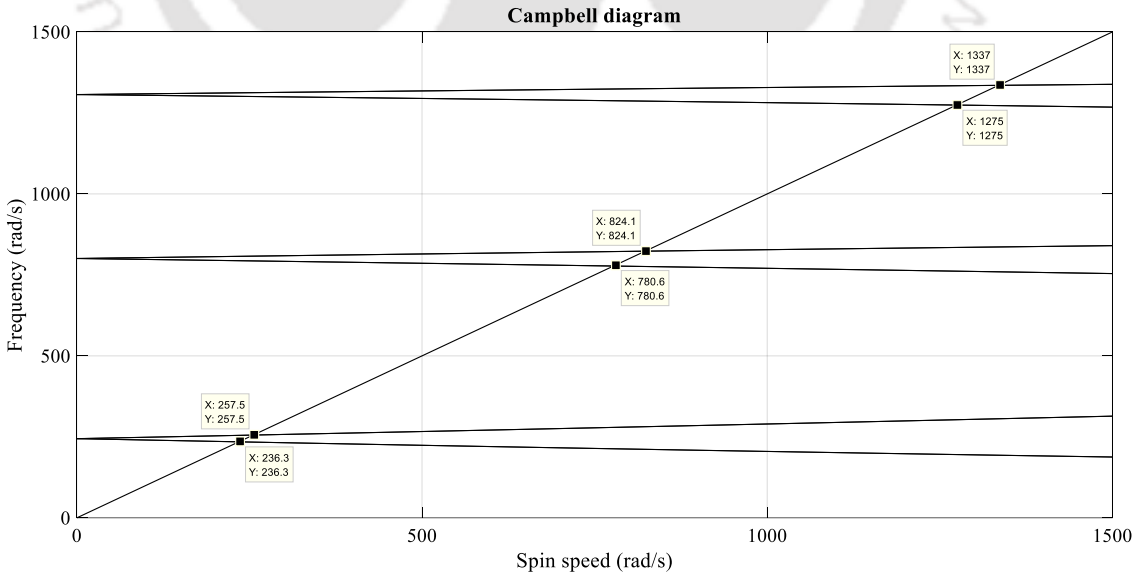


Fig. 4. 6. Campbell diagram of the dual-rotor system showing the forward and backward whirl frequencies.

TH-2966_176103027

Table 4. 1. Physical properties of the LPR and HPR system.

Physical Parameter	Value
Length of LPR shaft and elements (l_L)	0.67, (0.105, 0.30, 0.082, 0.083, 0.10) m
Length of HPR shaft and elements (l_H)	0.30 m, (0.100, 0.100, 0.100) m
Diameter of LPR shaft (d_L)	0.018 m
Inner ($d_{H,i}$) and outer diameter ($d_{H,o}$) of HPR shaft	0.026 and 0.030 m
Density of LPR and HPR shaft, ρ	7850 kg/m^3
Young's modulus of elasticity, E	2.06×10^{11} N/m^2
Mass, diametral and polar moment of inertia of rigid discs CD-1 and TD-1 in LPR	1.92 kg, (22.52 and 43.76) $\times10^{-4}$ kg-m^2
Mass, diametral and polar moment of inertia of rigid discs CD-2 and TD-2 in HPR	2.33 kg, (38.79 and 76.03) $\times10^{-4}$ kg-m^2
Mass, diametral and polar moment of inertia of AMB's core	0.88 kg, (5.17 and 3.98) $\times10^{-4}$ kg-m^2
Number of random unbalances in elements of LPR and HPR system	(10, 20, 20, 30, 20) and (30, 40, 30)
Magnitude and phase of residual unbalance at CD-1	3.85×10^{-5} kg-m, 1.2 rad
Magnitude and phase of residual unbalance at TD-1	5.77×10^{-5} kg-m, 2.1 rad
Magnitude and phase of residual unbalance at CD-2	4.66×10^{-5} kg-m, 2.1 rad
Magnitude and phase of residual unbalance at TD-2	6.99×10^{-5} kg-m, 1.2 rad
Stiffness coefficient of flexible bearing (FB-1, FB-2, FB-3)	$(5.5, 3.5 \text{ and } 4.5)\times10^7$ N/m
Damping coefficient of flexible bearing (FB-1, FB-2, FB-3)	(250, 240 and 260) N-s/m
Stiffness coefficient of intermediate flexible bearing, IFB	2×10^7 N/m
Damping coefficient of intermediate flexible bearing, IFB	210 N-s/m

TH-2966_176103027

The forward whirl frequencies of the dual-rotor system are found to be 257.5, 824.4, and 1337 rad/s, and the backward whirl frequencies are 236.3, 780.6, and 1275 rad/s. The rotor system is operated below the critical speeds to obtain the vibrational response of the system to validate the proposed balancing algorithm.

Table 4. 2. Physical properties of the AMB system

Physical Parameter	Value
Proportional gain of PID controller (k_P)	4200 A/m
Derivative gain of PID controller (k_D)	1 A-s/m
Integral gain of PID controller (k_P)	2000 A/m-s
Current stiffness factor, (k_i)	42.1 N/A
Displacement stiffness factor, (k_s)	105210 N/m

4.4.1 Vibration suppression in the dual-rotor system with AMB control

The rotor system is required to be operated at the desired level of vibration with the active control of the AMB system. The controller parameters of the AMB system affect the amount of reduction achieved in the rotor system. The Bode plot of PID controller as utilized in the present rotor-AMB system with controller parameter mentioned in Table 4.2 is shown in Fig. 4.7 below. The gain margin for the PID system is infinite and is stable for increase in controller gain. The proportional and the derivative gain of the AMB controller is varied in the stable region to check the level of reduction achieved in both LPR and HPR systems. The Bode plot of the rotor-AMB system with variation in the control parameters is shown in the Figs. 4.8 and 4.9 below. With the addition of the AMB, the maximum amplitude at critical speed is significantly reduced. The increment in the proportional gain generates stiffening effect in the system and the derivative gain improves the damping of the system. Now, the system is rotated at 100 rad/s with a frequency ratio ($\omega_r = \omega_H/\omega_L$) of

TH-2966_176103027

1.5, and the proportional gain (k_P) is varied with other controller parameters as constants. The percentage reduction of displacement responses in the time domain is obtained at different node locations in comparison to the displacement responses without AMB control, as shown in Fig. 4.10. With the increment of k_P from 4200 A/m to 5000 A/m, the displacement responses are reduced by 72 %, with the maximum amount of reduction achieved at the AMB and TD-1 disc nearer to the AMB location. A similar amount of reduction is seen at the discs locations in the HPR system, and the minimum reduction is obtained at the compressor disc in the LPR system. The time domain displacement responses of the system obtained without AMB control and with k_P = 4200 A/m, k_I = 2000 A/m-s and k_D = 1 A-s/m are shown in Fig. 4.11 (a) for CD-1 in LPR and 8 (c) for CD-2 in HPR.

The derivative gain of the AMB controller increases the damping property of the system, thereby affecting the maximum displacement response generated in the system while passing its critical speed. The rotor system is accelerated at an angular acceleration of 23.17 rad/s^2 for 20 sec with a frequency ratio (ω_r) of 1.5 to allow the rotor system to surpass its first critical speed. The value of derivative gain is increased from k_D = 1 to 3 A-s/m, while keeping the other controller parameters as constants. The displacement responses are reduced by 82% for a derivative gain of 3 A-s/m, as is seen in Fig. 4.12.

TH-2966_176103027

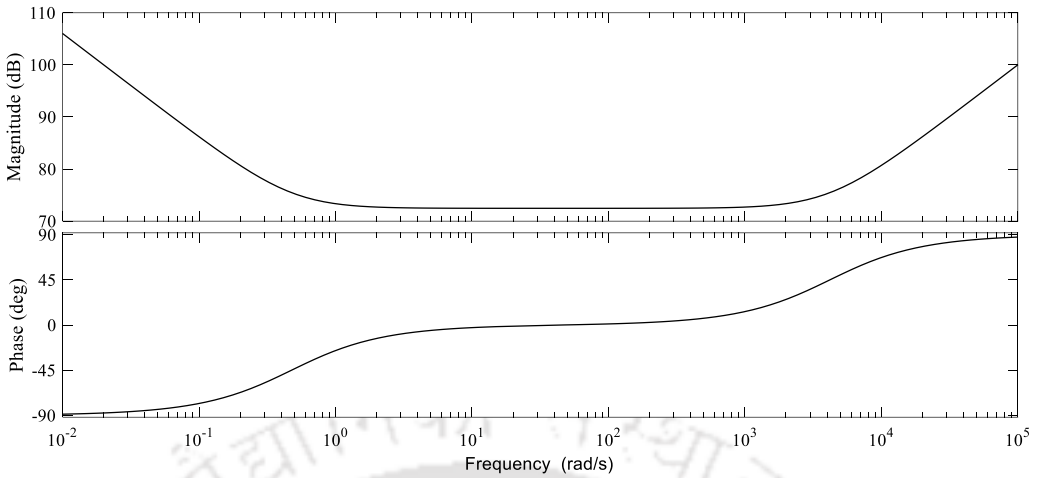


Fig. 4. 7. Bode plot for the PID controller utilized in the AMB system.

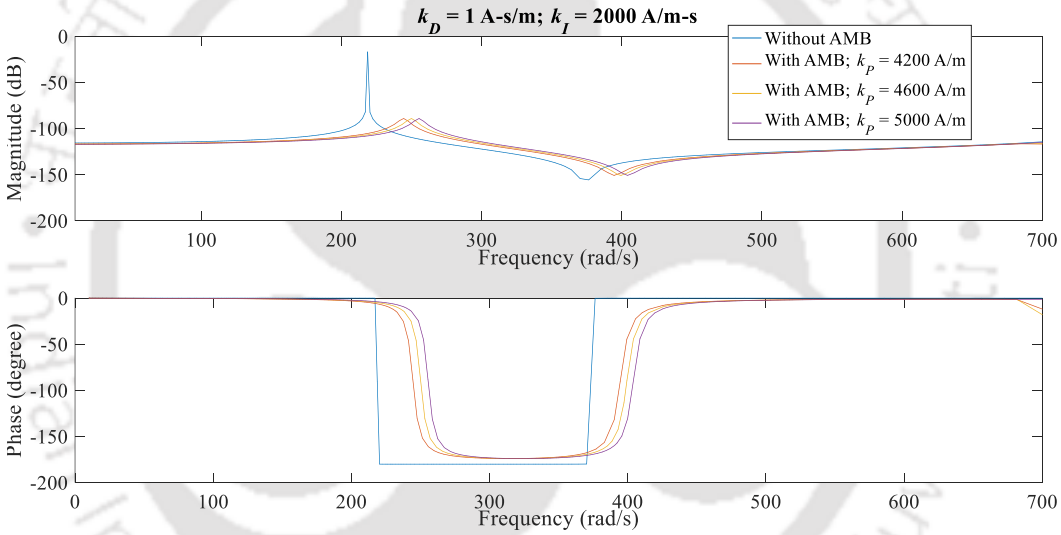


Fig. 4. 8. Bode plot for the dual rotor-AMB system at the disc location in LPR system with the variation in the proportional gain.

TH-2966_176103027

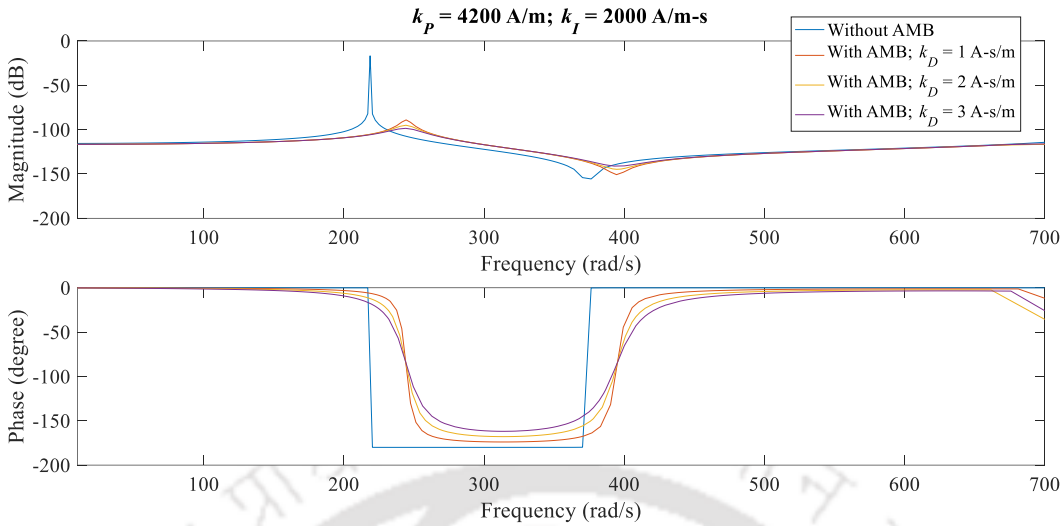


Fig. 4. 9. Bode plot for the dual rotor-AMB system at the disc location in LPR system with the variation in the derivative gain**.**

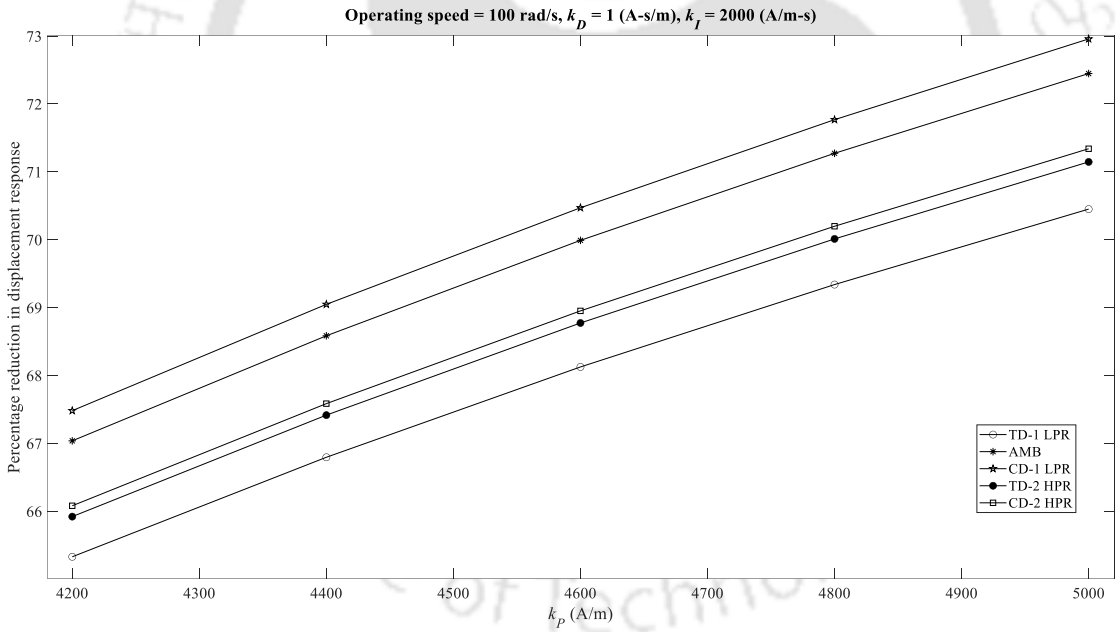


Fig. 4. 10. Percentage reduction of displacement amplitude of the dual rotor system with the variation of proportional gain (k_P) of the PID controller in the dual rotor-AMB system.

TH-2966_176103027

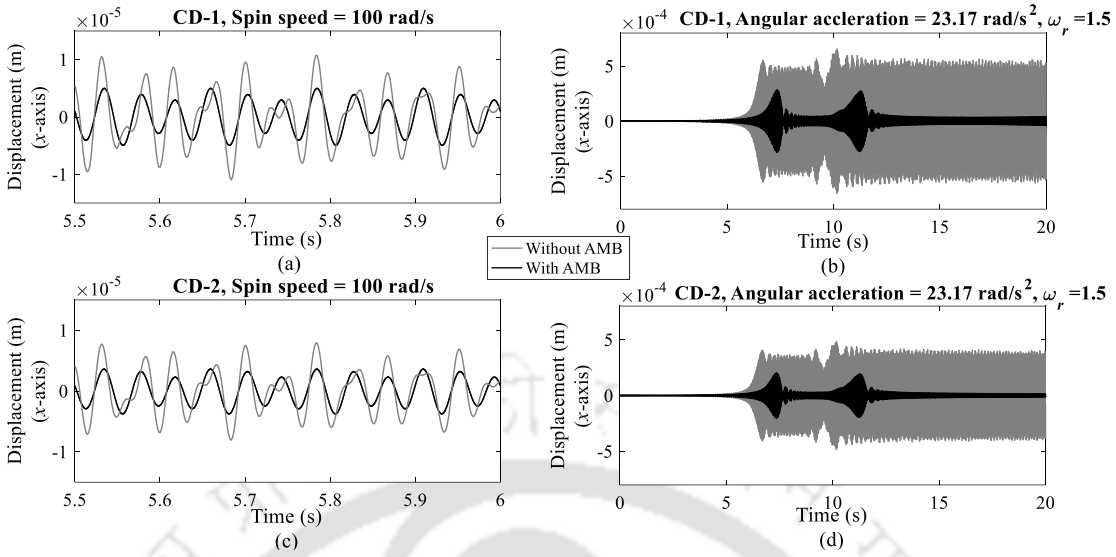


Fig. 4. 11. Displacement vs time plot at (a) CD-1 in LPR system, (c) CD-2 in HPR system at operating speed of 100 rad/s in LPR and ω_r = 1.5. Ramp-up displacement response vs time plot (b) CD-1 in LPR system, (d) CD-2 in HPR system with an angular acceleration of 23.17 rad/s^2 and ω_r = 1.5 with and without AMB control.

The percentage reduction of displacement responses with the variation of derivative gain has a similar pattern as seen in the variation of proportional gain with maximum reduction at AMB and TD-1 in LPR and minimum reduction at CD-1 in LPR. The time domain displacement responses of the run-up system obtained without AMB control, with k_P = 4200 A/m, k_I = 2000 A/m-s and k_D = 1 A-s/m, are shown in Fig. 4.11 (b) for CD-1 in LPR and 4.11 (d) for CD-2 in HPR.

TH-2966_176103027

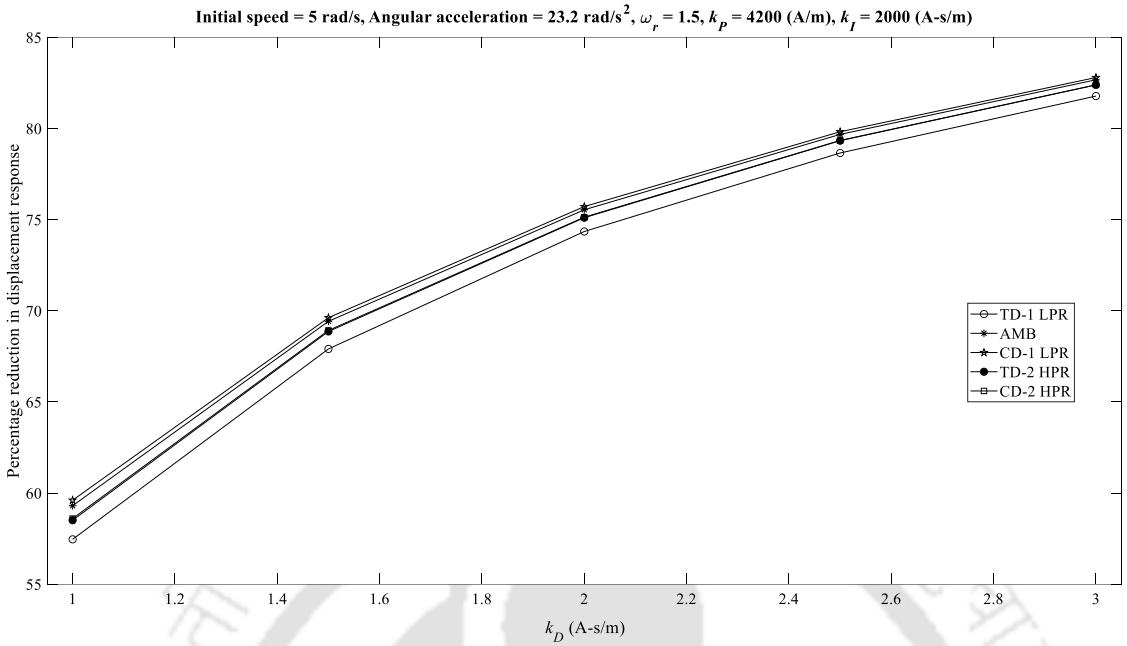


Fig. 4. 12. Percentage reduction of displacement amplitude of the dual rotor system with the variation of derivative gain (k_D) of the PID controller in the dual rotor-AMB system.

As the operating speed of the system increases with time, the first critical speed of the system occurs when the excitation frequency in HPR becomes equal to the first forward whirl speed of the system. After HPR, the operating speed in LPR also reaches the first forward whirl speed, and the first critical speed is again seen to be achieved in the dual rotor system as shown in Fig. 4.11 (b) and (d). The AMB system is found to be stable and can effectively control the vibrational response of the system in the desired limit.

4.4.2 Unbalance estimation of dual-rotor system with AMB control and MVEDRB

The resultant of the residual unbalances (both discrete disc unbalances and randomly distributed shaft unbalances) present in both HPR and LPR systems are identified at the respective disc locations using virtual trial unbalances and influence coefficient method as mentioned in Eqs. (4.1) through (4.14).

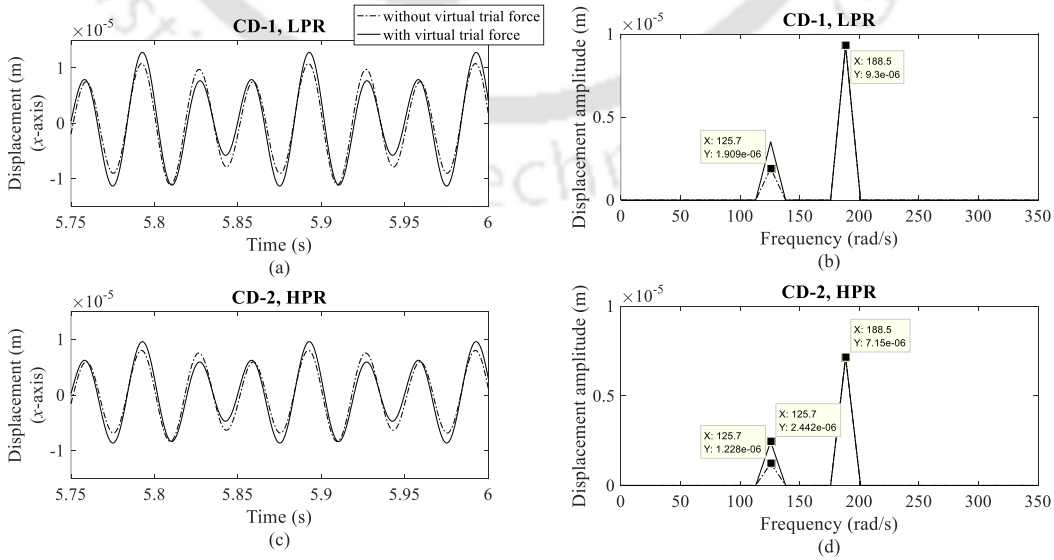
TH-2966_176103027

4.4.2.1 Initial run of rotor system without external excitation

The system is rotated below its first critical speed, i.e., at spin speeds (ω_L) of 125.7 rad/s and the frequency ratio of 1.5. Time domain displacement responses of the system are obtained at different node locations, with AMB, as shown in Fig. 4.13 (a) and (c) at compressor discs CD-1 and CD-2, respectively. The displacement amplitude and phase corresponding to the different operating speeds are obtained using FFT transform as shown in Fig. 4.13 (b) and (d).

4.4.2.2 Additional low-pressure rotor frequency (ω_L) magnetic excitation at the AMB

In the second run, a virtual trial unbalance (magnitude = 8×10^{-5} kg-m and phase = 20°) is introduced at the AMB location as the magnetic excitation force mentioned in Eq. (4.4) with the same excitation frequency as of LPR rotor system. The current stiffness factor (k_i) is obtained for the present AMB system in order to generate the equivalent amount of trial current in the AMB system. A load of 2 N is applied in the system at the AMB location at standstill condition, the static displacement generated by the load is reduced to zero by the static current developed at the AMB, as shown in Fig 4.14 (a) and (b).



TH-2966_176103027

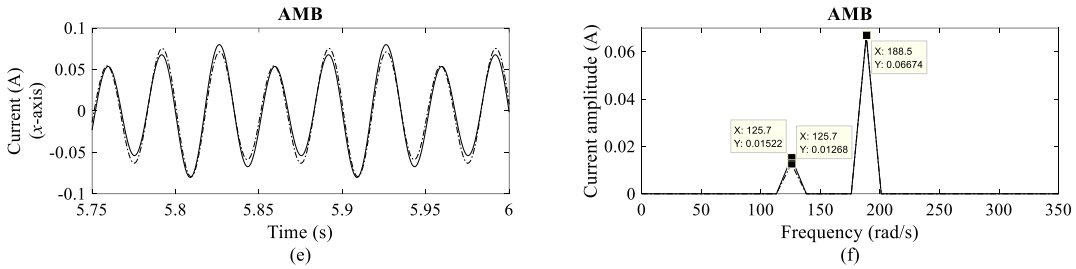


Fig. 4. 13. Displacement vs time plot at (a) CD-1 in LPR system, (c) CD-2 in HPR system, (e) AMB in LPR system and displacement amplitude vs frequency plot at (b) CD-1 in LPR system, (d) CD-2 in HPR system, (f) AMB in LPR system depicting change in displacement response with addition of virtual trial magnetic excitation of low-pressure rotor frequency (125.7 rad/s).

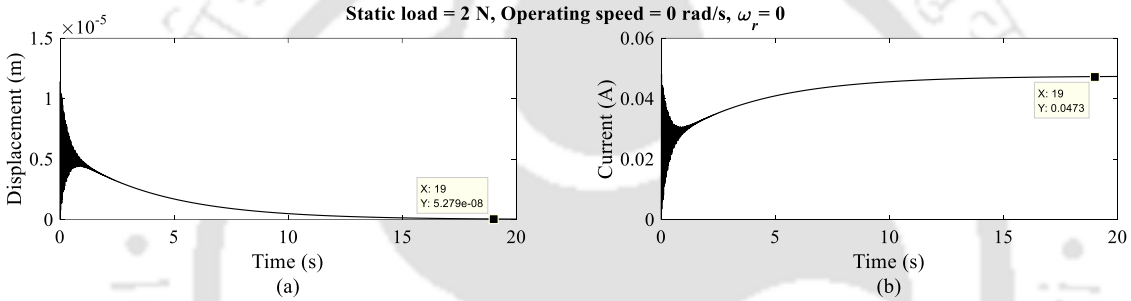


Fig. 4. 14. (a) Displacement vs time plot at AMB location in LPR system (b) control current vs time plot in AMB system due to static load of 2 N at AMB location.

The ratio of static current generated to the load applied is equivalent to the current stiffness factor and is obtained equal to 42.28 N/A, which varies by 0.42% from the assumed values.

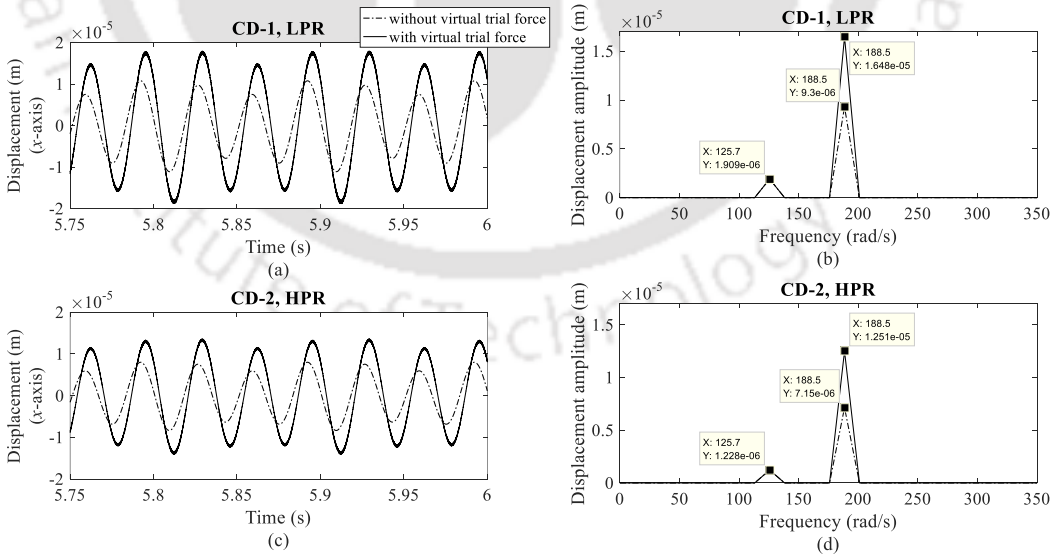
Now, after the application of the virtual trial unbalance, the displacement responses of the system are obtained, and the FFT of the responses is carried out. The influence coefficients corresponding to the unbalance forces at disc locations and the displacement responses at the AMB locations in LPR system are obtained as shown in Eq.(4.6). The displacement responses of the system before and after application of virtual trial unbalance is shown in Fig. 4.13 (a) and (c) at CD-1 and CD-2 locations, respectively. As the excitation frequency of the virtual trial unbalance is equivalent to the operating frequency

TH-2966_176103027

of the LPR system, the displacement amplitude corresponding to ω_L and the amplitude corresponding to the ω_H remains approximately constant as shown in Fig. 4.13 (b) and (d) in LPR and HPR system respectively. The control current generated in the AMB system with and without the introduction of the virtual trial unbalance is shown in Fig. 4.13 (e). The current amplitude in the frequency domain is shown in Fig. 4.13 (f), and the current amplitude is changed corresponding to the operating frequency of the LPR system.

4.4.2.3 Additional high-pressure rotor frequency (ω_H) magnetic excitation at the AMB

In the third run, the virtual trial unbalance is excited at the operating frequency of high pressure rotor (ω_H). The displacement responses of the rotor system at the required locations are obtained. The influence coefficients corresponding to the unbalance forces in the HPR system with respect to the displacement response at the AMB location are estimated using Eq. (4.9). The displacement response of the system in the time domain at both CD-1 and CD-2 location is shown in Fig. 4.15 (a) and (c), respectively.



TH-2966_176103027

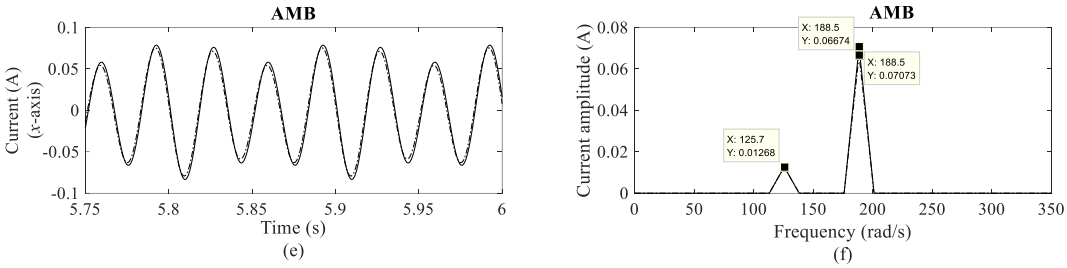


Fig. 4. 15. Displacement vs time plot at (a) CD-1 in LPR system, (c) CD-2 in HPR system, (e) AMB in LPR system and displacement amplitude vs frequency plot at (b) CD-1 in LPR system, (d) CD-2 in HPR system, (f) AMB in LPR system depicting change in displacement response with addition of virtual trial magnetic excitation of high-pressure rotor frequency (188.5 rad/s).

The corresponding displacement amplitudes after the FFT transform is shown in Fig. 4.15 (b) and (d). As the excitation frequency of virtual trial unbalances is the same as the operating frequency of HPR, the amplitude corresponding to ω_H is changed with the additional excitation. The estimated influence coefficients in both cases are obtained for different spin speeds, i.e., 100.53 to 150.79 rad/s with an increment of 6.28 rad/s. The influence coefficients, along with the displacement response in the initial run of the rotor system, are utilized to estimate the residual unbalances present in both HPR and LPR systems at the disc locations. In order to check the robustness of the identification algorithm with the variation in the level of random noise added to the time domain displacement responses, the estimation procedure of the residual unbalances is carried out in two cases.

Case I: Estimation of discrete disc unbalances

At first, the discrete disc unbalances are only considered in the rotor system and are estimated using the influence coefficients and displacement responses as per Eqs. (4.12) to (4.14). The estimated values of the residual unbalances at disc locations in LPR and HPR

TH-2966_176103027

system are given in Table 4.3 with the sequential addition of 5%, 8%, and 10% of random noise in the time domain displacement responses obtained from the FEM model. The estimated values of unbalance magnitudes are equal to the assumed values up to 3 decimal places for 0% of random noise. With the increment of random noise in the response, the level of variation in the estimated values increases to 7% for CD-1 and 5% for CD-2. Whereas, for the disc locations nearer to the AMB system, i.e., for TD-1 and TD-2, the percentage variation in the estimated values is less than 1%. The variation in the estimated phases with the random noises is shown in Table 4.4. The maximum variation in the estimated values of phase is at CD-1 location with a variation of 6%, followed by TD-1 with a maximum variation of 3%. The percentage variation of phases at CD-2 and TD-2 locations is nearer to 1%. The same estimation process is repeated for the frequency ratio of $\omega_r = -1.5$, and the estimated values of unbalance magnitude and phases are shown in Table 4.3 and 4.4, respectively. The percentage variation in the unbalance magnitude is slightly lower than that estimated for $\omega_r = 1.5$, i.e., about 5% at CD-2 location in HPR system. Similarly, the estimated values of phases have a lower variation than $\omega_r = 1.5$ condition. For frequency ratio $\omega_r = -1.5$, the displacement response corresponding to the operating frequencies are distributed in the positive and negative half spectrum of the FFT.

TH-2966_176103027

Table 4. 3. Assumed and estimated magnitude of residual discs unbalances with the variation of different percentages of noise for $\omega_r = 1.5$ and $\omega_r = -1.5$.

Residual disc unbalances magnitude ($\times 10^{-5}$) kg-m, $\omega_r = 1.5$								
	Assumed	Estimated						
		0% noise	5% noise	% variation	8% noise	% variation	10% noise	% variation
CD-1	3.848	3.848	3.712	–3.55	3.631	–5.64	3.578	–7.01
TD-1	5.772	5.772	5.764	–0.15	5.761	–0.19	5.761	–0.20
CD-2	4.660	4.660	4.546	–2.44	4.478	–3.91	4.431	–4.91
TD-2	6.990	6.990	7.024	0.48	7.043	0.76	7.056	0.95
Residual disc unbalances magnitude ($\times 10^{-5}$) kg-m, $\omega_r = -1.5$								
CD-1	3.848	3.848	3.891	1.12	3.918	1.80	3.935	2.26
TD-1	5.772	5.772	5.711	–1.05	5.675	–1.69	5.650	–2.11
CD-2	4.660	4.660	4.531	–2.76	4.455	–4.39	4.405	–5.46
TD-2	6.990	6.990	7.008	0.25	7.018	0.39	7.024	0.49

Whereas, for $\omega_r = 1.5$, the displacement responses are in the positive half spectrum only. Therefore, the displacement responses are estimated more accurately in the $\omega_r = -1.5$ condition through FFT. As the estimated value shows very less variation in unbalance magnitude and phases, the identification algorithm is found to be robust with the variation of different percentages of random noises.

TH-2966_176103027

Table 4. 4. Assumed and estimated phases of residual discs unbalances with the variation of different percentages of noise for $\omega_r = 1.5$ and $\omega_r = -1.5$.

Residual disc unbalances phase (rad), $\omega_r = 1.5$								
	Assumed	Estimated						
		0% noise	5% noise	% variation	8% noise	% variation	10% noise	% variation
CD-1	1.200	1.200	1.234	2.80	1.255	4.57	1.269	5.79
TD-1	2.100	2.100	2.073	–1.28	2.057	–2.05	2.046	–2.57
CD-2	2.100	2.100	2.098	–0.08	2.097	–0.15	2.095	–0.22
TD-2	1.200	1.200	1.207	0.57	1.211	0.92	1.214	1.15
Residual disc unbalances phase (rad), $\omega_r = -1.5$								
CD-1	1.200	1.200	1.215	1.25	1.224	1.99	1.230	2.48
TD-1	2.100	2.100	2.099	–0.03	2.099	–0.04	2.099	–0.05
CD-2	2.100	2.100	2.087	–0.63	2.078	–1.04	2.072	–1.33
TD-2	1.200	1.200	1.210	0.84	1.216	1.34	1.220	1.67

Case II: Simultaneous estimation of discrete disc unbalances, and randomly distributed shaft unbalances

Now, the randomly distributed shaft unbalances in considered in both LPR and HPR systems, as shown in Fig. 4.4, along with discrete disc unbalances. The estimation is carried out using Eqs. (4.12) through (4.14) at disc locations in the dual rotor system with variation of different percentages of noise for $\omega_r = 1.5$. For sequential addition of the noise percentage of 0%, 5%, 8%, and 10% in simulated responses, the estimated magnitude of unbalances is shown in Table 4.5.

TH-2966_176103027

Table 4. 5. Assumed and estimated magnitude of overall discrete discs and randomly distributed shaft unbalances with the variation of different percentages of noise for $\omega_r = 1.5$ and $\omega_r = -1.5$.

Residual disc and shaft unbalances magnitude ($\times 10^{-5}$) kg-m, $\omega_r = 1.5$							
	0% noise	5% noise	% variation	8% noise	% variation	10% noise	% variation
CD-1	5.329	5.571	4.54	5.716	7.26	5.813	9.08
TD-1	5.398	5.210	–3.48	5.098	–5.56	5.024	–6.93
CD-2	7.200	7.030	–2.36	6.930	–3.75	6.850	–4.86
TD-2	10.460	10.430	–0.29	10.410	–0.48	10.390	–0.67
Residual disc and unbalances magnitude ($\times 10^{-5}$) kg-m, $\omega_r = -1.5$							
CD-1	5.480	5.534	0.98	5.568	1.61	5.591	2.03
TD-1	5.077	5.108	0.61	5.128	1.00	5.141	1.26
CD-2	7.200	7.050	–2.08	6.960	–3.33	6.900	–4.17
TD-2	10.460	10.430	–0.29	10.410	–0.48	10.400	–0.57

The estimated magnitude varies by a maximum percentage of 9% with 0% noise at the CD-1 location. The estimates have relatively less variation of about 2% for the frequency ratio of $\omega_r = -1.5$. The variation in phase estimate with the different random noise levels is shown in Table 4.6. The maximum percentage variation in the phase estimates is about 2% for both $\omega_r = 1.5$ and $\omega_r = -1.5$ frequency ratio. As it is seen from Table 4.5 and 4.6, the presence of shaft unbalances changes the unbalance estimates at the disc locations, and therefore it is required to be considered and analyzed for a balancing problem in the rotating machinery.

TH-2966_176103027

Table 4. 6. Assumed and estimated phase of overall discrete discs and randomly distributed shaft unbalances with the variation of different percentages of noise for $\omega_r = 1.5$ and $\omega_r = -1.5$.

	0% noise	5% noise	% variation	8% noise	% variation	10% noise	% variation
Residual disc and shaft unbalances phase (rad), $\omega_r = 1.5$							
CD-1	3.058	3.073	0.49	3.081	0.75	3.086	0.92
TD-1	–2.434	–2.416	–0.74	–2.404	–1.23	–2.396	–1.56
CD-2	3.042	3.051	0.29	3.056	0.46	3.059	0.56
TD-2	0.699	0.707	1.14	0.712	1.85	0.716	2.43
Residual disc and shaft unbalances phase (rad), $\omega_r = -1.5$							
CD-1	3.140	3.118	–0.70	3.105	–1.11	3.096	–1.40
TD-1	–2.469	–2.448	–0.85	–2.435	–1.38	–2.427	–1.70
CD-2	3.042	3.049	0.23	3.053	0.36	3.056	0.46
TD-2	0.699	0.705	0.84	0.710	1.57	0.713	2.00

The reduction in variation percentage is possible with the accuracy in estimation of displacement amplitude and phases in the frequency domain with increase in measurement uncertainties. It can be done with increase in number of excitation planes (AMB). The number of rows in the identification matrices as mentioned in Eqns. 4.10 and 4.11 would increase and the estimation of influence coefficient can be performed with more accuracy. But it would require more AMBs in the system and the manufacturing cost would increase. Also, the accuracy can be improved by obtaining the influence coefficients at greater number of rotor runs as mentioned in Eq. 4.14. But the computational time and the operation time to obtain the responses at several runs would also increase.

TH-2966_176103027

4.4.3 Balancing of dual-rotor system with AMB control

The resultant estimates of the shaft and disc unbalances at the disc locations are utilized for balancing the dual rotor system. The residual unbalances estimated with 10% of measurement noise and $\omega_r = 1.5$, as shown in Table 4.5, are added at their respective planes at opposite phases obtained in Table 4.6. The system is accelerated at an angular acceleration of 23.17 rad/s^2. Above its first critical speed to check the level of vibration reduction achieved in both HPR and LPR rotor system as shown in Fig. 4.16.

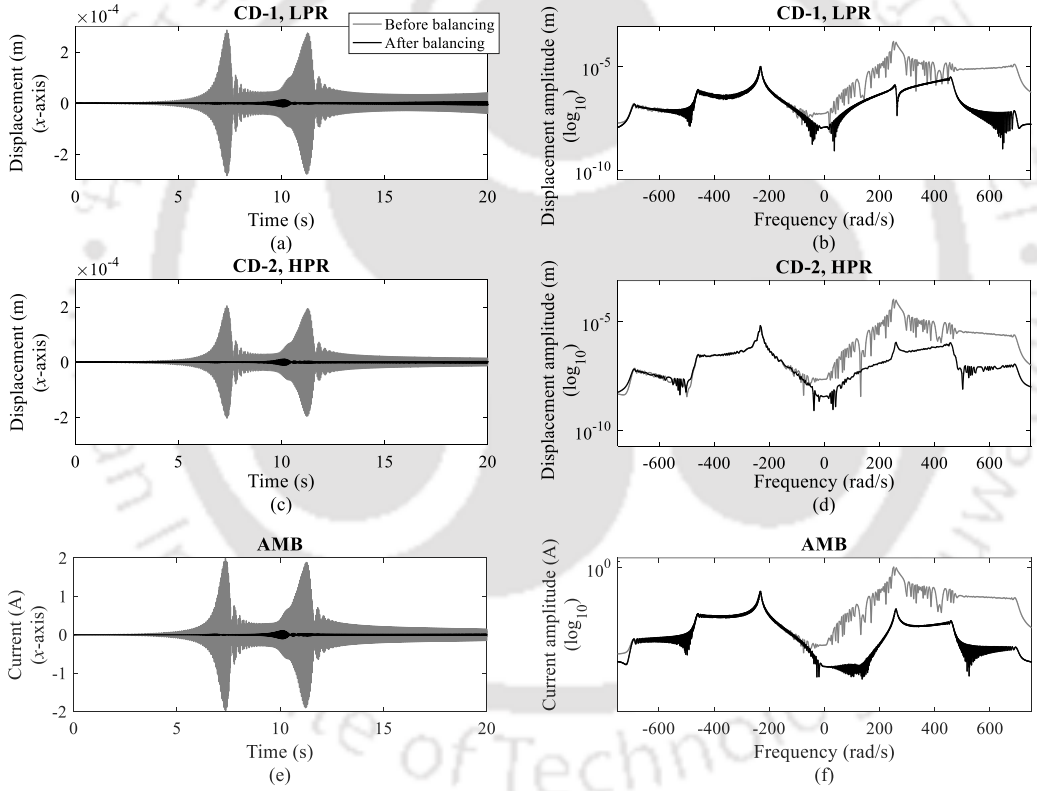
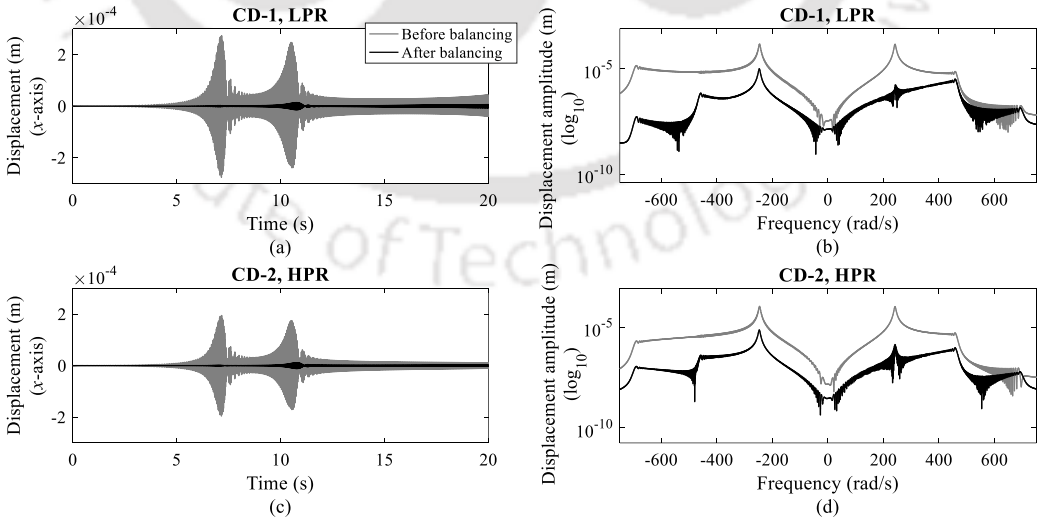


Fig. 4. 16. Ramp-up displacement vs time plot at (a) CD-1 in LPR system, (c) CD-2 in HPR system, (e) AMB in LPR system and ramp-up displacement amplitude vs frequency plot at (b) CD-1 in LPR system, (d) CD-2 in HPR system, (f) AMB in LPR system depicting change in displacement response after balancing of rotor system with an angular acceleration of 23.17 rad/s^2 and frequency ratio, $\omega_r = 1.5$.

TH-2966_176103027

As it is seen from, Fig. 4.16 (a) and (c), the time domain displacement responses of the LPR and HPR system at CD-1 and CD-2 location, respectively, are reduced from 2.87×10^{-4} m to 1.61×10^{-4} m (CD-1) and 2.05×10^{-4} m to 1.01×10^{-4} m (CD-2) by a percentage of 94% after balancing. Fig. 4.16 (b) and (d) show the reduction of displacement amplitude after balancing in the frequency domain. The grey line is the displacement response before balancing, and the black line represents the displacement response after balancing. The control current being utilized by the AMB to suppress the vibration response also gets reduced by 94%, i.e., from 1.98 A to 0.15 A after balancing as shown in Fig. 4.16 (e) and (f). The reduction of control current in the AMB reduces the overall power consumption of the system, and the AMB can respond to the other faults present in the rotor system without achieving a saturation limit. The same procedure is followed for the frequency ratio $\omega_r = -1.5$ and the displacement responses obtained before and after balancing are shown in Fig. 4.17 (a) and (c) at CD-1 and CD-2, respectively, with a percentage reduction of 94.9 %.



TH-2966_176103027

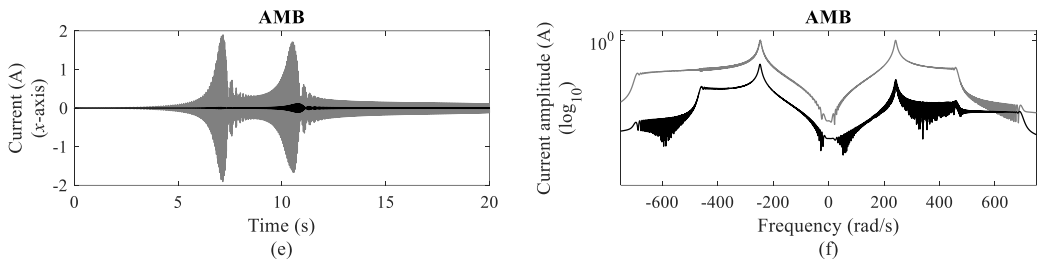


Fig. 4. 17. Ramp-up displacement vs time plot at (a) CD-1 in LPR system, (c) CD-2 in HPR system, (e) AMB in LPR system and ramp-up displacement amplitude vs frequency plot at (b) CD-1 in LPR system, (d) CD-2 in HPR system, (f) AMB in LPR system depicting change in displacement response after balancing of rotor system with an angular acceleration of 23.17 rad/s^2 and frequency ratio, $\omega_r = -1.5$.

The displacement amplitude in the frequency domain before and after balancing is shown in Fig. 4.17 (b) and (d), respectively. The control current in the AMB system before and after balancing is shown in Fig. 4.17 (e) and (f), and the percentage reduction is found to be 94.5 %. The results obtained in the above cases are able to reduce the vibration response of the dual-rotor system by an appreciable amount in both LPR and HPR rotor systems. The coupling of both rotor systems through IFB allows the AMB excitation in LPR and MVEDRB methodology to estimate the residual unbalances in both the inner and outer rotor systems simultaneously. The on-site unbalance estimation procedure with minimum information of the system will allow the efficient condition monitoring of the rotor system by reducing both mechanical and computational efforts. The virtual trial unbalances in the form of magnetic excitation can clearly overcome the difficulty in manual addition of trial unbalances and allow the balancing of the complex dual-rotor system at a regular interval.

TH-2966_176103027

4.5. Concluding Remarks

An on-site balancing methodology is developed for the dual rotor-bearing system with AMB control. The implementation of AMB in the LPR system reduces the vibrational response of both LPR and HPR systems with residual unbalances (discrete disc unbalances and randomly distributed shaft unbalances). The control loop of the AMB allows the system to be stable and within the limited amplitude of vibrational response in the presence of rotors faults and external magnetic excitations. Due to the coupling effect of the IFB present in the system, the external forces present in the LPR system affects the displacement response of the HPR system and vice versa. This effect is utilized for simultaneous estimation of residual unbalances in LPR and HPR systems with external magnetic excitation through AMB in the LPR system. With the minimum information of the dual rotor system, the residual unbalances can be effectively estimated at the required disc locations using the MVEDRB. The identification algorithm is able to estimate the residual unbalances for both positive and negative frequency ratios of the rotor system. The algorithm is found to be robust with the addition of different levels of measurement noises in the displacement responses. The balanced system is able to cross its critical speed with the desired level displacement response. The control current utilized in the suppression of the vibration is greatly reduced after balancing, which reduces the overall power consumption of the AMB system. The application of virtual trial unbalance can effectively replace the conventional procedure of balancing of dual rotor system with the manual addition of trial unbalances. The integration of AMB in the dual rotor system is therefore essential as a controller as well as an exciter for the simultaneous control and identification of the rotor faults present in the dual-rotor system. The application of AMB in controlling

TH-2966_176103027

vibration and its application in the estimation of residual unbalances in different rotor systems is shown in the recent chapters. Now, the experimental challenges in the application of AMB in the physical rotor system with the implementation of VTUs for balancing are described in the next chapter.

TH-2966_176103027

CHAPTER 5

EXPERIMENTAL INVESTIGATION ON THE BALANCING OF HIGH-SPEED ROTOR-AMB SYSTEMS WITH SWITCHING OF BIAS CURRENT USING VIRTUAL TRIAL UNBALANCE

This chapter deals with the high-speed balancing of experimental rotor test rig supported on the conventional bearings and integrated with the AMB as a controller as well as exciter. The physical and electrical connections with the working of different components of the rotor-AMB system are described. The control structure with the PID controller is developed based on the differential driving mode control. The practical difficulty in limiting the power consumption of the AMB system and the generation of virtual trial unbalances with synchronized excitation frequency is discussed in the present chapter. The comparison between the developed VTEICM and the conventional ICM is performed to show the effectiveness of VTEICM in balancing the rotor-AMB system operating above its critical speed with VTUs and AMB control. The optimization of power consumption by the AMB is shown with the variation of bias current at the different operating speeds of the rotor system.

5.1. Introduction

There is a lot of practical difficulty in high-speed balancing during the run-up of the rotor system above its critical speed. With AMB control, the system can be run-up to high speed, and displacement responses can be obtained. But the control structure of the AMB requires

TH-2966_176103027

a continuous large magnitude of bias current to accommodate the excessive control generated near the critical speed. The excessive supply of control and bias current in the run-time increases the heating of coils and power consumption of the AMB system. To limit the utilization of bias current, in the present work, switching of bias current is implemented that allows the rotor-AMB system to switch between high and low values of the bias current on the requirement. The bias current is increased at a higher value only near the critical speed to accommodate excessive control current. The VTUs are utilized along with VTEICM to estimate the residual unbalances in the rotor system. The VTUs are generated at the AMB location as magnetic excitation to mimic the behavior of the added unbalances in the accelerating system. The excitation frequency of the virtual trial unbalances is required to be generated at the operating speed in real-time. An algorithm is developed using the dSPACE-SIMULINK platform to operate the rotor system with voltage feedback to the motor speed control unit and simultaneous generation of the control current at the AMB actuator. The practical difficulties in synchronizing the excitation frequency and operating speed are addressed with voltage/speed factor and phase-lag correction in the motor speed control unit. The Synchronized VTUs are generated with the required correction, and VTEICM is applied to estimate the residual unbalances with the AMB control.

5.2. Description of the Rotor-AMB Test-Rig

In the present work, the experimental test rig consists of an RK-4 rotor kit, as shown in Fig. 5.1 (a), and was modified by integrating an AMB into it. The rotor system consists of a flexible mild-steel shaft of 510 mm length and 10 mm diameter supported on bush

TH-2966_176103027

bearings. The rigid discs are mounted on the shaft are utilized as the balancing planes. The discs are 800 grams in weight, and the grooves are at a 30 mm distance from the center of the discs. The zero-degree position in the discs is aligned with the reference slot present in the flexible coupling, as shown in Fig. 5.1 (b). The discs are provided with grooves at different orientations to add or remove the trial or balance masses, as shown in Fig. 5.1 (c). The torque is transmitted from the motor through a flexible coupling. The operating speed of the system varies from 5 Hz to 167 Hz with the help of a motor speed control unit (MSCU).

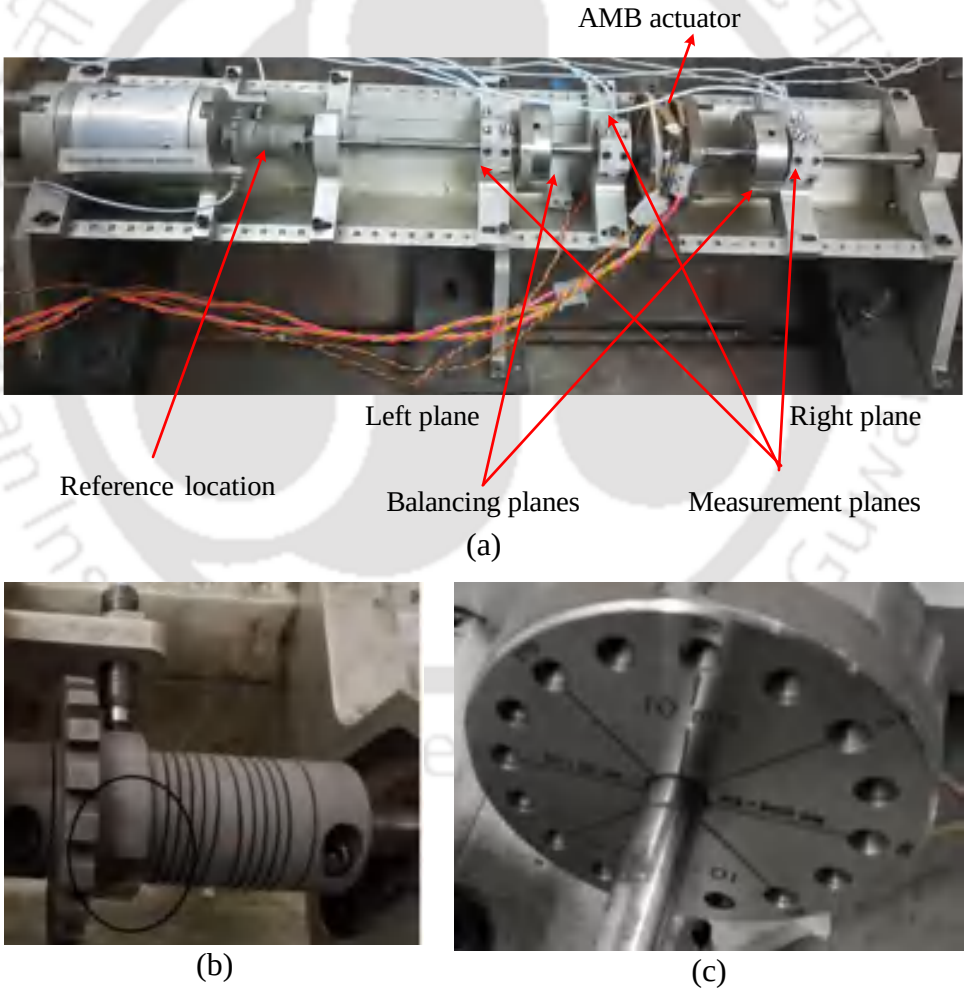


Fig. 5. 1 (a) An experimental RK4 rotor test-rig integrated with AMB, (b) slot near flexible coupling to obtain the reference signal, and (c) balancing disc mounting with groves.

TH-2966_176103027

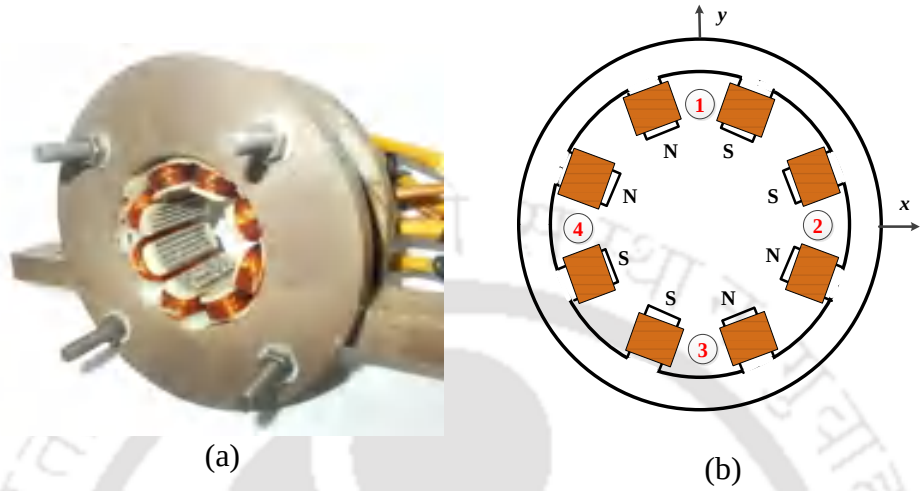
An AMB is integrated into the rotor test rig in between the two balancing discs to control the level of vibration as well as generate excitation forces to estimate the residual unbalances. The closed-loop control structure of the AMB is implemented with the help of components such as an 8-pole actuator, PID controller developed on SIMULINK-dSPACE interface, power amplifiers, eddy current sensors, and current probes. The journal bearing carries the load of the rotor system, and the AMB controls the displacement response of the rotor system within desired levels in real-time. The detailed description of the components of the AMB system required to establish the closed-loop control structure is described in the next section.

5.2.1 Electromagnetic actuator

The eight-pole electromagnetic actuator is made up of laminated silicon steel sheets that are stacked together to minimize the eddy current loss. The half-angle between poles of the electromagnet is 22.5°. The actuator has been taken from the DC stepper motor (12 V, 1.5 A) of 0.1 kg-m torque capacity, as shown in Fig. 5.2 (a). The geometrical dimensions of the actuator are mentioned in Table 5.1. The eight poles are divided into four pairs of electromagnets, i.e., two pairs of poles (2-4) for vibration control along the horizontal axis (x) and two pairs of poles (1-3) for control along the vertical axis (y). The windings of the copper coils are done in such a way that each pair of poles has two poles of opposite polarity. To minimize the flux leakage in the actuator, the orientation of the poles is kept as N-S-S-N-N-S-S-N or S-N-N-S-S-N-N-S in a clockwise manner, as shown in Fig. 5.2 (b). A ferromagnetic core made up of laminated silicon steel sheets is mounted on the shaft to maximize the flow of magnetic flux through the core. The air gap between the core and the

TH-2966_176103027

8-pole actuator is 0.4 mm. The actuator is mounted on the rotor test rig, as shown in Fig. 5.1 (a) with additional attachments.



(a) (b)

Fig. 5. 2 (a) An 8-pole electromagnetic actuator and (b) orientation of poles with minimum flux leakage.

Table 5. 1. Geometrical details of stator.

Parameters	Values
Leg width	0.45 cm
Stator length	2.65 cm
Stator diameter	5.3 cm
Poles	8
Number of coil turns in one pole	100
Coil diameter	0.315 mm (30 SWG)

5.2.2 Eddy current sensor

The displacement response of the rotor system was measured in the horizontal and vertical directions with the help of a non-contact proximity probe 3300 NSV, Bently Nevada, USA as shown in Fig. 5.3 (a). The vibration responses are obtained in terms of voltage output through the sensor. The output signal is then amplified through the five-channel Bently

TH-2966_176103027

Nevada proximitor assembly (Fig. 5.3 (b)) by utilizing an additional DC supply voltage of 13.7 volts. The gap between the sensor and the shaft is required to be maintained at a DC voltage range of -5.75 ± 0.5 volts. The sensitivity of the sensor is mentioned to be 1.27 V/mm. The description of the working of the eddy current sensor has been discussed in section 1.4.2.



(a) (b)

Fig. 5. 3. (a) Eddy current sensors mounted in horizontal and vertical directions and (b) Bently Nevada proximitor assembly for amplification of sensor output.

5.2.3 dSPACE-SIMULINK platform

In the present work, the controller was designed in the dSPACE-SIMULINK platform, and it is implemented in real-time with the help of Analog-to-Digital (A/D) and Digital-to-Analog (D/A) converters (DS2201 I/O panel) as shown in Fig. 5.4. The A/D converter system is utilized to convert the displacement response in terms of voltage to digital data that can be processed in the designed controller. The D/A converter system converts the control signal generated by the controller to the voltage signal. The dSPACE library consists of A/D and D/A SIMULINK blocks for I/O operation. The scaling of analog to a digital signal for A/D is +10 to -10 V taken as +1 to -1 Simulink input, and for DAC, +1 to

TH-2966_176103027

-1 Simulink input is taken as +10 to -10 V analog output. The SIMULINK model of the designed controller with I/O blocks is converted to a .sdf extension file that can be utilized in the dSPACE control desk, dSPACE GmbH, Germany.



Fig. 5. 4. The dSPACE hardware with A/D and D/A converters.

The control desk is a user interface on which real-time simulation is run. The control desk window consists of three regions, namely, tool window, navigator, and work area. In the tool window region, users have access to the variables tab to access the variables designed in the SIMULINK model, Platform tab that displays the dSPACE platform (DS1006) selected as per the hardware provided, and Messages tab that displays an error or warning messages as shown in Fig. 5.5.

The navigator region consists of the Experiment tab that shows the experiment numbers and saved real-time data sets and the Measurement tab that shows the data acquisition parameters. In the workspace region, the Graphics User Interface (GUI) tabs are present to change or view the variables of the designed model in real-time.

TH-2966_176103027

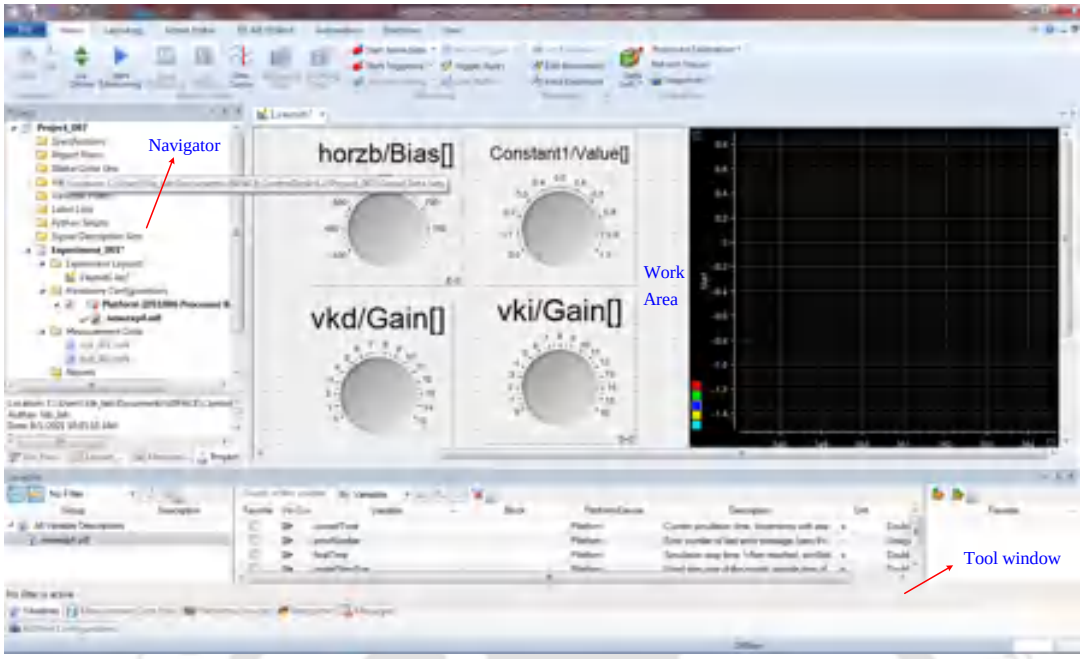


Fig. 5. 5. The dSPACE control desk for real-time simulation of the designed controller.

5.2.4 Power Amplifier

The control signal is amplified with the help of an A25A100 PWM servo drive, Advanced Motion Control, Camarillo, USA as shown in Fig. 5.6. The specification of the servo drive is shown in Table 5.2. The drive can be used stand-alone or with the digital controllers and requires a DC voltage power supply to amplify the signal. The input gain, output current limit, and offset can be adjusted with the help of 4 potentiometers, as shown in Fig. 5.6. The potentiometers have twelve active turns and one inactive turn and are approximately linear. The device can be operated in current mode or voltage mode as per the position of the six configuration switches, i.e., ON or OFF conditions. In the present work, the device is operated in the current mode control to reduce the phase lag and amplitude reduction in the required signal when connected to the inductive circuit. The gain parameters are tuned through the potentiometer to introduce a signal gain of 1 A/V. The amplifier contains 16

TH-2966_176103027

pin connections as the signal connector and five-pin connections as the power connector. Among the pin in the signal connector, pin 4 (+ve terminal) and pin 2 (ground) are used to receive the fluctuating DC supply from dSPACE to generate the controlling current. The pins in the power connector part are used to supply DC power to the amplifier and obtain the output to be supplied to the actuator. The amplifier circuit comprises of inbuilt PWM circuit, H-bridge MOSFET drive, and potentiometers for generating the required control and bias current to the actuator of AMB.

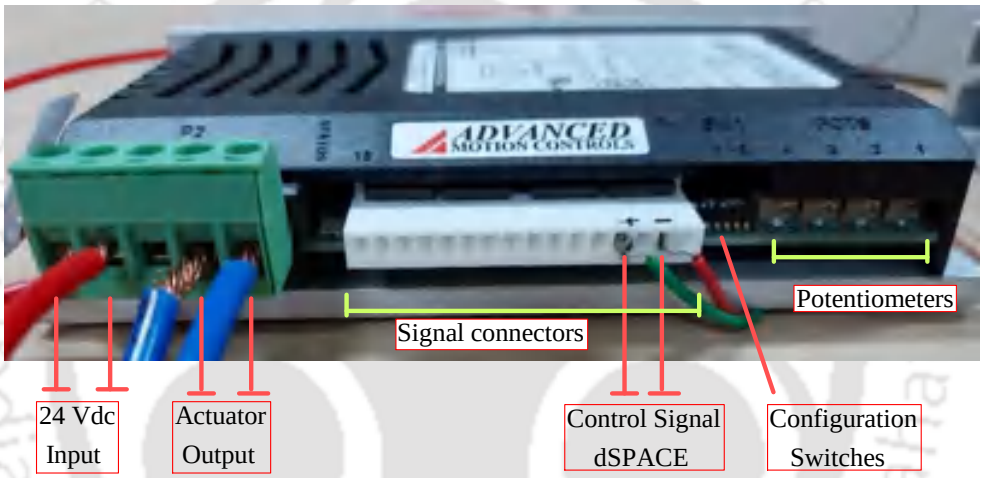


Fig. 5. 6. A servo drive with different pin settings used as an amplifier.

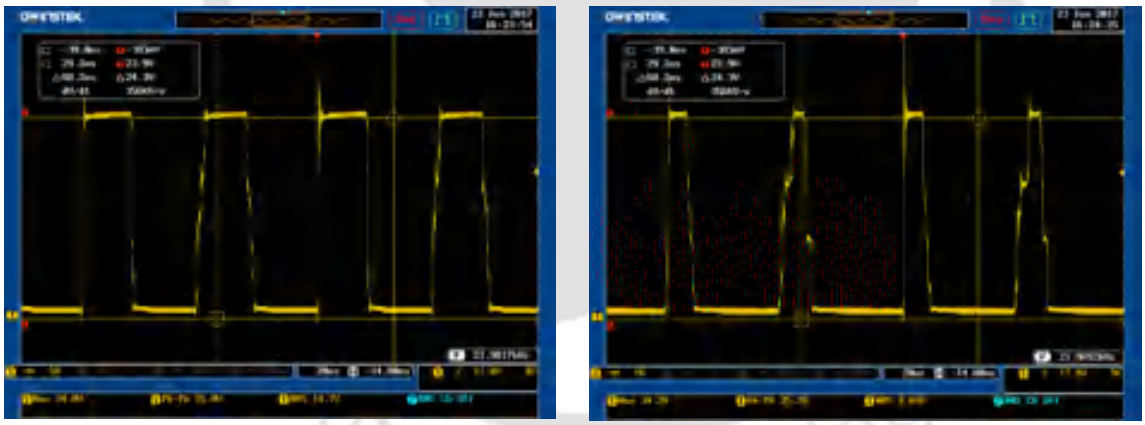
Table 5. 2. Specification of the A25A100 PWM servo drive.

Parameters	Values
Input voltage range	20-80 VDC
Maximum peak output current	25 A
Maximum continuous output current	15 A
Command voltage input	± 10 V Analog
Switching frequency	22 kHz
Modes of operation	Voltage, current, tachometer velocity

TH-2966_176103027

5.2.4.1. PWM (Pulse Width Modulation)

PWM is a technique to get analog results with digital means. Digital control is done by generating a square wave, a signal fluctuating at a very high frequency between on or off. The voltage in the device fluctuates between max and zero value by changing the duration of time for which the supply is on or off. The proportion of 'on' time to the 'period' of time refers to the duty cycle, and a low duty cycle corresponds to low power supplied. The main advantage of PWM is that power loss is very low. As for the 'off' time, no power is supplied to the load. In the amplifier with an increase in the voltage supplied to the signal connector (pins 4 and 2), the current in the circuit increase with the increase in the duty cycle. The variation of duty cycle with variation in voltage across signal connector is shown in Fig. 5.7.



(a) (b)

Fig. 5. 7. The high-frequency voltage output of the amplifier with a (a) large duty cycle, and (b) small duty cycle as measured in an oscilloscope.

TH-2966_176103027

5.2.4.1. H-bridge MOSFET driver

A simplified circuit of the H-bridge MOSFET driver is shown in Fig. 5.8. The MOSFET (Metal Oxide Semiconductor Field Effect Transistor) is a transistor used for amplifying or switching electronic signals.

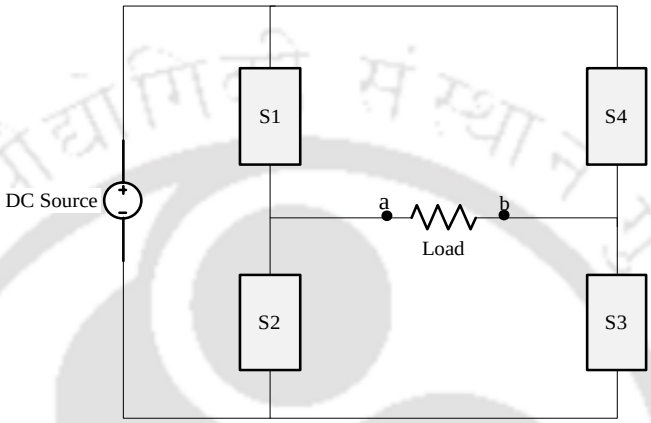


Fig. 5. 8. A block diagram of H-bridge MOSFET driver.

The driver consists of four MOSFETs (S1, S2, S3, and S4) that allow the flow of current to the load in both directions. The current in the load flows from '*a*' to '*b*' if S1 and S2 are turned 'on' and from '*b*' to '*a*' if S2 and S4 are turned 'on.'

5.2.5. Current probes

The 1146B KEYSIGHT AC/DC current probe, as shown in Fig. 5.9, is used to measure control current flowing through the coils in the actuator of the AMB. The probe measures the maximum peak current of 10 A at 100 mV/A and 100 A at 10 mV/A with a measurement frequency of 100 kHz.

TH-2966_176103027



Fig. 5. 9. The 1146B KEYSIGHT AC/DC current probe used for control current measurement.

5.3. Physical connection of the rotor-AMB system

The AMB generates a controlling magnetic force utilizing the displacement response of the system to reduce the vibration generated due to abnormalities in the rotor system, such as the presence of residual unbalances, crack, misalignment, etc. The physical connection of the rotor-AMB system is shown in Fig. 5.10. The voltage response ($V_{r,m}$) generated at the AMB location due to residual unbalance is obtained by the proximity sensor. The analog response is converted to displacement response (r_m) in meters through the A/D panel and then transferred to the controller for the generation of the control current (i_c). The control voltage ($V_{i,c}$) generated by the D/A panel is then amplified in the amplifier to obtain the requisite amount of control current in the actuator. The amplifiers are operated in the current control mode to reduce the amplitude and phase deviation in the inductive circuit of the AMB system. The magnetic force generated in real-time allows the rotor system to operate with minimum vibration.

TH-2966_176103027

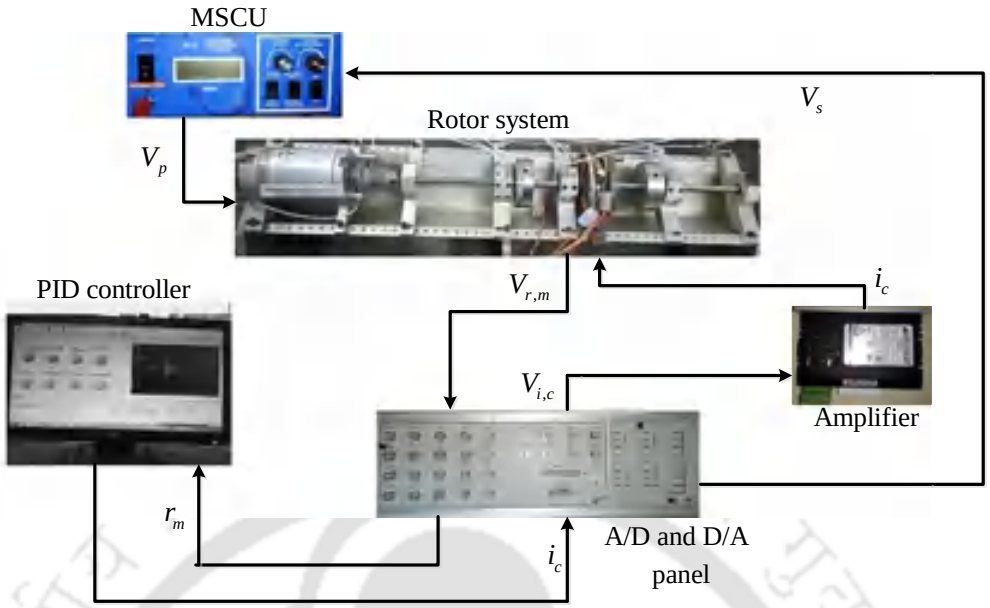


Fig. 5. 10. The physical connection of different components in the experimental rotor-AMB test rig.

The rotor system is operated with voltage (V_s) feed to the Motor Speed Control Unit (MSCU) that operates at 5 Hz to 167 Hz for 0 to 5 Volts of input. As shown in Fig. 5.10, the voltage is provided with the help of the SIMULINK model designed in the dSPACE interface, and the system is rotated with the corresponding voltage (V_p) required by the motor.

5.4. Control Structure for High-Speed Operation with Switching Mode Control of bias current

The PID controller utilized in controlling the vibration of the rotor system was developed in the dSPACE-SIMULINK interface, as shown in Fig. 5.11. The displacement responses from the eddy current sensors are utilized to generate the control current required in the control operation. The current is then converted to the voltage value as per the tuning of the amplifier. Then the bias voltage is added to the control voltage to generate both bias and

TH-2966_176103027

control currents in the AMB actuator simultaneously, as shown in Fig. 5.11. The limitation on the magnitude of coil current and the heating of coil due to excessive supply of control current for a long period of time are the major issues for the AMB system. As the system accelerates near its critical speed, the displacement response of the system increases, and hence the required amount of control current also increases. In order to maintain the working of AMB in the differential mode control, the control current is required to be lower than the bias current, so the magnitude of the bias current is made high enough to accommodate the rise in the amount of control current near the critical speed of the rotor system. The large amount of bias current flowing in the system throughout the run time results in the development of an excessive amount of heat in the coils of the actuator. The problem arising in the high-speed operation can be reduced by the switching of bias current in the system. The bias current is maintained at a lower value at the start till a higher value of control current is required. The bias current is switched to the higher value while approaching the critical speed of the system once the value of the control current exceeds the initial value of the bias current. The value of the bias current is switched back to its lower value using logic gates when the system crosses its critical speed, and less control current is required. The switching of bias current allows the operation of the system with a lower level of current throughout the run time, thereby reducing the power requirement and the heat generation at the coils of the actuator. The lower and higher value of the bias current is considered as 0.5 and 1 A.

The PID controller parameters also affect the maximum displacement of the rotor system at critical speeds. The increase in proportional gain 'k_P' reduces the magnitude of the displacement response at the operating speed of the rotor system. The derivative gain

TH-2966_176103027

'k_D' in the PID control algorithm decreases the maximum amplitude of the displacement response with an increase in its magnitude. To obtain the controller gains, in the PID controller, the values of proportional gain and derivative gain are varied from k_P = 0 to 10000 A/m and k_D = 0 to 15 A-s/m. The system was found to be stable for k_P > 2000 A/m and k_D > 3 A-s/m. The integral gain, k_I, is added to bring the rotor system in the equilibrium position, i.e., the position of the shaft at the AMB location without application of AMB. The variation in the displacement response with the variation of the controller parameters along the *y* –axis was examined at the operating condition of the rotor system. The system is rotated at 15 Hz without AMB control, and the displacement response was measured through sensors. Then after the addition of the AMB control loop considering 0.5 A bias current, the proportional gain of the PID controller was varied from k_P = 3000 A/m to 6000 A/m with a step of 500 A/m, and the displacement responses were measured. The percentage reduction of displacement amplitude with the increment of the proportional gain with respect to the displacement response obtained without AMB control was calculated. As shown in Fig. 5.12 (a), the percentage reduction increases with an increase in the proportional gain.

Now, the effectiveness of the derivative gain is evaluated in improving the damping property of the system. An impulsive force was applied to the system without AMB control, and the reduction in the displacement amplitude after four cycles was measured. The same process was repeated with AMB control by increasing the derivative gain by k_D = 3.5 A-s/m to 6 A-s/m with a step of 0.5 A-s/m.

TH-2966_176103027

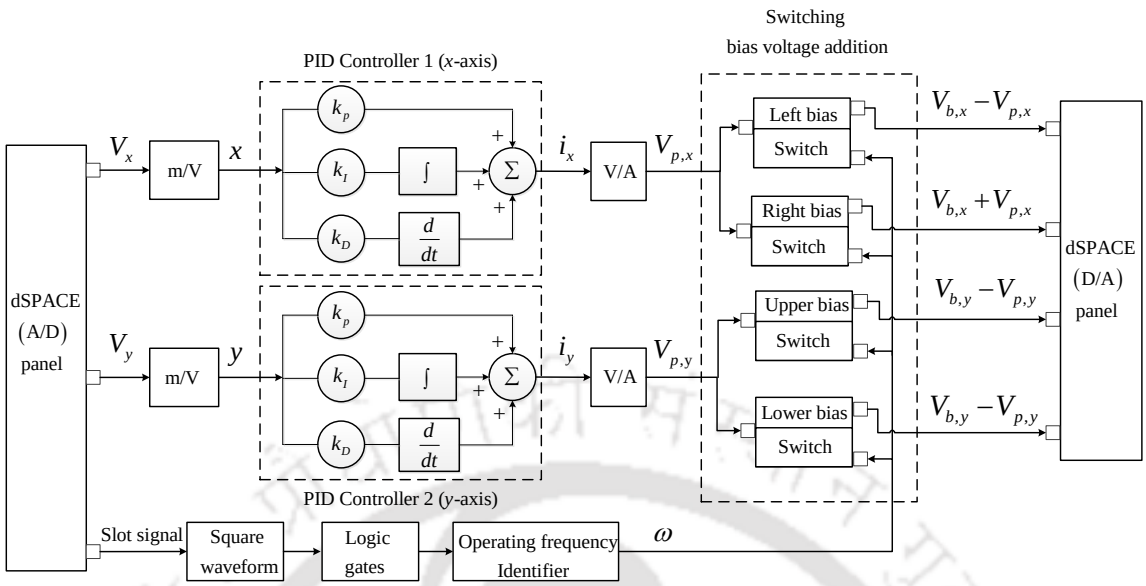


Fig. 5. 11. The block diagram of the AMB closed-loop control model developed at the dSPACE-SIMULINK interface with switching of bias current.

The percentage reduction in damped amplitude after four cycles increases with an increase in the derivative gain, and hence, the damping property is effectively increased, as shown in Fig. 5.12 (b). Now, to maintain the control current within the limit of the bias current applied in the actuator and prevent the contact of rotor and stator components while crossing the critical speed, the tuning of the control parameters was done, and the magnitude of proportional and derivative gain was adjusted to k_P =5000 A/m and k_D = 12 A-s/m, respectively. Also, switching of the bias current of 1 A requires adequate responsive integral gain 'k_I' to restore the system to its equilibrium location. The appropriate value of integral gain for the current experiment is considered to be k_I = 16000 A/m-s.

TH-2966_176103027

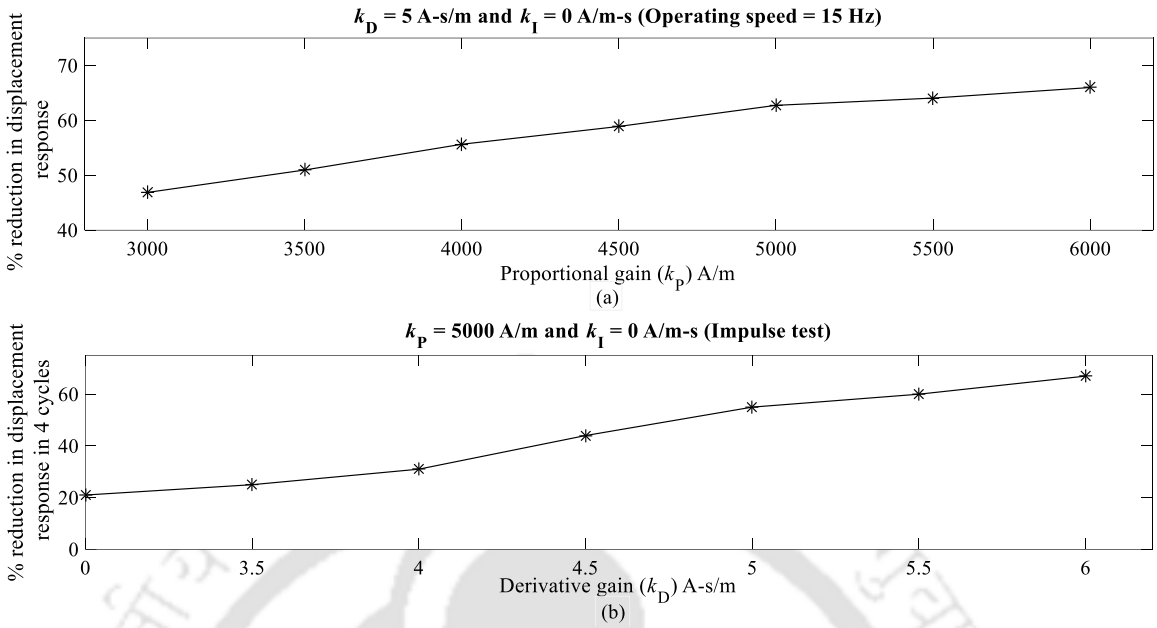


Fig. 5. 12. (a) Percentage reduction in displacement response with the variation of the proportional gain (k_P) at 15 Hz (b) Percentage reduction in the displacement amplitude after four cycles with the variation of the derivative gain (k_D) in the impulse test.

From Fig. 5.11, the voltage signal (V_x, V_y) of the proximity probe in the horizontal and vertical directions from the A/D panel is converted to the displacement response by multiplying a factor of 1.27×10^{-4} (m/V). The corresponding displacement response (x, y) is then transferred to the PID controller for the generation of control currents (i_x, i_y). The control currents are converted to the voltage signal ($V_{p,x}$, $V_{p,y}$) as per the gain set in the potentiometers of the amplifiers. The control voltages are added with the respective constant bias voltages, and then they are sent to the respective pair of poles in the actuator through the D/A panel. The bias voltages are switched between low and high values on the basis of the operating speed of the system. The operating speed of the system was identified based on the periodic signal acquired from the reference slot, as shown in Fig. 5.1 (b). The periodic signal is converted into a square wave, and the frequency of the wave in one cycle is estimated by the frequency identifier block shown in Fig. 5.11. The

TH-2966_176103027

frequency is identified within one complete rotation of the shaft allowing the switch block to operate immediately as the system approaches the speed at which bias current is changed. The switch block, as shown in Fig. 5.11 corresponding to different poles, adds the required magnitude to a bias voltage ($V_{b,x}$, $V_{b,y}$). As per the differential mode control algorithm described in Section 1.4.5, the control voltages are added and subtracted simultaneously in the opposite pair of poles. The overall control and bias voltages in the left and right poles are given by ($V_{b,x}$-$V_{p,x}$, $V_{b,x}$+$V_{p,x}$). Similarly, the overall control and bias voltages in the upper and lower poles are given by ($V_{b,y}$-$V_{p,y}$, $V_{b,y}$+$V_{p,y}$).

The natural frequency of the rotor system was estimated with the considered values of the controller gains in the impulse test as shown in Fig. 5.13. An impulsive force was given to the shaft of the rotor system with AMB control. The displacement response in the time domain at the AMB location was obtained with the help of a proximity sensor in the *y*-direction. The Fast Fourier Transform (FFT) of the signal is carried out. In the frequency domain plot, the first natural frequency of the system is estimated to be 41.3 Hz. In the present rotor system, for the operating frequency of 6.67 Hz to 25 Hz, the bias current supplied to the coil of the AMB is equivalent to 0.5 A. The level control current required is within the limit of the bias current supplied in the coils of the actuator. As the operating speed goes beyond 25 Hz, the magnitude of the control current increases, and hence the bias current is switched to 1 A with the help of logic gates in the SIMULINK model. From an operating speed of 25 to 55 Hz, the bias current of 1A was supplied to the rotor as the requirement of the control current is higher around critical speed (42 Hz). Beyond 55 Hz, the displacement response of the rotor system decreases, and therefore, the bias current was switched back to 0.5 A.

TH-2966_176103027

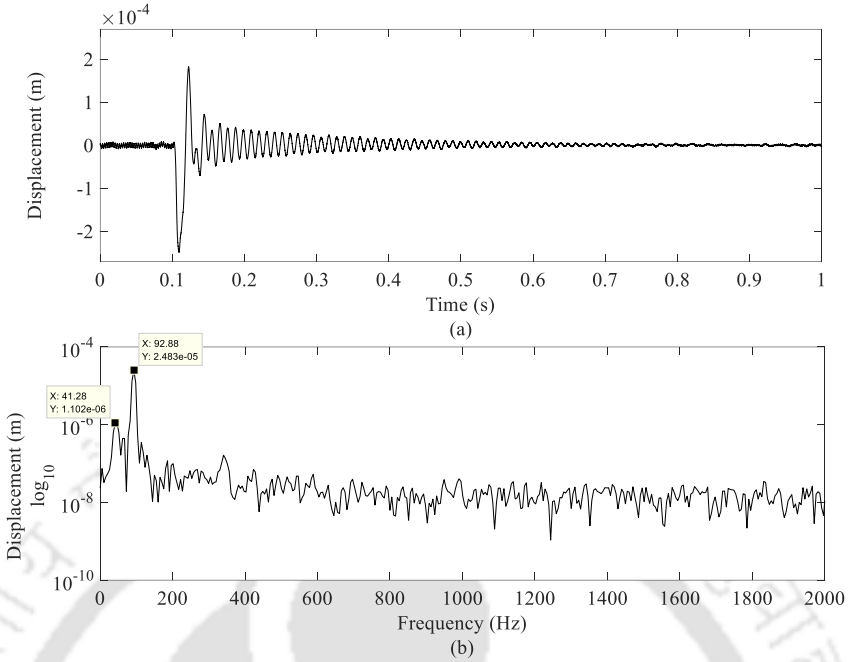


Fig. 5. 13. (a) Displacement at AMB location along *y*-axis vs. time plot with impulsive force and (b) displacement amplitude at AMB location vs. frequency plot.

This reduces the current consumption in the coils of AMB as well as prevents the heating of coils of the actuator. The displacement response of the rotor system operated from 6.67 Hz to 63 Hz at an angular acceleration of 12 rad/s^2 is shown in Fig. 5.14. The acceleration of the system is kept low so that the transients are avoided. The operating frequency with time is shown in Fig. 5.14 (a), and the total current (bias + control) current is shown in Fig. 5.14 (c). The bias current is switched from 0.5 to 1 A as the magnitude of the control current increases, as shown in Fig. 5.14 (c). With the application of SWC, the rotor system is able to cross its first critical speed with minimum vibration and less consumption of the current in the AMB. The percentage reduction in power consumption ($\propto$ square of bias current × time) due to switching of bias current in the rotor run-time is estimated to be 21%.

TH-2966_176103027

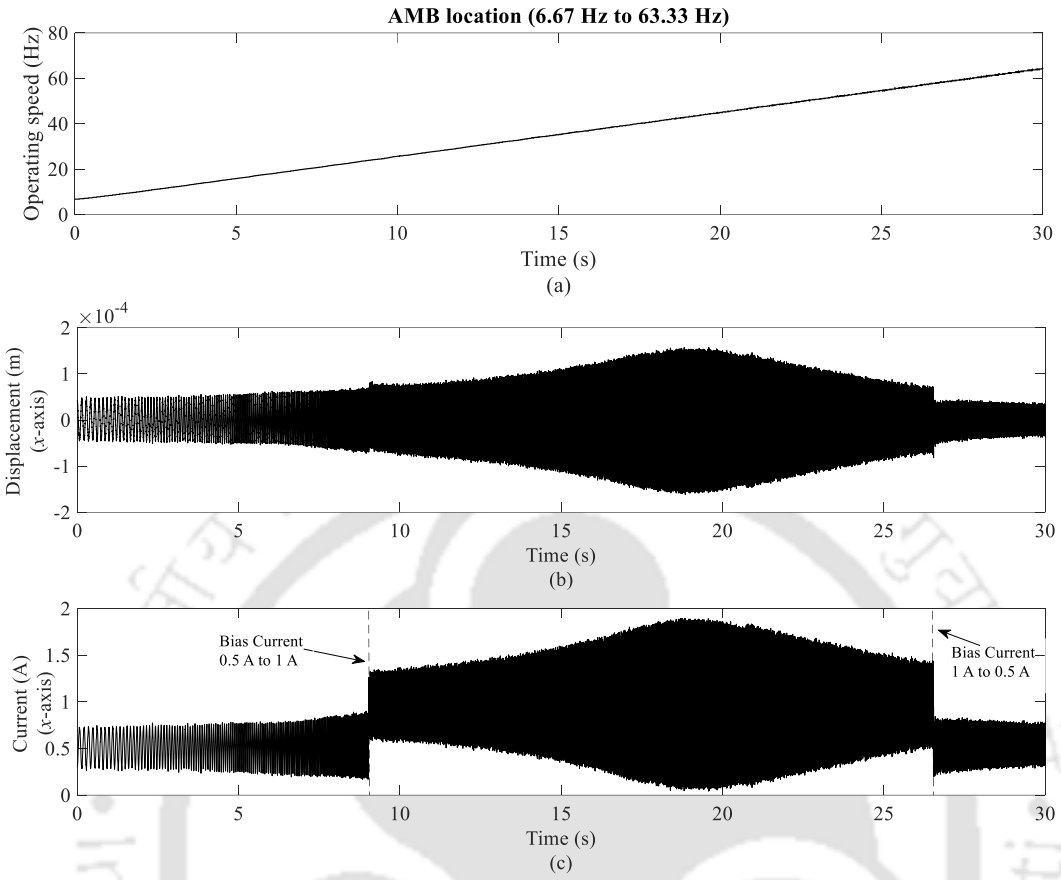


Fig. 5. 14. (a) Frequency (Hz) vs. time plot with AMB control for the system accelerating from 6.67 to 63.33 Hz with an acceleration of 12 rad/s^2, (b) displacement at AMB location vs. time plot, and (c) overall current (bias + control) at AMB vs. time plot along the *x*-axis.

5.5. Generation of Synchronized Virtual Trial Unbalances as Magnetic Excitations

The virtual trial unbalances replace the manual addition of the trial unbalances in the estimation procedure of residual unbalances through the influence coefficient method. In order to generate the excitation signals through AMB at the same operating frequency, the SIMULINK model was utilized, as shown in Fig. 5.15. The rotor system was operated with the input voltage (V_s) supplied through the I/O panel in the RK-4 motor speed control unit (MSCU). The problem that arises in tuning the excitation frequency with the operating

TH-2966_176103027

frequency is to determine the exact voltage/speed (V/S) factor of the MSCU, resetting the time clock in the SIMULINK model with the start time and adjustment of the phase lag generated in the MSCU. The voltage/speed factor of the MSCU determines the actual operating speed of the rotor system as per the transferred voltage signal. The deviation in the V/S factor results in a mismatch of the operating frequency and the desired frequency, and hence the angular acceleration of the system changes. In order to overcome the problem, the operating frequency of the rotor system was calculated in real-time through the waveform obtained at the slot present in the coupling of the rotor system.

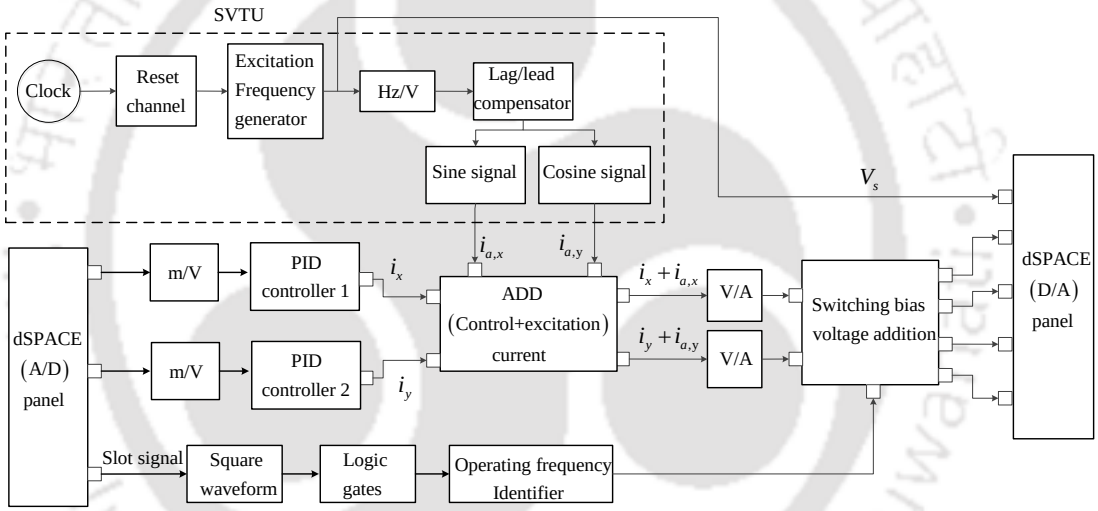


Fig. 5. 15. The block diagram of the AMB closed-loop control model developed at the dSPACE-SIMULINK interface with switching of bias current and SVTU.

The eddy current sensor present at the slot location generates a periodic signal with maximum amplitude when the sensor is in the direction of the slot and minimum when the sensor is away from the slot. The signal was then utilized to estimate the operating frequency in real-time with the help of the developed SIMULINK model, as shown in Fig. 5.15. The estimated operating speed of the system is reset after every complete cycle of the signal obtained from the slot. As a result of which, the increasing or decreasing operating

TH-2966_176103027

speed is easily identified in real-time. The slope of the excitation signal is matched with the slope of the operating signal by varying the V/S factor in real-time. Once the slope matches, the desired V/S ratio is recorded for the generation of the excitation signal.

As the system is accelerated, the timer selected to generate sinusoidal responses for the virtual trial unbalances is required to reset to zero. The clock timer in the SIMULINK model in synchronous to the operating time generates the excitation frequency similar to the operating frequency. In order to reset the clock, an additional reset block is developed, as shown in Fig. 5.15, that resets the clock timer to zero as soon as the operating voltage is supplied to the MSCU.

The additional problem is the lag in the voltage feed supplied to the MSCU, and the system starts to accelerate after a certain period of time. The lag generates a mismatch in the operating and the excitation frequency. In order to overcome the difficulty, the lag is estimated with the comparison of the estimated system's frequency and the excitation frequency in the system run time. The estimated lag value is introduced in the excitation frequency signal as shown in Fig. 5.15 to synchronize it with the operating frequency in real-time. The sinusoidal signal generated in the SIMULINK model is added to the control current generated at the PID controller. The control currents (i_x, i_y), along with the excitation currents ($i_{a,x}$, $i_{a,y}$) are supplied to the actuator of the AMB through the I/O panel and amplifiers, as shown in Fig. 5.15. The excitation current generated in the rotor-AMB system along the *x*-axis is shown in Fig. 5.16.

To describe the beat phenomenon in the displacement and current responses that arises with the presence V/S factor error and phase lag error, the excitation current is introduced in the rotor system. As shown in Fig. 5.17 (a), due to the presence of both

TH-2966_176103027

errors, the operating frequency diverges from the excitation frequency. The mismatch in the frequency generates beat phenomenon in the displacement and current responses of the rotor system, as shown in Fig. 5.17 (b) and 5.17 (c), respectively. More the frequencies diverge, the beat reduces, and the signal shifts to a multi-frequency waveform. Now, the V/S factor was corrected by adjusting the value in the Hz/V block shown in Fig. 5.15 as per the slope of the operating speed (ω) identified.

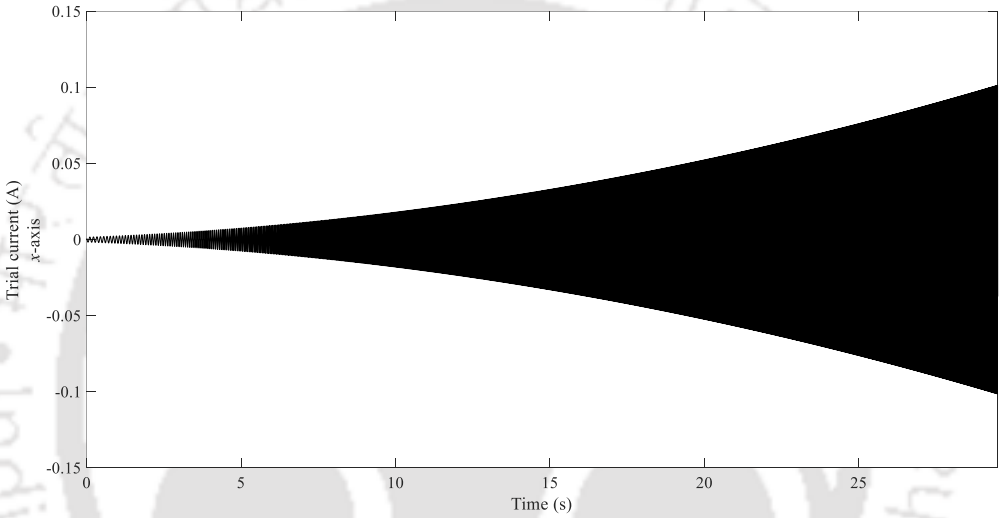
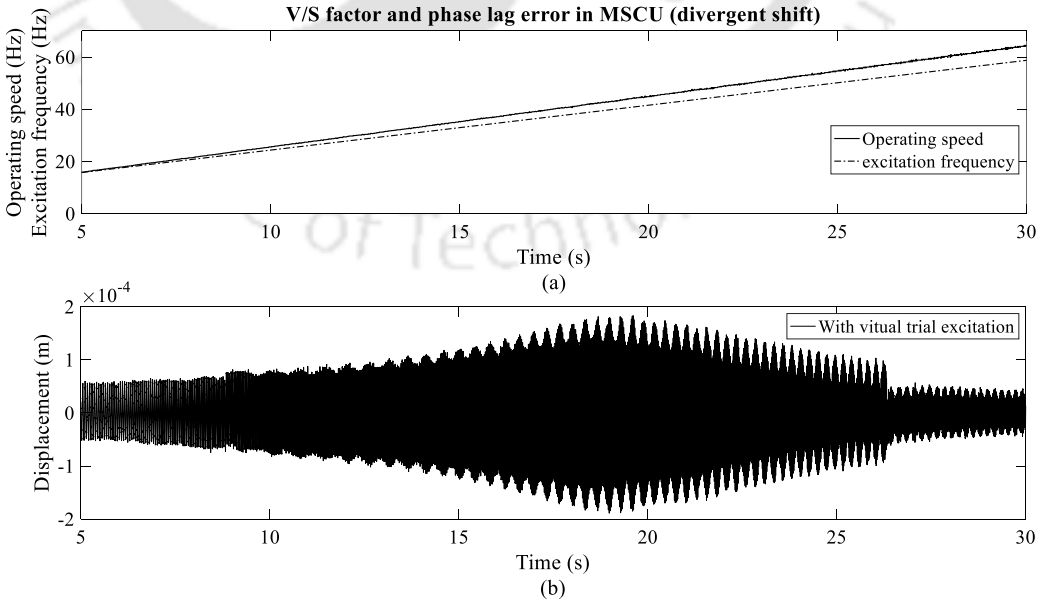


Fig. 5. 16. The trial excitation current along *x*-axis to generated magnetic excitation force in the rotor-AMB system.



TH-2966_176103027

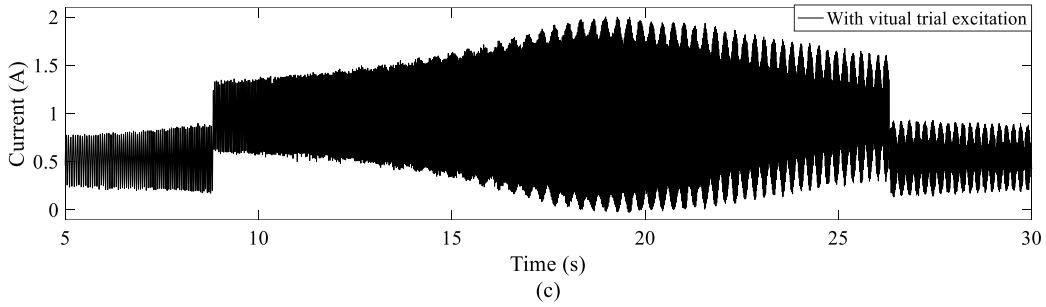
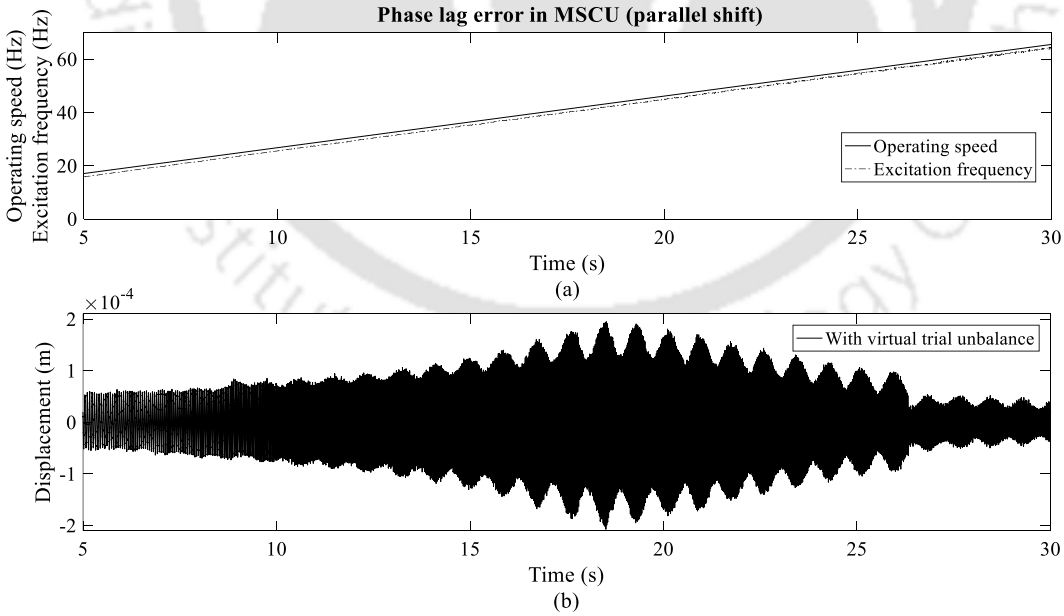


Fig. 5. 17. (a) Frequency (Hz) vs. time plot with AMB control for the accelerating rotor system with V/S error and lag error in SVTU generation, (b) displacement at AMB location vs. time plot, and (c) overall current (bias + control) at AMB along the *x*-axis vs. time plot.

The excitation current was introduced with the lag error, due to which the operating speed and the excitation frequency have the parallel shift as shown in Fig. 5.18 (a). As the frequencies are closer, the beat phenomenon is quite dominant and is shown in the displacement and current response of the rotor system (Fig. 5.18 (b) and 5.18 (c), respectively).



TH-2966_176103027

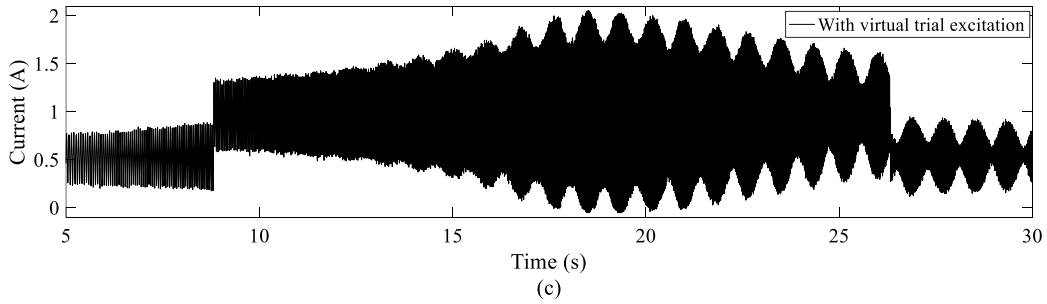
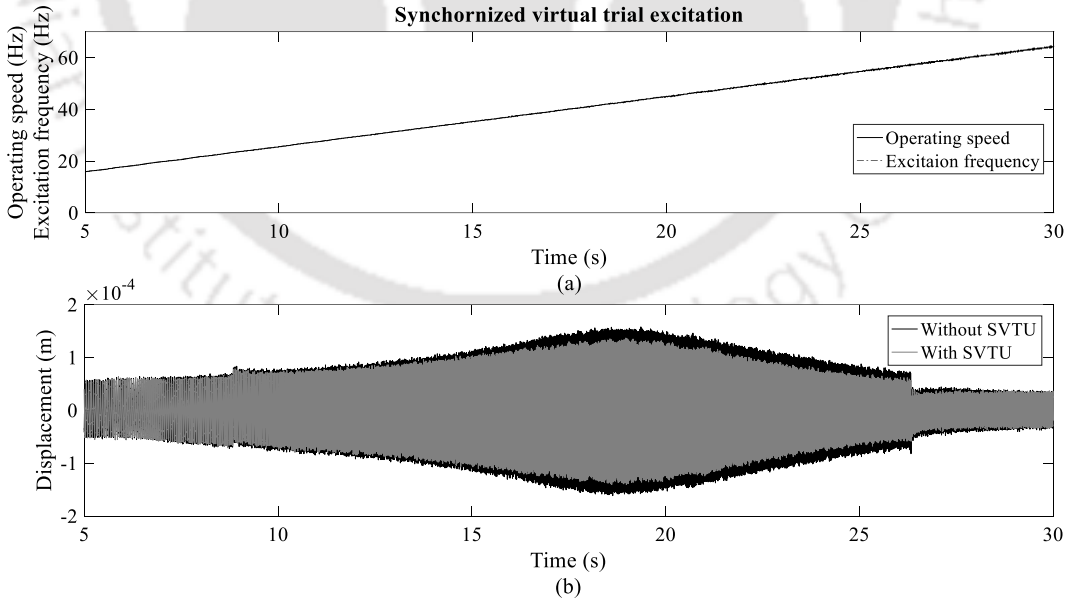


Fig. 5. 18. (a) Frequency (Hz) vs. time plot with AMB control for the accelerating rotor system with lag error in SVTU generation, (b) displacement at AMB location along *x*-axis vs. time plot, and (c) overall current (bias + control) at AMB along *x*-axis vs. time plot.

Now, after error correction, the SVTU was introduced in the rotor system, the operating frequency matches with the excitation frequency as shown in Fig. 5.19 (a), and the beat phenomenon is removed from the displacement and current responses. The displacement and current responses without and with the application of the SVTU at the AMB location along the *x*-axis are shown in Fig. 5.19 (b) and (c), respectively.



TH-2966_176103027

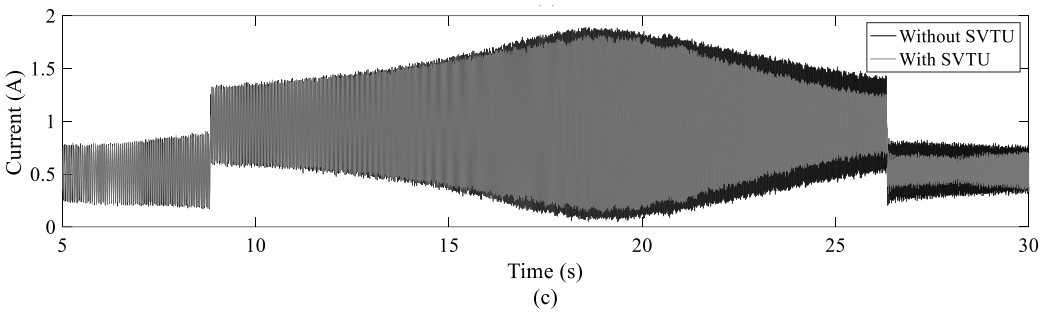


Fig. 5. 19. (a) Frequency (Hz) vs. time plot with AMB control for the accelerating rotor system without SVTU and with SVTU after error correction, (b) displacement at AMB location along *x*-axis vs. time plot, and (c) overall current (bias + control) at AMB along *x*-axis vs. time plot.

5.6. Estimation of Residual Unbalances at High-Speed

The residual unbalances present in the rotor system are estimated using both manually added trial unbalances as well as SVTU. The estimated unbalances using VTEICM are compared with those obtained using the conventional ICM with AMB control to show the effectiveness of the developed identification algorithm in the high-speed balancing of the rotor-AMB system.

5.6.1. Estimation of the phase and amplitude of the displacement signals

In the practical rotor system, to determine the phase and amplitude of the displacement signal, a reference position on the rotor system is required to be considered. The phase of the displacement response is measured with respect to the reference position. The key slot as shown in Fig. 5.1 (b), is considered as the reference location in the system. The reference signal obtained at the key slot shows peaks as the slot faces the sensor during the rotation of the shaft, as shown in Fig. 5.20. In the usual balancing procedure, the phase of the displacement signal is measured in the time domain by measuring the time difference between the peaks of a reference signal and the peaks of displacement responses. However,

TH-2966_176103027

due to uncertainties in the behavior of time-domain responses, the accurate measurement of phases is difficult to achieve.

To ensure that the orientation of estimated unbalance is with respect to the reference location, the zero-degree axis on the balance planes, i.e., discs as shown in Fig. 5.1 (c), is made coincident with the keyway. The sense of rotation of the rotor system is required to be from the horizontal (x) to vertical axis (y) in order to obtain the correct phase of displacement responses. The sensor utilized to measure the reference signal is required to be located in the horizontal direction, i.e., along the x-axis, as shown in Fig. 5.1 (b). The system is rotated by a motor along with the application of AMB to obtain the displacement along with both vertical and horizontal directions at the measurement planes. A reference signal is also obtained from the key slot, as mentioned above. In order to increase the accuracy of the measurement, the FFT (Fast Fourier Transform) of the discrete signal is carried out.

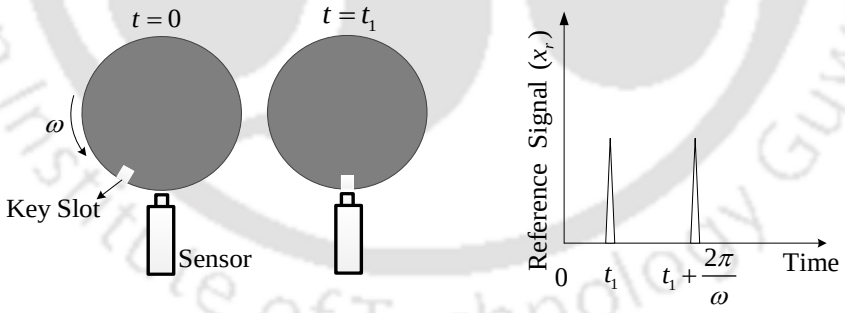


Fig. 5. 20. The schematic showing generation of the reference signal (x_g) with the orientation of the key slot and sensor for time $t = 0$ and $t = t_1$.

The amplitude and phase of displacement response corresponding to the 1X harmonics in the frequency domain are utilized. The displacement response for a particular

TH-2966_176103027

spin speed is selected for a particular time interval with respect to the reference signal as given below

$$x_g(p) = \sum_{i=1}^{n} x_g(p_i)\ ; \qquad x_d(p) = \sum_{i=1}^{n} x_d(p_i) \tag{5.1}$$

where, x_g and x_d are the reference signal and the displacement response, and p_i is the i^{th} number of data points present in the signal. If p_k and p_s are the peak locations for a particular time period, then the displacement response and the reference signal is taken as

$$x_g(p) = \sum_{i=k}^{s} x_g(p_i)\ ; \qquad x_d(p) = \sum_{i=k}^{s} x_d(p_i) \tag{5.2}$$

The same procedure is followed to obtain the displacement response (y_d) in the y-direction, and the complex response estimated at the measurement plane is given as $r_d = x_d + \mathrm{j}\ y_d$. Now, the FFT of x_g and r_d are carried out to obtain the phase and amplitude of both the reference and displacement signals. The complex representation of the discrete periodic signal in the expanded form as per Fourier transform can be given as

$$r_{d,n} = \sum_{k=0}^{Q-1} r_k \mathrm{e}^{-\mathrm{j}2\pi nk/\mathrm{Q}} \tag{5.3}$$

where, Q is the number of discrete data points presents in the periodic signal; $n = \{0, 1, 2, \ldots, Q\text{-}1\}$; $\mathrm{j} = \sqrt{-1}$. The complex response corresponding to different harmonics present in the displacement signal is given by

$$r_k = \frac{1}{N} \sum_{n=0}^{Q-1} r_{d,n} \mathrm{e}^{\mathrm{j}2\pi nk/\mathrm{Q}}\ ; \qquad n = \{0, 1, 2, \ldots, Q\text{-}1\} \tag{5.4}$$

TH-2966_176103027

The amplitude and phase corresponding to the fundamental frequency that is the operating speed of the rotor system is given as

$$r_s = A_s e^{j\phi_s}; \qquad x_{g,s} = A_{g,s} e^{j\phi_{g,s}} \tag{5.5}$$

Now, the required complex displacement signal of the rotor system is obtained as

$$r_p = A_s e^{j(\phi_s - \phi_{g,s})} \tag{5.6}$$

The complex displacement response corresponding to the operating frequency of the system at the AMB and discs locations are utilized in VTEICM to estimate the residual unbalance present in the system.

5.6.2. Estimation based on manually added trial unbalances (ICM)

The estimation of the residual unbalances in the experimental test rig was carried out using the conventional ICM with AMB control. The manually added trial unbalances were utilized to estimate the residual unbalances at the respective balancing planes. The displacement responses from the proximity sensors at the location of the discs were utilized for the identification algorithm. This conventional balancing procedure was carried out to compare the unbalance estimates with those obtained using the developed identification algorithm, i.e., the VTEICM. The conventional balancing procedure based on ICM is described below.

1. The rotor system was accelerated at the spin speed of 6.67 Hz to 63 Hz in 30 s with AMB control. The displacement responses generated at the measurement planes (disc locations) were obtained with the help of eddy current sensors, as shown in Fig. 5.1 (a).

TH-2966_176103027

2. Then, additional mass (0.4 gram) was added at the holes present in the left balancing disc. Again, the system was accelerated, and the corresponding displacement responses were obtained. The time-domain displacement response was converted to the frequency domain by FFT in both cases. The reference signal obtained at the slot location, as shown in Fig. 5.1(b), was utilized for phase compensation in the displacement signals.

3. The half-spectrum displacement amplitudes and phases corresponding to 25 to 55 Hz for both the rotor runs were utilized to identify the corresponding influence coefficients of the system at the left plane using Eqs. (2.1) – (2.4). As the switching of bias current affects the properties of rotor-AMB system, the displacement response in the range of 25 to 55 Hz were considered with higher bias current and adequate amplitude to facilitate the calculation of the balancing masses.

4. The added mass was removed from the left plane, and in the next run, a mass was added at different orientations at the right plane. The amplitude and phase were utilized to estimate the influence coefficients corresponding to the right balancing planes using Eqs. (2.1) – (2.4).

4. Now, the amplitudes and phases of the displacement responses at the measurement planes obtained in the first run and the influence coefficients corresponding to both balancing planes were utilized to estimate the residual unbalances at the balancing planes as per Eq. (2.6).

The same procedure was repeated for 6 different combinations of manual trial unbalances at different orientations between 0° to 360°, and the estimated values of the balance masses in the system are shown in Fig. 5.21. The procedure requires manual

TH-2966_176103027

addition and removal of the residual unbalances for different runs, which is a difficult procedure to perform in the rotor system. Also, the number of trial runs increases with an increase in the number of balancing planes. In order to reduce the difficulty, virtual trial unbalances are introduced as magnetic excitations instead of manually added trial unbalances.

5.6.3. Estimation based on virtual trial unbalances as magnetic excitation (VTEICM)

The synchronized virtual trial unbalances were generated as magnetic excitation in the rotor system through AMB. The additional currents were added to the control current of the AMB system, as shown in Fig. 5.15. The estimation of the residual unbalances in the experimental test rig was carried out using the VTEICM. The displacement responses at the positions of discs and AMB were utilized to estimate the residual unbalances at the balancing planes. The balancing procedure based on the developed balancing procedure, i.e., the VTEICM, is described below.

1. The frequency of the excitation current and the control current was synchronized as described in Section 5.5.

2. Firstly, the rotor system was rotated above the critical speed, and the system responses at the measurement planes and the AMB location were stored. The half-spectrum amplitude and phase of the displacement responses were obtained, and the phase correction was done with respect to the reference signal.

3. The system was again rotated with the additional excitation current, and the amplitude and phases of the displacement responses at the measurement planes and AMB location

TH-2966_176103027

were stored. The phase correction of the displacements and additional excitation current was done with respect to the reference signal.

4. The change in the displacement responses with the addition of the SVTU was utilized to calculate the influence coefficient of the system at the measurement planes related to the AMB location, as mentioned in Eq. (2.22). To obtain the influence coefficients of the system in VTEICM, the current stiffness factor of the AMB is required to be estimated, as shown in Eq. (2.22). The stiffness factor was identified experimentally by adding a static load on the shaft (standstill condition) in the vertical direction at the AMB location. Due to the applied load, the shaft displaces in the loading direction. The displacement of the shaft from its equilibrium position is brought back by the PID controller with the generation of static control current (i_s).

A static load of 50 grams was added at the AMB location, and the shift of the shaft position is shown in Fig. 5.22 (a). The developed static control current, as shown in Fig. 5.22 (b), brings back the shaft to its original position. From Eq. (2.15), the estimated value of the current stiffness factor is found to be 18.16 N/A.

5. Now, the identified influence coefficients and the amplitudes and phases of displacement responses at AMB location in the first run were utilized to estimate the residual unbalances in the system using Eq. (2.26).

TH-2966_176103027

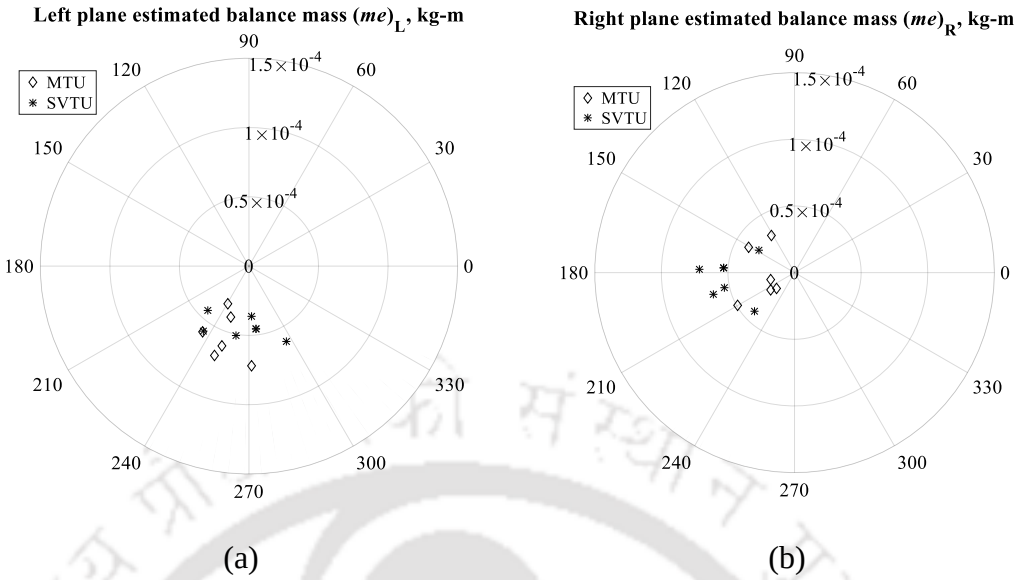


Fig. 5. 21. Estimated balance masses at (a) left and (b) right balancing plane utilizing the different combination of added MTU and generated SVTU.

The same procedure was repeated for 6 SVTUs with different phases between 0° to 360°, and the estimated values of the balance masses are shown in Fig. 5.21. The estimated values of the balance masses using virtual trial unbalances are found to be similar to those estimated using manual trial unbalances, as shown in Fig. 5.21. However, the virtual trial unbalances are beneficial to be utilized due to less manual effort, and fewer trial runs. The estimated values of the balance masses obtained using both methodologies were added to the slots in balancing discs at a distance of 30 mm from the center. The system was accelerated above critical speed to check the reduction in the displacement response. The four pairs of balance masses obtained with VTEICM as pair I (left plane: - 1.6 g∠225° and right plane: - 1.2 g∠225°), pair II (left plane: - 1.2 g∠270° and right plane: - 1.6 g∠200°), pair III (left plane: - 1 g∠270° and right plane: - 2 g∠200°) and pair IV (left plane: - 2 g∠270° and right plane: - 1 g∠150°) are utilized to balancing the rotor-AMB system.

TH-2966_176103027

The reduction in displacement responses before and after balancing of the rotor system is shown in Fig. 5.23. The displacement responses are found to be reduced by 53-62 % in the time domain, as shown in Table 5.3. The FFT of the time domain signal is carried out, and the displacement amplitudes before and after balancing with different pairs of balance masses are shown in Fig. 5.24. The percentage reduction in the displacement amplitudes is found out to be 55-75 % after balancing. The phases of the displacement amplitudes before and after balancing are shown in Fig. 5.25.

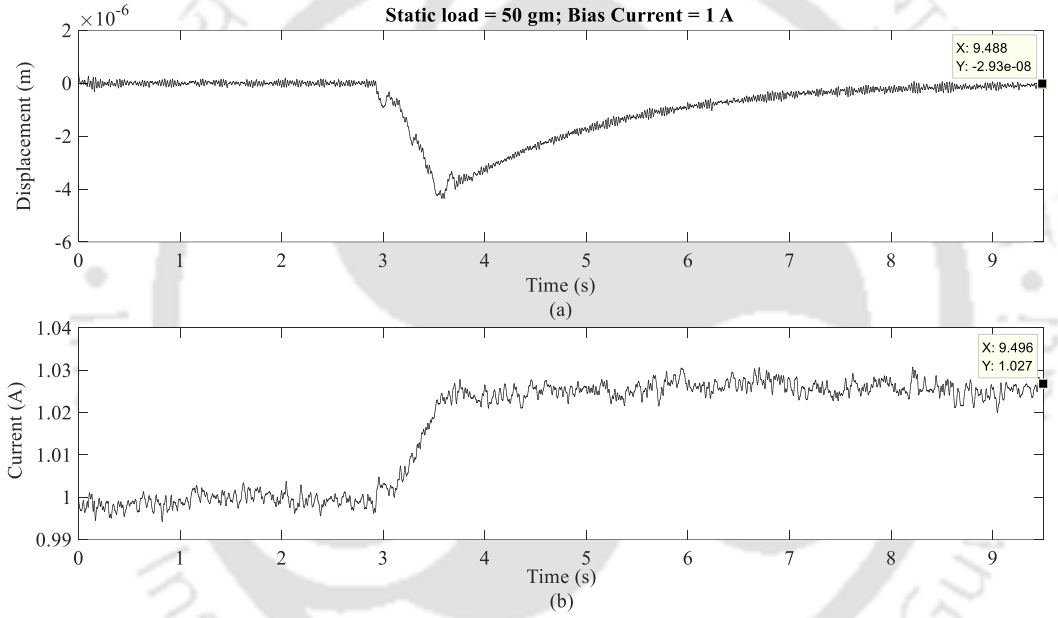
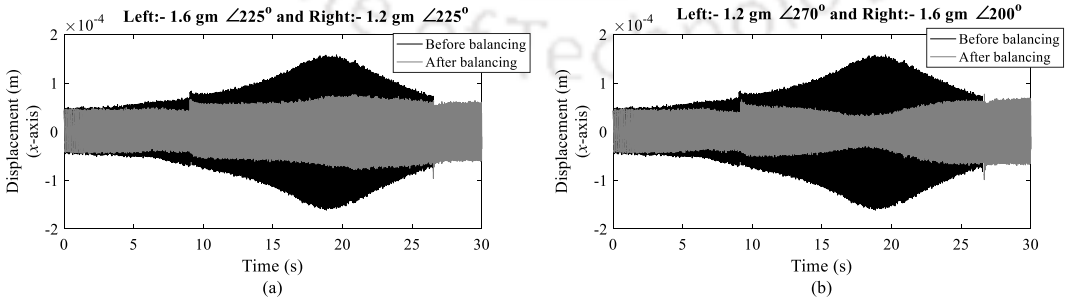


Fig. 5. 22. (a) Displacement response at AMB location (b) Control current for a load of 50 gm.



TH-2966_176103027

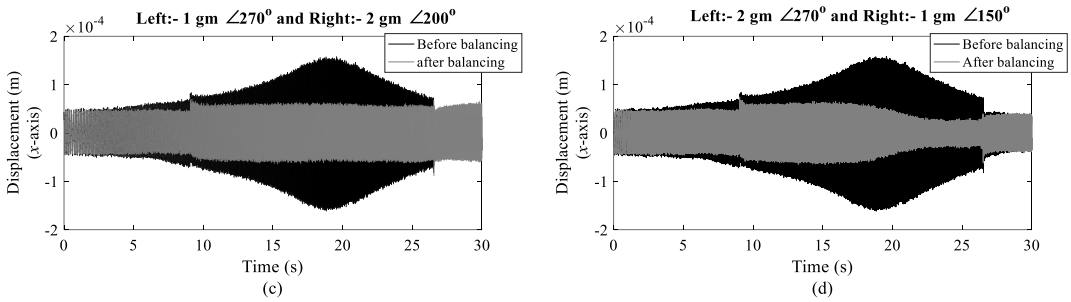


Fig. 5. 23. Displacement vs. time plot before and after balancing of rotor system utilizing estimated values of balance masses in VTEICM (a) pair I, (b) pair II, (c) pair III, and (d) pair IV.

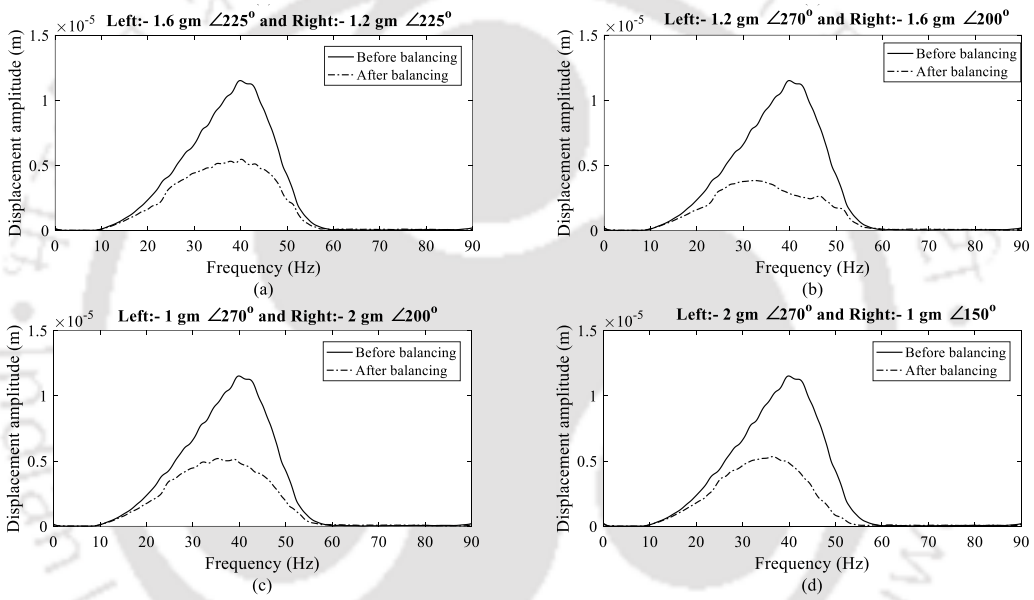
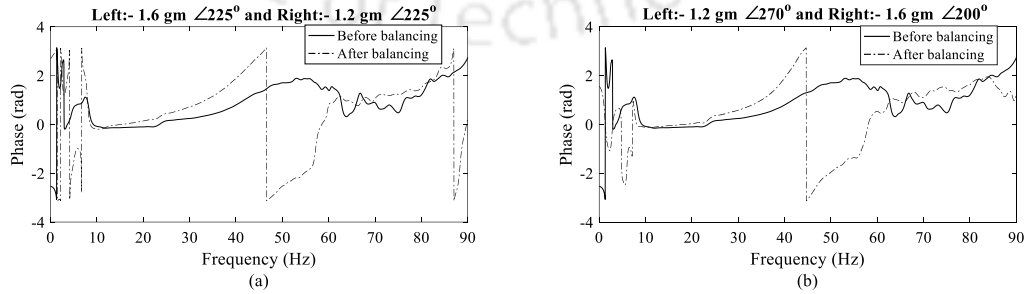


Fig. 5. 24. Displacement amplitude vs. frequency plot before and after balancing of rotor system utilizing estimated values of balance masses in VTEICM (a) pair I, (b) pair II, (c) pair III, and (d) pair IV.



TH-2966_176103027

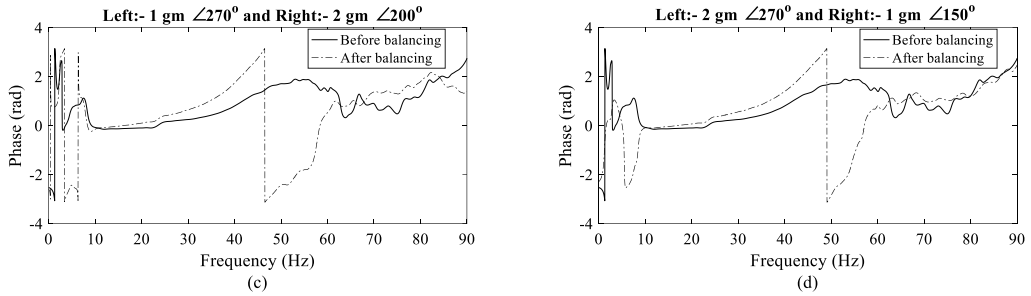


Fig. 5. 25. Displacement phase vs. frequency plot before and after balancing of rotor system utilizing estimated values of balance masses in VTEICM (a) pair I, (b) pair II, (c) pair III, and (d) pair IV.

Table 5. 3. Percentage reduction in displacement response and control currents in the time domain after balancing using different pairs of balance masses obtained in VTEICM.

Balance masses	Before balancing	After balancing	Reduction
Displacement responses (m)			
Pair I	1.55×10^{-4}	7.36×10^{-5}	53%
Pair II		6.61×10^{-5}	57%
Pair III		6.05×10^{-5}	61%
Pair IV		6.12×10^{-5}	60%
Control current (A)			
Pair I	0.89	0.43	52%
Pair II		0.39	56%
Pair III		0.34	62%
Pair IV		0.31	65%

The bias and control current generated at the AMB location before and after balancing is shown in Fig. 5.26. The percentage reduction in the control current after balancing in the time domain is found out to be 53-65 %.

TH-2966_176103027

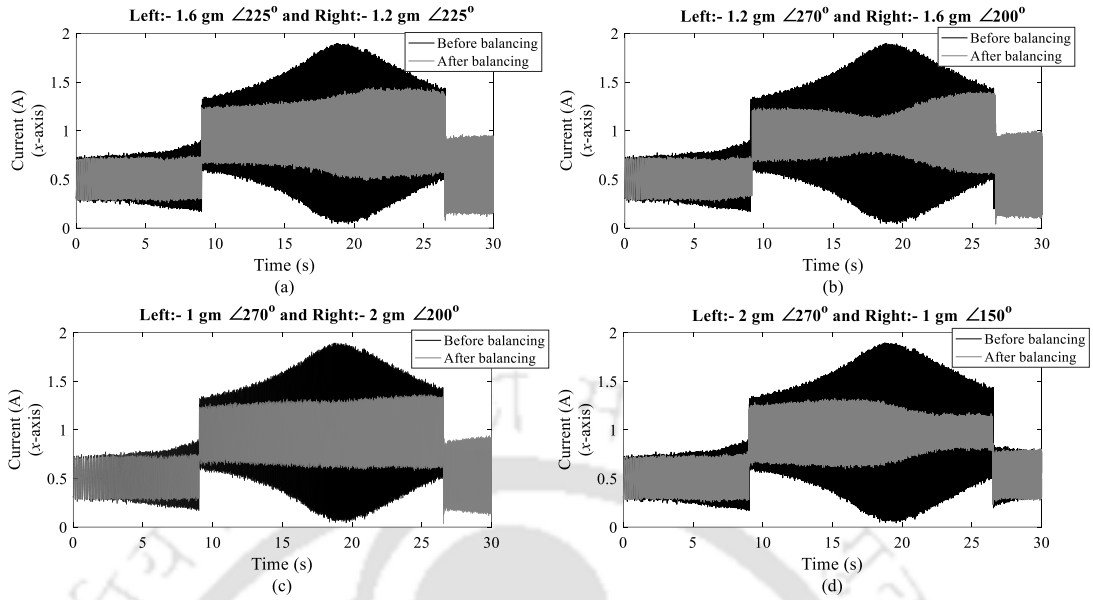


Fig. 5. 26. Overall current vs. time plot before and after balancing of rotor system utilizing estimated values of balance masses in VTEICM (a) pair I, (b) pair II, (c) pair III, and (d) pair IV.

This shows the effectiveness of the VTEICM using SVTU in the balancing of the rotor-AMB system. With the minimum information of the rotor system and switching of bias current, the rotor system can be balanced at high speeds. Also, the implemented balancing methodology consumes an adequate amount of power to allow the rotor system to accelerate above its critical speed.

5.7 Remarks

The high-speed balancing of the rotor system was carried out in the experimental rotor-AMB test rig with the application of SVTU. The excessive current utilization in accelerating the rotor-AMB system at high speeds results in heating of coils and power loss. The switching of bias current performed in the present work effectively allows the rotor system to cross its first critical speed with adequate utilization of the bias current. The integrated AMB system can be utilized to control and excite the rotor system

TH-2966_176103027

simultaneously in real-time. The implementation of SVTU instead of manually added trial unbalances is quite beneficial in the identification of the residual unbalances in the rotor system. The reduction in manual effort, lesser number of rotor runs, and minimum information of the rotor system to identify the fault parameters show that the VTEICM is an efficient strategy for balancing the rotor system at high speed. The present balancing methodology can be applied to the rotor system that requires a high-speed operation, periodic maintenance, and complex design. The contamination of the rotating parts can be avoided as the opening and closure of the machine casing are reduced with the application of SVTU. The practical difficulties in the tuning of the excitation frequency with respect to the operating speed of the rotor system are addressed. The deviation of both the frequencies, i.e., divergent and parallel shift, generates a different pattern of the beats in the vibration responses of the rotor system. With the voltage/speed factor and lag correction, the frequencies can be synchronized for the generation of virtual trial unbalances. The SVTU can effectively mimic the behavior of the manual trial unbalances in the rotor system as the estimated unbalances are found to be similar to the conventional influence coefficient methods with AMB control. The adequate reduction in the vibration responses and control currents is achieved with the addition of the identified balance masses at the corresponding balancing planes. The present work is limited to the identification of the unbalances in the rotor-AMB system with the application of magnetic excitations through AMB. The procedure can be extended to identify the intensity and characteristics of other faults, such as crack and misalignment of multi-harmonic nature, along with the residual unbalances using AMB control and additional excitations.

TH-2966_176103027

CHAPTER 6

ON-SITE ESTIMATION OF CRACKED ROTOR-AMB SYSTEM FAULT PARAMETERS USING MULTIPLE HARMONIC INFLUENCE COEFFICIENT METHOD

In the previous chapters, identification of unbalances present in the rotor-AMB system is carried out using VTEICM with virtual trial unbalances as magnetic excitation. The 1X harmonics of the displacement responses are utilized to identify the influence coefficients corresponding to the run-up operating speed of the system for the estimation of the unbalances. The identification algorithm is modified to identify the characteristics and intensity of additional multi-harmonic fault such as the crack, along with the unbalance using the multi-harmonic excitation through an AMB. The procedure for the identification of different cracked rotor faults, such as additive crack stiffness, internal damping, and the unbalances, is described using the Multi Harmonic Influence Coefficient Method. The numerical and experimental investigation of a rotor-AMB system with fatigue crack is described in this chapter.

6.1. Introduction

Most of the research works on the cracked rotor system are carried out to analyze the fault signatures in the vibration response or identify the system's faults on the basis of the numerical model of the industrial systems. The identification of the fault parameters is crucial to determine the severity of the fault or the life of the rotating machinery. Also, it would be beneficial to identify the fault parameters based on the system's response with

TH-2966_176103027

the least knowledge of the rotating machinery. The variation of the fault parameters increases with the variation in the assumed physical properties of the system. Therefore, in the present work, an identification algorithm is designed to obtain the fault parameters in the cracked rotor system with AMB based on the Multiple Harmonic Influence Coefficient Method (MHICM). The identification algorithm requires only the vibrational response of the system to estimate the fault parameters with the help of multi-harmonic magnetic excitation through AMB. The AMB is integrated into the system to facilitate the reduction of the vibrational response along with the generation of external magnetic excitation. The finite element model of a cracked shaft is developed supported on flexible bearings and integrated with AMB to verify the effectiveness of the present algorithm numerically. The rotating damping due to the rubbing of crack faces, friction between the rotating components, or material hysteresis is also introduced to analyze the stability condition of the system. The present approach allows us to monitor the presence of a crack in the system as well as successfully estimate the additive crack stiffness parameters, residual unbalances, and the internal damping in the system. Also, on-site estimation of multiple fault parameters has been performed in an experimental rotor test rig integrated with active magnetic bearing (AMB) with a fatigue crack generated in the shaft supported on ball bearings.

6.2. Description of the cracked rotor-AMB system

The rotor system comprises rigid discs mounted on a cracked shaft supported on the flexible bearings (CB), as shown in Fig. 6.1. The transverse fatigue crack generated due to cyclic loading stress is included in the present system that decreases the stiffness of the

TH-2966_176103027

shaft in its vicinity. The breathing or switching behavior of the crack generates a multi-harmonic response in the rotor system on rotation (Kulesza and Sawicki, 2012). The AMBs are also integrated into the system between the discs and the flexible bearing to reduce the level of vibration response. The AMB is utilized to generate multi-harmonic magnetic excitation force to predict different faults, such as additive crack stiffness, internal damping, and unbalances present in the cracked rotor system through the MHICM. The description of the identification algorithm is given in the next section.

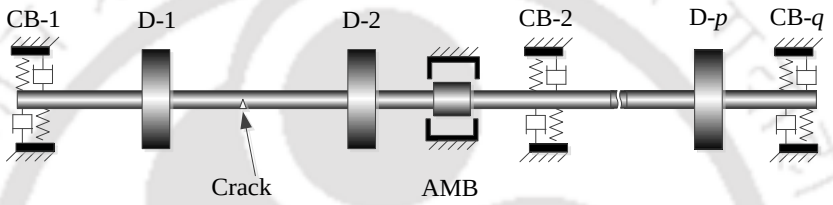


Fig. 6. 1. A rotor-AMB system with a cracked shaft supported on flexible bearings.

6.3. Development of the Multi Harmonic Influence Coefficient Method

In the present algorithm, the influence coefficients of the system are identified based on the displacement responses obtained and the magnitude and phase of multi-harmonic excitation applied through the AMB. The influence coefficients, along with the displacement responses of the system without any added excitations, are utilized to estimate the fault parameters. The influence coefficients of the system corresponding to discs and crack locations are identified with respect to the AMB locations at a particular spin speed. To obtain the influence coefficients, the system is first rotated at a particular speed, and the displacement responses generated at discs, AMB, and crack locations (measurement planes) are obtained, as shown in Fig. 6.2 (a). The displacement response

TH-2966_176103027

consists of multiple harmonics due to the presence of the crack, so for each harmonic ('h'), the complex displacement response at disc-1 is related to influence coefficients as

$$\left(\eta_1\right)_h = \sum_{i=1}^{p}\left(N_{1p}\right)_h f_{d,p} + \left(N_{1c}\right)_h \left(f_c + f_i\right) \tag{6.1}$$

with, $f_{d,p} = m_p e_p \omega^2 \mathrm{e}^{\mathrm{j}\phi_p}$; $\quad f_c = \Delta k w_s \sum P_i$; $\quad f_i = -\mathrm{j}\omega c_H w_s$

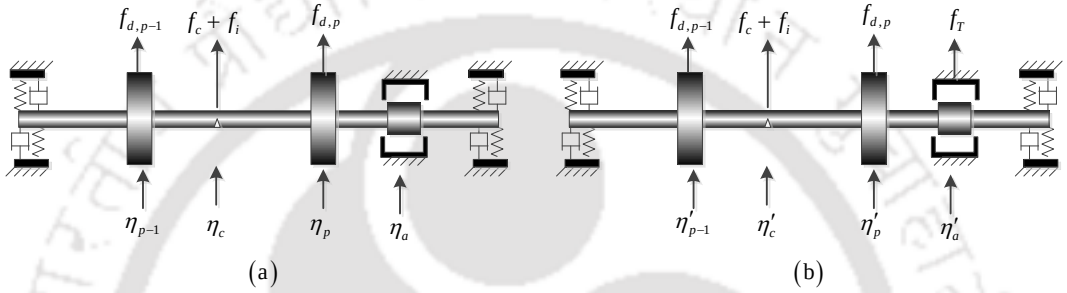


Fig. 6. 2. The rotor system showing forces and measurement locations of displacement responses (a) without and (b) with addition of multi-harmonic excitation force (f_T) at the AMB location.

where, m_p, e_p, and ϕ_p are the mass, eccentricity, and phase of the unbalance present at the disc locations; ω is the spin speed of the rotor; Δk is the additive crack stiffness, w_s is the static weight deflection of the rotor system; c_H is the internal damping coefficient of the system. η_1 is the complex displacement response corresponding to the disc-1 location. N_{1p} is the influence coefficient corresponding to the unbalance force at the p^{th} disc location. N_{1c} is the influence coefficient corresponding to the crack and internal damping force at the crack location. The detailed description of the relationship between the external forces and influence coefficient is provided in Section 6.4. Similarly, for the other measurement locations, Eq. (6.1) can be written as

$$\boldsymbol{\eta}_{r,1} = \mathbf{N}_r \mathbf{f}_{r,1} \tag{6.2}$$

TH-2966_176103027

with, $\boldsymbol{\eta}_{r,1} = \left\{ (\eta_1)_h \quad (\eta_2)_h \quad \cdots \quad (\eta_p)_h \quad (\eta_c)_h \quad (\eta_a)_h \right\}^T$

$$\mathbf{f}_{r,1} = \left\{ f_{d,1} \quad f_{d,2} \quad \cdots \quad f_{d,p} \quad f_c + f_i \quad 0 \right\}^T$$

where, $\mathbf{N}_r$ is the influence coefficients matrix corresponding to displacement response, i.e., described by Eq. A.4 in Appendix A. η_a is the complex displacement response corresponding to AMB location at which the excitation force is generated. In the second run, a multi-harmonic excitation force (f_T) is added to the system through AMB as additional current (i_T), as shown in Fig. 6.2 (b)

$$f_T = k_i i_T \tag{6.3}$$

with, $i_T = \sum f_h e^{\mathrm{j}\phi_h} / k_i$

where, f_h and ϕ_h are the excitation force amplitude, and phases are assumed corresponding to different harmonics. The additional current i_T is then added to the control current of the AMB as described in Section 2.3.2.2 to generate both control and excitation forces at the AMB location. The displacement responses in the second run are related to influence coefficients as

$$\boldsymbol{\eta}_{r,2} = \mathbf{N}_r \mathbf{f}_{r,2} \tag{6.4}$$

with, $\boldsymbol{\eta}_{r,2} = \left\{ (\eta_1')_h \quad (\eta_2')_h \quad \cdots \quad (\eta_p')_h \quad (\eta_c')_h \quad (\eta_a')_h \right\}^T$;

$$\mathbf{f}_{r,2} = \left\{ f_{d,1} \quad f_{d,2} \quad \cdots \quad f_{d,p} \quad f_c + f_i \quad f_T \right\}^T$$

On subtracting, Eq. (6.2) from Eq. (6.4), we obtain

TH-2966_176103027

$$\boldsymbol{\eta}_{r,2} - \boldsymbol{\eta}_{r,1} = \mathbf{N}_r \begin{Bmatrix} 0 & 0 & \cdots & 0 & 0 & f_T \end{Bmatrix}^T \tag{6.5}$$

So, the influence coefficients corresponding to the last column or the last row of the influence coefficient matrix can be estimated as

$$\left(N_{a,i}\right)_h = \left(N_{i,a}\right)_h = \frac{\left(\eta_i'\right)_h - \left(\eta_i\right)_h}{f_h e^{\mathrm{j}\phi_h}}; \quad \left(N_{a,c}\right)_h = \left(N_{c,a}\right)_h = \frac{\left(\eta_c'\right)_h - \left(\eta_c\right)_h}{f_h e^{\mathrm{j}\phi_h}}; \quad i = 1, 2, \ldots, p \tag{6.6}$$

Now, from Eq. (6.2), the influence coefficients related to AMB location can be written as

$$\left(\eta_a\right)_h = \sum_{i=1}^{p} \left(N_{a,i}\right)_h f_{d,i} + \left(N_{a,c}\right)_h \left(f_c + f_i\right) \tag{6.7}$$

Now, substituting the values of forces, Eq. (6.7) can be written corresponding to different harmonics as

$$\left(\eta_a\right)_0 = \left(N_{a,c}\right)_0 \Delta k w_s P_0 - \left(N_{a,c}\right)_0 \mathrm{j}\omega c_H w_s \qquad \text{for } h = 0 \tag{6.8}$$

$$\left(\eta_a\right)_1 = \sum_{i=1}^{p} \left(N_{a,i}\right)_1 f_{d,i} + \left(N_{a,c}\right)_1 \Delta k w_s P_1 \qquad \text{for } h = 1 \tag{6.9}$$

$$\left(\eta_a\right)_h = \left(N_{a,c}\right)_h \Delta k w_s P_h \qquad \text{for } h \neq 0 \text{ and } \neq 1 \tag{6.10}$$

The above equations are assembled in the matrix form as

$$\boldsymbol{\eta}_a(\omega) = \mathbf{A}_c(\omega)\mathbf{q} \tag{6.11}$$

With, $\boldsymbol{\eta}_a = \begin{Bmatrix} \left(\eta_a\right)_0 & \left(\eta_a\right)_1 & \left(\eta_a\right)_2 & \cdots & \left(\eta_a\right)_{-1} & \cdots \end{Bmatrix}^T$

$$\mathbf{q} = \begin{Bmatrix} \Delta k P_0 & c_H & \Delta k P_1 & m_1 e_1 \mathrm{e}^{\mathrm{j}\alpha_1} & \cdots & m_p e_p \mathrm{e}^{\mathrm{j}\alpha_p} & \Delta k P_2 & \cdots & \Delta k P_{-1} & \cdots \end{Bmatrix}^T$$

TH-2966_176103027

The detailed description of the identification matrix $\mathbf{A}_c$ matrix is given by Eq. C.1 in Appendix C. Similarly, Eq. (6.11) is obtained corresponding to different spin speeds and assembled together as

$$\mathbf{d} = \mathbf{Z}_d \mathbf{q} \tag{6.12}$$

with, $\mathbf{d} = \left\{ \boldsymbol{\eta}_a(\omega_1) \quad \boldsymbol{\eta}_a(\omega_2) \quad \cdots \quad \boldsymbol{\eta}_a(\omega_f) \right\}^T$;

$\mathbf{Z}_d = \left\{ \mathbf{A}_c(\omega_1) \quad \mathbf{A}_c(\omega_2) \quad \cdots \quad \mathbf{A}_c(\omega_f) \right\}^T$

where, ω_1, ω_2, …, ω_f are the spin speeds of the rotor system. To obtain the desired results, the virtual control currents are obtained corresponding to the displacement responses at the discs and crack locations, as

$$i_s(t) = k_P \eta_s(t) + k_D \dot{\eta}_s(t) + k_I \int \eta_s(t) dt \; ; \; s = 1, 2, \ldots, p \tag{6.13}$$

$$i_c(t) = k_P \eta_c(t) + k_D \dot{\eta}_c(t) + k_I \int \eta_c(t) dt \tag{6.14}$$

Now, the virtual currents and AMB currents are related to influence coefficients corresponding to different forces as

$$\mathbf{i}_{r,1} = \mathbf{J}_r \mathbf{f}_{r,1} \tag{6.15}$$

with, $\mathbf{i}_{r,1} = \left\{ (i_1)_h \quad (i_2)_h \quad \cdots \quad (i_p)_h \quad (i_c)_h \quad (i_a)_h \right\}^T$

where, $\mathbf{J}_r$ is the influence coefficients matrix corresponding to control current and is described by Eq. A.4 in Appendix A. The same process is repeated as shown in Eq. (6.3) to Eq. (6.12) to obtain the influence coefficient corresponding to the AMB location. So, the

TH-2966_176103027

relationship of AMB control current with the unbalance, crack, and internal damping forces can be written as

$$\mathbf{i}_a(\omega) = \mathbf{S}_c(\omega)\mathbf{q} \tag{6.16}$$

with, $\mathbf{i}_a = \left\{(i_a)_0 \quad (i_a)_1 \quad (i_a)_2 \quad \cdots \quad (i_a)_{-1} \quad \cdots\right\}^T$

where, $\mathbf{S}_c$ is the identification matrix with coefficients corresponding to the fault parameters (Appendix C, Eq. C.2). Now, the assembled equation for different operating speeds is given as

$$\mathbf{i}_g = \mathbf{Z}_c\mathbf{q} \tag{6.17}$$

with, $\mathbf{i}_g = \left\{\mathbf{i}_a(\omega_1) \quad \mathbf{i}_a(\omega_2) \quad \cdots \quad \mathbf{i}_a(\omega_f)\right\}^T$;

$\mathbf{Z}_d = \left\{\mathbf{S}_c(\omega_1) \quad \mathbf{S}_c(\omega_2) \quad \cdots \quad \mathbf{S}_c(\omega_f)\right\}^T$

Now, Eq. (6.12) and Eq. (6.17) are assembled together to obtain the final equation as

$$\begin{Bmatrix}\mathbf{d}\\ \mathbf{i}_g\end{Bmatrix} = \begin{bmatrix}\mathbf{Z}_d\\ \mathbf{Z}_c\end{bmatrix}\mathbf{q} \tag{6.18}$$

The required unbalance, additive crack stiffness, and internal damping factor can be estimated as

$$\mathbf{q} = \left(\begin{bmatrix}\mathbf{Z}_d\\ \mathbf{Z}_c\end{bmatrix}^T\begin{bmatrix}\mathbf{Z}_d\\ \mathbf{Z}_c\end{bmatrix}\right)^{-1}\begin{bmatrix}\mathbf{Z}_d\\ \mathbf{Z}_c\end{bmatrix}^T\begin{Bmatrix}\mathbf{d}\\ \mathbf{i}_g\end{Bmatrix} \tag{6.19}$$

The algorithm allows the quantitative estimation of the fault parameters with the utilization of the AMB in the system. This simplified approach reduces both manual effort and

TH-2966_176103027

downtime time in the condition monitoring of the system. The force current stiffness coefficient of the AMB, the time-domain displacement responses, and the control current at the AMB locations are only required to estimate the faults parameters. All the required properties can be obtained easily in any industrial rotor-AMB system, as described in the above sections, without any FEM modelling. This also reduces the computational efforts in the periodic estimation of the faults present in the systems.

6.4. Finite Element Modelling of the cracked rotor-AMB system

The rotor is subjected to the forces such as inertial force, gyroscopic couples, stiffness and damping forces due to flexible bearings, discrete disc unbalance forces, and AMB forces. The description of the modelling of the flexible shaft, rigid discs, support bearing, and AMB is explained in Section 2.4. In addition to the aforementioned forces, additive crack stiffness forces, internal damping force, multi-harmonic AMB excitation force has been included. The crack force and internal damping force of the rotor system are explained in the following subsections.

6.4.1. Crack force

The opening and closure behavior of the crack faces is crucial in the modeling of the crack forces in the rotor system. For the present work, a switching crack model is utilized in which the crack remains open for half of the cycle and closed for the next half of the cycle. This effect of the crack while undergoing a complete rotation depends on the orientation of the crack front. The presence of the crack decreases the stiffness of the shaft, and therefore, in order to introduce the effect in the FEM model, an additive crack stiffness (Δk) is added.

TH-2966_176103027

A switching crack excitation function ($\sigma(t)$) is also included in the crack force to generate the opening and closure behavior of the crack during rotation as given in Eq. (6.20). (Gasch, 1993)

$$\sigma(t) = \frac{1}{2} + \frac{2}{\pi}\cos(\omega t) - \frac{2}{3\pi}\cos(3\omega t) + \frac{2}{5\pi}\cos(5\omega t) - \frac{2}{7\pi}\cos(7\omega t) + \ldots \tag{6.20}$$

where, ω is the spin speed of the rotor. The crack is assumed to be closed (in the compression zone) when the position of the crack is in the upward direction. Whereas it is assumed to be open (in the tensile zone) when its position is in the downward direction. In order to incorporate crack fault in the rotor system, a rotating coordinate system with β and γ axes is defined. The free-body diagram of the disc element in the rotating coordinate system is shown in Fig. 6.3. The additive crack stiffness force ($\mathbf{f}_{c,r}$) in the rotating coordinate system at a particular node location is given as

$$\mathbf{f}_{c,r} = \sigma(t)\begin{bmatrix} \Delta k & 0 \\ 0 & 0 \end{bmatrix}\begin{Bmatrix} u_\beta \\ u_\gamma \end{Bmatrix} \tag{6.21}$$

where, Δk is the additive crack stiffness due to the crack present along the β direction. u_β and u_γ are the displacements along the β and γ axes, respectively. The crack force is transformed from the rotational coordinates to the translational coordinates (u_x, u_y) at the crack location as

$$\mathbf{f}_{c,t} = \sigma(t)\mathbf{T}_r\begin{bmatrix} \Delta k & 0 \\ 0 & 0 \end{bmatrix}\mathbf{T}_r^{\,T}\begin{Bmatrix} u_x + w_s \\ u_y \end{Bmatrix} \quad \text{with} \quad \mathbf{T}_r = \begin{bmatrix} \cos\omega t & \sin\omega t \\ -\sin\omega t & \cos\omega t \end{bmatrix} \tag{6.22}$$

where, $\mathbf{f}_{c,t}$ is the crack force in the translational coordinate system. w_s is the static displacement along the x-direction at the crack location.

TH-2966_176103027

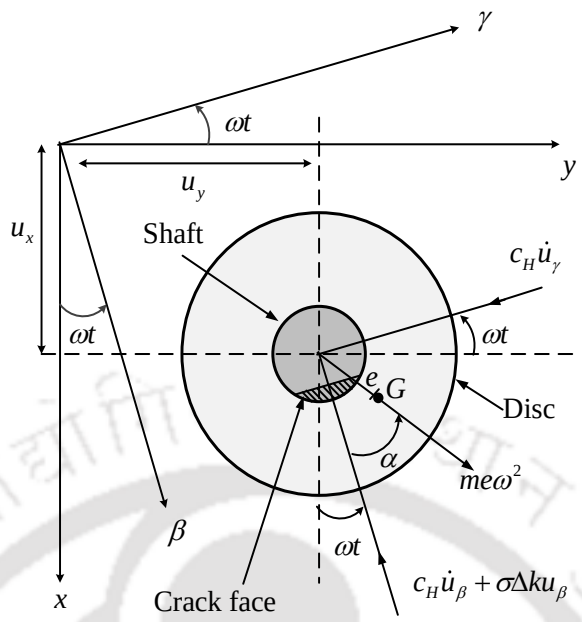


Fig. 6. 3. The representation of translational and rotational coordinate systems for the cracked shaft.

Considering the dynamic displacement to be small in comparison to the static displacement and neglecting it, we can write the complex crack force as

$$f_c = \sigma(t)\Delta k(1+e^{2\mathrm{j}\omega t})w_s \tag{6.23}$$

After substituting Eq. (6.20) in Eq. (6.23), we get

$$f_c = \Delta k w_s \left(P_0 + P_1 e^{\mathrm{j}\omega t} + P_2 e^{2\mathrm{j}\omega t} + P_3 e^{3\mathrm{j}\omega t} + \ldots + P_{-1} e^{-\mathrm{j}\omega t} + P_{-3} e^{-3\mathrm{j}\omega t} + \ldots\right) \tag{6.24}$$

$$f_c = \Delta k w_s \sum P_i e^{\mathrm{ij}\omega t} \tag{6.25}$$

where, P_i is the participation factor corresponding to the i^{th} harmonics in the crack force. The overall crack force in the system is given as

$$\mathbf{f}_c = \Delta k w_s \mathbf{v} \sum P_i e^{\mathrm{ij}\omega t} \tag{6.26}$$

TH-2966_176103027

with, $\mathbf{v} = \{0 \quad \cdots \quad 1 \quad \cdots \quad 0\}^T$

where, **v** is the location vector of the crack force, and '1' gives the nodal position of the crack force.

The static deflection (w_s) of the system at the crack position is given by utilizing the overall stiffness matrix of the system and the static weights at the different node locations due to discs as

$$\left(\mathbf{K}_s + \mathbf{K}_b\right)\boldsymbol{\eta}_{st} = \sum_{i=1}^{p} m_i g \mathbf{h}_i \tag{6.27}$$

$$\boldsymbol{\eta}_{st} = \left(\mathbf{K}_s + \mathbf{K}_b\right)^{-1} \sum_{i=1}^{p} m_i g \mathbf{h}_i \tag{6.28}$$

$$w_s = \mathbf{D}\left(\mathbf{K}_s + \mathbf{K}_b\right)^{-1} \sum_{i=1}^{p} m_i g \mathbf{h}_i \tag{6.29}$$

with, $\mathbf{D} = \begin{bmatrix} \ddots & 0 & 0 & 0 & 0 \\ & 1 & 0 & 0 & 0 \\ & & 0 & 0 & 0 \\ & & & \ddots & 0 \\ sym & & & & 0 \end{bmatrix}$

where, $\boldsymbol{\eta}_{st}$ is the static deflection vector corresponding to different node locations. The matrix **D** is the location matrix and '1' represents the node location corresponding to crack location.

TH-2966_176103027

6.4.2. Internal damping force

While rotation, the rubbing of two crack surfaces introduces an internal (rotating) damping in the system. The rotating damping force (f_i) in the cracked shaft, as shown in Fig. 6.3 along the stationary coordinate system, is given as (Roy and Tiwari, 2020)

$$f_{i,x} = c_H \dot{u}_\beta \cos\omega t - c_H \dot{u}_\gamma \sin\omega t \tag{6.30}$$

$$f_{i,y} = c_H \dot{u}_\beta \sin\omega t + c_H \dot{u}_\gamma \cos\omega t \tag{6.31}$$

$$f_i = f_{i,x} + \mathrm{j} f_{i,y} = c_H \dot{\zeta} e^{\mathrm{j}\omega t} \tag{6.32}$$

with, $\dot{\zeta} = \dot{u}_\beta + \mathrm{j}\dot{u}_\gamma$

where, c_H is the internal damping coefficient. The complex displacement of the system in stationary as well as rotating frame is given as, $s = u_x + w_s + \mathrm{j}u_y$ and $\zeta = u_\beta + \mathrm{j}u_\gamma$, respectively. The transformation of internal damping force from rotational to stationary coordinate system using $\zeta = s e^{\mathrm{j}\omega t}$ (in Eq. (6.32), can be written as

$$f_i = c_H\left(\dot{u}_x + \mathrm{j}\dot{u}_y\right) - \mathrm{j}\omega\left(u_x + w_s + \mathrm{j}u_y\right) \tag{6.33}$$

The overall internal damping force for the system is given as

$$\mathbf{f}_i = c_H \mathbf{D}\dot{\boldsymbol{\eta}} - \mathrm{j}\omega c_H \mathbf{D}\boldsymbol{\eta} - \mathrm{j}\omega c_H w_s \mathbf{v} \tag{6.34}$$

As it can be seen from Eq. (6.34), the internal damping force is applied at the crack location along with the translational nodes. In the present case, the breathing crack model is considered. This model is valid for the small crack depth in which during rotation opening and closure behavior is observed. When the crack size increases, then the crack

TH-2966_176103027

behavior is no longer governed by the breathing crack model instead, it becomes an open crack. The internal damping is prevalent in breathing cracks due to the rubbing of crack faces during opening and closure. However, the internal damping will be minimum or absent in open cracks, where crack faces remain open, and rubbing does not take place (Shravankumar and Tiwari, 2016; Singh and Tiwari, 2016; Shravankumar and Tiwari, 2019; Roy and Tiwari, 2020; Sarmah and Tiwari, 2020).

6.4.3. Equations of motion of the rotor system

The overall equation of motion of the system is given as

$$\mathbf{M}\ddot{\boldsymbol{\eta}}(t)+(\mathbf{C}-\omega\mathbf{G})\dot{\boldsymbol{\eta}}(t)+\mathbf{K}\boldsymbol{\eta}(t)=\mathbf{f}_d(t)-\mathbf{f}_m(t)+\mathbf{f}_c(t)+\mathbf{f}_i(t) \tag{6.35}$$

with, $\mathbf{M}=\mathbf{M}_s+\mathbf{M}_d$, $\mathbf{C}=\mathbf{C}_b$, $\mathbf{G}=\mathbf{G}_d$ and $\mathbf{K}=\mathbf{K}_s+\mathbf{K}_b$

On substituting Eq. (6.34) and Eq. (2.37) in Eq. (6.35), we get

$$\begin{aligned}\mathbf{M}\ddot{\boldsymbol{\eta}}(t)+(\mathbf{C}-\omega\mathbf{G})\dot{\boldsymbol{\eta}}(t)+\mathbf{K}\boldsymbol{\eta}(t)=\mathbf{f}_d(t)+\mathbf{f}_c(t)+c_H\mathbf{D}\dot{\boldsymbol{\eta}}-\mathrm{j}\omega c_H\mathbf{D}\dot{\boldsymbol{\eta}}-\mathrm{j}\omega c_H w_s\mathbf{v}\\ +k_s\mathbf{S}\boldsymbol{\eta}-k_i\mathbf{S}\left(k_P\boldsymbol{\eta}+k_D\dot{\boldsymbol{\eta}}+k_I\int\boldsymbol{\eta}dt\right)\end{aligned} \tag{6.36}$$

Rearranging the equation with displacement dependent terms on the left-hand side of the equation, we get

$$\begin{pmatrix}\mathbf{M}\ddot{\boldsymbol{\eta}}(t)+(\mathbf{C}-c_H\mathbf{D}-\omega\mathbf{G}+k_ik_D\mathbf{S})\dot{\boldsymbol{\eta}}(t)\\ +\left(\mathbf{K}+\mathrm{j}\omega c_H\mathbf{D}-k_s\mathbf{S}+k_ik_p\mathbf{S}\right)\boldsymbol{\eta}(t)+k_ik_I\mathbf{S}\int\boldsymbol{\eta}dt\end{pmatrix}=\mathbf{f}_d(t)+\mathbf{f}_c(t)-\mathrm{j}\omega c_H w_s\mathbf{v} \tag{6.37}$$

The solution for the present system is assumed as

$$\boldsymbol{\eta}=\sum\boldsymbol{\eta}_h\mathrm{e}^{hj\omega t} \tag{6.38}$$

TH-2966_176103027

where, 'h' is the index corresponding to the different harmonics present in the shaft displacement, i.e. h = (0, 1, 2, 3, .., -1, -3, -7). Substituting Eq. (6.38) into Eq. (6.37), we get

$$\left(\begin{array}{l} (h\mathrm{j}\omega)^2 \mathbf{M} + (h\mathrm{j}\omega)(\mathbf{C} - c_H \mathbf{D} - \omega \mathbf{G} + k_i k_D \mathbf{S}) \\ + (\mathbf{K} + \mathrm{j}\omega c_H \mathbf{D} - k_s \mathbf{S} + k_i k_p \mathbf{S}) + \dfrac{k_i k_I}{h\mathrm{j}\omega} \mathbf{S} \end{array} \right) \boldsymbol{\eta}_h \mathrm{e}^{h\mathrm{j}\omega t} = \mathbf{f}_d(t) + \mathbf{f}_c(t) - \mathrm{j}\omega c_H w_s \mathbf{v} \qquad (6.39)$$

or,

$$\boldsymbol{\eta}_h \mathrm{e}^{h\mathrm{j}\omega t} = \mathbf{N}_h \left(\mathbf{f}_d(t) + \mathbf{f}_c(t) - \mathrm{j}\omega c_H w_s \mathbf{v} \right) \qquad (6.40)$$

with

$$\mathbf{N}_h = \left((h\mathrm{j}\omega)^2 \mathbf{M} + (h\mathrm{j}\omega)(\mathbf{C} - c_H \mathbf{D} - \omega \mathbf{G} + k_i k_D \mathbf{S}) + (\mathbf{K} + \mathrm{j}\omega c_H \mathbf{D} - k_s \mathbf{S} + k_i k_p \mathbf{S}) + \frac{k_i k_I}{h\mathrm{j}\omega} \mathbf{S} \right)^{-1}$$

where, $\mathbf{N}_h$ is the influence coefficients matrix corresponding to the h^{th} harmonic. Now, Eq. (6.40) can be further separated corresponding to the different harmonics as

$$\boldsymbol{\eta}_0 = \mathbf{N}_0 \left(\Delta k w_s \mathbf{v} P_0 - \mathrm{j}\omega c_H w_s \mathbf{v} \right) \qquad \text{for } h = 0 \qquad (6.41)$$

$$\boldsymbol{\eta}_1 = \mathbf{N}_1 \left(\mathbf{f}_d(t) + \Delta k w_s \mathbf{v} P_1 \right) \qquad \text{for } h = 1 \qquad (6.42)$$

$$\boldsymbol{\eta}_h = \mathbf{N}_h \Delta k w_s \mathbf{v} P_h \qquad \text{for } h \neq 0 \text{ and } \neq 1 \qquad (6.43)$$

The above equations are utilized in the identification of additive crack stiffness, unbalance, and internal damping present in the system, as described in the next section.

TH-2966_176103027

The FEM model of the rotor system is developed to generate the displacement responses similar to an industrial rotor and determine the effectiveness of the present identification algorithm in the estimation of the fault parameters.

6.5. Numerical simulation of the proposed identification algorithm

Simulations are carried out for the cracked rotor-AMB system supported on two flexible bearings, as shown in Fig. 6.4. The rotating shaft is discretized into five elements with two rigid disc mountings. The assumed physical properties of the flexible bearings, cracked shaft, internal damping factor, and residual unbalances are given in Table 6.1. The element lengths are considered to be random in order to get the resemblance of the real rotor system in which the gaps between the components can be uneven. The aim of the FEM modeling is to obtain the displacement responses of the rotor system under the presence of different excitation forces, which is required to validate the developed identification algorithm. The location of the components at different nodes will not affect the identification algorithm. The shaft is discretized as per the point loads applied at the locations of components. The displacement responses at the rigid discs, AMB, and crack locations (the location of the crack is known in the present procedure) are only required to estimate the fault parameters. The controller gains and the stiffness factors of the AMB are shown in Table 6.2. The equation of motion, as mentioned in Eq. (6.35) is solved with the help of the SIMULINK model, as shown in Fig. 6.5. The displacement responses at the node locations are obtained using the Runge-Kutta solver at a sampling frequency of 2^{14} Hz in the SIMULINK-MATLAB platform.

TH-2966_176103027

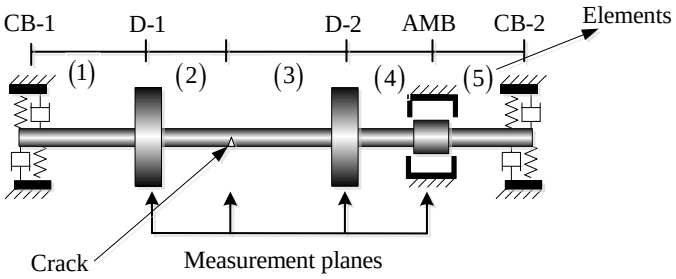


Fig. 6. 4. A pictorial representation of the rotor-AMB system with elements and measurement planes considered in FEM modeling.

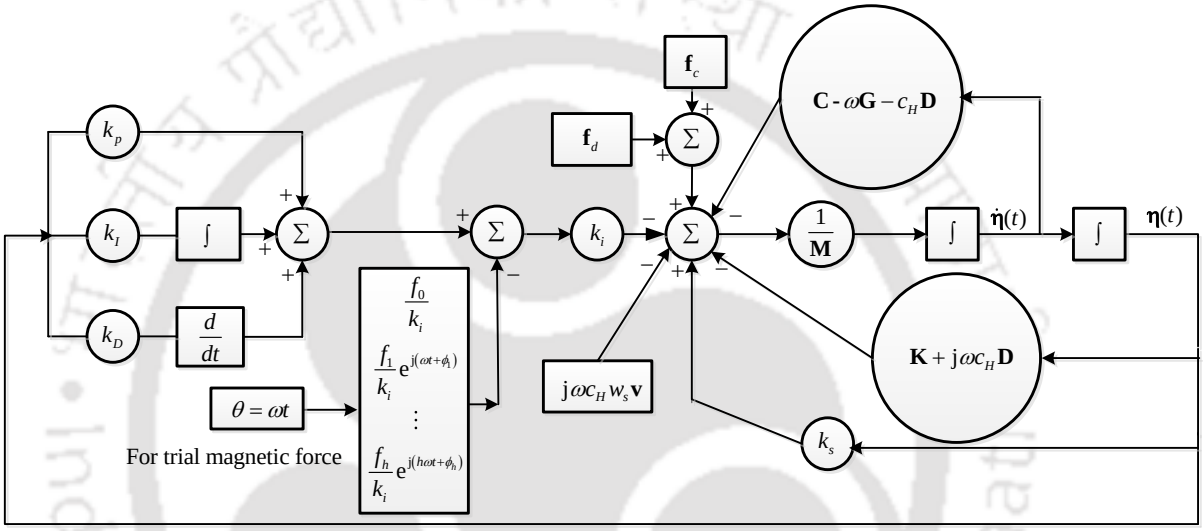


Fig. 6. 5. A schematic diagram of the SIMULINK model utilized in the generation of displacement responses.

To check the critical frequencies of the rotor with and without the application of AMB control, the eigenvalues of the system are obtained for the free vibration condition. The backward and forward whirl frequencies corresponding to the first critical speed without application of the AMB are 37.7 Hz and 38.4 Hz, respectively.

TH-2966_176103027

Table 6. 1. Design parameters of the rotor system

Symbol	Parameter	Value	Unit
	Flexible shaft		
l_z	Length of the elements	120, 100, 82, 83, 150	mm
d	Diameter	16	mm
ρ	Density	7850	kg/m^3
E	Young's modulus of elasticity	2.06×10^{11}	N/m^2
c_H	Internal damping factor	75	N-s/m
Δk	Additive crack stiffness	3×10^5	N/m
	Rigid discs (Disc-1 and Disc-2) and core of AMB		
m	Mass	1.8, 2 and 0.88	kg
I_D	Diametral moment of inertia ($\times10^4$)	19.01, 24.5 and 5.1688	kg-m^2
I_P	Polar moment of inertia ($\times10^4$)	28.02, 49.0 and 3.975	kg-m^2
me	Unbalance at D-1 and D-2: magnitude ($\times10^4$)	1.26 and 1.6	kg-m
α	Unbalance at D-1 and D-2: phase	68.75° and 120.32°	degree
	End support bearing (CB-1 and CB-2)		
k_b	Stiffness	5.5×10^7 and 4.5×10^7	N/m
c_b	Damping	250, 260	N-s/m

Table 6. 2. Design parameters of the AMB system.

Symbol	Parameter	Value	Unit
k_i	Current stiffness coefficient	42.1	N/A
k_s	Displacement stiffness coefficient	105210	N/m
k_P	Proportional gain	4200	A/m
k_I	Integral gain	15000	A/m-s
k_D	Derivative gain	3	A-s/m

TH-2966_176103027

After the application of AMB, the backward and forward whirls are found out to be 41.3 and 42.2, respectively, as shown in the Campbell diagram (Fig. 6.6).

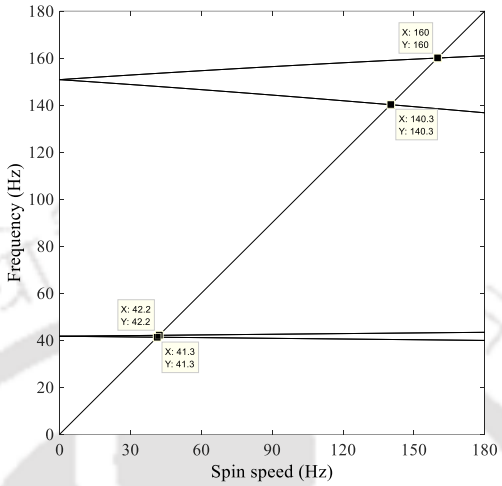


Fig. 6. 6. Campbell diagram depicting forward and backward whirl frequencies for the rotor system.

The system is rotated at 26 Hz to obtain the displacement response of the system in the time domain with the application of AMB. The displacement responses along the *x* and *y*-axis at different node locations are shown in Figs. 6.7 and 6.8, respectively. The orbit responses at different node locations are shown in Fig. 6.9. The irregular shape of the orbit plot is obtained due to the effect of the crack force with different harmonics along with the unbalance forces. The FFT of the complex displacement response at the Disc-1 location is done, and the full spectrum amplitude versus frequency curve is obtained, as displayed in Fig. 6.10. The positive and negative frequencies, as shown in Fig. 6.10, represent the forward and backward whirl components generated due to the presence of fatigue crack force in the rotor system. The full spectrum phase versus frequency curve is shown in Fig. 6.11.

TH-2966_176103027

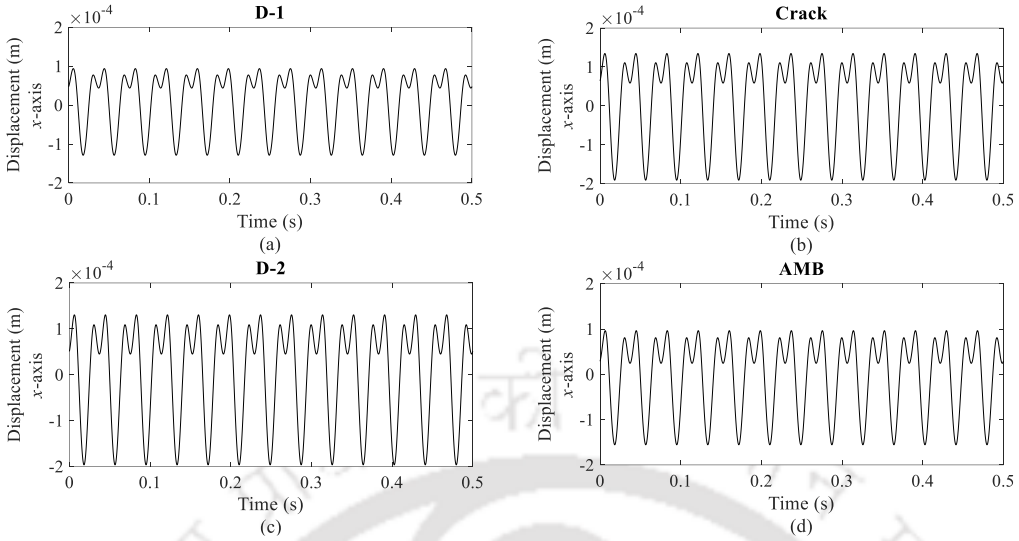


Fig. 6. 7. The displacement (m) vs time curve at (a) Disc-1, (b) crack, (c) Disc-2 and (d) AMB locations along *x*-axis.

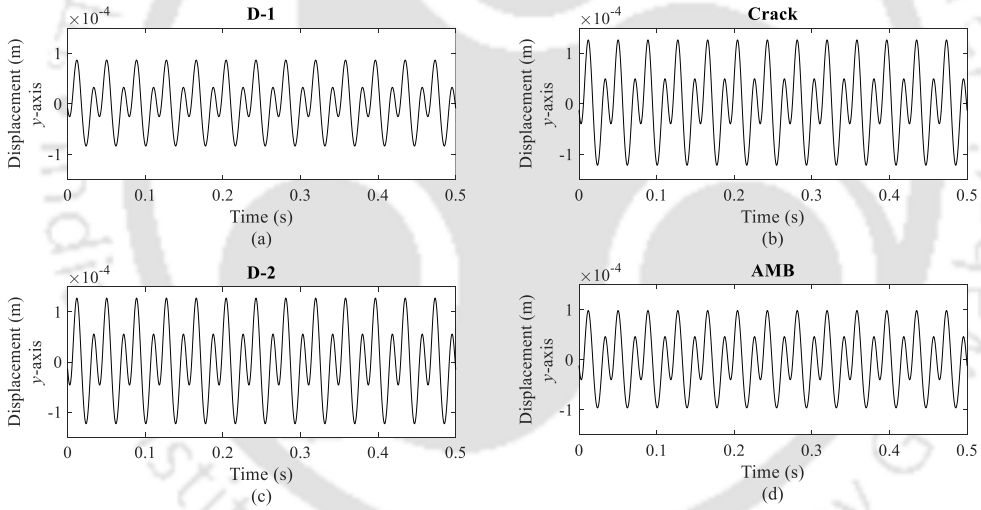


Fig. 6. 8. The displacement (m) vs time curve at (a) Disc-1, (b) crack, (c) Disc-2 and (d) AMB locations along *y*-axis.

TH-2966_176103027

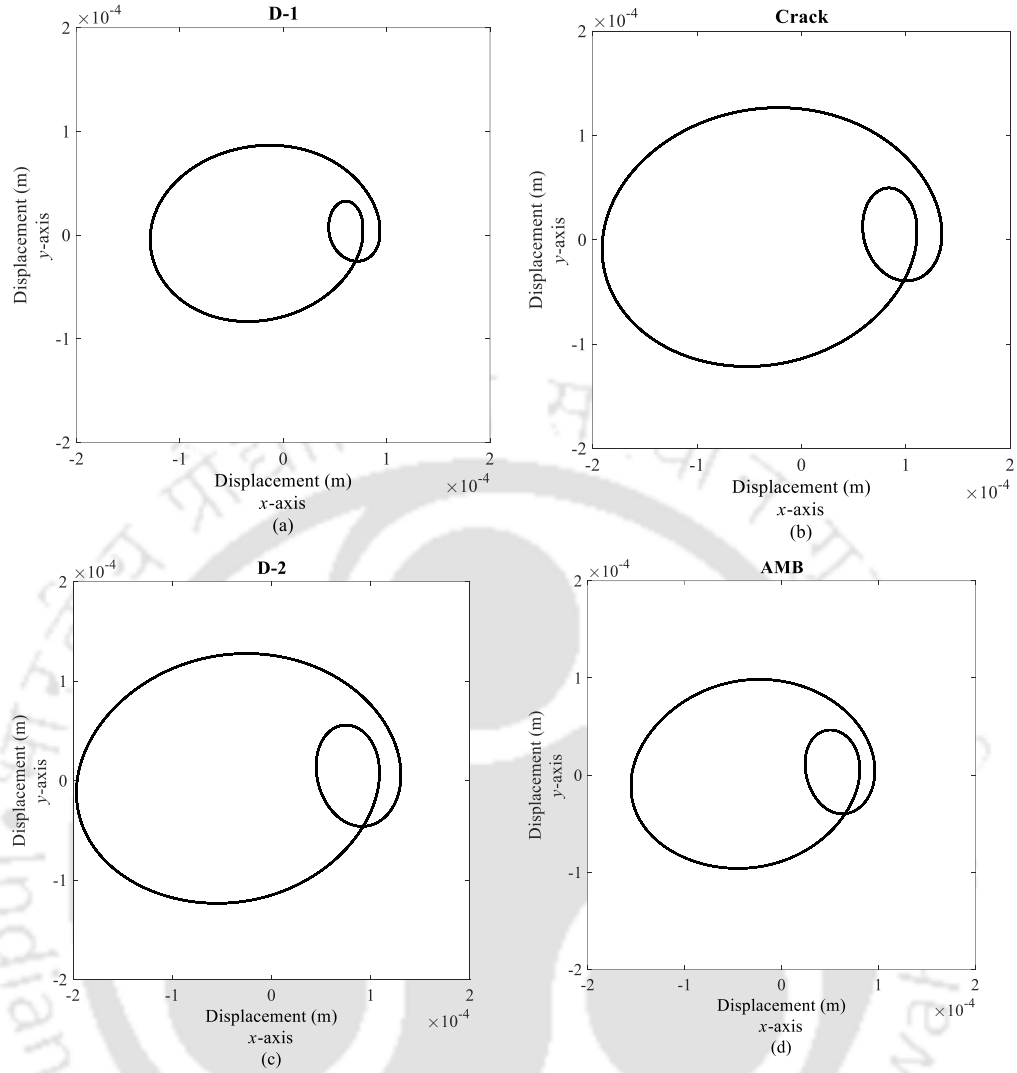


Fig. 6. 9. The orbit plot of the displacement response at (a) Disc-1, (b) crack, (c) Disc-2 and (d) AMB locations for 26 Hz spin speed.

6.5.1. Suppression of vibrational response using AMB control

To check the reduction in displacement response, the orbit plots have been obtained at 28 and 30 Hz with and without the application of the AMB, as shown in Figs. 6.12 (a) and (b), respectively. As it can be seen from Fig. 6.12, the displacement response at the Disc-1 location gets reduced with the application of the AMB in the system. The amplitudes of displacement responses at different nodes depend on the location of the node with respect

TH-2966_176103027

to the restoring forces (conventional bearing and AMB) and the excitation forces (unbalances and crack).

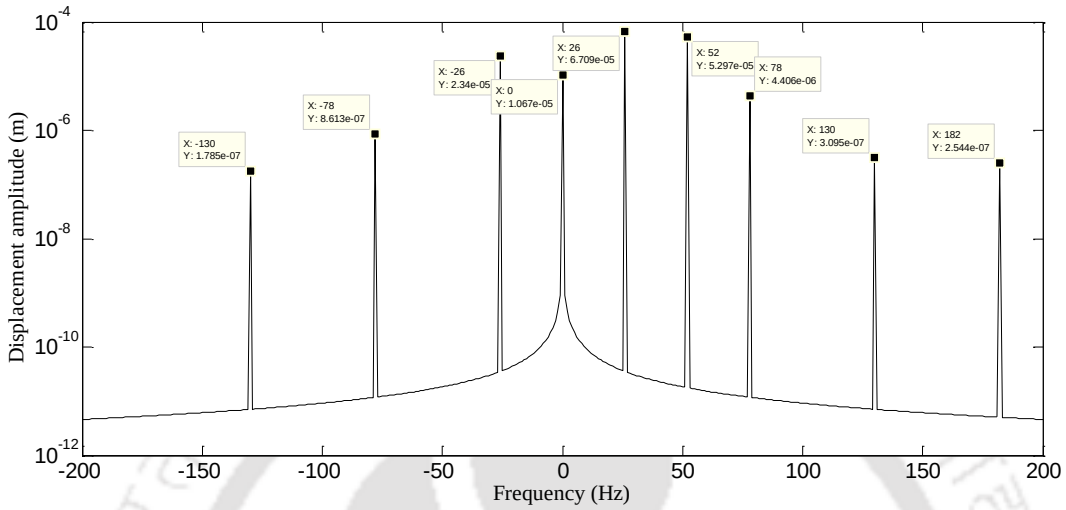


Fig. 6. 10. The full-spectrum response amplitude of the rotor system at Disc-1 location versus frequency.

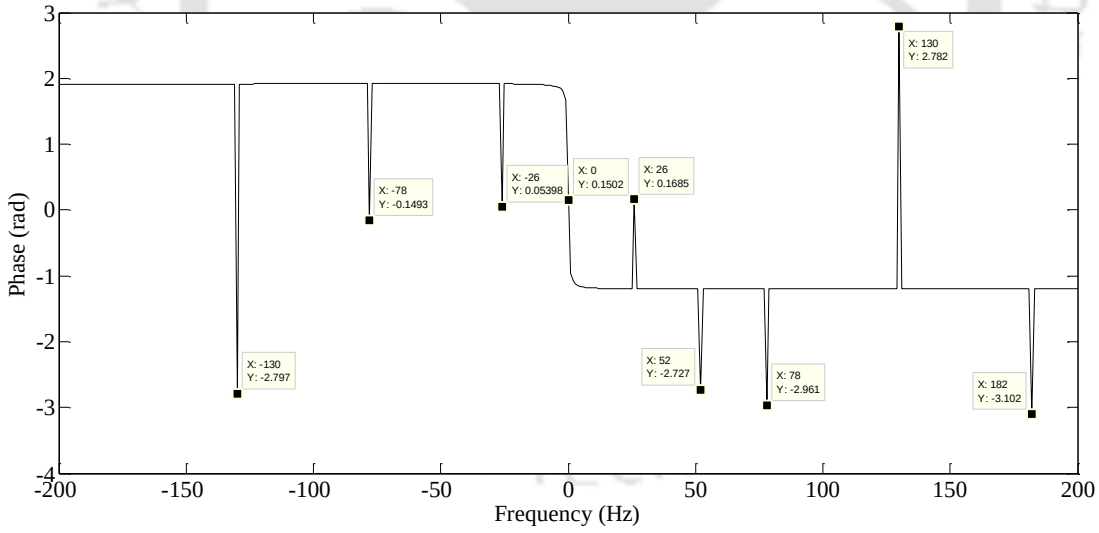


Fig. 6. 11. The full-spectrum response phase of the rotor system at Disc-1 location versus frequency.

As the response of the system is comprised of multiple harmonics due to unbalance and crack force, the shapes of the orbit plot change with the application of AMB. The reduction occurs

TH-2966_176103027

in different proportion for different harmonics with suppression through AMB control, therefore, the shapes of the orbit changes. The displacement response at all the node locations will get reduced with the application of the AMB in the system. However, the amplitude of responses at disc locations can be less or more than that at AMB location, depending on the distribution of the restoring and excitation forces. If the AMB is placed at the location of maximum amplitude, then the displacement response at the AMB location after suppression can be higher than that at other node locations. Also, the amount of suppression can be varied at the AMB location by varying the proportional gain parameter (k_P) in the AMB system. The increase in the proportional gain increases the amount of suppression at the AMB location. However, the internal damping in the system causes instability in the system above critical speeds, and it is essential to check the effectiveness of AMB to suppress the vibration at such speeds. The threshold speed (ω_o) at which the system becomes unstable due to the presence of internal damping in the system is given as (Chen *et al*., 1991; Tiwari, 2017)

$$\omega_o \leq \omega_{nf}\left(1+\frac{c_m}{c_H}\right) \tag{6.50}$$

where, ω_{nf} is the first natural frequency of the system, c_m is the external modal damping coefficient in the system corresponding to the first critical speed due to support bearing, and c_H is the magnitude of internal damping coefficient due to crack present in the shaft. The estimation procedure of the external modal damping is mentioned in Appendix B. For the calculated natural frequency without AMB, i.e., 38.4 Hz, the threshold speed ω_o is obtained equal to 40 Hz. So, the system is rotated above the threshold frequency, i.e., at 60 Hz, to check the effectiveness of AMB in displacement control. The orbit plots for with

TH-2966_176103027

and without AMB control for 60 Hz spin speed at Disc-1 location are shown in Figs. 6.13 (a) and (b), respectively. As it can be seen from Fig. 6.13, the AMB is able to control the operation of the system above the threshold limit.

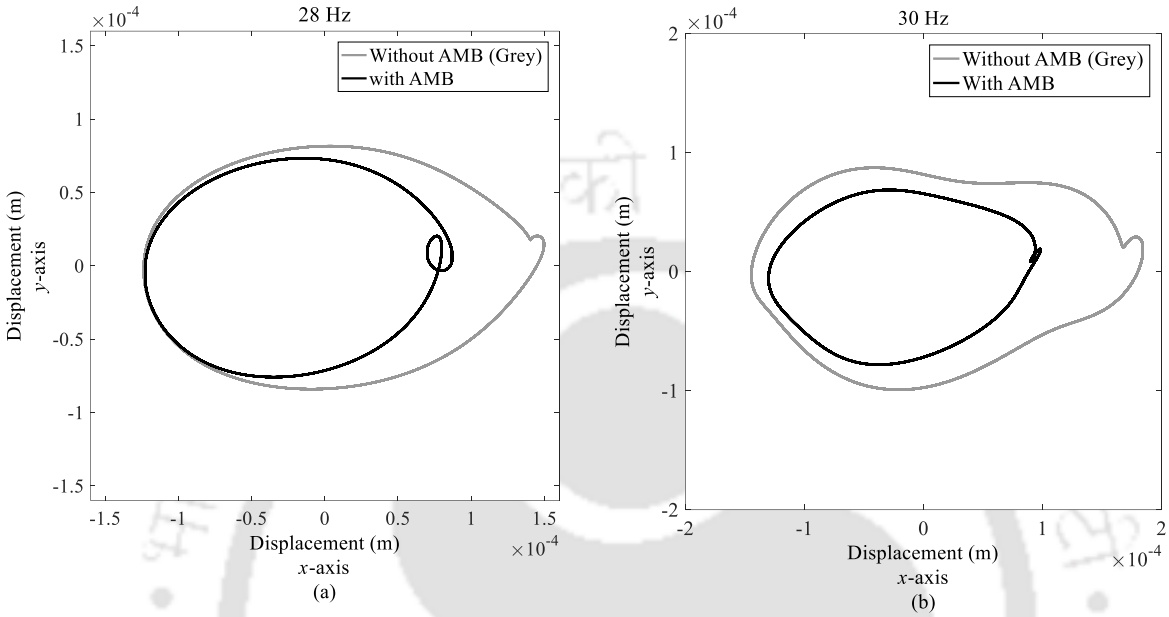
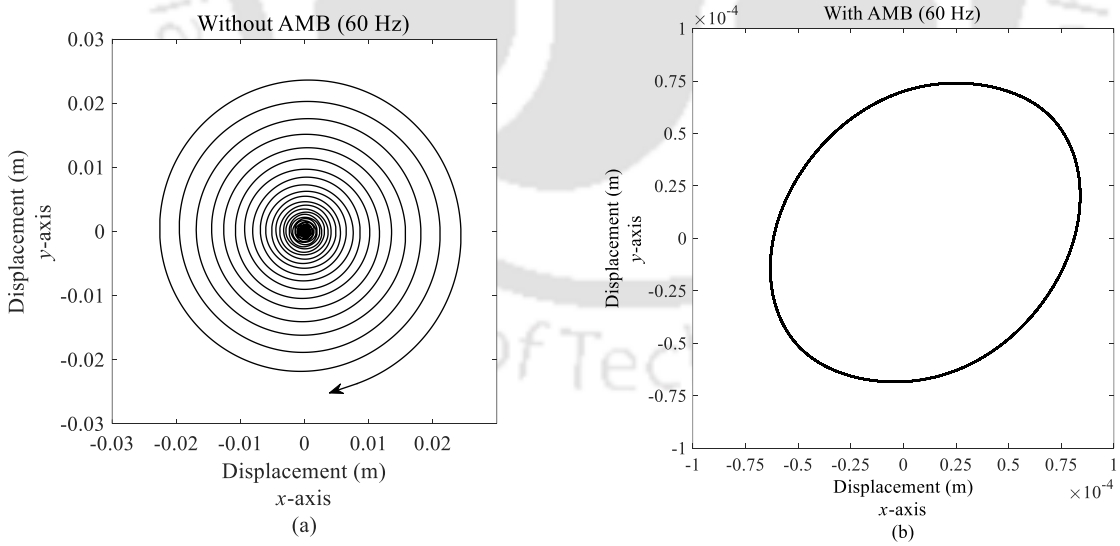


Fig. 6. 12. The orbit plot of the displacement response at Disc-1 location at (a) 28 Hz and (b) 30Hz.



TH-2966_176103027

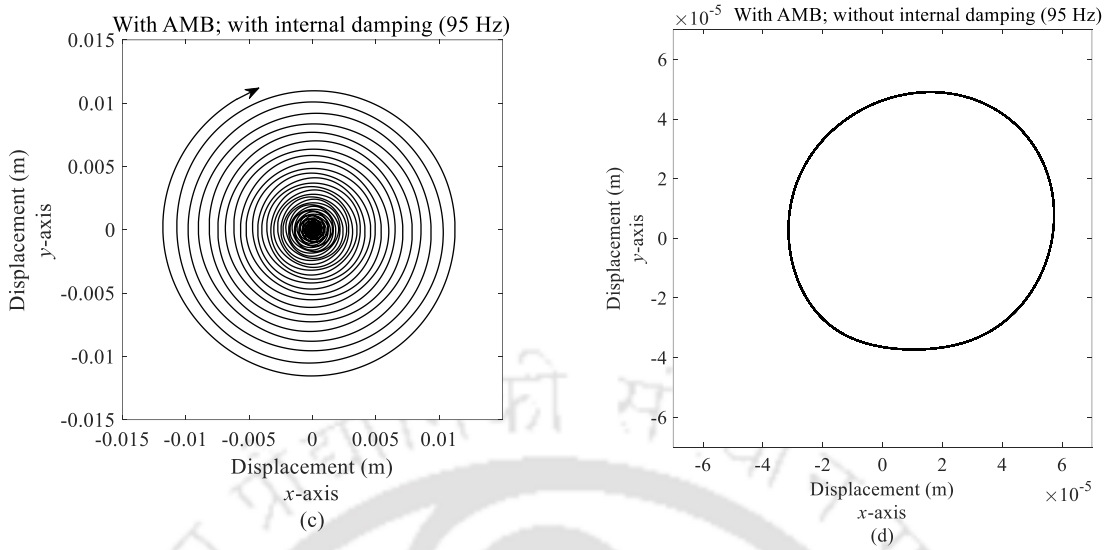


Fig. 6. 13. The orbit plot of the displacement response at Disc-1 location at 60 Hz (a) without AMB (b) with AMB and at 95 Hz with AMB and (c) with internal damping and (d) without internal damping.

With the introduction of AMB in the system, the stiffness and damping property of the system changes due to the introduction of proportional and derivative gain, respectively, and hence, the threshold speed changes. With the variation of the derivative gain (k_D) of the AMB controller, the threshold speed of the rotor system can be varied, as shown in Fig. 6.14. The new threshold speed of the rotor system for the AMB parameters, as mentioned in Table 6.2, is obtained equal to 93 Hz. So, the rotor system is rotated at 95 Hz, and the system is found to be unstable, as shown in Fig. 6.13 (c). However, without internal damping in the rotor AMB system, the system remains stable at 95 Hz operating speed, as shown in Fig. 6.13 (d). Therefore, it is important to estimate the internal damping coefficient of the system to obtain the safe operating speed of the rotor system and to control the threshold speed with the variation of the AMB control parameters. The value of the internal damping coefficient, c_H is taken closer to the values from the existing literature mentioned in the present chapter (Morais *et al.*, 2012; Peng *et al.*, 2017). The aim is to

TH-2966_176103027

generate the displacement responses through the FEM model in order to validate the developed identification algorithm. Other values of the internal damping factor can be selected and will not affect the estimation procedure if the system remains in the stable operating region, especially in the presence of AMB, as shown in Fig. 6.13 (b).

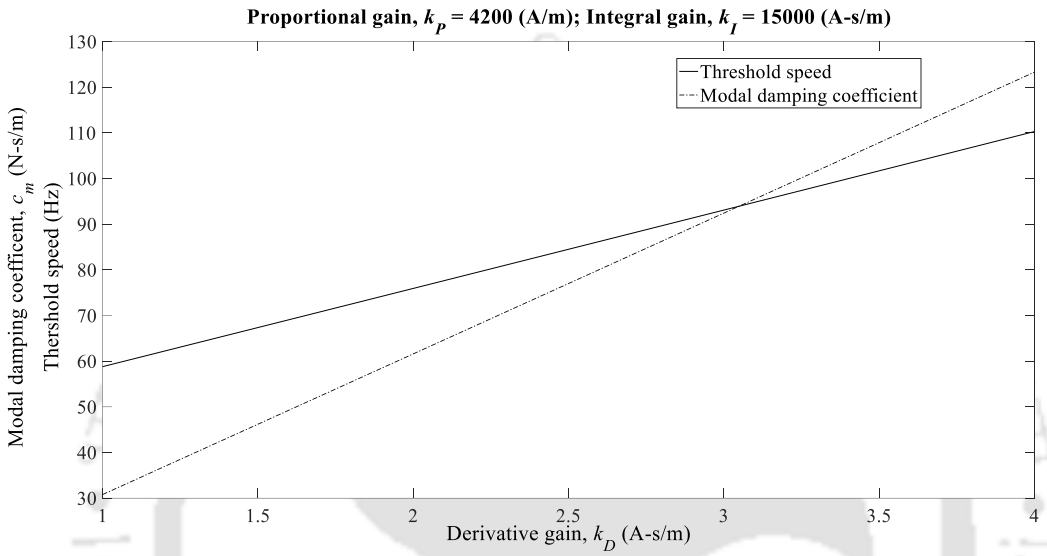


Fig. 6. 14. The variation in the modal damping coefficient (c_m) and the threshold speed of the rotor system with the variation of derivate gain (k_D) of the AMB controller.

6.5.2. Numerical estimation of AMB force current stiffness coefficient (k_i)

The value of the current stiffness coefficient of AMB force, as shown in Eq. (6.3), is essential for the generation of the multi-harmonic magnetic excitation force. To identify the value of k_i, a static weight of 5 N is applied at the location of AMB. The displacement response due to load applied decreases to zero with time as the AMB control force brings the rotor to its equilibrium position. The displacement response at the AMB location and control current generated by the PID controller are shown in Fig. 6.15(a) and (b). The static load gets balanced by the generated static control current that increases with time and

TH-2966_176103027

becomes constant, as shown in Fig. 6.15(b). Eq. (2.15) is utilized to identify the value of k_i, as mentioned in Table 6.3. The same process is repeated for different static loads to check the correctness of the identification procedure. The estimated values of k_i, as shown in Table 6.3, are found out to be consistent with the assumed values with a percentage variation of 0.01%.

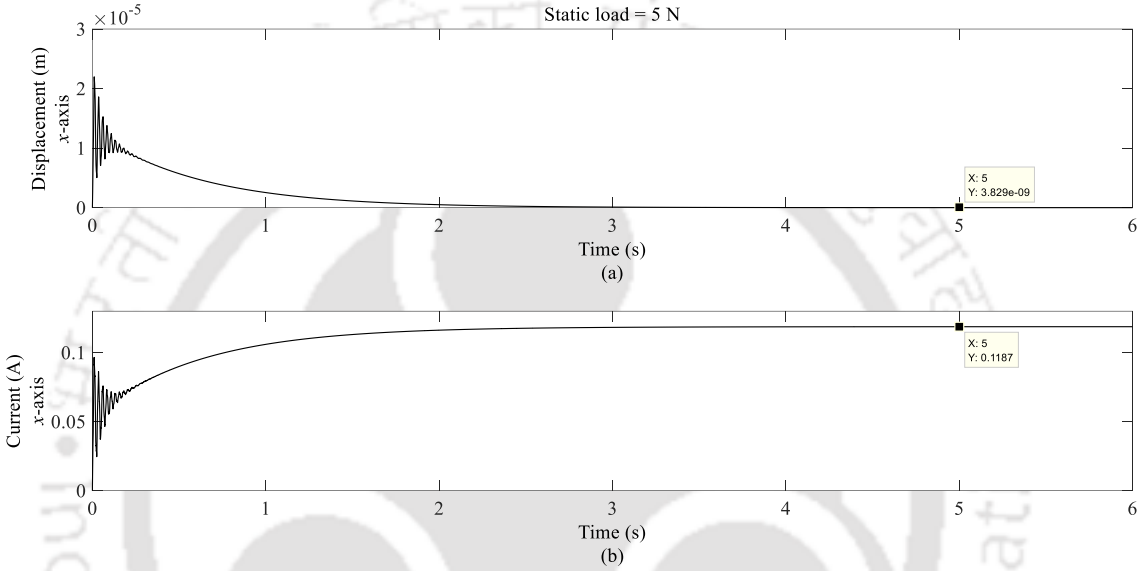


Fig. 6. 15. (a) Displacement (m) at AMB location versus time (s) plot and (b) Control current (A) versus time (s) plot along *x*-axis after the application of a static load of 5N.

Table 6. 3. Estimated values of force current stiffness coefficient (k_i) of AMB

Load (N)	Static current (A)	Force current stiffness, k_i (N/A)	Percentage variation
3	0.0713	42.099	0
5	0.1187	42.123	0.05
8	0.1900	42.105	0.01
10	0.2375	42.105	0.01

TH-2966_176103027

6.5.3. Estimation of fault parameters

The fault parameters of a cracked rotor system with residual unbalances are estimated with the help of multi-harmonic magnetic excitation at AMB and MHICM. The identification algorithm utilized in the estimation of the fault parameters is shown in Fig 6.16.

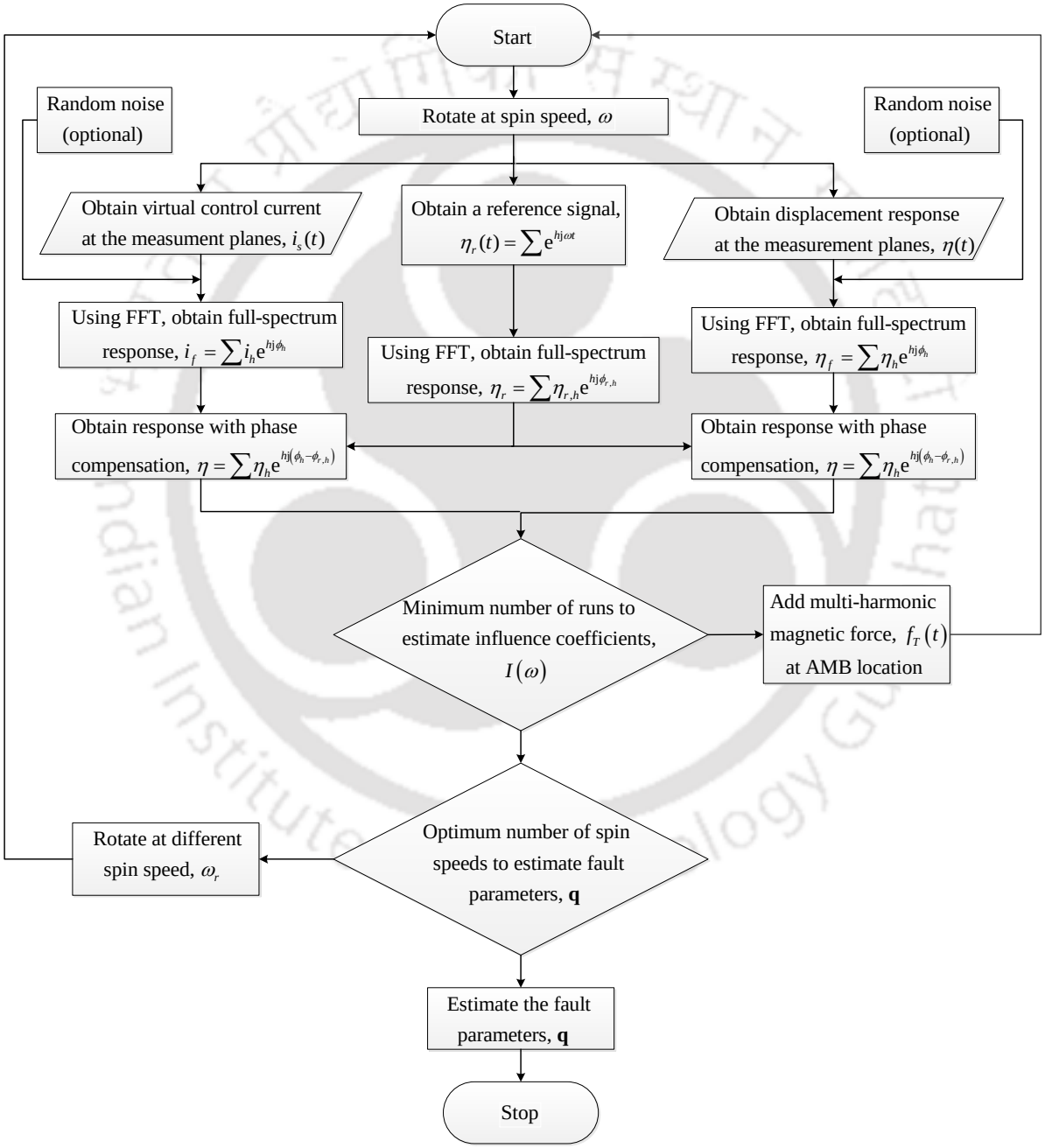


Fig. 6. 16. The flow chart describes the estimation algorithm (MHICM).

TH-2966_176103027

The system is rotated at a spin speed of 15 to 29 Hz with an increment of 2 Hz, and the complex displacement response corresponding to each run is evaluated. In the second run, a trial multi-harmonic magnetic force is applied at the AMB location, as shown in Fig. 6.5. The values of the force coefficients are randomly selected, as shown in Table 6.4. The magnitude of trial excitation forces can be considered similar to the selection procedure of trial unbalances in balancing of rotor system using influence coefficient method (ICM) (Tiwari, 2017). The selection procedure in ICM, as per ISO 1940 standard, is the additional trial force should generate at least 10% change in vibration level or be 10% of the actual rotor centrifugal force. In the present simulation, the magnitude of excitation force assumed at 1X harmonics is about 15% of the external force at the 30 Hz operating speed of the system. The trial magnetic force is introduced to estimate the change in displacement responses required to obtain the influence coefficients of the system. The rotor system can then be operated without additional magnetic excitation force.

Table 6. 4. The magnitude and phase of the trial multi-harmonic excitation force generated at the AMB location.

Trial Force coefficients	Force magnitude (N)	Current amplitude (A)	Phase (degree)
f_0	0.30	0.007	20
f_1	2.40	0.057	30
f_2	1.20	0.029	60
f_3	0.90	0.021	80
f_5	0.75	0.012	120
f_7	0.60	0.014	130
f_{-1}	1.50	0.036	150
f_{-3}	1.05	0.025	40
f_{-5}	0.84	0.020	70

TH-2966_176103027

The change in displacement response is dependent on the magnitude of the external excitation force and can be adjusted to obtain sufficient change in responses required for the estimation procedure. The displacement responses at the crack location and control current before and after implementation of the trial magnetic force at 30 Hz operating speed are shown in Fig. 6.17 (a) and (b), respectively. The influence coefficients corresponding to the displacement responses and fault parameters are obtained using Eq. (6.2) through Eq. (6.6). Also, the influence coefficients corresponding to virtual currents and fault parameters are estimated using Eq. (6.15) through Eq. (6.16). The obtained complex displacement, virtual current responses, and control current at AMB corresponding to different harmonics and spin speeds are then utilized along with the respective influence coefficients to identify the unbalances, crack parameters and internal damping factor using Eq. (6.19).

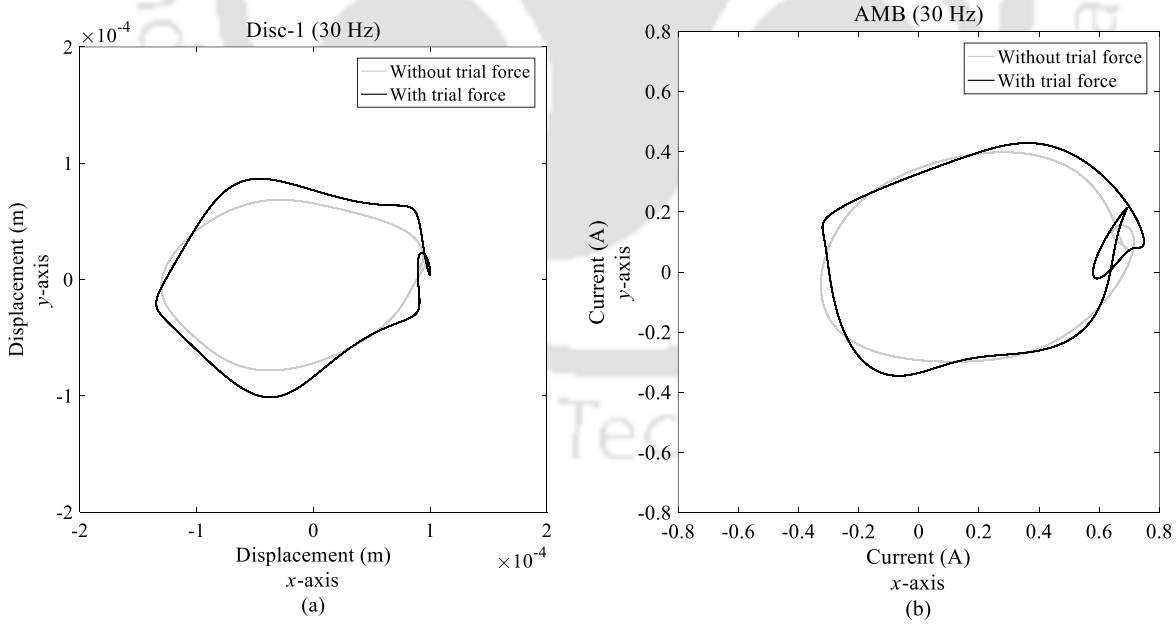


Fig. 6. 17. The orbit plot of the (a) displacement response at Disc-1 and (b) control current at 30 Hz before and after application of virtual trial multi-harmonic force as magnetic excitations.

TH-2966_176103027

The estimated fault parameters without the addition of noise are consistent as shown in Table 6.5. To verify the robustness of the algorithm, 5% of random noise is added to the displacement and current responses obtained at different speeds. The assumed and estimated parameters with the addition of noise are shown in Table 6.5, which gives a maximum variation of 6% in the unbalance estimation.

Table 6. 5. The assumed and estimated values of the fault parameters with and without the addition of 5% of random noise (15-29 Hz).

Parameters	Assumed Values	Estimated values (0% noise)	Estimated values (5% noise)	Percentage deviation
ΔkP_0 (N/m)	7.500×10^4	7.500×10^4	7.497×10^4	-0.03
ΔkP_1 (N/m)	9.570×10^4	9.570×10^4	9.569×10^4	-0.01
ΔkP_2 (N/m)	7.500×10^4	7.500×10^4	7.500×10^4	0
ΔkP_3 (N/m)	3.180×10^4	3.180×10^4	3.180×10^4	0
ΔkP_5 (N/m)	-0.630×10^4	-0.630×10^4	-0.629×10^4	-0.21
ΔkP_7 (N/m)	0.270×10^4	0.270×10^4	0.272×10^4	0.63
ΔkP_{-1} (N/m)	3.180×10^4	3.180×10^4	3.179×10^4	-0.01
ΔkP_{-3} (N/m)	-0.630×10^4	-0.630×10^4	-0.630×10^4	0.02
ΔkP_{-5} (N/m)	-0.270×10^4	-0.270×10^4	-0.270×10^4	0
c_H (N-s/m)	75	75.003	75.320	0.43
m_1e_1 (kg-m)	1.26×10^{-4}	1.260×10^{-4}	1.338×10^{-4}	6.21
φ_1 (rad)	1.2	1.200	1.2619	5.16
m_2e_2 (kg-m)	1.6×10^{-4}	1.600×10^{-4}	1.530×10^{-4}	-4.39
φ_2 (rad)	2.1	2.100	2.1045	0.21

To verify the applicability of the above algorithm at different range of operating speeds, the fault parameters are also estimated for the combination speed of 26 Hz through 32 Hz (clockwise direction) and 26 Hz through 32 Hz (counterclockwise direction) with an

TH-2966_176103027

increment of 2 Hz and 5% of random noise. From Table 6.6, it is seen that a combination of clockwise and anticlockwise speed ranges gives the estimated result with a maximum variation of 8% in ΔkP_7 value. Also, the system is rotated above its critical speed for a speed range of 55 through 69 Hz with an increment of 2 Hz, and the percentage variation in the estimated values are found to be 1%.

Table 6. 6. The assumed and estimated values of the fault parameters with the addition of 5% of random noise for a different combination of speeds.

	(26 to 32 Hz (clockwise) and 26 to 32 Hz (counterclockwise))		(55 to 69 Hz)	
Parameters	Estimated values (5% noise)	Percentage deviation	Estimated values (5% noise)	Percentage deviation
ΔkP_0 (N/m)	7.498×10^4	-0.03	7.510×10^4	-0.14
ΔkP_1 (N/m)	9.564×10^4	-0.06	9.560×10^4	-0.10
ΔkP_2 (N/m)	7.500×10^4	0	7.499×10^4	-0.01
ΔkP_3 (N/m)	3.175×10^4	-0.16	3.179×10^4	-0.02
ΔkP_5 (N/m)	-0.632×10^4	0.28	-0.627×10^4	-0.49
ΔkP_7 (N/m)	0.247×10^4	-8.47	0.271×10^4	-0.38
ΔkP_{-1} (N/m)	3.179×10^4	-0.01	3.179×10^4	-0.02
ΔkP_{-3} (N/m)	-0.633×10^4	0.49	-0.638×10^4	1.21
ΔkP_{-5} (N/m)	-0.270×10^4	-0.14	-0.270×10^4	0.08
c_H (N-s/m)	74.885	-0.15	74.934	-0.09
m_1e_1 (kg-m)	1.251×10^{-4}	-0.74	1.252×10^{-4}	-0.62
φ_1 (rad)	1.2255	2.13	1.2022	0.18
m_2e_2 (kg-m)	1.587×10^{-4}	-0.82	1.603×10^{-4}	0.16
φ_2 (rad)	2.0883	-0.56	2.0949	-0.24

TH-2966_176103027

6.6. Experimental identification of faults present in cracked rotor-AMB system

In the present work, the experimental test rig consists of a single disc mounted on a cracked mild steel shaft as shown in Fig. 6.18 and supported on the deep grooved ball bearings (Sarmah and Tiwari, 2020). The physical parameters of the rotor system are mentioned in Table 6.7. The fatigue crack present in the shaft, as shown in Fig. 6.19 (a), was generated by a three-point bending test and hence considered to show breathing behavior as described in Section 6.2.4. The close-view of the crack in the shaft is shown in Fig. 6.19 (c). The other additional components are 8- pole AMB actuator as shown in Fig. 6.19 (b), PID controller (dSPACE-SIMULINK platform), amplifiers, Analog-to-Digital (A/D), and Digital-to-Analog (D/A) input-output panels as shown in Fig. 6.20. The dimensions of the actuator are given in Table 6.7. The rotor system was operated with the help of an ER11 air-cooled CNC spindle motor with an operating speed range of 10 – 24000 RPM. The speed of the shaft is controlled with the help of a Delta-M series AC motor drive with an output power of 1.5 kW. To measure the displacement response of the rotor system, non-contact eddy current sensors are used. As described in Section 5.6.1, to obtain the amplitude and phase of full-spectrum response, the displacement response from the reference location was also obtained from the spindle of the motor, as shown in Fig. 6.18.

TH-2966_176103027

Table 6. 7. Physical properties of the rotor-AMB test rig.

Parameter	Value	Unit
Rotor system		
Length of the shaft	470	mm
Diameter of the shaft	16	mm
Young's modulus of elasticity	2.06×10^{11}	N/m^2
Offset position of disc from left bearing	305	mm
AMB actuator		
Outer diameter of stator	90	mm
Outer diameter of core	32.4	mm
Width of pole leg	8	mm
Air gap	0.6	mm
Diameter of coil	0.813 (21 SWG)	mm
Number of turns in one pole	100	

6.6.1 Electrical circuit

The block diagram of the electrical circuit developed for the present rotor system is described in Fig. 6.21. The displacement responses measured by the position sensors are sent to the A/D panel of the dSPACE input-output panel. Now, the voltage signals are converted to the digital signal, which is then processed in the controller model developed at dSPACE-SIMULINK platform as shown in Fig. 6.21. The displacement responses in terms of volts (V) are converted into meters (m) by multiplying with the conversion factor of (1/7874 m/V). Then the signal is sent to the PID controller for the generation of the controlling current.

TH-2966_176103027

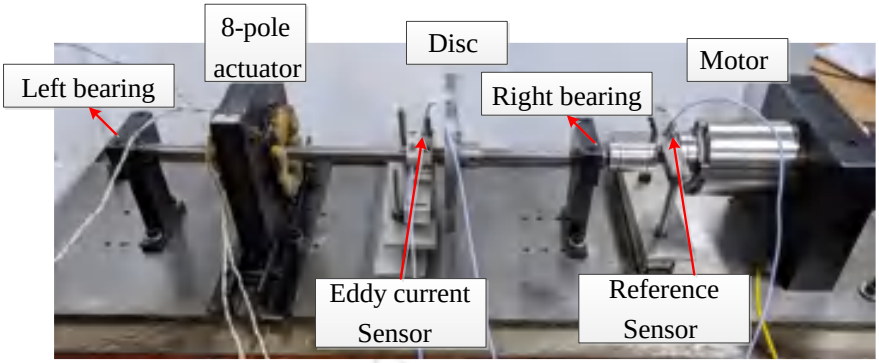


Fig. 6. 18. The experimental test rig setup supported on ball bearings and integrated with AMB.

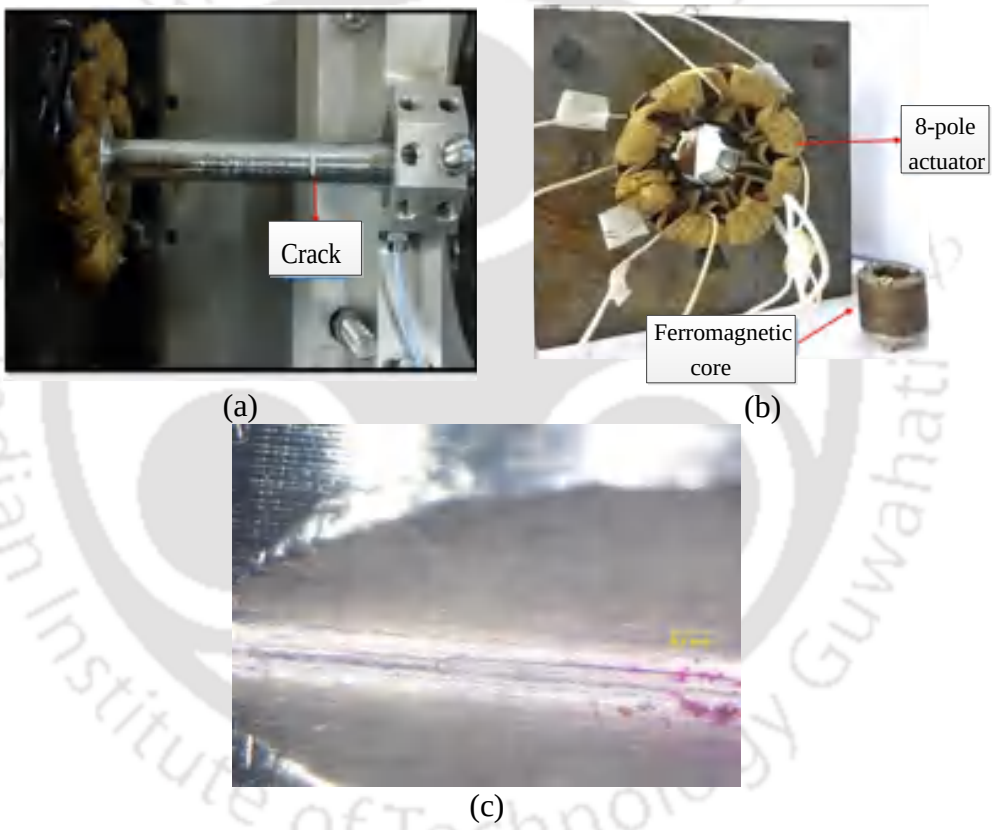


Fig. 6. 19. (a) Fatigue crack developed in the mild steel shaft at the notch location, (b) 8-pole AMB actuator with silicon steel core, and (c) zoomed view of crack surface in the shaft.

To generate excitations in the rotor system, a multi-harmonic excitation current is generated at the same time in the SIMULINK model with the same operating frequency of the rotor system as shown in Fig. 6.21. The excitation current is added with the control

TH-2966_176103027

current, and the overall current is then converted from Amperes to Volts as per the setting of the amplifiers. Now, the constant voltage required to generate the bias current is also added total voltage signal.

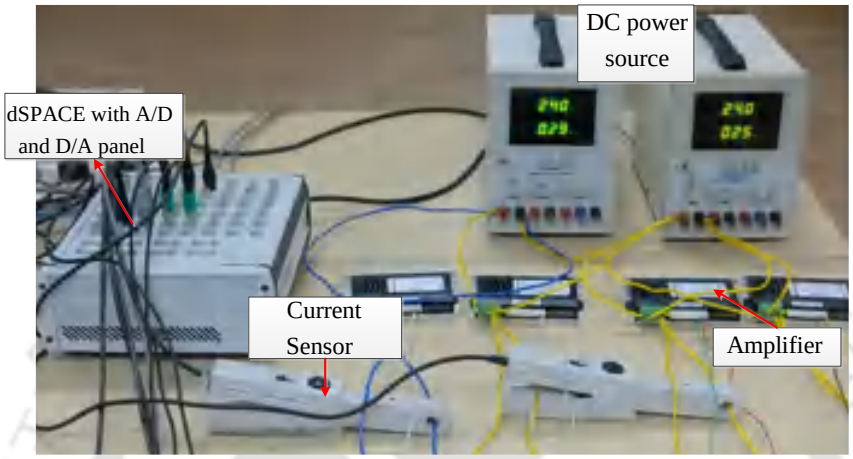


Fig. 6. 20. The additional component of AMB control structure with dSPACE A/D and D/A panel, amplifiers, and DC supply source.

The overall voltage signals (bias + control) are then sent to the D/A converter panel and then to the amplifiers corresponding to the different pairs of poles in the actuator to generate the required control and excitation force. The excitation signal is also added along with the control and bias current for the identification of the multi-harmonics influence coefficients described in the identification algorithm. The excitation signal is removed once the identification procedure is completed, and the system can operate with the control and bias current generated in the AMB circuit.

6.6.2 AMB control with run-up above the critical speed

The differential mode control of AMB is applied in controlling the vibration response of the system along the horizontal (x) and vertical axes (y). The bias current of 2 A is supplied in all pairs of electromagnets in the AMB actuator. When the shaft displaces from its

TH-2966_176103027

equilibrium position, the control current generated is added to the bias current in the AMB pole away from the displaced shaft and subtracted from the AMB pole nearer to the displaced shaft simultaneously. The proportional and derivative gains of the PID controller are increased from 3000 to 5000 A/m and 2 to 5 A-s/m, respectively, and the system was found to be stable in the given range. The selected control parameters for the PID controller are considered as proportional gain k_P = 4000 A/m, k_D = 3 A-s/m and k_I = 3000 A/m-s. An impulsive force was applied to the shaft to estimate the change in the natural frequency of the system with the addition of AMB in the system. The aim of the experiment was to rotate the system at the safe operating speed, and for the present work, the system is rotated below the first critical speed of the rotor system. The FFT of the displacement responses is carried out, and the amplitude vs. frequency curve is shown in Fig. 6.22. Due to the presence of the crack in the rotor, the stiffness of the system depends on the orientation of the crack with respect to the direction of the static load. For the crack orientation along the direction of load, the stiffness of the shaft decreases, and perpendicular to the direction of the load, the stiffness of the shaft remains the same. Therefore, the natural frequency of the system changes with the change in the orientation of the crack face. The natural frequency of the system without and with AMB is obtained for (a) crack face in a downward direction equal to 61.89 Hz and 64.71 Hz (b) crack face is in a horizontal direction equal to 65.04 Hz and 68.42 Hz (c) crack face is in the upward direction equal to 63.3 Hz and 67.71 Hz. The system was rotated below its critical speed, i.e., at 20 Hz, and the displacement response of the system at the disc location with AMB control is shown in Fig. 6.23 (a). The overall current, i.e., control + bias current utilized in the actuator of the AMB system, is shown in Fig. 6.23 (b). The orbit plot of displacement

TH-2966_176103027

response and the overall current is shown in Fig. 6.23 (c) and (d), respectively. The FFT of the displacement responses are carried out, and the full-spectrum amplitude and phases are shown in Fig. 6.24 (a) and (b), respectively.

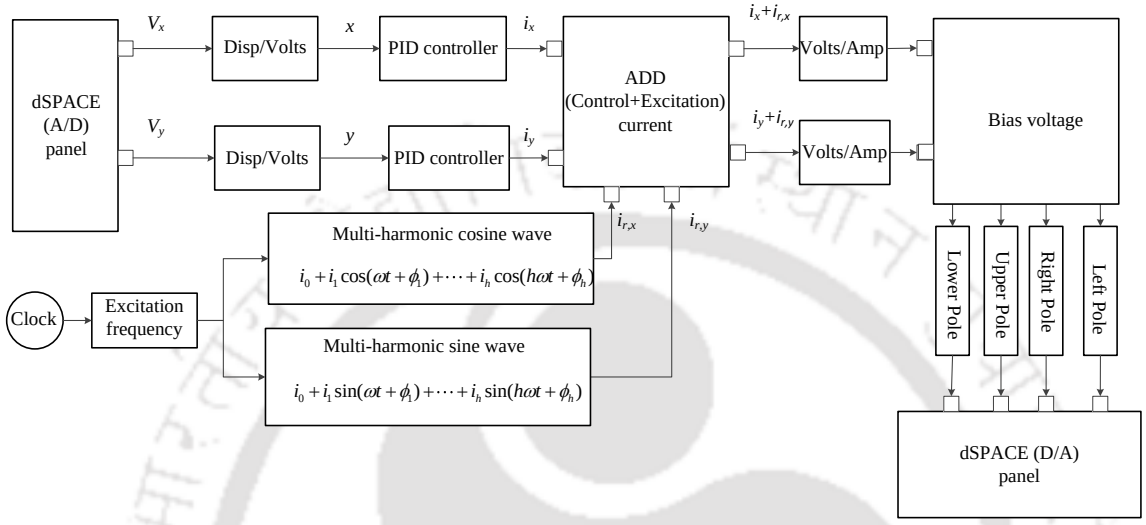


Fig. 6. 21. The block diagram of the AMB closed-loop control model developed at dSPACE-SIMULINK interface.

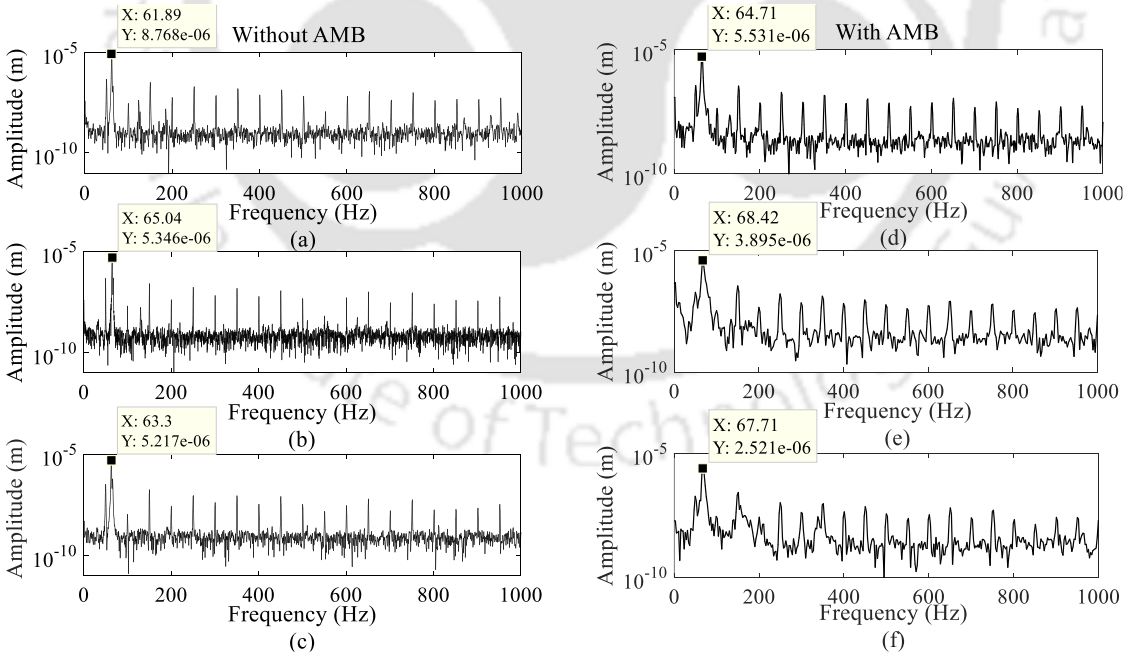
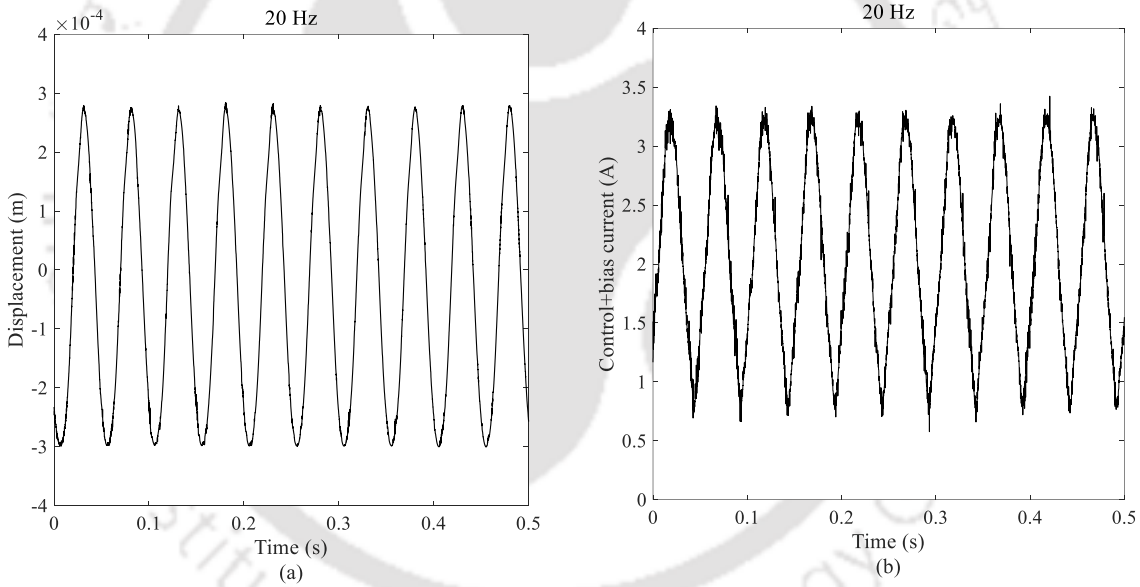


Fig. 6. 22. Natural frequency of the system without and with AMB {(a) , (d)} crack face in downward direction {(b), (e)} crack face is in horizontal direction {(c), (f)} crack face is in upward direction.

TH-2966_176103027

The orbit plot of the displacement response without and with AMB control is shown in Fig. 6.25. The reduction in the displacement response obtained after the addition of AMB in the system is found out to be 8%, i.e., from 3.065×10^{-4} to 2.83×10^{-4} corresponding to 1X harmonics of the system. The reduction is found to be less due to the presence of residual bow in the cracked shaft. The amount of shaft bow is quite high, and it is difficult for AMB to control the amount of displacement generated by residual shaft bow. However, the dynamic displacement generated due to unbalance and crack force is reduced by 40% with AMB control as per the displacement obtained after vectorially removing the shaft bow obtained at the slow run from the displacement responses.



TH-2966_176103027

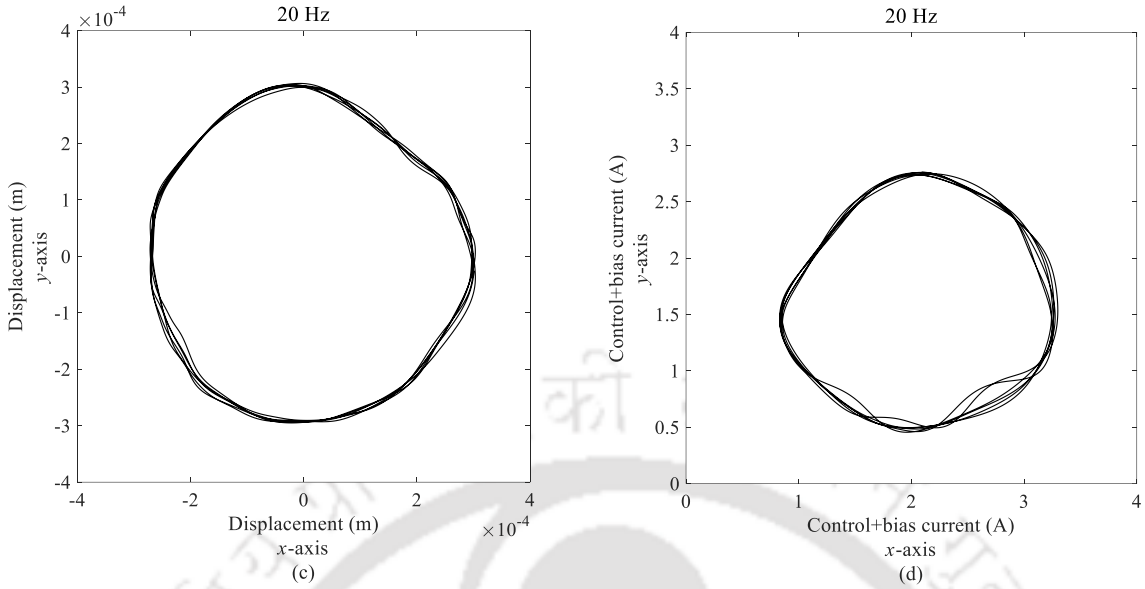
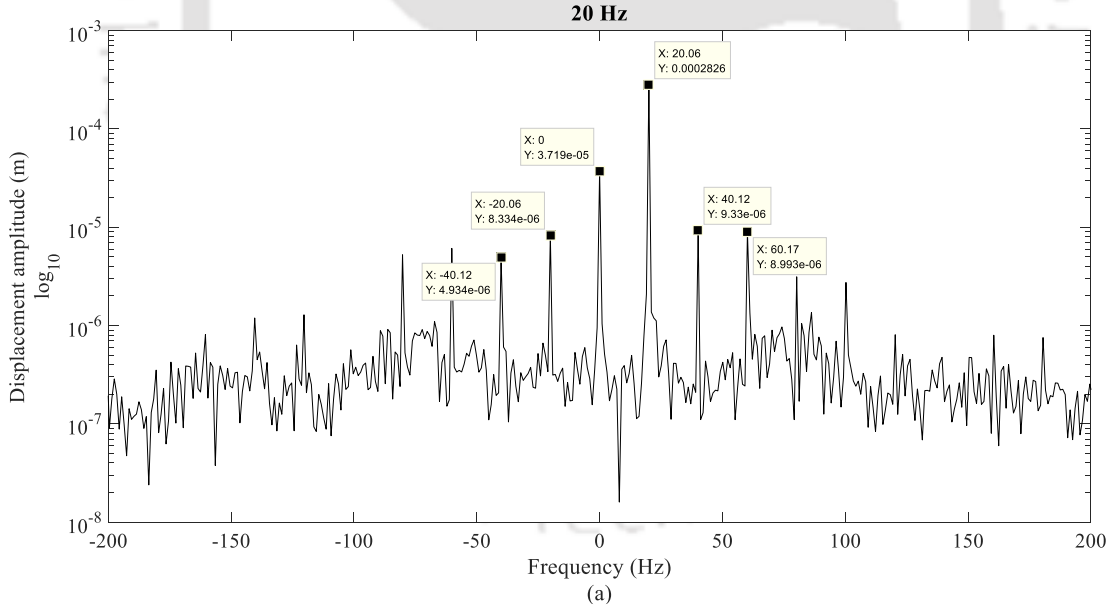


Fig. 6. 23. (a) Displacement response vs time plot at disc location with, (b) control + bias current plot vs. time, (c) orbit plot of displacement response and (d) orbit plot of control + bias current at 20 Hz operating speed.



TH-2966_176103027

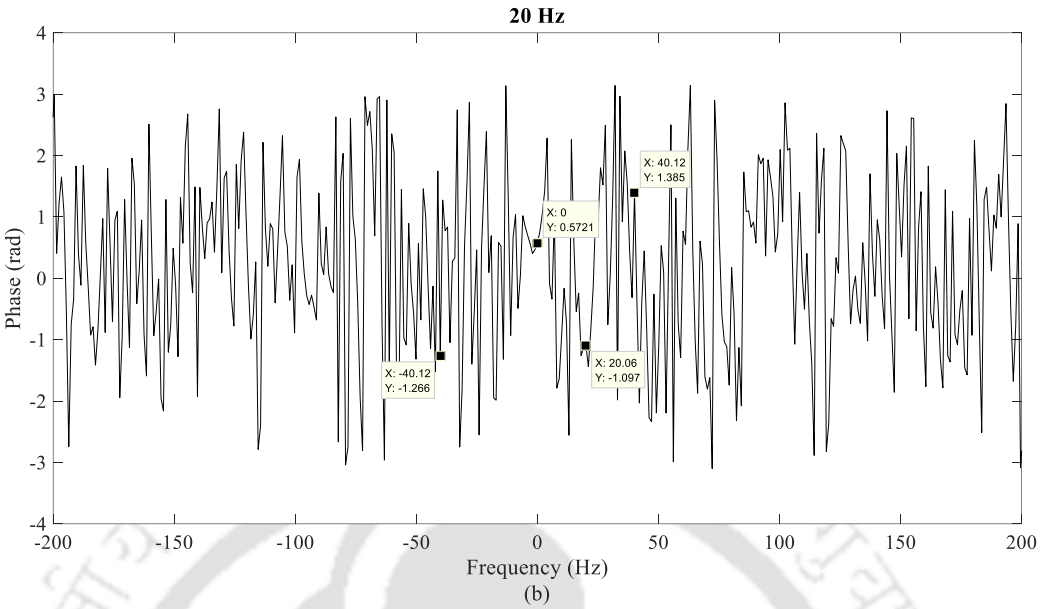


Fig. 6. 24. (a) Displacement amplitude vs. frequency plot at disc location with AMB control and (b) phase vs. frequency plot at 20 Hz operating speed.

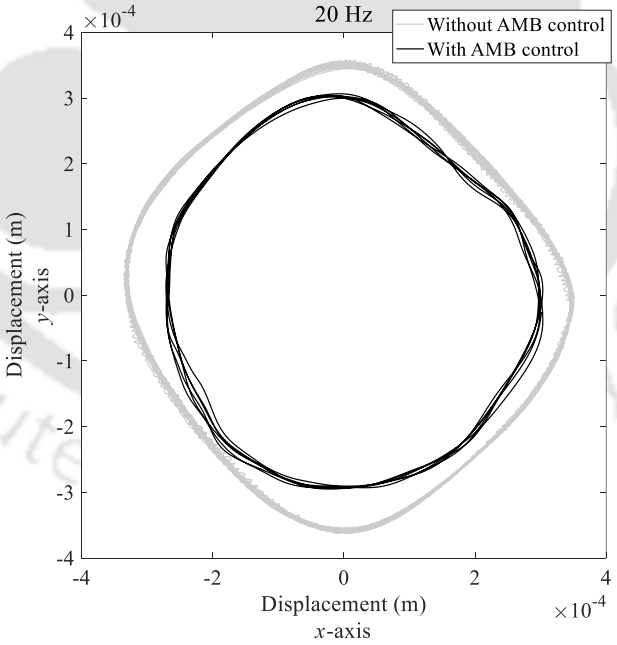


Fig. 6. 25. (a) Orbit plot of displacement response at disc location with and without AMB control.

TH-2966_176103027

6.6.3 Experimental estimation of the AMB current stiffness factor (k_i)

The AMB current stiffness factor (k_i) is required to calculate the trial force generated at the AMB location as described in Section 6.3. The stiffness factor is estimated as described in Section 6.5.2, which requires the addition of weight at the AMB location in the system. A weight of 500 gm was added to the shaft, and the displacement response generated is shown in Fig. 6.26. As it is seen from Fig. 6.26 (a), the shaft displaces on the addition of weight, and then the brought back to equilibrium location by the controller. The constant control current (0.3189 A) generated is considered for estimation of the stiffness factor, and the value is found to be equal to 15.38 N/A.

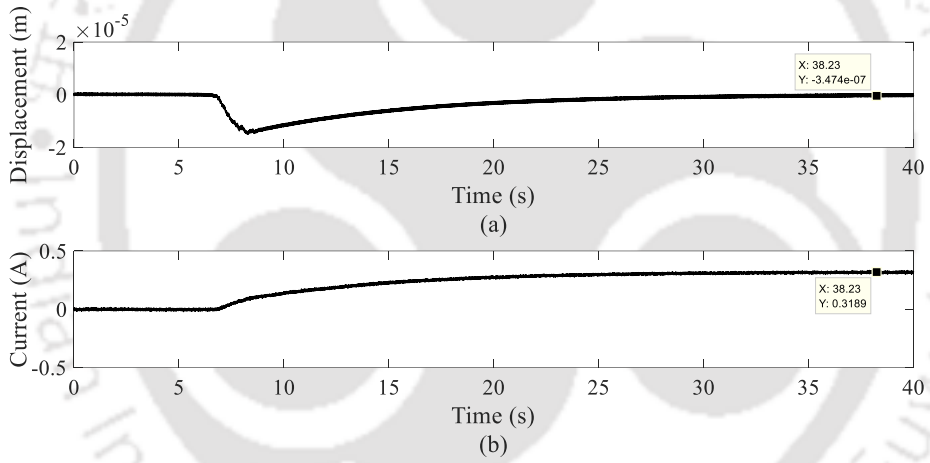


Fig. 6. 26. (a) Displacement (m) at AMB location versus time (s) plot and (b) Control current (A) versus time (s) plot along y-axis after the application of a static load of 500 gram.

6.6.4 Estimation of fault parameter of cracked rotor system

The fault parameters of the cracked rotor system with AMB control are estimated as per the developed identification algorithm based on the multi-harmonic influence coefficient method. The identification procedure applied in the estimation of the fault parameters are as follows:

TH-2966_176103027

1. The reference position was considered near the motor location with respect to which the displacement reference and phase are estimated as described in Section 5.6.1. The displacement response at the reference location is shown in Fig. 6.27. As two slots are present at the reference location, two peaks were seen in the reference signal. For reference purposes, the peak locations of slot 2 were considered for the present problem.
2. The system was operated at the slow speed of 4 Hz with disc shifted near the bearing location to obtain amplitude and phase of the residual shaft bow present in the system. The shaft bow is required to be removed from the 1X harmonics of the displacement responses at disc location to obtain the actual amplitude and phase of response due to unbalances and crack.
3. The system was operated at 20 Hz, and the amplitude and phase of displacement response corresponding to different harmonics are identified with respect to the reference signal as shown in Fig. 6.24 (a). The shaft residual bow displacement was subtracted vectorially from the displacement amplitude of 1X harmonics.
4. The system was rotated again at 20 Hz with the addition of the multi-harmonics trial magnetic force in the system, as shown in Fig. 6.21. The magnitude and phase of the trial current considered in the above experiment are shown in Table 6.8. The values considered are about 10% of the actual control current utilized at different harmonics in the rotor system. The displacement response was obtained after the addition of excitation current, and the orbit plots of the responses before and after addition of trial excitation are shown in Fig. 6.28 (a). The overall excitation current added to the

TH-2966_176103027

control current along both horizontal and vertical axes is shown in Fig. 6.28 (b), respectively.

5. The similar procedure was carried out for different operating speeds such as 15, 17, 19, 20, 22, 24, 26, 27, and 28 Hz. The displacement responses and control currents obtained with and without the addition of excitation force was utilized to estimate the influence coefficient of the system.

6. The influence coefficient obtained was utilized along with the displacement responses without excitation force to estimate the fault parameters present in the rotor system as per Eq. (6.19). For the estimation of fault parameters, a combination of 5 spin speeds is selected, and then the number of speed combinations is increased to arrive at the solution with less deviation from the previously estimated values. The estimated values, as shown in Table 6.9, were found to be converged after a combination of 9 spin speeds.

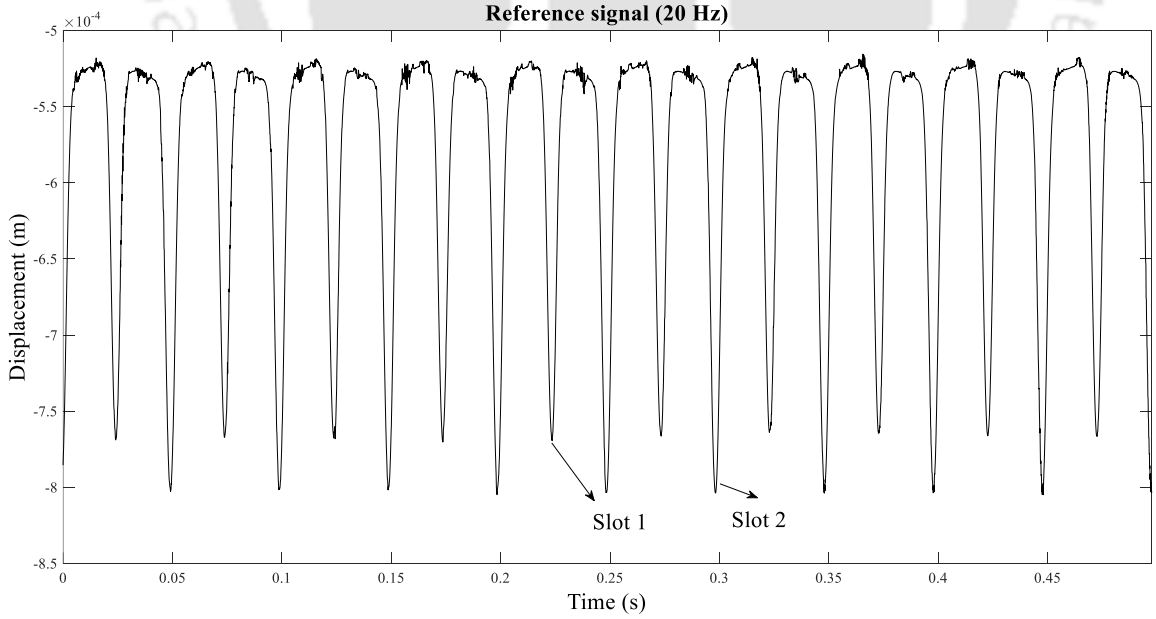


Fig. 6. 27. The reference signal obtained at the slots present in the spindle of the motor with respect to time.

TH-2966_176103027

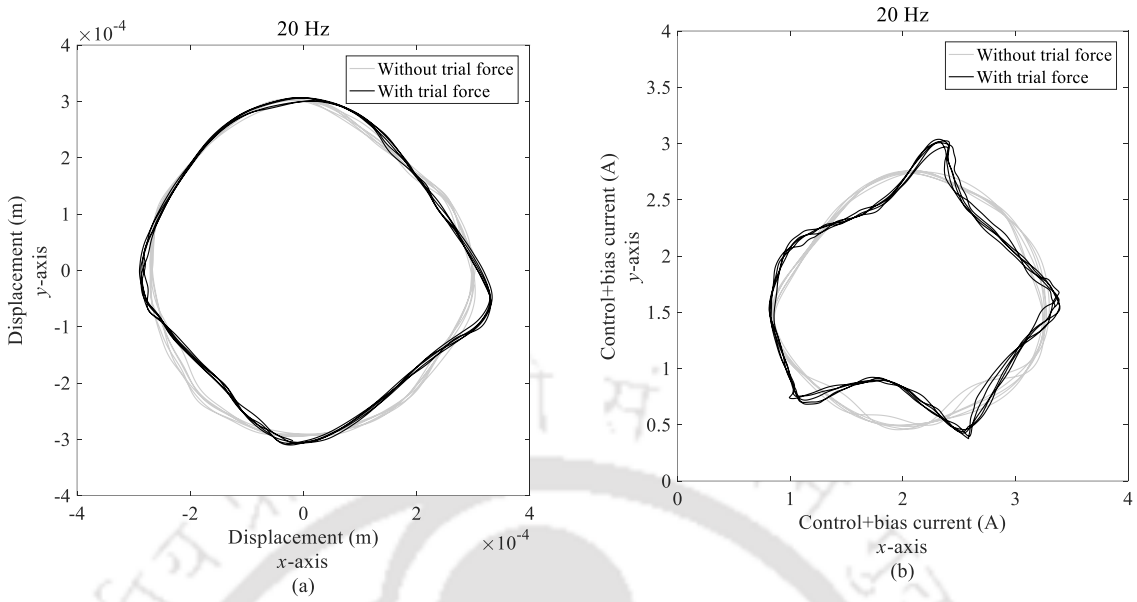


Fig. 6. 28. Orbit plot of (a) displacement response and (b) control + bias current without and with addition of multi harmonics excitation force.

Table 6. 8. Amplitudes and phases of the excitation current corresponding to different harmonics.

Trial current	Amplitude	Phase
i_0 (A)	0.04	10°
i_1 (A)	0.06	20°
i_2 (A)	0.07	30°
i_3 (A)	0.03	40°
i_4 (A)	0.05	50°
i_{-1} (A)	0.06	60°
i_{-2} (A)	0.04	70°
i_{-3} (A)	0.03	80°
i_{-4} (A)	0.06	100°

TH-2966_176103027

Table 6. 9. Estimated for parameters of the cracked rotor-AMB system for a different combination of the operating speed.

	Speed range [(s_1-s_9); (15, 17, 19, 20, 22, 24, 26, 27, 28) Hz]				
Parameter	(s_1-s_5)	(s_1-s_6)	(s_1-s_7)	(s_1-s_8)	(s_1-s_9)
ΔkP_0 (N/m) $\times 10^4$	4.840	2.640	3.025	3.105	3.614
ΔkP_1 (N/m) $\times 10^4$	11.869	9.475	5.092	7.169	8.072
ΔkP_2 (N/m) $\times 10^4$	2.358	2.346	1.586	2.897	2.538
ΔkP_3 (N/m) $\times 10^4$	0.799	0.909	1.024	1.054	0.989
ΔkP_4 (N/m) $\times 10^4$	0.455	0.454	0.434	0.443	0.445
ΔkP_{-1} (N/m) $\times 10^4$	3.589	3.735	3.835	3.754	3.571
ΔkP_{-2} (N/m) $\times 10^4$	1.674	1.584	1.523	1.308	0.997
ΔkP_{-3} (N/m) $\times 10^4$	0.689	0.807	0.839	0.830	0.817
ΔkP_{-4} (N/m) $\times 10^4$	0.653	0.667	0.672	0.677	0.681
Δk (N/m) $\times 10^5$	2.693	2.262	1.803	2.124	2.172
me (kg-m) $\times 10^{-4}$	4.391	3.366	1.616	2.221	2.514
ϕ (rad)	211°	122°	111°	123°	123°
c_H (N-s/m)	220.064	70.503	124.631	87.081	110.017

The participation factor (P_h) corresponding to the different harmonics of the crack force was then utilized to obtain the behavior of the fatigue crack in the rotor system along with the horizontal and vertical directions. The behavior of the estimated crack factors is compared with the switching crack function commonly utilized to describe the behavior of fatigue crack, as shown in Fig. 6.29. The resemblance of the crack behavior shows the effectiveness of the present algorithm in the estimation of the fault parameters.

TH-2966_176103027

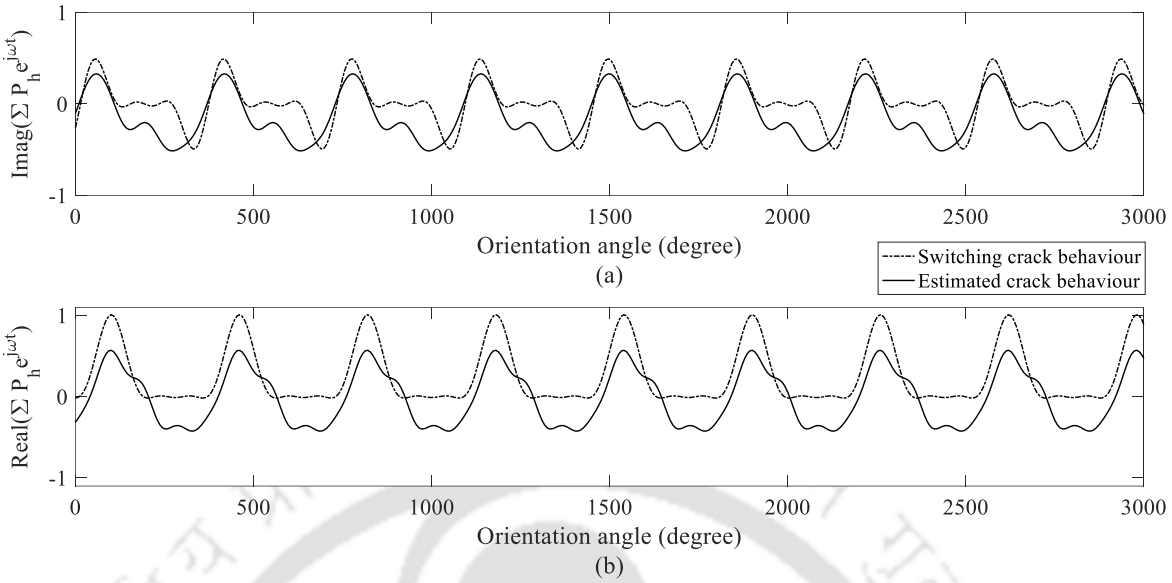


Fig. 6. 29. The fatigue crack behavior as per estimated participation factor of experimental crack force and switching crack force along (a) *y*-axis and (b) *x*-axis with respect to the orientation of the crack face

6.6. Final Remarks

The severity of damage augments with the increase in operating speed for the case of residual unbalances present in rotating systems. Faults such as cracks propagate with time and cause the failure of the components of machinery. Also, the internal damping due to the rubbing effect in cracks generates instability at high operating speed. Therefore, quantitative estimation of fault parameters is essential in order to reduce the cause of vibration (balancing with the estimated residual unbalances), to determine the safe operating speed (estimating threshold speed with the help of internal damping factor), and to prevent the critical damage in the machinery (inspecting deviation of the stiffness of the system due to presence of crack). The present chapter focuses on the development of an identification algorithm to estimate the crack parameters as well as unbalances present in the system based on Multi Harmonic Influence Coefficient Method (MHICM). The FEM

TH-2966_176103027

model of the cracked rotor system is developed integrated with the AMB, which is used to generate a simulated response to numerically test the identification algorithm. The fault parameters, such as the additive crack stiffness, discrete disc unbalances, and internal damping due to rubbing of crack faces, are included in the rotor system. The AMB is able to suppress the vibration response at high speed in the cracked rotor system. The instability generated by the internal damping above the threshold speed is successfully contained within the required level of displacement response by the AMB control. The AMB current stiffness coefficient is estimated with the variation of the static load and found to be accurate in comparison to the assumed values of the system. The full-spectrum amplitude and phases of the vibration responses at different node locations are utilized in the identification of the fault parameters. The identified fault parameters are found to be consistent with the addition of random noise at different speed ranges. This shows the effectiveness of the present algorithm in the estimation of faults with single harmonic, such as unbalances, and multiple harmonics, such as cracks, in the rotor system. As MHICM requires only vibration responses of the rotor system to predict the values of the faults, the additional computational and mechanical effort required for the development of numerical models of the system is reduced accordingly. The algorithm successfully estimates the fault parameters with considerable levels of random noises. This will help in the accurate estimations of faults in real systems with noisy environmental conditions.

The experimental identification of the fault parameters in the rotor system was also carried out using the multi-harmonic influence coefficient method with the utilization of magnetic excitation forces. The excitation signal is generated in the dSPACE-SIMULINK platform and added to the control current of the AMB system. The estimation of the fault

TH-2966_176103027

parameters such as unbalance, additive crack stiffness, and internal damping is carried out successfully with the help of displacement responses for a different combination of speeds. The participation factor of the crack force estimated in the present algorithm shows similar behavior to a switching crack. Also, the unbalance and internal damping values have been found to be converged with the increase in the number of combinations of speeds. Hence, the developed MHICM is effective in estimating the faults of the cracked rotor system without any prior knowledge of the physical properties of the rotor system and with the utilization of AMB as a controller as well as exciter. The present procedure is advantageous in detecting the severity of the rotor faults that changes over a period of time in the operating machinery with AMB control. The present work is limited to the identification of additive crack stiffness and the crack behavior, whereas the crack location and depth have not been analyzed. The present work assumes the linear relationship between the displacement responses and the fault parameters, the nonlinear modelling of the rotor components can be done to study the effectiveness of the present algorithm in the identification of the cracked rotor faults. Also, the bow effect has been removed from the 1X harmonics of the displacement response, but it can be modelled and identified with other fault parameters by modification in the identification algorithm.

TH-2966_176103027

TH-2966_176103027

CHAPTER 7

CONCLUSIONS AND SCOPES FOR FUTURE WORK

This chapter discusses the overall contributions and conclusions from the research work carried out in the thesis. The limitations and the future scope that can be derived from the present work are also listed.

7.1. Summary of Present Work

This work has centered on a concept of on-site balancing of the rotor system supported on conventional bearings and integrated with the radial AMB. As balancing is required for a high-speed rotor system, it would be difficult to run the system supported on conventional bearings up to operating speed for obtaining balance masses. The conventional bearings may get damaged at high speed while running without balancing for acquiring measurements. The implementation of AMB is necessary for obtaining the residual balance masses as it reduces the vibration and prevents the system from getting damaged at high speed, and ensures more reliable data. The reliability and accuracy of the balancing procedure increase with the utilization of the minimum information of dynamics of the system. In the present work, the estimation procedure developed using the influence coefficient method requires only vibrational responses and the value of trial unbalances to predict the residual unbalances in the system.

The conventional ICM is modified with the implementation of AMB in the system as a controller as well as exciter. The AMB controls the level of vibration while crossing critical speeds of the system and replaces the physical trial unbalances with virtual trial

TH-2966_176103027

unbalances (VTUs) as magnetic excitations at the AMB location. The FEM modeling of the rotor-AMB system is done in MATLAB-SIMULINK^{TM} platform to obtain the vibrational responses without and with the addition of the VTUs to show the effectiveness of the algorithm in balancing the high-speed rotor system. The half-spectrum amplitudes and phases of the displacement responses are obtained using Fast Fourier Transformation (FFT) to estimate the residual unbalances. The procedure is extended for high-speed balancing of the rotor system by operating it at low speeds. A Virtual Excitation at Low-Speed for High-Speed Balancing (VELSHSB) method is developed that utilizes the influence coefficients obtained at high speed and unbalances identified at the low speed to effectively estimate the balance masses required for the high-speed flexible rotor balancing. The influence coefficients are required to be obtained just once, whereas the balance masses can be estimated periodically by identifying the unbalances at low speeds. After balancing, the system can easily cross its critical speeds with less vibration.

The identification algorithm is also utilized in the balancing of the complex rotor system, such as the dual rotor system utilized in the aero-engines. The compactness and the complexity of the rotor system make it difficult to model the rotor system as well as utilize physical trial unbalances to estimate the unbalances. Therefore, an on-site balancing methodology is developed for the dual rotor system with AMB control and VTUs. The implementation of AMB in the Low Pressure Rotor (LPR) system reduces the vibration responses of both LPR and High Pressure Rotor systems (HPR) with residual unbalances (discrete disc unbalances and randomly distributed shaft unbalances). Due to the coupling effect of the IFB present in the system, the external forces present in the LPR system affects the displacement response of the HPR system and vice versa. This effect is utilized

TH-2966_176103027

for simultaneous estimation of residual unbalances in LPR and HPR systems with external magnetic excitation through AMB in the LPR system. With the minimum information of the dual rotor system, the residual unbalances can be effectively estimated at the required disc locations using the Multiple Virtual Excitation for Dual rotor Balancing (MVEDRB) method.

To validate the effectiveness of the developed identification algorithm experimentally, with AMB as an exciter as well as controller, balancing of developed rotor-test rig integrated with AMB is carried out. A standard Bently Nevada Rotor Kit is used to mount the radial 8-pole magnetic bearing to perform the test. The balancing of the rotor system during run-up above critical speed is carried out utilizing the concept of VTUs. The bias current supply in the rotor system is optimized with switching of bias current between high and low value to optimize the power consumption in the rotor system at high speeds with the desired level of vibration. The SVTUs are implemented with the tuning of excitation (excitation force) and operating frequency (MSCU) for the accelerating system. The acceleration of the system is kept low so that the transients are avoided. The comparison between the residual unbalances obtained using physical trial unbalances and VTUs with AMB control is also provided.

It is also important to check the effectiveness of the above algorithm in the estimation of residual unbalances along with other rotor faults. The identification of multiple fault parameters is carried out in a cracked rotor system integrated with AMB. A shaft with fatigue crack supported on the conventional bearings with offset disc is considered for the present work. The system is also integrated with the AMB that acts as a controller as well as an exciter to introduce multi-harmonic virtual trial magnetic forces.

TH-2966_176103027

Both external viscous damping arising due to conventional bearings and internal damping arising due to the presence of crack are considered. An identification algorithm is proposed to identify the additive crack stiffness, internal damping, and residual unbalances present in the system based on the influence coefficient method. A virtual multi-harmonic magnetic force is introduced in the system to identify the influence coefficients of the system corresponding to different harmonics present in the displacement responses. The robustness of the proposed identification algorithm is also tested considering different levels of random measurement noise in responses of the system. The validation of the proposed identification algorithm is carried out in the experimental rotor-AMB test rig with artificially generated fatigue crack.

7.2. Major conclusions from the present work

1. The AMB integrated into the system can be utilized for control of the level of vibration and introduction of virtual trial unbalances (VTUs) as magnetic excitations simultaneously.
2. The residual unbalances estimated with the developed identification algorithms, based on VTEICM, have a very close resemblance with the conventional ICM, which shows the effectiveness of the algorithm with less manual effort and controlled vibration levels.
3. Less number of trial runs using VTUs can provide the accepted level of balancing, which is beneficial as conventional ICM requires minimum three trial unbalances for the flexible rotor balancing.

TH-2966_176103027

4. The locations of AMB in the system have very less effect on the balancing of the rotor system. However, the VTUs generated through the AMB at a specific location should generate appreciable change in the displacement responses at the balancing planes.

5. With the utilization of one-time estimation of the influence coefficients at high speeds and the unbalances estimated at the low speeds, the high-speed balancing (i.e., VELSHSB) of the rotor system can be performed periodically.

6. Also, the change in bearing properties with time has less effect on the estimated values of the unbalances obtained using the VELSHSB with one-time estimates of high-speed influence coefficients.

7. The present identification algorithm can be applied to complex and compact systems, such as dual-rotor systems, where the LPR and HPR systems can operate in the same or opposite sense of rotations.

8. The bias current utilized in controlling the rotor system during run-up above critical speed is required to be optimized to reduce the consumption of power and heating of the actuator coils. The switching of bias current performed in the present work is able to switch the bias current to a higher value near the critical speed and then reduce it to a lower value when less control current is required.

9. The mismatch in the excitation and operating frequency of the rotor system during run-up with residual unbalances generates a beat phenomenon and affects the estimation procedure of the balance masses. The control of the voltage/speed factor of the MSCU and removal of the phase lag in the supplied frequency and excitation frequency can effectively reduce the frequency mismatch.

TH-2966_176103027

10. The multi-harmonics virtual excitations through AMB can also allow the identification of multiple faults in the cracked rotor systems that require to be monitored continuously.

11. The presence of the AMB in the cracked rotor system can prevent the occurrence of instability due to internal damping by shifting the threshold speed of the system.

7.3. Major contributions from present work

1. Conventionally in the rotor system, active magnetic devices are utilized as a support bearing (AMB) to control the level of vibration or as active magnetic actuators (AMA) to excite the rotor system different amplitude and frequency of vibration signals or as an active damper also to reduce the fluctuations of the vibrating signals. In the present work, the combination of the AMB and AMA is utilized in the rotor system with the utilization of ICM to estimate the residual unbalances for high-speed balancing.
2. The balancing of the rotor-AMB system supported on conventional bearings is carried out with VTUs and VTEICM that reduces the manual effort and requires less information of the rotor system.
3. The balancing strategy has been designed for the periodic high-speed balancing of the rotor system with unbalance estimates at low speeds with the utilization of one-time estimates of high-speed influence coefficients.
4. The estimation of unbalances in both the inner and outer rotors of the dual rotor system is carried out with additional low, and high frequency magnetic excitations through AMB integrated into the inner rotor system.

TH-2966_176103027

5. The experimental implementation of the VTUs is demonstrated, and the rotor system is balanced while run-up above its critical speeds. The integration of the AMB system in the rotor test rig supported on conventional bearings is carried out with PID control.
6. The switching of bias current is performed to reduce the power consumption of the AMB system, and difficulty in the generation of the SVTUs is also demonstrated.
7. Multiple faults are estimated in the cracked rotor-AMB system with the application of MHICM both through numerical simulations and experiments.

7.4. Limitations of the present work

1. The present work assumes a linear relationship between the displacement responses and external forces. Hence, the deviation of the system from the linear range may affect the accuracy of the algorithm. However, as AMB reduces the vibration levels, the non-linear forces due to bearing ambiguity that depends on the vibration levels also get reduced.
2. The system or fault parameters that are dependent on the dynamic responses of the rotor system cannot be estimated with the magnetic excitations as such, the parameters will get included in the influence coefficients of the system.
3. The rotor systems with a higher level of noise and disturbances from the neighboring machines or structures will affect the estimation of the unbalances as the accuracy of the estimation procedure is based on the effective measurement of displacement responses.

TH-2966_176103027

4. The displacement generated by additional excitation forces is required to be at the desired level, or it may damage the rotor system at high speeds. Also, the AMB may go into the unstable region due to an excessive amount of vibration.
5. The stiffness and damping generated by the AMB system may affect the mode shapes and natural frequency of the system. Therefore, the analysis of critical speeds is required before operating the rotor system.

7.5. Scope for future work

1. In the present work, the control action of AMB is performed with the help of a PID controller to check the effectiveness of the identification algorithm. As the tuning of the PID controller gains is difficult to perform, a new controller can also be implemented based on adaptive algorithms or based on fuzzy logic to control the rotor system effectively.
2. The experiments can be carried out to balance the rotor system at high speeds with the unbalances estimated at the low speed as described in VELSHSB.
3. The balancing of the dual-rotor test rig can be done with the application of VTUs through AMB integrated into the LPR system. The experimental test rig of the dual rotor system can be designed with the integration of AMB in the inner rotor system. Then with synchronized low and high frequency magnetic excitations, the balance masses can be estimated in both inner and outer rotor systems.
4. The balancing experiments can be carried out for the rotor system during run-up above its second critical speed to check the effectiveness of the designed algorithm. The

TH-2966_176103027

flexible rotor balancing can be carried out in the experimental test rig with the utilization of three balancing planes and VTEICM.

5. The MHICM can be extended to identify multiple faults in the misaligned rotor systems with residual unbalances. The finite element model of the rotor-AMB system with misaligned shafts can be developed to test the above algorithm, followed by the application of the identification procedure in the experimental test rig.
6. The residual shaft bow has been removed from the 1X amplitude of the displacement responses. To estimate the amount of residual shaft bow, the identification algorithm can be modified with the inclusion of bow as an additional fault parameter.
7. The estimation of the AMB stiffness parameters can be carried out along with the fault parameters with the utilization of excitation or control force of the AMB.
8. In the present work, the rotor system is supported on the conventional bearings, which can be extended with the application of AMB as a support bearing and the unbalances and other fault parameters can be identified with additional magnetic excitations.
9. The present work assumes a linear model of the AMB and support bearings to estimate the unbalances. The nonlinear behavior of the rotor components can be included in the system, and the effectiveness of the identification algorithm can be studied.
10. In the cracked rotor-AMB system, the location of the crack is assumed to be known for the identification of the fault parameters. Therefore, the localization of the crack parameters can be included in the identification algorithm.

From here, a multitude of possibilities for further research and development on the theme lies waiting to be explored, with numerous interesting and useful discoveries surely to be made.

TH-2966_176103027

TH-2966_176103027

APPENDIX A. Influence Coefficient Matrices

1. The influence coefficient matrices utilized in the description of conventional ICM and VTEICM in sections 2.3.1 and 2.3.2 are given as

$$\mathbf{B}_I(\omega)=\begin{bmatrix}\beta_{d_1 1}(\omega) & \beta_{d_1 2}(\omega) & \dots & \beta_{d_1 n}(\omega)\\ \beta_{d_2 1}(\omega) & \beta_{d_2 2}(\omega) & \dots & \beta_{d_2 n}(\omega)\\ \vdots & \vdots & \ddots & \vdots\\ \beta_{d_h 1}(\omega) & \beta_{d_h 2}(\omega) & \dots & \beta_{d_h n}(\omega)\end{bmatrix};$$

$$\mathbf{A}(\omega)=\begin{bmatrix}\alpha_{11}(\omega) & \alpha_{12}(\omega) & \cdots & \alpha_{1n}(\omega) & \alpha_{1m}(\omega)\\ \alpha_{21}(\omega) & \alpha_{22}(\omega) & \cdots & \alpha_{2n}(\omega) & \alpha_{2m}(\omega)\\ \vdots & \vdots & \ddots & \vdots & \vdots\\ \alpha_{n1}(\omega) & \alpha_{n2}(\omega) & \cdots & \alpha_{nn}(\omega) & \alpha_{nm}(\omega)\\ \alpha_{m1}(\omega) & \alpha_{m2}(\omega) & \cdots & \alpha_{mn}(\omega) & \alpha_{mm}(\omega)\end{bmatrix} \quad \text{(A.1)}$$

2. The influence coefficient matrices utilized in the description of VELSHSB in sections 3.2 and 3.3 are given as

$$\boldsymbol{\gamma}_r(\omega)=\begin{bmatrix}\gamma_{1,1}(\omega) & \gamma_{1,2}(\omega) & \cdots & \gamma_{1,p}(\omega)\\ \gamma_{2,1}(\omega) & \gamma_{2,2}(\omega) & \cdots & \gamma_{2,p}(\omega)\\ \vdots & \vdots & \ddots & \vdots\\ \gamma_{k,1}(\omega) & \gamma_{k,2}(\omega) & \cdots & \gamma_{k,p}(\omega)\end{bmatrix};\quad \boldsymbol{\gamma}_b(\omega)=\begin{bmatrix}\gamma_{1,1}(\omega) & \gamma_{1,2}(\omega) & \cdots & \gamma_{1,n}(\omega)\\ \gamma_{2,1}(\omega) & \gamma_{2,2}(\omega) & \cdots & \gamma_{2,n}(\omega)\\ \vdots & \vdots & \ddots & \vdots\\ \gamma_{k,1}(\omega) & \gamma_{k,2}(\omega) & \cdots & \gamma_{k,n}(\omega)\end{bmatrix} \quad \text{(A.2)}$$

3. The influence coefficient matrices utilized in the description of MVEDRB in sections 4.2.2 and 4.2.3 are given as

$$\begin{bmatrix}\mathbf{a}_1 & \mathbf{a}_2 & \mathbf{a}_3\end{bmatrix}=\begin{bmatrix}\chi_{L_1,L_1} & \chi_{L_1,L_2} & \chi_{L_1,m}\\ \chi_{L_2,L_1} & \chi_{L_2,L_2} & \chi_{L_2,m}\\ \chi_{m,L_1} & \chi_{m,L_2} & \chi_{m,m}\end{bmatrix};\quad \begin{bmatrix}\mathbf{b}_1 & \mathbf{b}_2 & \mathbf{b}_3\end{bmatrix}=\begin{bmatrix}\kappa_{H_1,H_1} & \kappa_{H_1,H_2} & \lambda_{H_1,m}\\ \kappa_{H_2,H_1} & \kappa_{H_2,H_2} & \lambda_{H_2,m}\\ \lambda_{m,H_1} & \lambda_{m,H_2} & \lambda_{m,m}\end{bmatrix} \quad \text{(A .3)}$$

TH-2966_176103027

4. The influence coefficient matrices utilized in description of VELSHSB in section 6.3 are given as

$$\mathbf{N}_r = \begin{bmatrix} N_{1,1} & N_{1,2} & \cdots & N_{1,p} & N_{1,c} & N_{1,a} \\ N_{2,1} & N_{2,2} & \cdots & N_{2,p} & N_{2,c} & N_{2,a} \\ \vdots & \vdots & \ddots & \vdots & \vdots & \vdots \\ N_{p,1} & N_{p,2} & \cdots & N_{p,p} & N_{p,c} & N_{p,a} \\ N_{c,1} & N_{c,2} & \cdots & N_{c,p} & N_{c,c} & N_{c,a} \\ N_{a,1} & N_{a,2} & \cdots & N_{a,p} & N_{a,c} & N_{a,a} \end{bmatrix}; \quad \mathbf{J}_r = \begin{bmatrix} J_{1,1} & J_{1,2} & \cdots & J_{1,p} & J_{1,c} & J_{1,a} \\ J_{2,1} & J_{2,2} & \cdots & J_{2,p} & J_{2,c} & J_{2,a} \\ \vdots & \vdots & \ddots & \vdots & \vdots & \vdots \\ J_{p,1} & J_{p,2} & \cdots & J_{p,p} & J_{p,c} & J_{p,a} \\ J_{c,1} & J_{c,2} & \cdots & J_{c,p} & J_{c,c} & J_{c,a} \\ J_{a,1} & J_{a,2} & \cdots & J_{a,p} & J_{a,c} & J_{a,a} \end{bmatrix} \tag{A.4}$$

where, $N_{p,p}$ is the influence coefficient corresponding to the displacement response at p^{th} measurement planes due to unit load at p^{th} disc locations. $J_{p,p}$ is the influence coefficient corresponding to virtual current at the p^{th} measurement planes due to unit load at p^{th} disc locations. $J_{c,p}$ is the influence coefficient corresponding to virtual current at the c^{th} measurement planes due to unit load at p^{th} disc locations. $J_{a,p}$ is the influence coefficient corresponding to control current at the a^{th} measurement planes due to unit load at p^{th} disc locations.

TH-2966_176103027

APPENDIX B. Eigenvalues and damping coefficient estimation

The equation of motion of the rotor system with AMB control is given as

$$\mathbf{M}\ddot{\boldsymbol{\eta}}(t)+\left(\mathbf{C}+k_i k_D\mathbf{S}\right)\dot{\boldsymbol{\eta}}(t)+\left(\mathbf{K}-k_s\mathbf{S}+k_i k_p\mathbf{S}\right)\boldsymbol{\eta}(t)=0 \tag{B.1}$$

$$\mathbf{M}\ddot{\boldsymbol{\eta}}(t)+\mathbf{C}_T\dot{\boldsymbol{\eta}}(t)+\mathbf{K}_T\boldsymbol{\eta}(t)=0;\ \mathbf{C}_T=\mathbf{C}+k_i k_D\mathbf{S};\ \mathbf{K}_T=\mathbf{K}-k_s\mathbf{S}+k_i k_p\mathbf{S} \tag{B.2}$$

The Eq. (B.2) is converted into state-space form to evaluate the eigenvalues of the system corresponding to different modes of the rotor system as

$$\mathbf{A}\begin{Bmatrix}\boldsymbol{\eta}\\ \dot{\boldsymbol{\eta}}\end{Bmatrix}=\begin{bmatrix}[0]_{n\times n} & [I]_{n\times n}\\ -\mathbf{K}_T/\mathbf{M} & \mathbf{C}_T\end{bmatrix}\begin{Bmatrix}\boldsymbol{\eta}\\ \dot{\boldsymbol{\eta}}\end{Bmatrix}=0 \tag{B.3}$$

The eigenvalue (z_I) obtained in Eq. (B.3) corresponding to the first natural frequency is utilized to evaluate the modal damping coefficient (c_m) of the system utilized in section 6.5.1 as

$$z_I=\left(\xi\omega_{nf}\pm \mathrm{j}\sqrt{\left(1-\xi^2\right)}\omega_{nf}\right) \tag{B.4}$$

$$c_m=2\xi m\omega_{nf} \tag{B.5}$$

where, ξ is the damping ratio corresponding to the first natural frequency (ω_{nf}) and m is the total mass of the rotor system.

TH-2966_176103027

TH-2966_176103027

APPENDIX C. Identification matrices

The identification matrices developed for estimation of the fault parameters (MHICM) present in the cracked rotor system, as mentioned in section 6.3, are given as

$$\mathbf{A}_c = \begin{bmatrix} w_s\left(N_{a,c}\right)_0 & -\mathrm{j}\omega w_s\left(N_{a,c}\right)_0 & 0 & 0 & 0 & 0 & 0 & 0 & 0 & 0 \\ 0 & 0 & w_s\left(N_{a,c}\right)_1 & \omega^2\left(N_{a,1}\right)_1 & \cdots & \omega^2\left(N_{a,p}\right)_1 & 0 & 0 & 0 & 0 \\ 0 & 0 & 0 & 0 & \cdots & 0 & w_s\left(N_{a,c}\right)_2 & 0 & 0 & 0 \\ \vdots & \vdots & \vdots & \vdots & \ddots & \vdots & \vdots & \ddots & \vdots & \vdots \\ 0 & 0 & 0 & 0 & \cdots & 0 & 0 & 0 & w_s\left(N_{a,c}\right)_{-1} & 0 \\ \vdots & \vdots & \vdots & \vdots & \ddots & \vdots & \vdots & \vdots & \vdots & \ddots \end{bmatrix} \tag{C.1}$$

$$\mathbf{S}_c = \begin{bmatrix} w_s\left(I_{a,c}\right)_0 & -\mathrm{j}\omega w_s\left(J_{a,c}\right)_0 & 0 & 0 & 0 & 0 & 0 & 0 & 0 & 0 \\ 0 & 0 & w_s\left(J_{a,c}\right)_1 & \omega^2\left(J_{a,1}\right)_1 & \cdots & \omega^2\left(J_{a,p}\right)_1 & 0 & 0 & 0 & 0 \\ 0 & 0 & 0 & 0 & \cdots & 0 & w_s\left(J_{a,c}\right)_2 & 0 & 0 & 0 \\ \vdots & \vdots & \vdots & \vdots & \ddots & \vdots & \vdots & \ddots & \vdots & \vdots \\ 0 & 0 & 0 & 0 & \cdots & 0 & 0 & 0 & w_s\left(J_{a,c}\right)_{-1} & 0 \\ \vdots & \vdots & \vdots & \vdots & \ddots & \vdots & \vdots & \vdots & \vdots & \ddots \end{bmatrix} \tag{C.2}$$

TH-2966_176103027

TH-2966_176103027

REFERENCES

Adams M L (2000) *Rotating Machinery Vibration: From Analysis to Troubleshooting*. CRC Press, New York.

Aenis M, Knopf E, and Nordmann R (2002) Active magnetic bearings for the identification and fault diagnosis in turbomachinery. *Mechatronics* 12(8): 1011-1021.

Ait Ben Ahmed A, Touache A, El Hakimi A, and Chamat A (2020) A new hybrid method for rigid and flexible rotor balancing without phase response measurements. *Australian Journal of Mechanical Engineering*:1-13.

Akash K, Lijesh K, Chittlangia V, and Hirani H (2014) Design and implementation of adaptive PID controller for active magnetic bearings. *Technology Letters* 1(12): 18-24.

Al-Badour F, Sunar M, and Cheded L (2011) Vibration analysis of rotating machinery using time-frequency analysis and wavelet techniques. *Mechanical Systems and Signal Processing* 25(6): 2083-2101.

Al-Hussain K (2003) Dynamic stability of two rigid rotors connected by a flexible coupling with angular misalignment. *Journal of Sound And Vibration* 266(2): 217-234.

Al-Hussai K, and Redmond I (2002) Dynamic response of two rotors connected by rigid mechanical coupling with parallel misalignment. *Journal of Sound and Vibration* 249(3): 483-498.

Al-Shudeifat M A, and Butcher E A (2011) New breathing functions for the transverse breathing crack of the cracked rotor system: approach for critical and subcritical harmonic analysis. *Journal of Sound and Vibration* 330(3): 526-544.

TH-2966_176103027

Austerlitz H (2002) *Data Acquisition Techniques Using PCs*. Academic Press, California.

Azeem N, and Xiaoqing Y (2018) Experimental study on the Condition Monitoring of Shaft Unbalance by using Vibrations Spectrum and phase Analysis. *2018 Condition Monitoring and Diagnosis* (CMD). IEEE, 1-6, 23-26 Sept. 2018, Perth, Australia.

Bachovchin K D, Hoburg J F, and Post R F (2012) Stable levitation of a passive magnetic bearing. *IEEE Transactions on Magnetics* 49(1): 609-617.

Bachschmid N, Pennacchi P, and Tanzi E (2010) *Cracked Rotors: A Survey on Static and Dynamic Behaviour Including Modelling and Diagnosis*. Springer Science and Business Media, Chennai.

Bachschmid N, Pennacchi P, Vania A, Gregori L, and Zanetta G (2004) Unbalance identification in a large steam turbogenerator using model-based identification and modal foundation. *Eighth International Conference on Vibrations in Rotating Machinery, Institution of Mechanical Engineers*, 383-392, Sept. 2004, Swansea, UK.

Beltran-Carbajal F, Silva-Navarro G, and Arias-Montiel M (2013) Active unbalance control of rotor systems using on-line algebraic identification methods. *Asian Journal of Control* 15(6): 1627-1637.

Bi C, Wu D, Jiang Q, and Liu Z (2005) Automatic learning control for unbalance compensation in active magnetic bearings. *IEEE Transactions on Magnetics* 41(7): 2270-2280.

Brito L C, Susto G A, Brito J N, and Duarte M A (2022) An explainable artificial intelligence approach for unsupervised fault detection and diagnosis in rotating machinery. *Mechanical Systems and Signal Processing* 163: 108105.

TH-2966_176103027

Broch J T (1980) *Mechanical Vibration and Shock Measurements*. Brüel & Kjaer, Denmark.

Cao G, and Lee C-W (2004) Development of PWM power amplifier for active magnetic bearings. *Fifth World Congress on Intelligent Control and Automation* (IEEE Cat. No. 04EX788), IEEE, 3475-78, 15-19 June 2004, Hangzhou, China.

Chandra N H, and Sekhar A (2016) Fault detection in rotor bearing systems using time frequency techniques. Mechanical systems and signal processing 72: 105-133.

Changsheng Z, and Zhiwei M (2005) A PWM based switching power amplifier for active magnetic bearings. *2005 International Conference on Electrical Machines and Systems*, IEEE, 27-29 Sept. 2005, Nanjing, China.

Chatterton S, Ricci R, and Pennacchi P (2010) Application and comparison of high breakdown-point and bounded-influence estimators to rotor balancing. *Journal of Vibration and Acoustics* 132(6): 064502.

Chen J, Hu W, Cao D, Zhang B, Huang Q, Chen Z, and Blaabjerg F (2019) An imbalance fault detection algorithm for variable-speed wind turbines: A deep learning approach. *Energies* 12(14): 2764.

Chen L-W, Ku D-M (1991) Analysis of whirl speeds of rotor-bearing systems with internal damping by C0 finite elements. *Finite Elements in Analysis and Design* 9(2): 169-176.

Chen M, and Knospe C R (2007) Control approaches to the suppression of machining chatter using active magnetic bearings. *IEEE Transactions on Control Systems Technology* 15(2): 220-232.

TH-2966_176103027

Chen Q, Liu G, and Han B (2017) Unbalance vibration suppression for AMBs system using adaptive notch filter. *Mechanical Systems and Signal Processing* 93: 136-150.

Chen S-L, and Liu K-Y (2017) Sensorless Control for a Three-pole Active Magnetic Bearing System. *Applied Computational Electromagnetics Society Journal* 32(8).

Chiba A, Fukao T, Ichikawa O, Oshima M, Takemoto M, and Dorrell D G (2005) *Magnetic Bearings and Bearingless Drives*. Elsevier, Burlington.

Cohen L (1995) *Time-Frequency Analysis*. Prentice Hall, New Jersey.

Cole M O, Keogh P S, Sahinkaya M N, and Burrows C R (2004) Towards fault-tolerant active control of rotor–magnetic bearing systems. *Control Engineering Practice* 12(4): 491-501.

Combet F, and Gelman L (2007) An automated methodology for performing time synchronous averaging of a gearbox signal without speed sensor. *Mechanical Systems and Signal Processing* 21(6): 2590-2606.

Cooley J W, and Tukey J W (1965) An algorithm for the machine calculation of complex Fourier series. *Mathematics of Computation* 19(90): 297-301.

da Silva I, Cardoso J R, and Horikawa O (2011) Design considerations for achieving high radial stiffness in an attraction-type magnetic bearing with control in a single direction. *IEEE Transactions on Magnetics* 47(10): 4112-4115.

da Silva Tuckmantel F W, and Cavalca K L (2019) Vibration signatures of a rotor-coupling-bearing system under angular misalignment. *Mechanism and Machine Theory* 133: 559-583.

TH-2966_176103027

Darpe A, Gupta K, and Chawla A (2004a) Transient response and breathing behaviour of a cracked Jeffcott rotor. *Journal of Sound and Vibration* 272(1-2): 207-243.

Darpe A, Gupta K, and Chawla A (2004b). Coupled bending, longitudinal and torsional vibrations of a cracked rotor. *Journal of Sound and Vibration* 269(1-2): 33-60.

Darpe A, Gupta K, and Chawla A (2006) Dynamics of a bowed rotor with a transverse surface crack. *Journal of Sound and Vibration* 296(4-5): 888-907.

Davies A (1998) Visual inspection systems. In *Handbook of Condition Monitoring* (pp. 57-77): Springer, Dordrecht.

De Castro H F, Cavalca K L, De Camargo L W F, and Bachschmid N (2010) Identification of unbalance forces by metaheuristic search algorithms. *Mechanical Systems And Signal Processing* 24(6): 1785-1798.

De Silva, C W (2007) *Vibration Monitoring, Testing, and Instrumentation*. CRC Press, Boca Raton.

Deepthikumar M, Sekhar A, and Srikanthan M (2014) Balancing of flexible rotor with bow using transfer matrix method. *Journal of Vibration and Control* 20(2): 225-240.

Defoy B, Alban T, and Mahfoud J (2014) Experimental assessment of a new fuzzy controller applied to a flexible rotor supported by active magnetic bearings. *Journal of Vibration and Acoustics* 136(5).

Den Hartog J P (1985) *Mechanical Vibrations*. Courier Corporation, New York.

Deng H, Diao Y, Zhang J, Zhang P, Ma M, Zhong X, and Yu L (2018) Three-dimensional identification for unbalanced mass of rotor systems in operation. *Applied Sciences* 8(2): 173.

TH-2966_176103027

Di L, and Lin Z (2014) Control of a flexible rotor active magnetic bearing test rig: a characteristic model based all-coefficient adaptive control approach. *Control Theory and Technology* 12(1): 1-12.

Dimentberg M (2005) Vibration of a rotating shaft with randomly varying internal damping. *Journal of Sound and Vibration* 285(3): 759-765.

Diniz P S, Da Silva E A, and Netto S L (2010) *Digital Signal Processing: System Analysis and Design*. Cambridge University Press New York.

Dohnal F, and Sekhar A (2014) Current signature analysis for unbalance fault detection in a rotor supported by active magnetic bearings. *International Journal of Condition Monitoring* 4(1): 2-8.

Dyer S W, Shi J, Ni J, and Shin K-K (2002) Robust optimal influence-coefficient control of multiple-plane active rotor balancing systems. *J. Dyn. Sys., Meas., Control* 124(1): 41-46.

Eaton D, Rama J, and Singhal S (2010) Magnetic bearing applications & economics. 57th Annual Petroleum and Chemical Industry Conference (PCIC), IEEE, 20-22 Sept. 2010, (pp. 1-9), Texas, USA.

Ebrahimi A, Heydari M, and Behzad M (2018) Optimal vibration control of rotors with an open edge crack using an electromagnetic actuator. *Journal of Vibration and Control* 24(1): 37-59.

Edwards S, Lees A, Friswell M (2000) Experimental identification of excitation and support parameters of a flexible rotor-bearings-foundation system from a single run-down. *Journal of Sound and Vibration* 232(5): 963-992.

TH-2966_176103027

El-Shafei A, El-Kabbany A, and Younan A (2004) Rotor balancing without trial weights. *J. Eng. Gas Turbines Power* 126(3): 604-609.

El Arem S, and Maitournam H (2008) A cracked beam finite element for rotating shaft dynamics and stability analysis. *Journal of Mechanics of Materials and Structures* 3(5): 893-910.

Fang J, Wang Y, Han B, and Zheng S (2013) Field balancing of magnetically levitated rotors without trial weights. *Sensors* 13(12): 16000-16022.

Feldman M (2011) Hilbert transform in vibration analysis. *Mechanical Systems and Signal Processing*, 25(3): 735-802.

Feng Z, Liang M, and Chu F (2013) Recent advances in time–frequency analysis methods for machinery fault diagnosis: A review with application examples. *Mechanical Systems and Signal Processing* 38(1): 165-205.

Ferraris G, Andrianoely M-A, Berlioz A, and Dufour R (2006) Influence of cylinder pressure on the balancing of a rotary compressor. *Journal of Sound and Vibration* 292(3-5): 899-910.

Fischer J, and Strackeljan J (2006) Stability analysis of high speed lab centrifuges considering internal damping in rotor-shaft joints. *Scientific Journal for Fundamentals and Applications of Engineering Mechanics* 26(2): 131-147.

Foiles W, Allaire P, and Gunter E (1998) Rotor balancing. *Shock and Vibration* 5(5, 6): 325-336.

Folea S, Muresan C I, De Keyser R, and Ionescu C M (2015) Theoretical analysis and experimental validation of a simplified fractional order controller for a magnetic

TH-2966_176103027

levitation system. *IEEE Transactions on control systems technology 24*(2): 756-763.

Fu C (2015) The effect of switching cracks on the vibration of a continuous beam bridge subjected to moving vehicles. *Journal of Sound and Vibration* 339: 157-175.

Gangsar P, Pandey R K, and Chouksey M (2021) Unbalance detection in rotating machinery based on support vector machine using time and frequency domain vibration features. *Noise and Vibration Worldwide* 52(4-5): 75-85.

Gasch R (1993) A survey of the dynamic behaviour of a simple rotating shaft with a transverse crack. *Journal of Sound and Vibration* 160(2): 313-332.

Guo D, and Peng Z (2007) Vibration analysis of a cracked rotor using Hilbert–Huang transform. *Mechanical Systems and Signal Processing 21*(8): 3030-3041.

Guo H, Jack L B, and Nandi A K (2005) Feature generation using genetic programming with application to fault classification. *IEEE Transactions on Systems, Man, and Cybernetics, Part B (Cybernetics)* 35(1): 89-99.

Han D-J (2007) Generalized modal balancing for non-isotropic rotor systems. *Mechanical Systems and Signal Processing 21*(5): 2137-2160.

Han Q, and Chu F (2013) Dynamic response of cracked rotor-bearing system under time-dependent base movements. *Journal of Sound and Vibration* 332(25): 6847-6870.

Hassenpflug H L, Flack R D and Gunter E J (1981) Influence of acceleration on the critical speed of a Jeffcott rotor. Journal of Engineering for Gas Turbines and Power, 103: 108-113.

TH-2966_176103027

Hong S-K, and Langari R (2000) Robust fuzzy control of a magnetic bearing system subject to harmonic disturbances. *IEEE Transactions on Control Systems Technology* 8(2): 366-371.

Hsu C-T, and Chen S-L (2003) Nonlinear control of a 3-pole active magnetic bearing system. *Automatica* 39(2): 291-298.

Hung J Y (1993) Magnetic bearing control using fuzzy logic. *Conference Record of the 1993 IEEE Industry Applications Conference Twenty-Eighth IAS Annual Meeting*, IEEE, 2-8 Sept. 1993, Toronto, Canada.

Hutterer M, Hofer M, and Schrödl M (2015) Selfsensing unbalance rejection and reduction of the gyroscopic effect for an active magnetic bearing system. *2015 10th Asian Control Conference (ASCC)*, IEEE, 31 May - 03 June, Kota Kinabalu, Malaysia.

Inoue T, Liu J, Ishida Y, and Yoshimura Y (2009) Vibration control and unbalance estimation of a nonlinear rotor system using disturbance observer. *Journal of Vibration and Acoustics* 131(3).

ISO 1940/1 (1986) Balance Quality Requirements of Rigid Rotors, International Organization for Standardization.

ISO 11342 (1998) Mechanical vibration – methods and criteria for the mechanical balancing of flexible rotors.

ISO 14839-2 (2004) Mechanical vibration – vibration of rotating machinery equipped with active magnetic bearings.

Jardine A K, Lin D, and Banjevic D (2006) A review on machinery diagnostics and prognostics implementing condition-based maintenance. *Mechanical Systems and Signal Processing* 20(7): 1483-1510.

TH-2966_176103027

Jiang K, and Zhu C (2011) Multi-frequency periodic vibration suppressing in active magnetic bearing-rotor systems via response matching in frequency domain. *Mechanical Systems and Signal Processing* 25(4): 1417-1429.

Johnson M E, Nascimento L P, Kasarda M, and Fuller C R (2003) The effect of actuator and sensor placement on the active control of rotor unbalance. *J. Vib. Acoust.* 125(3): 365-373.

Jun O S (2004) Influence coefficients on rotor having thick shaft elements and resilient bearings. *Journal of Sound and Vibration* 272(3-5): 657-673.

Kang Y, Lin T-W, Chang Y-J, Chang Y-P, and Wang C-C (2008) Optimal balancing of flexible rotors by minimizing the condition number of influence coefficients. *Mechanism and Machine Theory* 43(7): 891-908.

Kang Y, Shih Y-P, and Lee A-C (1992) Investigation on the steady-state responses of asymmetric rotors. *Journal of Vibration and Acoustics* 114: 194-208

Kang Y, Tseng M-H, Wang S-M, Chiang C-P, and Wang C-C (2003) An accuracy improvement for balancing crankshafts. *Mechanism and Machine Theory* 38(12): 1449-1467.

Kasarda M, Marshall J, and Prins R (2007) Active magnetic bearing based force measurement using the multi-point technique. *Mechanics Research Communications* 34(1): 44-53.

Kejian J, Changsheng Z, and Liangliang C (2015) Unbalance compensation by recursive seeking unbalance mass position in active magnetic bearing-rotor system. *IEEE Transactions on Industrial Electronics,* 62: 5655-5664.

TH-2966_176103027

Khader S A, Liu B, and Sjöberg J (2014) System identification of active magnetic bearing for commissioning. *Proceedings of 2014 International Conference on Modelling, Identification and Control*, IEEE, 3-5 Dec. 2014, Melbourne, Australia.

Khulief Y, Mohiuddin M A, and El-Gebeily M (2014a) A new method for field-balancing of high-speed flexible rotors without trial weights. *International Journal of Rotating Machinery* 2014: 1-11.

Khulief Y, Oke W, and Mohiuddin M (2014b) Modally tuned influence coefficients for low-speed balancing of flexible rotors. *Journal of Vibration and Acoustics* 136(2).

Kıral Z, and Karagülle H (2006) Vibration analysis of rolling element bearings with various defects under the action of an unbalanced force. *Mechanical Systems and Signal Processing* 20(8): 1967-1991.

Kirianaki N V, Yurish S Y, Shpak N O, and Deynega V P (2002) *Data Acquisition And Signal Processing For Smart Sensors*. Wiley Chichester, England.

Kulesza Z (2015) Virtual collocation method for a flexible rotor supported by active magnetic bearings. *Journal of Vibration and Control* 21(8): 1522-1538.

Kulesza Z, and Sawicki J T (2012) Rigid finite element model of a cracked rotor. *Journal of Sound and Vibration* 331(18): 4145-4169.

Kumar C, and Rastogi V (2009) A brief review on dynamics of a cracked rotor. *International Journal of Rotating Machinery* 2009: 1-6.

Lacey S J (2008) An overview of bearing vibration analysis. *Maintenance and Asset Management* 23(6): 32-42.

TH-2966_176103027

Lee C-W, Ha Y-H, Joh C-Y, and Kim C-S (1996) In-situ identification of active magnetic bearing system using directional frequency response functions. *J. Dyn. Sys. Meas. Control* 118: 586-592.

Lee C-W, Joh Y-D, and Kim Y-D (1990) Automatic modal balancing of flexible rotors during operation: Computer controlled balancing head. *Proceedings of the Institution of Mechanical Engineers, Part C: Mechanical Engineering Science* 204(1): 19-28.

Lee C-W, and Kim Y (1987) Modal balancing of flexible rotors during operation: design and manual operation of balancing head. *Proceedings of the Institution of Mechanical Engineers, Part C: Journal of Mechanical Engineering Science* 201(5): 349-355.

Lee Y-S, and Lee C-W (1999) Modelling and vibration analysis of misaligned rotor-ball bearing systems. *Journal of Sound and Vibration* 224(1): 17-32.

Lees A, Sinha J, and Friswell M (2009) Model-based identification of rotating machines. *Mechanical Systems and Signal Processing* 23(6): 1884-1893.

Lees A, Sinha J K, and Friswell M I (2004) The identification of the unbalance of a flexible rotating machine from a single rundown. *J. Eng. Gas Turbines Power* 126: 416-21.

Levecque N, Mahfoud J, Violette D, Ferraris G, and Dufour R (2011) Vibration reduction of a single cylinder reciprocating compressor based on multi-stage balancing. *Mechanism and Machine Theory* 46(1): 1-9.

TH-2966_176103027

Li K, Peng C, Deng Z, Huang W, and Zhang Z (2021) Field dynamic balancing for active magnetic bearings supporting rigid rotor shaft based on extended state observer. *Mechanical Systems and Signal Processing* 158: 107801.

Li X, Zheng L, and Liu Z (2013) Balancing of flexible rotors without trial weights based on finite element modal analysis. *Journal of Vibration and Control* 19(3): 461-470.

Lin Y, and Chu F (2010) The dynamic behavior of a rotor system with a slant crack on the shaft. *Mechanical Systems and Signal Processing* 24(2): 522-545.

Lindlau J D, and Knospe C R (2002) Feedback linearization of an active magnetic bearing with voltage control. *IEEE Transactions on Control Systems Technology* 10(1): 21-31.

Liu S, and Qu L (2008) A new field balancing method of rotor systems based on holospectrum and genetic algorithm. *Applied Soft Computing* 8(1): 446-455.

Lum K-Y, Coppola V T, and Bernstein D S (1998) Adaptive virtual autobalancing for a rigid rotor with unknown mass imbalance supported by magnetic bearings. *J. Vib. Acoust* 120: 557-570.

Lyu M, Liu T, Wang Z, Yan S, Jia X, and Wang Y (2018) A control method of the rotor re-levitation for different orbit responses during touchdowns in active magnetic bearings. *Mechanical Systems and Signal Processing* 105: 241-260.

Marshall J T, Kasarda M E, and Imlach J (2001) *A Multi-Point Measurement Technique for the Enhancement of Force Measurement with Active Magnetic Bearings* (Vol. 78538). American Society of Mechanical Engineers, New Orleans.

TH-2966_176103027

Martynenko G (2016) Resonance mode detuning in rotor systems employing active and passive magnetic bearings with controlled stiffness. *International Journal of Automotive and Mechanical Engineering* 13: 3293.

Maslen E H, and Schweitzer G (2009) *Magnetic Bearings: Theory, Design, and Application to Rotating Machinery*. Springer, London.

Matsuda K, Kanemitsu Y, and Kijimoto S (2007) Optimal number of stator poles for compact active radial magnetic bearings. *IEEE Transactions on Magnetics* 43(8): 3420-3427.

Matsushita O, Tanaka M, Kanki H, Kobayashi M, and Keogh P (2017) Stability problems in rotor systems. *Vibrations of Rotating Machinery*, Springer, 287-319, Tokyo.

McFadden P, and Toozhy M (2000) Application of synchronous averaging to vibration monitoring of rolling element bearings. *Mechanical Systems and Signal Processing* 14(6): 891-906.

McMillan R B (2020) *Rotating Machinery: Practical Solutions to Unbalance and Misalignment*. CRC Press, Denmark.

Mendes R U, and Dohnal F (2018) Modal balancing using parametric combination resonance. *International Conference on Rotor Dynamics*, Springer, 129-144, 23-27 Sept. 2018, Rio de Janeiro, Brazil.

Menshikov Y (2013) Identification of rotor unbalance as inverse problem of measurement. *Advances in Pure Mathematics* 9A (2013): 1-6.

Mitenkov F, Znyshev V, Kiryushina E, Nikolaev M Y, Ovchinnikov V, and Fadeev A (2007) An algorithm for determination of the disbalance of a rotor with

TH-2966_176103027

electromagnetic bearings. *Journal of Machinery Manufacture and Reliability* 36(4): 309-313.

Morais T S, Steffen Jr V, and Mahfoud J (2012) Control of the breathing mechanism of a cracked rotor by using electro-magnetic actuator: numerical study. *Latin American Journal of Solids and Structures* 9(5): 581-596.

Mushi S E, Lin Z, and Allaire P E (2011) Design, construction, and modeling of a flexible rotor active magnetic bearing test rig. *IEEE/ASME Transactions on Mechatronics* 17(6): 1170-1182.

Nayana B, and Geethanjali P (2017) Analysis of statistical time-domain features effectiveness in identification of bearing faults from vibration signal. *IEEE Sensors Journal* 17(17): 5618-5625.

Nelson H, and Nataraj C (1986) The dynamics of a rotor system with a cracked shaft. *J. Vib., Acoust.* 108: 189-196.

Nelson H D (2002) Steady synchronous response and balancing of rotor systems with residual shaft bow. *International Journal of Rotating Machinery* 8(6): 431-438.

Nicholas J, Gunter E, and Allaire P (1976a) Effect of residual shaft bow on unbalance response and balancing of a single mass flexible rotor—Part I: Unbalance response. *J. Eng. Power* 98(2): 171-181.

Nicholas J, Gunter E, and Allaire P (1976b) Effect of Residual Shaft Bow on Unbalance Response and Balancing of a Single Mass Flexible Rotor—Part II: Balancing. *J. Eng. Power* 98(2): 182-187.

TH-2966_176103027

Noshadi A, Shi J, Lee W S, Shi P, and Kalam A (2016) Optimal PID-type fuzzy logic controller for a multi-input multi-output active magnetic bearing system. *Neural computing and applications* 27(7): 2031-2046.

Nyce D S (2004) *Linear Position Sensors: Theory and Application*. John Wiley and Sons, New Jersey.

Ocampo J C, Wing E S G, Moroyoqui F J R, Pliego A A, Ortega A B, and Mayén J (2017) A novel methodology for the angular position identification of the unbalance force on asymmetric rotors by response polar plot analysis. *Mechanical Systems and Signal Processing* 95: 172-186.

Patel T H, and Darpe A K (2009a) Experimental investigations on vibration response of misaligned rotors. *Mechanical Systems and Signal Processing* 23(7): 2236-2252.

Patel T H, and Darpe A K (2009b) Vibration response of misaligned rotors. *Journal of Sound and Vibration* 325(3): 609-628.

Peng H, He Q, Zhai P, and Zhen, Y (2017) Stability analysis of an open cracked rotor with the anisotropic rotational damping in rotating operation. *Applied Mathematical Modelling* 45: 405-421.

Pennacchi P, Bachschmid N, and Vania A (2006) A model-based identification method of transverse cracks in rotating shafts suitable for industrial machines. *Mechanical Systems and Signal Processing* 20(8): 2112-2147.

Penny J E, Friswell M I, and Zhou C (2006) Condition monitoring of rotating machinery using active magnetic bearings. *Proceedings of the ISMA International Conference on Noise and Vibration Engineering*, 3497-3506, 18-20 Sept. 2006, Heverlee, Belgium.

TH-2966_176103027

Pham M N, and Ahn H-J (2014) Experimental optimization of a hybrid foil–magnetic bearing to support a flexible rotor. *Mechanical Systems and Signal Processing* 46(2): 361-372.

Polajzer B (2010) *Magnetic Bearings, Theory and Applications*. Sciyo, Croatia.

Polajžer B, Ritonja J, Štumberger G, Dolinar D, and Lecointe J-P (2006) Decentralized PI/PD position control for active magnetic bearings. *Electrical Engineering* 89(1): 53-59.

Prabhakar S, Sekhar A S, and Mohanty A R (2002) Transient lateral analysis of a slant-cracked rotor passing through its flexural critical speed. Mechanism and Machine Theory, 37: 1007-1020.

Prasad V, and Tiwari R (2019) Identification of speed-dependent active magnetic bearing parameters and rotor balancing in high-speed rotor systems. *Journal of Dynamic Systems, Measurement, and Control* 141(4).

Provenza A J, Montague G T, Jansen M J, Palazzolo A B and Jansen R H (2003) High temperature characterization of a radial magnetic bearing for turbomachinery. In Turbo Expo: Power for Land, Sea, and Air, 16-19 June, 2003, 36878: pp. 633-642, Georgia, USA.

Psonis T K, Nikolakopoulos P G, and Mitronikas E (2015) Design of a PID controller for a linearized magnetic bearing. *International Journal of Rotating Machinery* 2015: 1-12.

Quinn D D, Mani G, Kasarda M E, Bash T, Inman D J, and Kirk R G (2005) Damage detection of a rotating cracked shaft using an active magnetic bearing as a force

TH-2966_176103027

actuator-analysis and experimental verification. *IEEE/ASME Transactions on Mechatronics* 10(6): 640-647.

Racic Z, and Hidalgo J (2007) Practical balancing of flexible rotors for power generation. *2007 International Design Engineering Technical Conferences and Computers and Information in Engineering Conference*, ASME, 1143-1152, 4-7 Sept. 2007, Las Vegas, USA.

Randall R B (2021) *Vibration-Based Condition Monitoring: Industrial, Automotive and Aerospace Applications*. John Wiley and Sons, New Jersey.

Ricci R, and Pennacchi P (2012) Discussion of the dynamic stability of a multi-degree-of-freedom rotor system affected by a transverse crack. *Mechanism and Machine Theory* 58: 82-100.

Rieger N F (1986) *Balancing of Rigid and Flexible Rotors*. Shock and Vibration Information Center, US Department of Defense, Washington.

Rodrigues D, Champneys A, Friswell M, and Wilson R (2008) Automatic two-plane balancing for rigid rotors. *International Journal of Non-Linear Mechanics* 43(6): 527-541.

Roques S, Legrand M, Cartraud P, Stoisser C and Pierre C (2010) Modeling of a rotor speed transient response with radial rubbing. Journal of Sound and Vibration, 329(5): pp.527-546.

Roy D K, and Tiwari R (2019) Development of identification procedure for the internal and external damping in a cracked rotor system undergoing forward and backward whirls. *Archive of Mechanical Engineering*: 229-255.

TH-2966_176103027

Roy D K, and Tiwari R (2020) Estimation of the internal and external damping from the forward and backward spectrum of a rotor with a fatigue crack. *Propulsion and Power Research* 9(1): 62-74.

Sabirin C R, Binder A, Popa D D, and Craciunescu A (2007) Modeling and digital control of an active magnetic bearing system. *Romanian Journal of Technical Sciences Electrotechnics and Energy Series* 52(2): 157.

Sabnavis G, Kirk R G, Kasarda M, and Quinn D (2004) Cracked shaft detection and diagnostics: a literature review. *Shock and Vibration Digest* 36(4): 287.

Saeed N, and Kamel M (2017) Active magnetic bearing-based tuned controller to suppress lateral vibrations of a nonlinear Jeffcott rotor system. *Nonlinear Dynamics* 90(1): 457-478.

Sahinkaya M N, Abulrub A-H G, and Burrows C R (2011) An adaptive multi-objective controller for flexible rotor and magnetic bearing systems. *J. Dyn. Sys., Meas., Control* 133: 031003, 1-9.

Sanches F D, and Pederiva R (2016) Theoretical and experimental identification of the simultaneous occurrence of unbalance and shaft bow in a Laval rotor. *Mechanism and Machine Theory* 101: 209-221.

Sarmah N, and Tiwari R (2020) Analysis and identification of the additive and multiplicative fault parameters in a cracked-bowed-unbalanced rotor system integrated with an auxiliary active magnetic bearing. *Mechanism and Machine Theory* 146: 103744.

TH-2966_176103027

Sawicki J T, Friswell M I, Kulesza Z, Wroblewski A, and Lekki J D (2011) Detecting cracked rotors using auxiliary harmonic excitation. *Journal of Sound and Vibration* 330(7): 1365-1381.

Sawicki J T, Friswell M I, Pesch A H, and Wroblewski A (2008) Condition monitoring of rotor using active magnetic actuator. *Turbo Expo: Power for Land, Sea, and Air*, ASME, 1257, 1265, 9-13 Jun 2008, Berlin.

Schuhmann T, Hofmann W, and Werner R (2011) Improving operational performance of active magnetic bearings using Kalman filter and state feedback control. *IEEE Transactions on Industrial Electronics* 59(2): 821-829.

Schweitzer G, and Maslen E H (2009) *Magnetic Bearings. Theory, Design, and Application to Rotating Machinery*. Springer, London.

Sekhar A (2003) Identification of a crack in a rotor system using a model-based wavelet approach. *Structural Health Monitoring* 2(4): 293-308.

Sekhar, A. (2004). Crack identification in a rotor system: a model-based approach. *Journal of Sound and Vibration, 270*(4-5), 887-902.

Setiawan J D, Mukherjee R, and Maslen E H (2002) Synchronous sensor runout and unbalance compensation in active magnetic bearings using bias current excitation. *J. Dyn. Sys., Meas., Control* 124(1): 14-24.

Shravankumar C, and Tiwari R (2013) Identification of stiffness and periodic excitation forces of a transverse switching crack in a Laval rotor. *Fatigue and Fracture of Engineering Materials and Structures* 36(3): 254-269.

Shravankumar C, and Tiwari R (2016) Detection of a fatigue crack in a rotor system using full-spectrum based estimation. *Sadhana* 41(2): 239-251.

TH-2966_176103027

Shravankumar C, and Tiwari R (2019) Experimental identification of cracked rotor system parameters from the forward and backward whirl responses. *Archive of Mechanical Engineering* 66(3).

Shrivastava A, and Mohanty A R (2019) Identification of unbalance in a rotor system using a joint input-state estimation technique. *Journal of Sound and Vibration* 442: 414-427.

Sinclair I (2000) *Sensors and Transducers*. Elsevier, Woburn.

Singh S, and Tiwari R (2016) Model-based switching-crack identification in a Jeffcott rotor with an offset disk integrated with an active magnetic bearing. *Journal of Dynamic Systems, Measurement, and Control* 138(3): 031006.

Singh S, and Vishwakarma M (2015) A review of vibration analysis techniques for rotating machines. *International Journal of Engineering Research and Technology* 4(03): 757-761.

Sinha J K (2015) *Vibration Analysis, Instruments, and Signal Processing* (Vol. 1): CRC press, Boca Raton.

Sinou J-J, and Lees A (2005) The influence of cracks in rotating shafts. *Journal of Sound and Vibration* 285(4-5): 1015-1037.

Song G, Yang Z, Ji C, and Wang F (2013) Theoretical–experimental study on a rotor with a residual shaft bow. *Mechanism and Machine Theory* 63: 50-58.

Spagnol J P, Wu H, and Xiao K (2018) Dynamic response of a cracked rotor with an unbalance influenced breathing mechanism. *Journal of Mechanical Science and Technology* 32(1): 57-68.

TH-2966_176103027

Sperling L, Ryzhik B, Linz C, and Duckstein H (2002) Simulation of two-plane automatic balancing of a rigid rotor. *Mathematics and Computers in Simulation* 58(4-6): 351-365.

Srinivas R S, Tiwari R, Kannababu Ch (2018) Application of active magnetic bearings in flexible rotordynamic systems–A state-of-the-art review. *Mechanical Systems and Signal Processing* 106: 537-572.

Stefanescu D M (2011) *Handbook of Force Transducers: Principles and Components*. Springer Science and Business Media, Berlin.

Su H, and Chong K-T (2006) A Practical Method of Balancing a Rigid Rotor. *International Journal of Precision Engineering and Manufacturing* 7(2): 36-40.

Su H and Chong K T (2004) An efficient method for the mass unbalance analysis of a rotor system using FFT and Lissajous diagram. International conference on control automation and systems: Proceedings of the Conference, pp.1612-1617, Bangkok, Thailand.

Sudhakar G, and Sekhar A (2011) Identification of unbalance in a rotor bearing system. *Journal of Sound and Vibration* 330(10): 2299-2313.

Sujatha C (2010) *Vibration and Acoustics*. Tata McGraw-Hill Education, New Delhi.

Takizuka T, Takada S, Yan X, Kosugiyama S, Katanishi S, and Kunitomi K (2004) R&D on the power conversion system for gas turbine high temperature reactors. Nuclear Engineering and Design, 233(1-3): pp.329-346.

Taylor H (1940) Critical-speed behavior of unsymmetrical shafts. *J. Appl. Mech.* 7: A71-A79.

TH-2966_176103027

Tessarzik J M, Badgley R H, and Anderson W J (1972) Flexible rotor balancing by the exact point-speed influence coefficient method. *J. Eng. Ind.* 94: 148-158.

Thanh L T, Thien N D, and Le Chi C (2018) Study on the Applicability of Influence Coefficient Method Combined with Vector Analysis in Dynamic Balancing Rigid Rotor Using Flexible Supports. *2018 4th International Conference on Green Technology and Sustainable Development (GTSD)*, IEEE, 23-24 Nov. 2018, Ho Chi Minh City, Vietnam.

Tiwari R (2005) Conditioning of regression matrices for simultaneous estimation of the residual unbalance and bearing dynamic parameters. *Mechanical Systems and Signal Processing* 19(5): 1082-1095.

Tiwari R (2017) *Rotor Systems: Analysis and Identification*. CRC press, Boca Raton.

Tiwari R, and Chakravarthy V (2009) Simultaneous estimation of the residual unbalance and bearing dynamic parameters from the experimental data in a rotor-bearing system. *Mechanism and Machine Theory* 44(4): 792-812.

Tiwari R, and Chougale A (2014) Identification of bearing dynamic parameters and unbalance states in a flexible rotor system fully levitated on active magnetic bearings. *Mechatronics* 24(3): 274-286.

Tiwari R, Dohnal F, and Markert R (2012) An extended field balancing procedure for flexible rotors fully levitated by active magnetic bearings. *Tenth International Conference on Vibrations in Rotating Machinery*, Institution of Mechanical Engineers, 11-13 Sept. 2012, London.

Tiwari R, Lees A, Friswell M I (2002) Identification of speed-dependent bearing parameters. *Journal of Sound and Vibration* 254(5): 967-986.

TH-2966_176103027

Tung P-C, Tsai M-T, Chen K-Y, Fan Y-H, and Chou F-C (2011) Design of model-based unbalance compensator with fuzzy gain tuning mechanism for an active magnetic bearing system. *Expert Systems with Applications* 38(10): 12861-12868.

Untaroiu C D, Allaire P E, and Foiles W C (2008) Balancing of flexible rotors using convex optimization techniques: optimum min-max LMI influence coefficient balancing. *Journal of Vibration and Acoustics* 130(2): 021006.

Usher M J, and Keating D (1996) *Sensors and Transducers: Characteristics, Applications, Instrumentation, Interfacing*. Macmillan International Higher Education, London.

Van Loan C (1992) *Computational Frameworks for the Fast Fourier Transform*. SIAM, Philadelphia.

Venkatasubramanian V, Rengaswamy R, and Kavuri S N (2003) A review of process fault detection and diagnosis: Part II: Qualitative models and search strategies. *Computers and Chemical Engineering* 27(3): 313-326.

Villafane Saldarriaga M, Steffen Jr V, Der Hagopian J, Mahfoud J (2011). On the balancing of flexible rotating machines by using an inverse problem approach. *Journal of Vibration and Control* 17(7): 1021-1033.

Vuojolainen J, Nevaranta N, Jastrzebski R, and Pyrhönen O (2017) Comparison of excitation signals in active magnetic bearing system identification. *Modelling Identification and Control* 38: 123-33.

Walker R, Vayanat R, Perinpanayagam S, and Jennions I (2014) Unbalance localization through machine nonlinearities using an artificial neural network approach. *Mechanism and Machine Theory* 75: 54-66.

TH-2966_176103027

Wang A, Cheng X, Meng G, Xia Y, Wo L, and Wang Z (2017) Dynamic analysis and numerical experiments for balancing of the continuous single-disc and single-span rotor-bearing system. *Mechanical Systems and Signal Processing* 86: 151-176.

Wang D, Wang N, Chen K, and Ye C, (2019) Dynamic characteristics of magnetic suspended dual-rotor system by Riccati transfer matrix method. Shock and Vibration, 2019.

Wang D, Wang N and Chen K, (2019) Unbalance response of a magnetic suspended dual-rotor system. Proceedings of the Institution of Mechanical Engineers, Part G: Journal of Aerospace Engineering, 233(15): pp.5758-5772.

Wang N, and Jiang D (2018) Vibration response characteristics of a dual-rotor with unbalance-misalignment coupling faults: theoretical analysis and experimental study. *Mechanism and Machine Theory* 125: 207-219.

Wang N, Jiang D, and Xu H (2019) Dynamic characteristics analysis of a dual-rotor system with inter-shaft bearing. *Proceedings of the Institution of Mechanical Engineers, Part G: Journal of Aerospace Engineering* 233(3): 1147-1158.

Wang X (2007) SQP algorithms in balancing rotating machinery. *Mechanical Systems and Signal Processing* 21(3): 1469-1478.

Wang Y, Fang J, and Zheng S (2014) A field balancing technique based on virtual trial-weights method for a magnetically levitated flexible rotor. *Journal of Engineering for Gas Turbines and Power* 136(9): 092502.

Wang Z-Y, Lin W, and Wen B-C (2010) Analysis on stiffness of rotor system with a switching crack. *Zhendong yu Chongji(Journal of Vibration and Shock)* 29(9): 69-72.

TH-2966_176103027

Wauer J r (1990) On the dynamics of cracked rotors: a literature survey. *Appl. Mech. Rev.* 43: 13-17.

Weißbacher C, Stelzer H, and Hameyer K (2009) Application of a tubular linear actuator as an axial magnetic bearing. *IEEE/ASME Transactions on Mechatronics* 15(4): 615-622.

Xia Y, Ren, X., Qin, W., Yang, Y., Lu, K. and Fu, C., 2020. Investigation on the transient response of a speed-varying rotor with sudden unbalance and its application in the unbalance identification. Journal of Low Frequency Noise, Vibration and Active Control, 39(4): pp.1065-1086.

Xu B, Qu L, and Sun R (2000) The optimization technique-based balancing of flexible rotors without test runs. *Journal of Sound and Vibration* 238(5): 877-892.

Xu S, and Fang J (2013) A novel conical active magnetic bearing with claw structure. *IEEE Transactions on Magnetics* 50(5): 1-8.

Xu X, Chen S, and Zhang Y (2016) Automatic balancing of AMB systems using plural notch filter and adaptive synchronous compensation. *Journal of Sound and Vibration* 374: 29-42.

Xu X, and Chen S (2015) Field balancing and harmonic vibration suppression in rigid AMB-rotor systems with rotor imbalances and sensor runout. *Sensors* 15(9): 21876-21897.

Xu X, and Fan P P (2013) Rigid rotor dynamic balancing by two-plane correction with the influence coefficient method. *Applied Mechanics and Materials* 365-366: 211-215.

TH-2966_176103027

Xu Y, Zhou J, Di L, and Zhao C (2017) Active magnetic bearings dynamic parameters identification from experimental rotor unbalance response. *Mechanical Systems and Signal Processing* 83: 228-240.

Yang J, He S, and Wang L (2004) Dynamic balancing of a centrifuge: application to a dual-rotor system with very little speed difference. *Journal of Vibration and Control* 10(7): 1029-1040.

Yang Y, Cao D, Yu T, Wang D, and Li C (2016) Prediction of dynamic characteristics of a dual-rotor system with fixed point rubbing—theoretical analysis and experimental study. *International Journal of Mechanical Sciences* 115: 253-261.

Yao J, Liu L, Yang F, Scarpa F, and Gao J (2018) Identification and optimization of unbalance parameters in rotor-bearing systems. *Journal of Sound and Vibration* 431: 54-69.

Yao J, Yang F, Su Y, Scarpa F, Gao J (2020) Balancing optimization of a multiple speeds flexible rotor. *Journal of Sound and Vibration* 480: 115405.

Ye R, Wang L, Hou X, Luo Z, and Han Q (2018) Balancing method without trial weights for rotor systems based on similitude scale model. *Frontiers of Mechanical Engineering* 13(4): 571-580.

Yu J J (2009) Relationship of influence coefficients between static-couple and multiplane methods on two-plane balancing. *Journal of Engineering for Gas Turbines and Power* 131(1).

Zhang Y, Li M, Yao H, Gou Y, and Wang X (2021) A modal-based balancing method for a high-speed rotor without trial weights. *Mechanical Sciences* 12(1): 85-96.

TH-2966_176103027

Zhang Y, Mei X, Zou D, Sun N, and Zhang J (2011) A new field unbalance estimation method for flexible rotors. *2011 International Mechanical Engineering Congress and Exposition*, ASME, 11-17 Nov 2011, Denver, Colorado.

Zhang Z, Wan K, Li J, and Li X (2018) Synchronization identification method for unbalance of dual-rotor system. *Journal of the Brazilian Society of Mechanical Sciences and Engineering* 40(4): 1-11.

Zhao S, Ren X, Deng W, Lu K, Yang Y, and Fu C (2021) A transient characteristic-based balancing method of rotor system without trail weights. *Mechanical Systems and Signal Processing* 148: 107117.

Zheng S, Han B, Wang Y, and Zhou J (2014) Optimization of damping compensation for a flexible rotor system with active magnetic bearing considering gyroscopic effect. *IEEE/ASME Transactions on Mechatronics* 20(3): 1130-1137.

Zhong Z, and Zhu C (2013) Vibration of flexible rotor systems with two-degree-of-freedom PID controller of active magnetic bearings. *Journal of Vibroengineering* 15(3): 1302-1310.

Zhou J, Di L, Cheng C, Xu Y, and Lin Z (2016) A rotor unbalance response based approach to the identification of the closed-loop stiffness and damping coefficients of active magnetic bearings. *Mechanical Systems and Signal Processing* 66: 665-678.

Zhou S, Dyer S W, Shin K K, Shi J and Ni J (2004) Extended influence coefficient method for rotor active balancing during acceleration. J. Dyn. Sys., Meas., Control, 126(1): pp.219-223.

TH-2966_176103027

Zhou T, Sun Z, Xu J, and Han W (2005) Experimental analysis of cracked rotor. *J. Dyn. Sys., Meas., Control.* 127: 313-20

Zhu C, Robb D A, and Ewins D J (2003) The dynamics of a cracked rotor with an active magnetic bearing. *Journal of Sound and Vibration* 265(3): 469-487.

भारतीय प्रौद्योगिकी संस्थान गुवाहाटी • Indian Institute of Technology Guwahati •

TH-2966_176103027

TH-2966_176103027

List of Publications from the Present Research

Papers communicated/accepted in journals from the thesis work

- G. Ranjan and R. Tiwari, "Application of active magnetic bearings for in situ flexible rotor residual balancing using a novel generalized influence coefficient method," *Inverse Problems in Science and Engineering*, *27*(7), 943-968, 2019.
- G. Ranjan and R. Tiwari, "On-Site High-Speed Balancing of Flexible Rotor-Bearing System Using Virtual Trial Unbalances at Slow Run," *International Journal of Mechanical Sciences*, 105786, 2020.
- G. Ranjan, R. Tiwari, and H. Nemade, "Fault identification in cracked rotor-AMB system using magnetic excitations based on multi harmonic influence coefficient method," *Inverse Problems in Science and Engineering*, pp. 1-31, 2021.
- G. Ranjan, R. Tiwari, and H. B. Nemade, "On-line field balancing technique using virtual trial unbalances in rotor-bearing system incorporated with active magnetic bearing," *Sādhanā*, 47(2), pp.1-18, 2022.
- G. Ranjan, R. Tiwari and H.B. Nemade, "Robust Dynamic Balancing of Dual Rotor-AMB System Through Virtual Trial Unbalances as Low and High Frequency Magnetic Excitation," *ASCE-ASME J Risk and Uncert in Engrg Sys Part B Mech Engrg*, 011203 (page 1-19), 2022.
- G. Ranjan, R. Tiwari and H.B. Nemade, "Experimental Identification of Residual Unbalances in High-Speed Rotor-AMB System with Switching Mode Bias Current Control," *Mechatronics*, Elsevier. (Under review).

TH-2966_176103027

Papers presented in conferences

- G. Ranjan and R. Tiwari, "Sensitivity Analysis of Residual Unbalances in Dynamic Balancing of Rigid Rotors using Influence Coefficient Methods Based on Measurement Error". *National Symposium on Rotor Dynamics- NSRD 2017*, December 12th to 13th, 2017, IIT Patna, India.
- G. Ranjan, R. Tiwari and H. B. Nemade, " Experimental Identification of Residual Unbalances for Two Plane Balancing in a Rigid Rotor System integrated with AMB". *International Conference on Machines and Mechanisms- iNaCoMM, 2019*, December 5th to 7th, 2019, IIT Mandi, India.
- G. Ranjan, R. Tiwari and H. B. Nemade, " Experimental Identification of Residual Unbalances for Single Plane Balancing in a Rigid Rotor System with virtual trial unbalances". *International Conference on Vibration Engineering and Technology of Machinery- VETOMAC, 2021*, December 16th to 18th, 2021, BMS College of Engineering, Bengaluru, India.

TH-2966_176103027